

# **Solution-Processed Perovskite Photodetectors**

Kai Shen

A thesis submitted to UCL for the degree of  
*Doctor of Philosophy (PhD)*

**Department of Electronic and Electrical Engineering**  
**UCL**

January 2021

## **Statement of Originality**

I, Kai Shen confirm that the work presented in this thesis is my own.

Where information has been derived from other sources, I confirm that this has been indicated in the thesis.

Name:

---

Signature:

---

Date:

---

*To my families,  
thank you for the support.*



## ABSTRACT

Photodetectors enable conversion from light signals to electrical signals and are widely used in both the civil and military field for applications such as missile guidance, optical communication, imaging and biomedical sensing. Although various semiconductors have been employed in photodetectors, their high cost and complexity of fabrication have hindered their further development.

Recently, perovskites have attracted substantial interest due to their impressive optoelectronic properties, including tuneable bandgaps, large absorption coefficient, long diffusion length and high carrier mobility. However, perovskites are generally not stable when exposed to ambient air, which seriously degrades the device performance.

In this thesis, all-inorganic perovskite quantum dot (QD)-based photodetectors are investigated to enhance the material quality, device photoresponse and environmental stability. Three efficient strategies are developed to optimise the material film morphology and optical properties, as well as light confinement. I also managed to develop perovskite QD detectors on flexible substrates. Firstly, caesium lead bromide ( $\text{CsPbBr}_3$ ) QDs were optimised by blending ZnO nanoparticles (NPs), and further employed in a heterostructured photodetector. The as-fabricated device exhibited an improved photoresponse, including a 10-fold improved responsivity ( $0.4 \text{ mA W}^{-1}$ ) and a short response time of 73.5 ms, as well as an excellent air stability ( $\sim 7$  month) due to the enhanced film morphology and optical properties after the decoration of ZnO NPs. Secondly, CsBr/KBr additives and a photovoltaic architecture were developed to further boost the device performance. An enhanced surface morphology and crystal quality with reduced defects were achieved by CsBr/KBr mediation. The resulting flexible photodetectors exhibited a better photoresponse, good flexibility and outstanding electrical stability. Specifically, this optimized photodetector showed a high responsivity of  $10.1 \text{ A W}^{-1}$ , a large detectivity approaching  $10^{14}$  Jones, and an on/off ratio around  $10^4$ . In

addition to the material optimisations, anodic aluminium oxide plasmonic structures were adopted with control of geometry and decoration of metallic NPs in the perovskite photodetectors, which enabled efficient light transmission and collection, and resulted in a 40-fold enhancement in device photoresponse.

In the future, I will continue to focus on material and structural optimisations to develop high-performance and stable optoelectronics. In addition, perovskite-based focal plane arrays have great potential to be investigated.

## IMPACT STATEMENT

This PhD research project focuses on the fabrication and characterisation of all-inorganic metal halide perovskite photodetectors. During my PhD research career, I have published three research papers as the leading authors and a few collaborative publications as a co-author in high-impact research journals, including *Advanced Materials*, *Journal of Materials Chemistry A*, *etc.* Moreover, one oral talk and one poster were also presented in two international conferences, e.g. The 5<sup>th</sup> Seminar on Photoelectric Detection and Sensing Technology (EMN), and European Materials Research Society (E-MRS). The high-performance and low-cost perovskite photodetectors demonstrated in this thesis have a clear impact on the academia and potentially industry in the area of photodetection. For example, the synthesis method of CsPbBr<sub>3</sub> QDs and the fabrication method of photodetectors on flexible substrate and AAO nanostructures provide an alternative solution to improve the device performance, which are beneficial for the potential industrialisation of perovskite-based photodetectors.

Long-term stability of metal halide perovskite-based devices is an urgent issue worldwide. CsPbBr<sub>3</sub> quantum dots (QDs) are very promising building blocks for practical optoelectronic devices due to the improved stability. In this thesis, an improved device performance has been demonstrated in ZnO nanoparticles (NPs) decorated CsPbBr<sub>3</sub> QD perovskite photodetectors, as work presented in chapter 4. The work shows that the surface morphology of CsPbBr<sub>3</sub> QD film was significantly enhanced by the introduction of ZnO NPs. With the help of ZnO NPs, the gaps between QDs were effectively filled, resulting in efficient carrier transport and collection. Accordingly, the photodetectors decorated by ZnO NPs exhibited a fast response speed (~ 73.5 ms) and long-term stability (~ 7 month). This work was awarded in the Rolls-Royce Scheme from Armourers & Brasiers.

With the rapid development of the 5G and the Internet of Things (IoT), the demand of wearable optoelectronics is ever increasing. Solution-processed CsPbBr<sub>3</sub> QDs show a huge potential in the fabrication of flexible devices in large-scale. In this work, a flexible CsPbBr<sub>3</sub> QD photodetector array is presented (chapter 5). A CsBr/KBr additive strategy was developed to optimise the crystal quality, surface morphology, emission efficiency, and carrier transport of CsPbBr<sub>3</sub> QDs. The resulted flexible devices exhibited an impressive photoresponse, i.e. a responsivity of 9.35 A W<sup>-1</sup> and detectivity over 10<sup>14</sup> Jones, which was comparable or even superior than commercial photodetectors. Moreover, mechanical flexibility, electrical stability as well as spatial uniformity were achieved. Such high-performance and stable flexible devices are promising for the demonstration of the wearable imaging systems.

Due to the limited absorption volume in photodetectors based on low-dimensional materials, a plasmonic structure made of an anodic aluminium oxide (AAO) template decorated by metallic NPs was demonstrated, as presented in chapter 6. With the fine control of the pore size in AAO matrixes, the photoresponse of QD photodetectors has apparently improved over 36 times. Moreover, the device performance was further boosted via the incorporation of aluminium NPs. The metallic NPs concentrated the reflected light beams back to the CsPbBr<sub>3</sub> QD layer, resulting in a cyclic light utilization. Such strategy can also be used in other material systems that suffer from limited light absorption.

## ACKNOWLEDGEMENTS

Firstly, I would like to express my sincere thanks to my primary supervisor, Prof. Jiang Wu, for his guidance and support. He shared not only his knowledge of perovskite materials but also his experience as a PhD researcher with me. His rigorous working attitude and chilled lifestyle also inspired me. Without him, nothing would have been possible. Moreover, I would also like to acknowledge Prof. Kwang-Leong Choy for being my present supervisor. Her rich knowledge reserve inspired me with numerous research ideas. Both of them provided generous support and meticulous solicitude in directing my research work.

I have also received enthusiastic help from members of the MBE group and would like to thank Prof. Huiyun Liu for his support and guidance, Dr. Mingchu Tang, Dr. Dongyoung Kim, Dr. Daqian Guo, Dr. Mengya Liao, Zizhuo Liu, Steven Chan and Xiao Li for guiding and helping me with the photodetector fabrications, Dr. Siming Chen, Dr. Yunyan Zhang, Dr. Xuezhe Yu, Fan Cui, Pouyan Martin, Keshuang Li, Junjie Yang, Haotian Zeng, Huiwen Deng, Shujie Pan and Ying Lu for their support along my research journey. Thanks to Dr. Xiaoyu Han for organising academic events and daily activities, and providing valuable opportunities to communicate with many researchers. I would also like to thank Dr. Mingqing Wang, Dr. Jian Guo, Dr. Ting Zhang, Dr. Mingyu Li, Dr. Aobo Ren and Hao Wang for their valuable contribution to my research work. Special gratitude goes to Dr. Hao Xu, who has supported and provided efficient consultancy to me during my work. There is no doubt that he helped me to develop the solid physics I needed to understand perovskite-based photodetectors.

Finally, I would like to extend my appreciation to my family for their unconditional support throughout my life. Thanks to my parents for their trust and their confidence in me, as well as accepting my regular absence. Especially, thank you so much Chenqiu for your company, for comforting me when I was upset, for encouraging me when I needed it, and for being proud of any successes I achieved. You are my most precious fortune.

# TABLE OF CONTENTS

<b>ABSTRACT</b> .....	1
<b>IMPACT STATEMENT</b> .....	3
<b>ACKNOWLEDGEMENTS</b> .....	5
<b>TABLE OF CONTENTS</b> .....	6
<b>LIST OF FIGURES</b> .....	12
<b>LIST OF TABLES</b> .....	23
<b>LIST OF ABBREVIATIONS, MATERIALS AND ELEMENTS</b> .....	24
Abbreviations .....	24
Materials and Elements .....	26
<b>LIST OF SYMBOLS</b> .....	29
<b>LIST OF PUBLICATIONS AND CONFERENCES</b> .....	32
Publications .....	32
Conferences .....	32
<b>CHAPTER 1. INTRODUCTION</b> .....	33
1.1 Photodetector Overview .....	33
1.2 Development of Perovskite-Based Optoelectronics .....	36
1.3 Challenges and Motivation .....	40
1.4 Objectives .....	42
1.5 Thesis Outline .....	43
1.6 References .....	46

<b>CHAPTER 2. FUNDAMENTALS OF PEROVSKITES .....</b>	<b>50</b>
2.1 Crystal Structures and Chemical Compositions.....	50
2.2 Absorption.....	54
2.3 Recombination .....	59
2.4 Perovskite Morphology .....	61
2.4.1 Bulk Crystals.....	62
2.4.2 Nanostructured Crystals.....	65
2.5 Deposition of Perovskite .....	71
2.6 Figure of Merits.....	72
2.7 Photodetector Architecture.....	74
2.7.1 Photoconductors.....	75
2.7.2 Photodiodes.....	76
2.7.3 Phototransistors.....	76
2.8 Challenges .....	76
2.9 References .....	81
<b>CHAPTER 3. EXPERIMENTAL METHODS.....</b>	<b>86</b>
3.1 Perovskite Preparation.....	86
3.1.1 Chemicals.....	86
3.1.2 CsPbBr <sub>3</sub> QDs .....	87
3.1.3 ZnO NPs Decorated with CsPbBr <sub>3</sub> QDs.....	89
3.1.4 CsBr/KBr Assisted CsPbBr <sub>3</sub> Quantum Dots.....	89

3.2	Material Characterisations.....	91
3.2.1	X-ray Diffraction .....	91
3.2.2	Transmission Electron Microscopy .....	92
3.2.3	X-ray Photoelectron Spectroscopy .....	93
3.2.4	Element Dispersive X-ray Spectroscopy .....	95
3.2.5	Ultraviolet Photoelectron Spectroscopy .....	96
3.3	Optical Characterisations .....	97
3.3.1	Steady-State and Time-Resolved Photoluminescence Measurements .....	97
3.3.2	Absorption Measurements .....	99
3.4	Morphological Characterisations .....	100
3.4.1	Atomic Force Microscopy .....	100
3.4.2	Scanning Electron Microscopy .....	102
3.5	Photodetector Fabrications .....	103
3.5.1	Substrate Preparation .....	103
3.5.2	Photolithography .....	104
3.5.3	Anodic Aluminium Oxide Nanostructure Fabrication.....	105
3.5.4	Electron Transport Layer Deposition.....	106
3.5.5	Active Layer Deposition .....	109
3.5.6	Hole Transport Layer Deposition .....	109
3.5.7	Electrode Deposition.....	110
3.6	Device Characterisations.....	111

3.7	References .....	113
<b>CHAPTER 4. THE STUDY OF ZnO NPs DECORATED ALL-INORGANIC PEROVSKITE PHOTODETECTORS .....</b>		
<b>115</b>		
4.1	Introduction .....	115
4.2	Material Characterisations.....	117
4.2.1	Structural Analysis.....	117
4.2.2	Morphological Evolution .....	120
4.2.3	Optical Characterisations .....	122
4.2.4	Recombination Analysis .....	123
4.3	Device Performance .....	126
4.4	Device Characterisations.....	127
4.4.1	Performance Evolution .....	127
4.4.2	Mechanism.....	130
4.4.3	Photoresponse of ZnO NPs Decorated QDs Photodetector .....	131
4.4.4	Stability .....	134
4.5	Summary .....	135
4.6	References .....	136
<b>CHAPTER 5. THE STUDY OF FLEXIBLE AND SELF-POWERED ALL-INORGANIC CsPbBr<sub>3</sub> QDs PHOTODETECTOR ARRAYS.....</b>		
<b>139</b>		
5.1	Introduction .....	139
5.2	Material Characterisations.....	142
5.2.1	Crystal Structure .....	142

5.2.2	Element Distribution and Composition .....	145
5.2.3	Morphological Evolution .....	149
5.2.4	Optical Properties.....	152
5.2.5	Carrier Dynamics .....	155
5.2.6	Mechanism of Improvements .....	157
5.3	Device Architecture.....	158
5.4	Device Characterisations.....	159
5.4.1	Photoresponse Comparison.....	159
5.4.2	Band Structure .....	163
5.4.3	Performance Comparison.....	165
5.4.4	Photoresponse of CsBr/KBr Doped CsPbBr <sub>3</sub> QDs Photodetector .....	167
5.4.5	Bending Test .....	171
5.4.6	Performance Uniformity .....	173
5.5	Summary .....	174
5.6	References .....	175
<b>CHAPTER 6. THE STUDY OF HYBRID PLASMONIC NANOSTRUCTURE-BASED ALL-INORGANIC PEROVSKITE PHOTODETECTORS .....</b>		<b>178</b>
6.1	Introduction .....	178
6.2	Pore-Size Dependence of Ag/AAO Nanostructure .....	179
6.3	Metallic NP-Decorated AAO Matrix .....	189
6.4	Summary .....	195
6.5	References .....	196

<b>CHAPTER 7. CONCLUSION AND FUTURE PLANS.....</b>	<b>198</b>
7.1 Overall Discussion and Conclusion .....	198
7.2 Future Plans and Outlook.....	201
7.3 References .....	205

## LIST OF FIGURES

<b>Figure 1.1</b> Global semiconductor total sales between 1999 to 2019. <sup>[5]</sup> .....	33
<b>Figure 1.2</b> Distribution of worldwide semiconductor sales by product segment in 2019. <sup>[5]</sup> ..	34
<b>Figure 1.3</b> The PCE development of perovskite solar cells in the last ten years. <sup>[26]</sup> Accessed at 1 <sup>st</sup> April, 2021.....	38
<b>Figure 2.1</b> Typical crystal structure of perovskites.....	52
<b>Figure 2.2</b> Crystal structure of the CsPbBr <sub>3</sub> perovskite in different phases. Reproduced from ref. [18] with permission from Royal Society of Chemistry, copyright 2020. ....	53
<b>Figure 2.3</b> The band diagrams of (a) direct and (b) indirect semiconductors.....	55
<b>Figure 2.4</b> Absorption coefficient of various semiconductor materials in a range of wavelength. <sup>[23]</sup> .....	56
<b>Figure 2.5</b> The tuneable bandgaps with different compositions. <sup>[26]</sup> .....	58
<b>Figure 2.6</b> Recombination pathways of semiconductors. <sup>[31]</sup> .....	60
<b>Figure 2.7</b> Morphology of perovskite single crystal with different dimensions. Reproduced from ref. [32] with permission from Elsevier, copyright 2019. ....	62
<b>Figure 2.8</b> (a) Schematic diagram of the crystallisation process. Reproduced from ref. [33] with permission from The American Association for the Advancement of Science, copyright 2015. (b) Digital images of CH <sub>3</sub> NH <sub>3</sub> PbBr <sub>3</sub> bulk crystals. Reproduced from ref. [34] with permission from American Chemical Society, copyright 2018.....	63
<b>Figure 2.9</b> (a) The setup for bulk single-crystal growth. Reproduced from ref. [35] with permission from The American Association for the Advancement of Science, copyright 2015.	

(b) Digital images of perovskite crystals with varied halide compositions. Reproduced from ref. [36] with no permission. ....64

**Figure 2.10** (a) Schematic representation of the setup for crystallisation. (b)  $\text{CH}_3\text{NH}_3\text{PbBr}_3$  crystal growth at different time intervals. Reproduced from ref. [37] with permission from Nature Publishing Group, copyright 2015. ....65

**Figure 2.11** (a) Low-magnification SEM image of 2D ultrathin  $\text{CsPbBr}_3$  nanosheets. (b) Representation of  $\text{CsPbBr}_3$  nanosheet-based photodetectors. (c) Stability comparisons between  $\text{CsPbBr}_3$  and  $\text{CH}_3\text{NH}_3\text{PbBr}_3$  detectors. Reproduced from ref. [39] with permission from The John Wiley and Sons, copyright 2016. (d) Schematic representation of growth process. (e) Illustration of a phototransistor. Reproduced from ref. [40] with permission from American Chemical Society, copyright 2016. ....66

**Figure 2.12** (a) Schematic illustration of synthesis of porous  $\text{CH}_3\text{NH}_3\text{PbBr}_3$  nanowires. Reproduced from ref. [41] with permission from American Chemical Society, copyright 2016. (b) Synthesis of perovskite nanowire arrays in AAO substrate. Reproduced from ref. [42] with permission from American Chemical Society, copyright 2016. ....67

**Figure 2.13** (a) The overall process for growth of  $\text{CH}_3\text{NH}_3\text{SnI}_3$  nanowires. Reproduced from ref. [43] with permission from American Chemical Society, copyright 2016. (b) Schematic representation of VLS growth process using the Sn catalysts. (c) Responsivity of nanowire photodetectors under illumination with various light intensity. Reproduced from ref. [44] with permission from American Chemical Society, copyright 2019. ....68

**Figure 2.14** (a) Optical images of  $\text{CH}_3\text{NH}_3\text{PbBr}_{3-x}\text{Cl}_x$  and  $\text{CH}_3\text{NH}_3\text{PbBr}_{3-x}\text{I}_x$  colloidal solutions. Reproduced from ref. [49] with permission from American Chemical Society, copyright 2016. (b) Schematic illustration of the synthesis of  $\text{CsPbBr}_3$  nanocrystals.<sup>[51]</sup> Reproduced from ref. [51] with permission from Nature Publishing Group, copyright 2017. ....70

<b>Figure 2.15</b> Summary of photodetector architectures and their advantages and disadvantages. <sup>[58]</sup> .....	75
<b>Figure 2.16</b> Mapping of 138 perovskite materials. Red dots and black dots represent stable and unstable regions, respectively. Reproduced from ref. [62] with permission from American Chemical Society, copyright 2017. ....	78
<b>Figure 2.17</b> Chemical instability of perovskites.....	78
<b>Figure 3.1</b> Synthesis of CsPbBr <sub>3</sub> QDs. <sup>[1]</sup> .....	89
<b>Figure 3.2</b> Synthesis of ZnO NP-decorated CsPbBr <sub>3</sub> QDs. Reproduced from ref. [2] with permission from Royal Society of Chemistry, copyright 2019.....	89
<b>Figure 3.3</b> Synthesis of CsBr/KBr-assisted CsPbBr <sub>3</sub> QDs. Reproduced from ref. [3] with permission from John Wiley and Sons, copyright 2020.....	90
<b>Figure 3.4</b> The working mechanism of XRD. ....	91
<b>Figure 3.5</b> Schematic operation mechanism of TEM. ....	93
<b>Figure 3.6</b> The illustration of XPS. ....	95
<b>Figure 3.7</b> The operation mechanism of PL. <sup>[5]</sup> .....	98
<b>Figure 3.8</b> The working principle of UV-Vis. <sup>[6]</sup> .....	100
<b>Figure 3.9</b> Schematic representation of AFM. <sup>[7]</sup> .....	101
<b>Figure 3.10</b> Schematic drawing of SEM.....	103
<b>Figure 3.11</b> The process of photolithography. ....	105
<b>Figure 3.12</b> Schematic fabrication of the metallic NP-decorated AAO plasmonic nanostructure. ....	106
<b>Figure 3.13</b> The fabrication of glassy graphene. ....	107

<b>Figure 3.14</b> Operation mechanism of $\text{TiO}_2$ deposition by ALD. <sup>[16]</sup> .....	108
<b>Figure 3.15</b> Overview of the thermal evaporator.....	110
<b>Figure 3. 16</b> (a) An overview of the anti-vibration probe stage. (b) Characterising electrical properties of photodetectors under light illumination. ....	112
<b>Figure 4.1</b> XRD measurements for different injections of ZnO NPs from 0 $\mu\text{L}$ to 100 $\mu\text{L}$ . The black dot circle represents the peak at $11.65^\circ$ .....	118
<b>Figure 4.2</b> High-resolved TEM image of (a) pristine $\text{CsPbBr}_3$ QDs and (b) 60 $\mu\text{L}$ ZnO NP-assisted $\text{CsPbBr}_3$ QDs. Insets are the corresponding FFT patterns. (c) Low-magnification TEM image of 60 $\mu\text{L}$ ZnO NP-assisted $\text{CsPbBr}_3$ QDs. (d) The corresponding size distribution of treated QDs.....	119
<b>Figure 4.3</b> The element mappings of ZnO NP-blended $\text{CsPbBr}_3$ QDs.....	120
<b>Figure 4.4</b> SEM images of $\text{CsPbBr}_3$ QD thin films with increasing amount of ZnO NPs from 20 $\mu\text{L}$ to 100 $\mu\text{L}$ . Insets are the corresponding high-magnification SEM images. Samples were all deposited on the glass substrate. ....	121
<b>Figure 4.5</b> AFM images of as-prepared $\text{CsPbBr}_3$ QD films measured under ambient condition. (a) Using soft tapping mode for measuring surface roughness. (b) Using current-sensing mode for verifying surface current. The scale bar is 1 $\mu\text{m}$ . Reproduced from ref. [15] with permission from Royal Society of Chemistry, copyright 2019. ....	122
<b>Figure 4.6</b> Optical properties of ZnO NP-assisted $\text{CsPbBr}_3$ thin film with increasing amount of ZnO. (a) Steady-state absorption spectra. (b) Steady-state PL measurements. (c) The corresponding peak locations and (d) FWHMs extracted from PL spectra.....	123

<b>Figure 4.7</b> (a) TRPL spectra of QDs with ZnO NP decoration. (b) The corresponding decay time and (c) decay component fractions extracted from TRPL as a function of amount of ZnO addition. ....	125
<b>Figure 4.8</b> (a) Schematic device configuration. (b) Digital photograph of as-fabricated photodetector. Reproduced from ref. [15] with permission from Royal Society of Chemistry, copyright 2020. ....	126
<b>Figure 4.9</b> Typical I–V curves of (a) PGH_2 and (b) PGH_1 in dark and illuminated by white light, 405 nm and 520 nm laser diodes. ....	128
<b>Figure 4.10</b> (a) The current comparison between PGH_1 and PGH_2 photodetectors. (b) Their corresponding responsivity under violet and green light. ....	129
<b>Figure 4.11</b> The response time of PGH_1 and PGH_2 under 405 nm laser illumination with an applied bias of 1 V. ....	129
<b>Figure 4.12</b> Schematic illustration of impact of decorating ZnO NPs on photodetectors. Reproduced from ref. [15] with permission from Royal Society of Chemistry, copyright 2019. ....	130
<b>Figure 4.13</b> (a) I–V curves and (b) I–t curves of the photodetectors excited by a 405 nm laser as a function of the light intensity. ....	131
<b>Figure 4.14</b> The fitted intensity-dependent photocurrent. ....	132
<b>Figure 4.15</b> (a) The I–t curves of PGH_1 photodetector employing 405 nm and 520 nm lasers as light source ( $22.8 \text{ mW cm}^{-2}$ ) at 1 V and -1 V, respectively. (b) The time-resolved photocurrent of PGH_1 device under self-powered mode. The corresponding rise and fall time under (c) 1 V and (d) 0 V bias. ....	133

<b>Figure 4.16</b> (a) Stability test of PGH_1 device over 7 months. (b) Time-resolved current in the middle of the stability test. ....	134
<b>Figure 5.1</b> The chemical reaction during the synthesis. ....	141
<b>Figure 5.2</b> TEM images of (a), (b) pristine CsPbBr <sub>3</sub> QDs and (c), (d) 0.025 CsBr/KBr-doped CsPbBr <sub>3</sub> QDs with different magnifications, respectively. The scale bars are 100 nm and 50 nm. ....	142
<b>Figure 5.3</b> High-resolution TEM and corresponding lattice parameters. (a) Pristine QDs, (b) 0.025 CsBr/KBr-assisted QDs. ....	143
<b>Figure 5.4</b> Size distribution of (a) pristine and (b) 0.025 CsBr/KBr-treated CsPbBr <sub>3</sub> QDs. ....	144
<b>Figure 5.5</b> (a) XRD measurements with different ratios of CsBr/KBr treatment from 0.025 to 0.3. (b) The enlarged XRD measurement results. ....	145
<b>Figure 5.6</b> (a) Overview of TEM image and (b) the corresponding mapping of K element. ....	145
<b>Figure 5.7</b> XPS measurements of CsPbBr <sub>3</sub> QD films with different fractions of CsBr/KBr incorporation. (a) Survey spectra and high-resolved scans of the core energy level of (b) Cs 3d, (c) Pb 4f and (d) Br 3d. ....	146
<b>Figure 5.8</b> (a) XPS measurements of K 2p in additive-treated QD thin film. (b) K 2p core level of as-prepared pristine and treated perovskite thin film. Peaks were fitted by CasaXPS. ....	147
<b>Figure 5.9</b> SEM images of pristine and CsBr/KBr-assisted CsPbBr <sub>3</sub> QD films. Scale bar is 3 $\mu\text{m}$ . <sup>[15]</sup> ....	149
<b>Figure 5.10</b> Contact angle measurements for different colloidal perovskite solutions. ....	150
<b>Figure 5.11</b> The corresponding AFM images of each sample. The scale bar is 700 nm. <sup>[15]</sup> ....	151

<b>Figure 5.12</b> (a) Absorptance of each QD film. Absorptions plotted using the Tauc method for the (b) pristine, (c) 0.025, (d) 0.075, (e) 0.2 and (f) 0.3 CsBr/KBr-assisted perovskite QD films. ....	153
<b>Figure 5.13</b> (a) Steady-state PL spectra along with CsBr/KBr treatment. (b) PL peak positions with slight blue-shift.....	154
<b>Figure 5.14</b> (a) TRPL decay curves of each film. The bi-exponential function fitted TRPL decays of (b) pristine, (c) 0.025, (d) 0.075, (e) 0.2, and (f) 0.3 CsBr/KBr doped CsPbBr <sub>3</sub> QDs film. ....	156
<b>Figure 5.15</b> Schematic representation of mediating CsPbBr <sub>3</sub> QDs with CsBr/KBr additives. Reproduced from ref. [15] with permission from John Wiley and Sons, copyright 2020. ....	158
<b>Figure 5.16</b> (a) Digital photographs of flexible photodetector arrays with schematic illustration of device configuration. Images of the flexible devices (b) without and (c) with laser illumination. Reproduced from ref. [15] with permission from John Wiley and Sons, copyright 2020.....	159
<b>Figure 5.17</b> The photoresponse of as-prepared photodetector arrays with different fractions of CsBr/KBr, including pristine (black), 0.025 (red), 0.075 (green), 0.2 (blue) and 0.3 (violet). They were measured (a) in dark, and under (b) 405nm, (c) 450 nm and (d) 520 nm laser illumination, respectively.....	161
<b>Figure 5.18</b> (a) Open-circuit voltage variation under different light illuminations. The corresponding $I/I_d$ extracted from the $I-V$ curves under different illuminations (405 nm, 450 nm and 520 nm) at a bias voltage of (b) 0 V and (c) -1.5 V. ....	162
<b>Figure 5.19</b> Schematic band structure of devices. (a) Before contact. (b) After contact. (c) Operation in self-powered mode. (d) $V_{oc}$ distribution. ....	163

**Figure 5.20** UPS measurements for each sample, showing the binding energy secondary electron cutoffs. (a) Pristine, (b) 0.025 CsBr/KBr, (c) 0.075 CsBr/KBr, (d) 0.2 CsBr/KBr, (e) 0.3 CsBr/KBr. The corresponding work function ( $W_F$ ) can be determined by taking the difference between the photon energy (21.22 eV) and secondary electron cutoff ( $E_{\text{cutoff}}$ ).  $E_{\text{Fermi}} = 0$  eV, using Ag as the metal sample for calibration. .... 164

**Figure 5.21** Responsivity and detectivity of CsBr/KBr-assisted devices under (a) 405 nm, (b) 450 nm and (c) 520 nm light illumination. (d) Summary of performance at a bias voltage of 0 V. .... 166

**Figure 5.22** Typical  $I$ - $V$  curves as a function of intensity in logarithmic scale with excitation of (a) 405 nm, (b) 450 nm and (c) 520 nm laser diodes. .... 168

**Figure 5.23** The fitted power-dependent photocurrent under 405 nm and 450 nm light illumination at (a) 0 V, (b) -0.5 V, (c) -1 V and (d) -1.5 V bias. .... 169

**Figure 5.24** Transient photoresponse at different bias voltages under (a) 405 nm and (b) 450 nm laser diode excitation with a power intensity of  $13.4 \text{ mW cm}^{-2}$ . .... 170

**Figure 5.25** Photoresponse comparison between pristine (black line) and 0.025  $\text{Cs}^+/\text{K}^+$ -treated (red line) photodetectors at 0 V under 405 nm laser illumination. (a) Time-resolved photoresponse. (b) The corresponding response time. .... 170

**Figure 5.26** (a) The switching photoresponse at  $0^\circ$  (solid line) and  $60^\circ$  (dashed line), employing a 405 nm, 450 nm and 520 nm laser as light source, respectively. The insets are digital images of the device when tested. (b) The normalised transient photoresponse under up to 1600 bending cycles, with excitation of 405 nm laser diode ( $13.2 \text{ mW cm}^{-2}$ ).<sup>[15]</sup> .... 172

**Figure 5.27** The long-term stability characterisations of  $\text{CsPbBr}_3$  QD photodetector with assistance of 0.025 CsBr/KBr. (a)  $I$ - $V$  curves under illumination of 405 nm (purple), 450 nm

(blue) and 520 nm (green) lasers. (b) The transient photoresponse under self-powered mode. (c) Time-dependent photoresponse at different biases under 405 nm laser illumination..... 172

**Figure 5.28** (a) Optical image of a single section in photodetector arrays. The performance mapping for the corresponding section, including (b) open-circuit voltage, (c) responsivity and (d) detectivity. .... 174

**Figure 6.1** SEM images of the Ag/AAO structures with varied pore sizes. (a) 120 nm, (b) 170 nm and (c) 220 nm. Insets are enlarged SEM images. .... 180

**Figure 6.2** (a) Reflectance spectra and (b) average reflectance of the AAO matrices with and without Ag NP decoration. The corresponding schematic diagrams of light-matter interaction within the AAO matrices (c) without and (d) with metallic NPs..... 182

**Figure 6.3** SEM images of the CsPbBr<sub>3</sub> QD films on Ag/AAO substrates with different pore sizes. (a) Bare AAO, Ag/AAO with pore sizes of (b) 120, (c) 170 and (d) 220 nm. Insets are the corresponding SEM images of the localised morphologies..... 183

**Figure 6.4** XRD measurements of CsPbBr<sub>3</sub> QD samples on glass and Ag/AAO plasmonic nanostructures with different pore sizes. .... 184

**Figure 6.5** Schematic fabrication of the perovskite AAO structure-based photodetectors. Reproduced from ref. [19] with permission from John Wiley and Sons, copyright 2020. .... 184

**Figure 6.6** I–V curves of as-fabricated devices (a) in dark and (b) under 490 nm light illumination. .... 185

**Figure 6.7** Responsivities of the photodetectors fabricated with difference pore sizes. .... 186

**Figure 6.8** The EM field distribution of the Ag/AAO plasmonic structures as a function of pore sizes. Reproduced from ref. [19] with permission from John Wiley and Sons, copyright 2020. .... 186

<b>Figure 6.9</b> Power-dependent transient photoresponse of CsPbBr <sub>3</sub> QD photodetectors as a function of pore sizes. ....	187
<b>Figure 6.10</b> Power-dependent (a) current and (b) R of the perovskite photodetectors under 490 nm light illumination.....	188
<b>Figure 6.11</b> Response speed on different substrates under 365 nm light illumination at 1 V bias. (a) Bare glass. Ag/AAO with a pore size of (b) 120 nm, (c) 170 nm and (d) 220 nm.....	189
<b>Figure 6.12</b> SEM images of (a) bare AAO matrices, (b) Ag/AAO, (c) Al/AAO and (d) Cu/AAO plasmonic nanostructures. ....	189
<b>Figure 6.13</b> (a) Reflection and (b) average reflectance of the AAO nanostructures decorated with metallic NPs. ....	190
<b>Figure 6.14</b> SEM images of CsPbBr <sub>3</sub> QD films on (a) bare AAO matrices, (b) Ag, (c) Al and (d) Cu NP-decorated AAO matrices. ....	191
<b>Figure 6.15</b> (a) XRD and (b) reflection measurements of the CsPbBr <sub>3</sub> QD film AAO structures with different metallic NPs. Insets are optical images of the samples. (c) Room-temperature PL spectra.....	191
<b>Figure 6.16</b> (a) Dark current and (b) light current of the photodetectors under 490 nm light illumination (13.4 mW cm <sup>-2</sup> ). ....	192
<b>Figure 6.17</b> (a) Transient photoresponse of each device at 1 V bias under illumination (490 nm, 13.4 mW cm <sup>-2</sup> ). (b) Responsivity. ....	193
<b>Figure 6.18</b> Response time of photodetectors with different structures within a single on-off period under 490 nm light illumination. (a) Bare AAO matrices, (b) Ag/AAO, (c) Al/AAO and (d) Cu/AAO plasmonic nanostructure. ....	194

<b>Figure 6.19</b> The power-dependent (a) light current and (b) responsivity of photodetectors under 490 nm laser illumination at 1 V bias voltage.....	194
<b>Figure 6.20</b> (a) Transient photoresponse and (b) R of the Al/AAO plasmonic nanostructure photodetectors as a function of incident light wavelength.....	195
<b>Figure 7.1</b> The proposed device architecture for extending the spectral response. ....	202
<b>Figure 7.2</b> Schematic illustration of flexible perovskite solar capacitor nanosystem. ....	203
<b>Figure 7.3</b> The illustration of photodetector arrays for real-time imaging. ....	204

## LIST OF TABLES

<b>Table 1.1</b> The performance comparison between photodetectors with different semiconductors.	40
<b>Table 2.1</b> The radius of each element and the tolerance factors of $\text{CH}_3\text{NH}_3\text{PbI}_3$ and $\text{CsPbBr}_3$ .	53
<b>Table 2.2</b> The temperature required for phase transitions of $\text{CH}_3\text{NH}_3\text{PbI}_3$ and $\text{CsPbBr}_3$ .	54
<b>Table 3.1</b> The list of chemicals used in experiments.	86
<b>Table 4.1</b> The values of decay components and fractions obtained by fitting with decay function.	125
<b>Table 4.2</b> Summarised device performance of metal halide perovskite based photodetectors reported in recent works.	135
<b>Table 5.1</b> The quantified atomic ratio of Cs:Pb:Br:K from $\text{CsPbBr}_3$ QD film with various amounts of CsBr/KBr treatment.	148
<b>Table 5.2</b> Surface roughness extracted from AFM results, where $R_q$ is the root mean square of surface roughness, $R_a$ represents the average value of surface roughness and $R_{\text{max}}$ denotes the maximum peak height of surface roughness.	152
<b>Table 5.3</b> Summarised peak positions, bandgaps, peak intensities and FWHM from PL spectra, along with QDs containing different fractions of CsBr/KBr injection.	154
<b>Table 5.4</b> Decay constants and their fractions as extracted from the TRPL measurements, using bi-exponential decay fitting: $I(t) = A_1\exp(-t/\tau_1) + A_2\exp(-t/\tau_2)$ .	157
<b>Table 5.5</b> Summary of device performance of reported perovskite photodetectors.	167

# LIST OF ABBREVIATIONS, MATERIALS AND ELEMENTS

## Abbreviations

AAO: Anodic Aluminium Oxides

AFM: Atomic Force Microscopy

ALD: Atomic Layer Deposition

CBM: Conduction Band Minimum

CVD: Chemical Vapour Deposition

EDX: Element Dispersive X-Ray spectroscopy

EQE: External Quantum Efficiency

ETL: Electron Transport Layer

FAST: Fluorescence Analysis Software Technology

FFT: Fast Fourier Transform

FWHM: Full-Width at Half Maximum

HMHPs: Organic-Inorganic Hybrid Metal Halide Perovskites

HTL: Hole Transport Layer

I-t: Current-Time

I-V: Current-Voltage

IMHPs: All-Inorganic Metal Halide Perovskites

IoT: Internet of Things

LCN: London Centre of Nanotechnology

LDR: Linear Dynamic Range

LED: Light-Emitting Diodes

MBE: Molecular Beam Epitaxy

MIR: Mid-Infrared

MOCVD: Metal-Organic Chemical Vapour Deposition

NEP: Noise Equivalent Power

NIR: Near-Infrared

OHP: Organic Halide Perovskite

PAD: Polymer-Assisted Approach

PAT: Porous Alumina Template

PCE: Power Conversion Efficiency

PL: Photoluminescence

QDs: Quantum Dots

SCS: Semiconductor Characterisation System

SEM: Scanning Electron Microscopy

SRH: Shockley-Read-Hall

SMU: Source Measure Unit

TCSPC: Time-Correlated Single Photon Counting

TEM: Transmission Electron Microscopy

TRPL: Time-Resolved Photoluminescence

UPS: Ultraviolet Photoelectron Spectroscopy

UV-Vis: Ultraviolet-Visible

UV: Ultraviolet

VBM: Valence Band Maximum

VLS: Vapour-Liquid-Solid

XPS: X-ray Photoelectron Spectroscopy

XRD: X-ray Diffraction

## Materials and Elements

a-Si: Amorphous Silicon

Ag: Silver

Al: Aluminium

Al<sub>2</sub>O<sub>3</sub>: Aluminium oxide

Au: Gold

BF<sub>4</sub>: Tetrafluoroborate

Br: Bromide

BuAm: Butylamine

c-Si: Crystalline Silicon

CaTiO<sub>3</sub>: Calcium Titanate

CB: Chlorobenzene

CF: Chloroform

CH(NH<sub>2</sub>)<sub>2</sub><sup>+</sup> (FA<sup>+</sup>): Formamidinium

CH<sub>3</sub>NH<sub>3</sub><sup>+</sup> (MA<sup>+</sup>): Methylammonium

Cl: Chloride

Cs: Caesium

Cs<sub>2</sub>CO<sub>3</sub>: Caesium Carbonate

CsBr: Caesium Bromide

Cu: Copper

DMF: Dimethylformamide

DMSO: Dimethyl Sulfoxide

GaAs: Gallium Arsenide

GaN: Gallium Nitride

Ge: Germanium

H<sub>2</sub>O: Hydrogen Peroxide

H<sub>3</sub>PO<sub>4</sub>: Phosphoric Acid

HBr: Hydrogen Bromide

HCl: Hydrochloric Acid

HEX: Hexane

HI: Hydrogen Iodide

I: Iodide

IPrOH/IPA: 2-Propanol

ITO: Indium Tin Oxide

K: Potassium

KBr: Potassium Bromide

MCT: Mercury Cadmium Telluride

Ni: Nickel

O: Oxygen

OAm: Oleylamine

OE: Oleic Acid

Pb: Lead

PbBr<sub>2</sub>: Lead Bromide

PbCl<sub>2</sub>: Lead Chloride

PbI<sub>2</sub>: Lead Iodide

PCBM: Phenyl-C<sub>61</sub>-Butyric Acid Methyl Ester

PEDOT:PSS: poly(3,4-ethylenedioxythiophene):Poly Styrenesulfonate

PEI: Polyethyleneimine

PEIE: Polyethylenimine Ethoxylated

PET: Polyethylene Teraphthalate

PF<sub>6</sub>: Hexafluorophosphate

PrAc: Propionic Acid

PTAA: Poly(triarlyamine)

SCN: Thiocyanate

Si: Silicon

Sn: Tin

Spiro-OMeTAD: 2,2',7,7'-Tetrakis-(N,N-Di-P-Methoxyphenylamine)9,9'-Spirobifluorene

TiO<sub>2</sub>: Titanium dioxide

Tol: Toluene

Zn: Zinc

ZnO: Zinc Oxide

## LIST OF SYMBOLS

E: Energy

F: Fraction

h: Planck Constant

v: Speed of Light

$\lambda$ : Incident Light Wavelength

$L_D$ : Carrier Diffusion Length

k: Boltzmann's Constant

T: Temperature

$\mu$ : Carrier Mobility

$\tau$ : Carrier Lifetime

e: Elementary Charge

t: Tolerance Factor

m: Octahedral Factor

$R_A$ : Radius of A Cations

$R_B$ : Radius of B Cations

$R_X$ : Radius of X Anions

K: Kelvin

$E_g$ : Bandgap Energy

$\alpha$ : Absorption Coefficient

$E_b$ : Binding Energy

R: Responsivity

$J_{ph}$ : Photocurrent Density

$I_{light}$ : Light Intensity

$D^*$ : Detectivity

$A$ : Active Area  
 $\Delta f$ : Electrical Bandwidth  
 $i_n$ : Noise Current  
 $J_d$ : Dark Current Density  
 $\tau_{rise}$ : Rise Time  
 $\tau_{fall}$ : Fall Time  
 $J_{upper}$ : Maximum Current Density  
 $J_{lower}$ : Minimum Current Density  
 $d$ : Lattice Spacing  
 $E_k$ : Kinetic Energy  
 $\phi$ : Work Function  
 $I_p$ : Photocurrent  
 $\beta$ : Power Exponent  
 $V_{oc}$ : Open-Circuit Voltage  
 $E_f$ : Fermi Level  
 $V_{bi}$ : Built-In Potential  
 $E_{f,e}$ : Electron Quasi-Fermi Level  
 $E_{f,h}$ : Hole Quasi-Fermi Level  
 $D_0$ : Ideal Diffusivity  
 $\gamma_{Ag}$ : Activation Energy of Ag  
 $T$ : Annealing Temperature  
 $R_1$ : Reflected Light  
 $d$ : Thickness of AAO  
 $\theta_1$ : Angle of Incident Light  
 $n_{AAO}$ : Refractive Index

$\rho$ : Fitting Constant

$\delta$ : Surface Roughness

# LIST OF PUBLICATIONS AND CONFERENCES

## Publications

- [1] **K. Shen**, X. Li, H. Xu, M. Wang, X. Dai, J. Guo, T. Zhang, S. Li, G. Zou, K. Choy, I. P. Parkin, Z. Guo, H. Liu, J. Wu. Enhanced Performance of ZnO Nanoparticle Decorated All-inorganic CsPbBr<sub>3</sub> Quantum Dots Photodetector. *J. Mater. Chem. A* **2019**, 7, 6134.
- [2] **K. Shen**, H. Xu, X. Li, J. Guo, S. Sathasivam, M. Wang, A. Ren, K. L. Choy, I. P. Parkin, Z. Guo, J. Wu. Flexible and Self-Powered Photodetector Arrays Based on All-Inorganic CsPbBr<sub>3</sub> Quantum Dots. *Adv. Mater.* **2020**, 32, 2000004.
- [3] M. Li, **K. Shen**, H. Xu, A. Ren, J. Lee, S. Kunwar, S. Liu, J. Wu. Enhanced Spatial Light Confinement of All Inorganic Perovskite Photodetectors on Hybrid Plasmonic Nanostructures. *Small* **2020**, 16, 2004234.
- [4] A. Ren, J. Zou, Y. Huang, L. Yuan, H. Xu, **K. Shen**, H. Wang, S. Wei, Y. Wang, X. Hao, J. Zhang, D. Zhao, J. Wu, Z. Wang. Direct Laser-Patterned MXene-Perovskite Image Sensor Arrays for Visible-Near Infrared Photodetection. *Mater. Hori.* **2020**, 7, 1901.
- [5] X. Li, X. Dai, H. Xu, **K. Shen**, J. Guo, C. Li, G. Zou, K. L. Choy, I. P. Parkin, Z. Xiao, H. Liu, J. Wu. Multifunctional Two-Dimensional Glassy-Graphene Devices for Vis-NIR Photodetection and Volatile-Organic-Compound Sensing. *Sci. China Mater.* **2021**.

## Conferences

- [1] European Materials Research Society (E-MRS), 27<sup>th</sup> May - 31<sup>st</sup> May, 2019, Nice, Paris.
- [2] The 4<sup>th</sup> Conference on Micro-Nano Optical Technology and Application, 26<sup>th</sup> Sep. - 28<sup>th</sup> Sep., 2020, Chengdu, China
- [3] The 5<sup>th</sup> Seminar on Photoelectric Detection and Sensing Technology (EMN), 11<sup>st</sup> Dec. – 13<sup>rd</sup> Dec., 2020, Kunming, China

# CHAPTER 1. INTRODUCTION

## 1.1 Photodetector Overview

In the mid-20<sup>th</sup> century, the third technological revolution arrived with the rapid development of transistors and integrated circuits. Accordingly, semiconductors and other related technologies were intensively expanded. At the same time, optoelectronic technologies were also improved thorough explorations, wide applications and superior fabrications using micro/nano-electronic techniques. A variety of semiconductors have been used as active layers in optoelectronics, including solar cells, photodetectors and light-emitting diodes (LEDs).<sup>[1–4]</sup> These devices have been extensively explored and widely applied, and the related industries and communities have been rapidly developed, inducing a tremendous impact on every aspect of humans' daily lives. A large number of applications, including optical communications, remote control systems, biomedical sensors, imaging and cameras, would not be possible without the support of optoelectronic technologies. The American Semiconductor Association stated that the scale of the global semiconductor market had reached \$412.3 billion in 2019, with 10.1% of the market share occupied by optoelectronic devices, as presented in Figure 1.1 and Figure 1.2.<sup>[5]</sup>

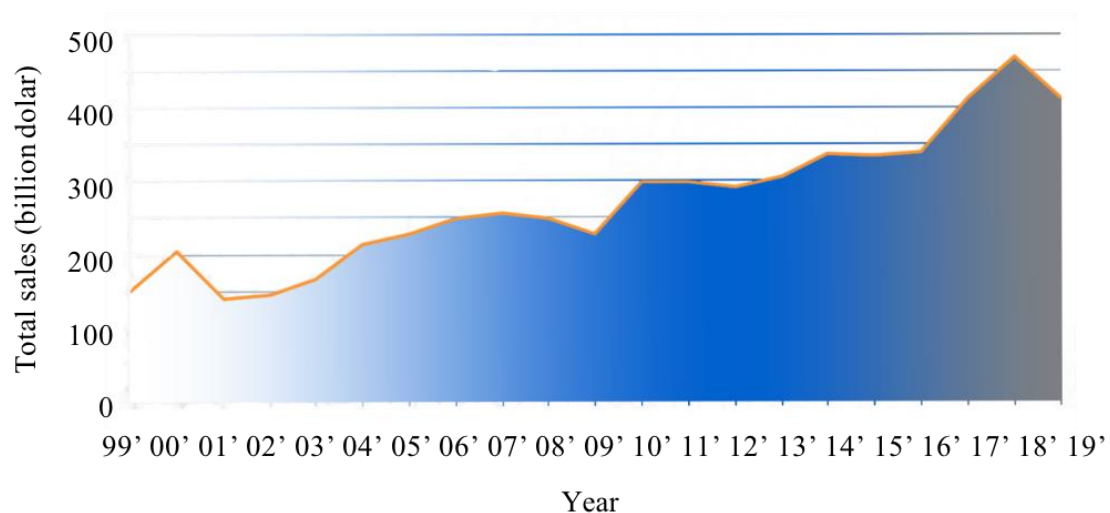


**Figure 1.1** Global semiconductor total sales between 1999 to 2019.<sup>[5]</sup>

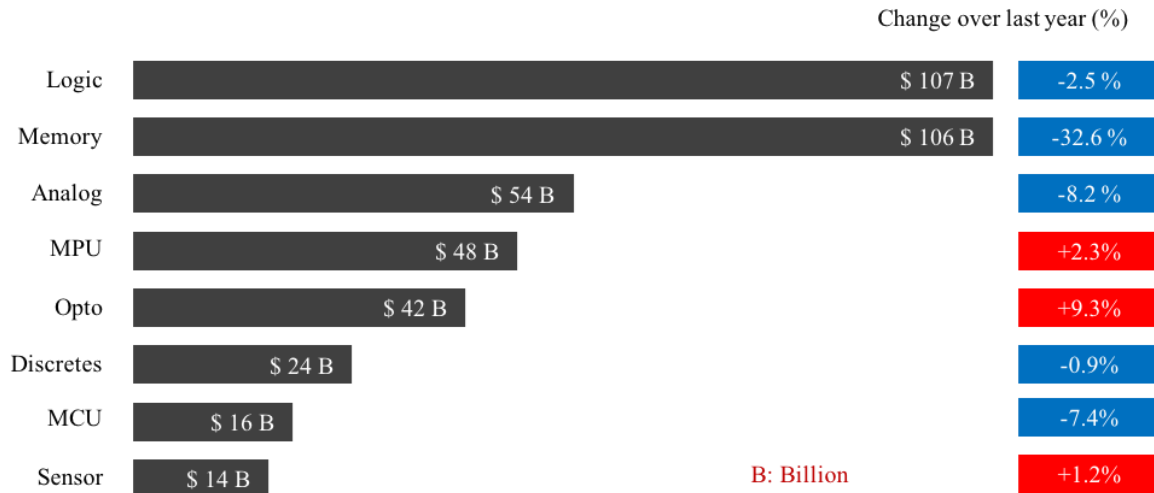


**Figure 1.2** Distribution of worldwide semiconductor sales by product segment in 2019.<sup>[5]</sup>

Photodetectors are one of the important components of optoelectronic devices. Like the human eye, they are essential to detect and explore electromagnetic (EM) waves. In general, there are a few types of photodetectors, including photocathodes, photomultipliers and semiconductor photodetectors.<sup>[6–8]</sup> Among these different types of photodetectors, semiconductor photodetectors have the advantages of simple device configuration, low operation voltage and small volume, have been globally employed in the military and in our daily lives, in applications such as visible light imaging, infrared spectroscopy, missile guidance, photometry and optical communication.<sup>[8–10]</sup> The numerous applications can be attributed to their excellent performance, high reliability and ease of integration into electronic circuits.

It is known that semiconductor photodetectors convert incident light signals to electric signals, manifested as photocurrent. In detail, the incident photons are absorbed by semiconductor layers due to the photoelectric effect ( $E = h\nu / \lambda$ ), and generate electron-hole pairs followed by relaxation. These photoexcited carriers subsequently affect the carrier concentration in semiconductor material, and are transported and collected by the terminals owing to the presence of internal or external electric fields. As a result, the transportation and collection of photoinduced carriers generates a current or a voltage at both ends of the

electrodes, realising the conversion between incident light and current. So far, the detection of X-ray, ultraviolet (UV), visible and infrared regions has been realised by conventional semiconductors, such as gallium nitride (GaN), silicon (Si), germanium (Ge) and mercury cadmium telluride (MCT).<sup>[10–12]</sup> These conventional semiconductors exhibit good optical and electrical properties, including a large absorption coefficient, good carrier mobility and low defect densities. In addition, they are compatible with large-scale integration and miniaturisation, which enable complex photonics systems. However, the high performance is accompanied by a complex process and high cost of fabrication. The temperature required for epitaxial growth of conventional semiconductors is higher than 700 °C. In addition, in order to achieve high purity the process is complicated and time-consuming.<sup>[12]</sup> For example, the commercial electronic grade silicon must be at least 99.9999999% pure in composition.<sup>[13]</sup> Meanwhile, conventional semiconductors are not compatible with flexible substrates due to their intrinsic bulk properties, which cannot be used for portable and wearable electronics. Last but not least, many developing countries suffer from lagging technologies, immature fabrication processes and high-cost instruments, resulting in a dependence on imports. These severely limit their domestic defence constructions and informatisation levels, which also restrict the development of high-tech equipment manufacturing.

Therefore, it is critical to develop a new-generation semiconductor with the integration of low cost, facile growth, solution-processability and good photo-electron conversion properties for constructing high-performance photodetectors. Thanks to the emerging organic and perovskite materials, they can be synthesised at low temperature via a fast and facile process, and can be fabricated by simple spin-coating, spray-coating and dip-coating techniques. Such techniques do not typically require high vacuum or high temperatures, and are much faster and cheaper than conventional wafer processing or vacuum deposition. They are also compatible with flexible substrate for roll-to-roll processing, significantly increasing

the throughput. Meanwhile, perovskites exhibit excellent optoelectronic properties, leading to a huge potential for constructing high-performance devices at a fraction of the cost of conventional semiconductors.

## 1.2 Development of Perovskite-Based Optoelectronics

The word “perovskite” originated from the mineral ore with the corresponding chemical formula  $\text{CaTiO}_3$ , which was discovered in the Ural mountains of Russia by Gustav Rose in 1839, and further named after the Russian mineralogist Lev Perovski. Corner-sharing  $\text{TiO}_6$  octahedra were adopted in the crystal structure of perovskites, where Ca occupied the cuboctahedral cavity in each unit cell. With the increasing explorations of metal oxide perovskites, many of the unique properties found have made them suitable for wide application in the ferroelectric, thermoelectric and catalysis fields.<sup>[14–18]</sup>

Recently, metal halide perovskites have been regarded as having the same crystal structure as  $\text{CaTiO}_3$  with the common stoichiometry of  $\text{ABX}_3$ , where A denotes organic groups including methylammonium ( $\text{CH}_3\text{NH}_3^+$ ,  $\text{MA}^+$ ) and formamidinium ( $\text{CH}(\text{NH}_2)_2^+$ ,  $\text{FA}^+$ ) and inorganic cations  $\text{Cs}^+$ ; B represents  $\text{Pb}^{2+}$ ,  $\text{Sn}^{2+}$  and  $\text{Ge}^{2+}$ ; X can be classified into  $\text{Cl}^-$ ,  $\text{Br}^-$ ,  $\text{I}^-$ ,  $\text{BF}_4^-$ ,  $\text{PF}_6^-$  and  $\text{SCN}^-$  or mixed halide. Such metal halide perovskites are widely employed in optoelectronics, which is the emphasis of this thesis. They are further classified into two categories as organic-inorganic hybrid metal halide perovskites (HMHPs) and all-inorganic metal halide perovskites (IMHPs), where organic cations ( $\text{MA}^+$ ,  $\text{FA}^+$ ) and inorganic cations ( $\text{Cs}^+$ ) occupy A sites, respectively. The details of perovskites are comprehensively presented in Chapter 2.

Back in the year 2009, Japanese scientists Miyasaka *et al.* first employed perovskites ( $\text{CH}_3\text{NH}_3\text{PbI}_3$  nanocrystals) as the active layer for dye-sensitised solar cells, with an impressive power conversion efficiency (PCE) of 3.8%.<sup>[19]</sup> This great achievement of perovskite-based

solar cells attracted enormous attention, leading to an upsurge in perovskite-based research. Two years later, the PCE was further improved to 6.5% by the Korea Park Research Group. They replaced electrolyte with redox, and modified the synthesis of the perovskite layer ( $\text{CH}_3\text{NH}_3\text{PbI}_3$  quantum dots) and the thickness of the  $\text{TiO}_2$  electron transport layer (ETL).<sup>[20]</sup> In 2012, Spiro-OMeTAD, as solid-state hole transport layer (HTL) material, was employed in perovskite solar cells for the first time, which successfully overcame the leakage of electrolytes in dye-sensitised solar cells, and achieved a PCE of 9.7%.<sup>[21]</sup> Subsequently, British scientists Snaith *et al.* precisely doped Cl in  $\text{CH}_3\text{NH}_3\text{PbI}_3$  as an absorption layer, and used a mesoporous  $\text{Al}_2\text{O}_3$  layer as an effective scaffold, with a PCE reaching up to 10.9%.<sup>[22]</sup> Meanwhile, they also examined the diffusion length of this perovskite ( $\text{MAPbI}_{3-x}\text{Cl}_x$ ), which exceeded  $1\ \mu\text{m}$ .<sup>[23]</sup> Since then, perovskite-based solar cells have been rapidly developed, and continuously achieved new PCE limits. Gratzel and co-workers pioneered a two-step deposition method to deposit perovskite thin films, resulting in an excellent efficiency of 15%.<sup>[24]</sup> Meanwhile, Yang's group modified the indium tin oxide (ITO) electrode using polyethylenimine ethoxylated (PEIE), achieving an impressive maximum efficiency of 19.3% and an average PCE of 16.6%.<sup>[25]</sup> With the extensive efforts made in perovskite solar cells, the PCE has exceeded 25.5% within 11 years, as shown in Figure 1.3.<sup>[26]</sup> This impressive scientific progress was nominated as the runner-up for Breakthrough of the Year by the editors of *Science* in 2013.<sup>[27]</sup>

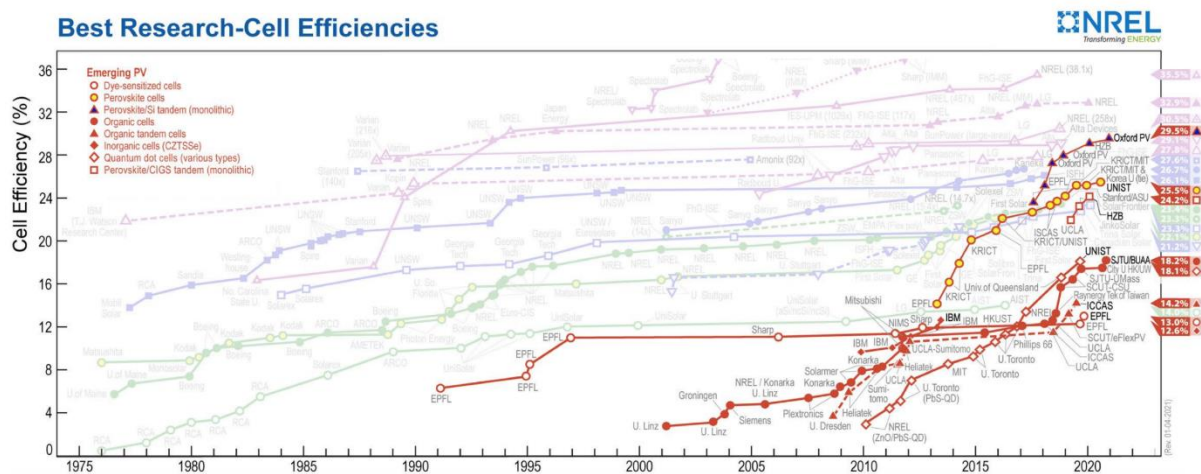


**Figure 1.3** The PCE development of perovskite solar cells in the last ten years.<sup>[26]</sup> Accessed at 1<sup>st</sup> April, 2021.

Accordingly, HMHPs have been proven to exhibit excellent optical and electrical properties, such as high absorbance, suitable bandgap, high carrier mobility, long diffusion length and good defect tolerance, which are promising candidates for optoelectronics (solar cells, photodetectors and LEDs).<sup>[28–30]</sup> Therefore, as one of the critical components, photodetectors have gained extensive research attention since 2014. In the last few years, thousands of reports based on perovskite photodetectors have been published in high-quality scientific journals. Various perovskite photodetectors with different architectures have been successively developed and have exhibited a surprisingly good performance.

In 2014, Dou's research group made advances in the research of perovskite, and fabricated a solar-cell-like photodiode via a spin-coating technique.<sup>[31]</sup> They employed  $\text{CH}_3\text{NH}_3\text{PbI}_{3-x}\text{Cl}_x$  as the absorption layer, and poly(3,4-ethylenedioxythiophene):poly styrenesulfonate (PEDOT:PSS) and phenyl- $\text{C}_{61}$ -butyric acid methyl ester (PCBM) as the HTL and ETL, respectively. The as-fabricated device exhibited a high detectivity of over  $10^{13}$  Jones, a fast response time of  $<1 \mu\text{s}$ , and a large linear dynamic range (LDR; 100 dB). Meanwhile, Lee *et al.* established a study of perovskite-graphene heterostructure phototransistors.<sup>[32]</sup> They employed graphene as an ETL to efficiently separate charge carriers by a vertical electric field and further transport them horizontally. A high responsivity ( $180 \text{ A W}^{-1}$ ) was achieved with an illuminating power of 1 pW, and the rise/fall times were determined as 87 ms and 540 ms, respectively, which was expected to promote the development of imaging sensors. Two years later, Huang *et al.* fabricated an X-ray perovskite ( $\text{CH}_3\text{NH}_3\text{PbBr}_3$  single crystal) photodetector, which achieved an impressive mobility lifetime product of  $1.2 \times 10^{-2} \text{ cm}^2 \text{ V}^{-1}$ , and demonstrated a very small surface charge recombination velocity ( $64 \text{ cm s}^{-1}$ ). Under self-powered mode, this X-ray detector exhibited a charge-collection efficiency of 16.4%, and

realised a more sensitive X-ray detection than  $\alpha$ -Se X-ray detectors.<sup>[33]</sup> In 2019, Pan *et al.* presented flexible photodetector arrays with  $10 \times 10$  pixels, which realised a resolution of 63.5 dpi. They cleverly designed an  $\text{Al}_2\text{O}_3$ -assisted hydrophilic-hydrophobic layer to fabricate arrays. The device not only exhibited an excellent photoresponse, but was also able to capture the real-time light trajectory, which is promising for artificial electronic skin applications.<sup>[34]</sup>

Although hybrid perovskite photodetectors have achieved impressive progress, they suffer from long-term stability, especially compared with highly stable inorganic semiconductors (e.g. Si and GaAs), as their organic parts are sensitive to oxygen and moisture.<sup>[35]</sup> One effective way to overcome this is by replacing the organic parts with inorganic cations ( $\text{Cs}^+$ ), which are proven to be more thermally and structurally stable than HMHP compounds.<sup>[36,37]</sup> This strongly suggests caesium lead bromide ( $\text{CsPbBr}_3$ ) to be a competitive candidate for the development of chemically stable optoelectronic applications.

In 2016, Zeng *et al.* successfully grew atom-thin  $\text{CsPbBr}_3$  nanosheets (3.3 nm) for the first time, which enabled large-area and crack-free film assembly in wearable optoelectronics. The as-fabricated flexible photodetectors demonstrated a competitive responsivity of  $0.25 \text{ A W}^{-1}$  and a high on/off ratio ( $10^3$ ). Moreover, a good stability and excellent flexibility ( $>10,000$  cycles) was demonstrated.<sup>[38]</sup> One year later, Han *et al.* synthesised  $\text{CsPbBr}_3$  microcrystals with a low density of trap states via a simple growth method. Benefiting from fast carrier mobility exceeding  $100 \text{ cm}^2 \text{ v}^{-1} \text{ s}^{-1}$ , efficient charge transport and collection was realised. The as-fabricated photodetectors showed an impressive responsivity of  $6 \times 10^4 \text{ A W}^{-1}$  with one-photon excitation.<sup>[39]</sup> In 2018, phase-stabilised  $\alpha$ - $\text{CsPbI}_3$  perovskite nanocrystals were synthesised and employed as an absorber in a photodetector. P3HT, as an HTL, was deposited onto  $\alpha$ - $\text{CsPbI}_3$  nanocrystal layers. Moreover, this P3HT layer functioned as an efficient passivation layer that reduced interface defects and accordingly achieved a noise-equivalent power of  $1.6 \times 10^{-13} \text{ W Hz}^{-0.5}$ .<sup>[40]</sup> Recently, Liao *et al.* employed  $\text{CsPbBr}_3$  thin film and ITO nanowires in a hybrid

photodetector. The metallic ITO nanowires efficiently extracted photocarriers from CsPbBr<sub>3</sub> thin film, resulting in a fast response time of 0.55 s. Meanwhile, long-term stability (200 h) and outstanding flexibility were demonstrated, providing another insight into the design of hybrid material systems.<sup>[41]</sup>

### 1.3 Challenges and Motivation

Perovskites possess favourable optical and electrical properties, which are promising in optoelectronic devices. However, similar to solar cells, perovskite-based photodetectors still present many challenges; for example, competitive performance, toxicity, stability and ion migration issues.

#### 1) Performance

Ideally, photodetectors should exhibit an excellent performance, including good photoresponse, low noise, fast response speed, broad wavelength selectivity and long-term stability. However, these performance parameters cannot be achieved in a single device at the same time, requiring to find and understand the trade-offs of balancing these parameters. On the other hand, compared with commercial photodetectors, only part of the figure of merit has been achieved in perovskite photodetectors (Table 1.1).

**Table 1.1** The performance comparison between photodetectors with different semiconductors.

Materials	Spectral response (nm)	Responsivity (A W <sup>-1</sup> )	Detectivity (Jones)	Response time (ns)
GaN	200 - 365	~ 1.7	~ 10 <sup>11</sup>	50
Si	400 - 1100	~ 0.6	~ 10 <sup>11</sup>	~ 10
Ge	800 - 1800	~ 0.85	~ 10 <sup>11</sup>	~ 220
CH <sub>3</sub> NH <sub>3</sub> PbI <sub>3</sub> <sup>[42]</sup>	400 - 750	0.5	~ 10 <sup>13</sup>	~ 300

CsPbBr <sub>3</sub> <sup>[43]</sup>	350 - 550	30	~10 <sup>12</sup>	~ 900
CsPbI <sub>3</sub> <sup>[40]</sup>	400 - 700	0.03	~10 <sup>12</sup>	~ 10000

## 2) Long-Term Stability

The long-term stability of perovskite-based optoelectronics under ambient conditions is a key issue, and determines the lifetime of the device. Unfortunately, compared with commercial devices, perovskites easily degrade, with exposure to oxygen and moisture being the primary causes of decomposition and degradation. So far, there have been various studies performed to improve the long-term stability of perovskite solar cells, with approaches including interface engineering, surface passivation, adopting sandwich configurations, controlling perovskite morphologies of crystallisation and encapsulation.<sup>[44–49]</sup> Similar approaches can be applied to photodetectors. Although these approaches have been demonstrated to effectively improve the stability of perovskite devices, they are still not comparable with commercial applications. Typically, the lifetime of commercial Si photodetector is over 20 years, but that of the perovskite-based photodetectors is less than 1 year. Especially, the commercial photodetectors can even operate in harsh conditions. Therefore, it is much more significant to develop strategies to address the stability issues at the fabrication stage of perovskites, by developing chemically stable perovskites, which is beneficial for the development of long-term stable perovskite-based optoelectronics.

## 3) Toxicity

Although impressive progress has been achieved with perovskite semiconductors, their toxicity issues hinder their further development in practical applications. The toxicity mainly results from the use of lead (Pb) element in the widely explored perovskite semiconductors, including CH<sub>3</sub>NH<sub>3</sub>PbI<sub>3</sub>, CsPbBr<sub>3</sub> and CH(NH<sub>2</sub>)<sub>2</sub>PbCl<sub>3</sub>, which inevitably

causes contamination and environmental damage. Thus, more and more efforts need to be devoted to explore environmentally friendly perovskite photodetectors by substituting  $\text{Pb}^{2+}$  with other non-poisonous elements, such as  $\text{Sn}^{2+}$ ,  $\text{Mn}^{2+}$  and  $\text{Ge}^{2+}$ . At the same time, it is critical to retain or even improve the material stability and device performance for future commercialisation.

#### 4) Ion Migration

Owing to the ionic-electronic characteristics of perovskite materials, the performance of perovskite devices is often affected by ion conduction. However, until now, the impact of ion migration is still unknown, and so a more comprehensive and systematic investigation is required.

Therefore, it is of much significance to adapt successful strategies from the pioneering work of conventional semiconductors, as well as generating new ideas, to address these existing limitations, while maintaining the high performance and stability.

## 1.4 Objectives

In this thesis, I focus on all-inorganic perovskite colloidal quantum dots (QDs), e.g.  $\text{CsPbBr}_3$  QDs, which are solution-processed and offer the benefits of facile and cost-effective synthesis. Due to the imperfection of state-of-the-art photodetectors, these colloidal QDs were applied to develop high-performance light detectors for industrial applications.

The objective of the thesis is to expose the research carried out at UCL under the supervision of Prof. Jiang Wu and Prof. Kwang-Leong Choy to extend the results achieved on conventional photodetectors to the growth of high-performance perovskite photodetectors, and present the solid physics learnt during my PhD lifetime. Specifically, the aim is to address and understand the listed key challenges, including performance limitation, stability issue and physics behind, ultimately demonstrating stable and high-performance photodetectors. In order

to deeply understand these issues, both passivation strategies and device configurations optimisations were proposed to improve the perovskite crystal quality and enhance light-matter interaction.

## 1.5 Thesis Outline

This thesis mainly focusses on developing high-performance perovskite photodetectors, studying the material properties and device performance. Seven chapters are contained in the thesis, including the introduction, fundamentals, experimental procedures, perovskite-based photodetectors and future plans. In particular, the stability issues are investigated by optimising perovskite semiconductors and adopting effective device architectures. At the same time, the characteristics of perovskite semiconductors and photodetectors are comprehensively studied, successfully realising the measurements of responsivity, external quantum efficiency, response time and long-term stability. The work lays the foundation for perovskite-based optoelectronics and further paves the way for their future commercialisation.

The first introduction chapter presents the history of the photodetector industry and gives the general background of the research carried out. In particular, it describes where the need for high-efficiency and low-cost photodetectors stems from. In this frame, the solution-processed perovskite system is introduced, and the objectives of the research performed under the direction of Professor Jiang Wu and Professor Kwang-Leong Choy are presented.

The second chapter gives a comprehensive introduction to the fundamentals of perovskites, including their crystal structures, chemical compositions, absorption and recombination. Meanwhile, the morphology of perovskites and their derivatives are presented. Stability issues that limit the efficiency of photodetectors are addressed, and the photodetector architectures and their figures of merit are introduced.

An introduction to synthesis methods and the equipment used to grow, fabricate and characterise experimental all-inorganic perovskite QD photodetectors is given in the third chapter. In particular, perovskite synthesis, material quality, optical properties and surface morphology characterisation tools are discussed in detail. This is followed by a presentation of the detailed steps of device fabrication, including substrate preparation, the photolithography procedure and layer depositions. Moreover, another three chapters of research work were carried out to improve the perovskite QD and photodetector performance.

The fourth chapter details the efforts to improve the material quality of reference CsPbBr<sub>3</sub> QD photodetectors grown on glassy graphene-coated glass by decorating zinc oxide nanoparticles (ZnO NPs). A better film morphology and material quality and a lower leakage current are observed, resulting in improvements in device performance such as higher responsivity, larger detectivity, shorter response time and better stability. The heterostructure is formed by inserting a few layers of glassy graphene, resulting in a self-powered characteristic, and achieving an energy-saving purpose. Moreover, key parts of this chapter have been published in Journal of Materials Chemistry A.<sup>[50]</sup>

The fifth chapter presents the experimental results obtained in the growth of CsBr/KBr-assisted CsPbBr<sub>3</sub> QDs fabricated on ITO-coated PET substrate. TiO<sub>2</sub> deposited by atomic layer deposition (ALD) and Spiro-OMeTAD are employed as the ETL and HTL for efficiently extracting electrons and holes, respectively. The CsPbBr<sub>3</sub> QD thin films are drastically enhanced in terms of material quality, film formation, carrier lifetime and photoluminescence (PL) efficiency when incorporating the CsBr/KBr additives. Accordingly, improvement in the device performance is achieved by selecting the optimal proportion of additives, while maintaining good stability (over 7 months). The corresponding mechanism of such improvement by blending CsBr/KBr is further explained. Moreover, a series of experiments, such as blending degree and cycle tests, demonstrated that the device possesses good flexibility

and electrical stability as it is bent. Finally, a uniform photoresponse is achieved in the as-fabricated photodetector arrays, which is promising for imaging applications. The key contents of this chapter were published in *Advanced Materials*.<sup>[51]</sup>

In Chapter 6, anodic aluminium oxide (AAO) plasmonic nanostructures decorated with metallic NPs were employed in the CsPbBr<sub>3</sub> QD photodetectors to facilitate light utilisation. By controlling the pore size of the AAO matrix, multiple dramatic interferences were induced by plasmonic coupling, resulting in a highly efficient collection of incident photons. Moreover, the introduction of metallic NPs benefited the cyclic utilisation of light. Accordingly, the device performance was significantly boosted by the hybrid strategy, which has been published in *Small*.<sup>[52]</sup> In this work, my contribution was carrying out the synthesis of CsPbBr<sub>3</sub> QDs, characterising material properties, measuring electrical characteristics and analysing experimental results.

The seventh and final chapter is a conclusion of the work performed during the past three and a half of years of this PhD project and outlines the research to be carried out in the future to further apply perovskite systems into various advanced optoelectronics, aiming for practical applications. Moreover, more efforts will be made to further improve the device performance and solve the stability issues.

## 1.6 References

- [1] H. Tan, A. Jain, O. Voznyy, X. Lan, F. P. García de Arquer, J. Z. Fan, R. Quintero-Bermudez, M. Yuan, B. Zhang, Y. Zhao, F. Fan, P. Li, L. N. Quan, Y. Zhao, Z.-H. Lu, Z. Yang, S. Hoogland, E. H. Sargent, *Science*. **2017**, 355, 722.
- [2] J. Lu, A. Carvalho, H. Liu, S. X. Lim, A. H. Castro Neto, C. H. Sow, *Angew. Chemie - Int. Ed.* **2016**, 55, 11945.
- [3] Y. Shi, W. Wu, H. Dong, G. Li, K. Xi, G. Divitini, C. Ran, F. Yuan, M. Zhang, B. Jiao, X. Hou, Z. Wu, *Adv. Mater.* **2018**, 30, 1.
- [4] Y. Liu, Y. Zhang, Z. Yang, D. Yang, X. Ren, L. Pang, S. F. Liu, *Adv. Mater.* **2016**, 28, 9204.
- [5] S. Jose, *World Semicond. Trade Stat.* **2020**, 1.
- [6] R. P. Riesz, *Rev. Sci. Instrum.* **1962**, 33, 994.
- [7] H. R. Krall, F. A. Helvy, D. E. Persyk, *IEEE Trans. Nucl. Sci.* **1970**, 17, 71.
- [8] T. P. Pearsall, *J. Opt. Commun.* **1981**, 2, 42.
- [9] J. Tang, K. W. Kemp, S. Hoogland, K. S. Jeong, H. Liu, L. Levina, M. Furukawa, X. Wang, R. Debnath, D. Cha, K. W. Chou, A. Fischer, A. Amassian, J. B. Asbury, E. H. Sargent, *Nat. Mater.* **2011**, 10, 765.
- [10] J. Michel, J. Liu, L. C. Kimerling, *Nat. Photonics* **2010**, 4, 527.
- [11] S. Maimon, E. Finkman, G. Bahir, S. E. Schacham, J. M. Garcia, P. M. Petroff, *Appl. Phys. Lett.* **1998**, 73, 2003.
- [12] D. Guo, Q. Jiang, M. Tang, S. Chen, Y. I. Mazur, Y. Maidaniuk, M. Benamara, M. P. Semtsiv, W. T. Masselink, G. J. Salamo, H. Liu, J. Wu, *Semicond. Sci. Technol.* **2018**, 33, 094009.
- [13] M. D. Johnston, M. Barati, *Sol. Energy Mater. Sol. Cells* **2010**, 94, 2085.
- [14] W. Zhong, R. D. King-Smith, D. Vanderbilt, *Phys. Rev. Lett.* **1994**, 72, 3618.

- [15] J. F. Scott, M. Dawber, *Appl. Phys. Lett.* **2000**, 76, 3801.
- [16] L. Bocher, M. H. Aguirre, D. Logvinovich, A. Shkabko, R. Robert, M. Trottmann, A. Weidenkaff, *Inorg. Chem.* **2008**, 47, 8077.
- [17] P. Roy, I. Bose, T. Maiti, *Integr. Ferroelectr.* **2016**, 174, 34.
- [18] R. Jacobs, J. Hwang, Y. Shao-Horn, D. Morgan, *Chem. Mater.* **2019**, 31, 785.
- [19] A. Kojima, K. Teshima, Y. Shirai, T. Miyasaka, *J. Am. Chem. Soc.* **2009**, 131, 6050.
- [20] J. H. Im, C. R. Lee, J. W. Lee, S. W. Park, N. G. Park, *Nanoscale* **2011**, 3, 4088.
- [21] H. S. Kim, C. R. Lee, J. H. Im, K. B. Lee, T. Moehl, A. Marchioro, S. J. Moon, R. Humphry-Baker, J. H. Yum, J. E. Moser, M. Grätzel, N. G. Park, *Sci. Rep.* **2012**, 2, 1.
- [22] M. M. Lee, J. Teuscher, T. Miyasaka, T. N. Murakami, H. J. Snaith, *Science*. **2012**, 338, 643.
- [23] S. D. Stranks, G. E. Eperon, G. Grancini, C. Menelaou, M. J. P. Alcocer, T. Leijtens, L. M. Herz, A. Petrozza, H. J. Snaith, *Science*. **2013**, 342, 341.
- [24] J. Burschka, N. Pellet, S.-J. Moon, R. Humphry-Baker, P. Gao, M. K. Nazeeruddin, M. Grätzel, *Nature* **2013**, 499, 316.
- [25] H. Zhou, Q. Chen, G. Li, S. Luo, T. -b. Song, H.-S. Duan, Z. Hong, J. You, Y. Liu, Y. Yang, *Science*. **2014**, 345, 542.
- [26] National Renewable Energy Laboratory, Best Research-Cell Efficiencies, <https://www.nrel.gov/pv/assets/pdfs/best-research-cell-efficiencies.20200104>. **2020**.
- [27] Focus News, *Science*. **2013**, 342, 1438.
- [28] W. Nie, H. Tsai, R. Asadpour, A. J. Neukirch, G. Gupta, J. J. Crochet, M. Chhowalla, S. Tretiak, M. A. Alam, H. Wang, *Science*. **2015**, 347, 522.
- [29] M. I. Saidaminov, V. Adinolfi, R. Comin, A. L. Abdelhady, W. Peng, I. Dursun, M. Yuan, S. Hoogland, E. H. Sargent, O. M. Bakr, *Nat. Commun.* **2015**, 6, 8724.
- [30] D. Liu, Y. Wang, H. Xu, H. Zheng, T. Zhang, P. Zhang, F. Wang, J. Wu, Z. Wang, Z.

- Chen, S. Li, *Sol. RRL* **2019**, 3, 1800292.
- [31] L. Dou, Y. M. Yang, J. You, Z. Hong, W. H. Chang, G. Li, Y. Yang, *Nat. Commun.* **2014**, 5, 5404.
- [32] Y. Lee, J. Kwon, E. Hwang, C.-H. Ra, W. J. Yoo, J.-H. Ahn, J. H. Park, J. H. Cho, *Adv. Mater.* **2015**, 27, 41.
- [33] H. Wei, Y. Fang, P. Mulligan, W. Chuirazzi, H. H. Fang, C. Wang, B. R. Ecker, Y. Gao, M. A. Loi, L. Cao, J. Huang, *Nat. Photonics* **2016**, 10, 333.
- [34] W. Wu, X. Wang, X. Han, Z. Yang, G. Gao, Y. Zhang, J. Hu, Y. Tan, A. Pan, C. Pan, *Adv. Mater.* **2019**, 31, 1805913.
- [35] E. Edri, S. Kirmayer, S. Mukhopadhyay, K. Gartsman, G. Hodes, D. Cahen, *Nat. Commun.* **2014**, 5, 3461.
- [36] S. Wang, K. Wang, Z. Gu, Y. Wang, C. Huang, N. Yi, S. Xiao, Q. Song, *Adv. Opt. Mater.* **2017**, 5, 1700023.
- [37] L. Zhang, X. Yang, Q. Jiang, P. Wang, Z. Yin, X. Zhang, H. Tan, Y. Yang, M. Wei, B. R. Sutherland, E. H. Sargent, J. You, *Nat. Commun.* **2017**, 8, 15640.
- [38] J. Song, L. Xu, J. Li, J. Xue, Y. Dong, X. Li, H. Zeng, *Adv. Mater.* **2016**, 4861.
- [39] B. Yang, F. Zhang, J. Chen, S. Yang, X. Xia, T. Pullerits, W. Deng, K. Han, *Adv. Mater.* **2017**, 29, 1703758.
- [40] K. M. Sim, A. Swarnkar, A. Nag, D. S. Chung, *Laser Photonics Rev.* **2018**, 12, 1.
- [41] Y. Hou, L. Wang, X. Zou, D. Wan, C. Liu, G. Li, X. Liu, Y. Liu, C. Jiang, J. C. Ho, L. Liao, *Small* **2020**, 16, 1.
- [42] H. L. Zhu, J. Cheng, D. Zhang, C. Liang, C. J. Reckmeier, H. Huang, A. L. Rogach, W. C. H. Choy, *ACS Nano* **2016**, 10, 6808.
- [43] X. Liu, D. Yu, F. Cao, X. Li, J. Ji, J. Chen, X. Song, H. Zeng, *Small* **2017**, 13, 1.
- [44] B. R. Sutherland, A. K. Johnston, A. H. Ip, J. Xu, V. Adinolfi, P. Kanjanaboos, E. H.

- Sargent, *ACS Photonics* **2015**, 2, 1117.
- [45] J. Song, J. Li, L. Xu, J. Li, F. Zhang, B. Han, Q. Shan, H. Zeng, *Adv. Mater.* **2018**, 30, 1800764.
- [46] Q. Lin, Z. Wang, M. Young, J. B. Patel, R. L. Milot, L. Martinez Maestro, R. R. Lunt, H. J. Snaith, M. B. Johnston, L. M. Herz, *Adv. Funct. Mater.* **2017**, 27, 1702485.
- [47] A. Dualeh, N. Tétreault, T. Moehl, P. Gao, M. K. Nazeeruddin, M. Grätzel, *Adv. Funct. Mater.* **2014**, 24, 3250.
- [48] F. Zhao, K. Xu, X. Luo, W. Lv, Y. Peng, Y. Wang, F. Lu, S. Xu, *Org. Electron. physics, Mater. Appl.* **2017**, 46, 35.
- [49] D. H. Kang, S. R. Pae, J. Shim, G. Yoo, J. Jeon, J. W. Leem, J. S. Yu, S. Lee, B. Shin, J. H. Park, *Adv. Mater.* **2016**, 28, 7799.
- [50] K. Shen, X. Li, H. Xu, M. Wang, X. Dai, J. Guo, T. Zhang, S. Li, G. Zou, K. Choy, I. P. Parkin, Z. Guo, H. Liu, J. Wu, *J. Mater. Chem. A* **2019**, 7, 6134.
- [51] K. Shen, H. Xu, X. Li, J. Guo, S. Sathasivam, M. Wang, A. Ren, K. L. Choy, I. P. Parkin, Z. Guo, J. Wu, *Adv. Mater.* **2020**, 32, 2000004.
- [52] M. Li, K. Shen, H. Xu, A. Ren, J. Lee, S. Kunwar, S. Liu, J. Wu, *Small* **2020**, 16, 2004234.

## CHAPTER 2. FUNDAMENTALS OF PEROVSKITES

*This chapter presents an overview of the background knowledge required for understanding the rest of the thesis. In order to be as coherent as possible, the chapter opens with the fundamentals of perovskites, starting with the crystal structures and chemical compositions of perovskite. The chapter then concentrates on explaining absorption and recombination processes, followed by a comprehensive description of perovskite morphology. Various deposition methods of perovskites are subsequently discussed and explained. A more detailed section is dedicated to the photodetector architectures and figures of merits, including the operation mechanism of various device structures. In the last section, the current challenges of perovskite-based photodetectors are listed, especially the long-term stability issue.*

### 2.1 Crystal Structures and Chemical Compositions

As mentioned previously, perovskites were first discovered in 1839 by German scientist Gustav Rose in mineral ores composed of calcium, titanium and oxygen ( $\text{CaTiO}_3$ ).<sup>[1]</sup> Similar structures of these kinds of oxide compounds were subsequently classified into the metal oxide perovskites, with the general chemical formula  $\text{ABO}_3$ . A is generally a rare-earth or alkaline-earth ion with a large ionic radius. It coordinates with 12 oxygen ions to form the densest cubic pile, which can stabilise the perovskite structure. B normally represents a transition element ion with a smaller ionic radius, which coordinates with six oxygen ions and occupies the centre of the octahedron in the densest cubic pile. A and B are able to be replaced by other metal ions with similar radius while retaining their original crystal structure, which makes them functional for tuneable photodetection. After extensive research, it was found that such metal oxide compounds possess various unique properties, and they have been widely explored and applied

in condensed matter physics and materials science. For example, they can be used as anode materials for solid fuel cells, colossal magnetoresistive materials, microwave dielectric materials and multiferroic materials.<sup>[2-4]</sup>

Nowadays, novel three-dimensional (3D) HMHPs have gained substantial attention in optoelectronic applications owing to their excellent optical and electrical properties, including their tuneable direct bandgap, good optical absorption, long diffusion length ( $\sim 175 \mu\text{m}$ ) and high carrier mobility ( $\sim 200 \text{ cm}^2 \text{ V}^{-1} \text{ s}^{-1}$ ), making them perfect light harvesters.<sup>[5-12]</sup> For example, the carrier diffusion length ( $L_D$ ) is associated with the charge-collection efficiency, which is defined as the average distance a carrier can move before it recombines. Typically, the diffusion length can be estimated from their mobilities and carrier lifetimes using 1D diffusion mode:

$$L_D = \sqrt{kT\mu\tau/e} \quad \text{Equation 2.1}$$

where  $L_D$  is the carrier diffusion length,  $k$  represents Boltzmann's constant,  $T$  denotes temperature,  $\mu$  is the carrier mobility,  $\tau$  is the carrier lifetime and  $e$  is the elementary charge. With a longer diffusion length, carriers can move longer distance before recombination, thus they are more likely to be collected and contribute to the photocurrent. It is known that the thickness of the active layer is normally smaller than or similar to the carrier diffusion length. Therefore, the photocarriers can be efficiently transferred. The longer diffusion length also suggests a higher carrier mobility and a prolonged carrier lifetime, which indicates a lower defect density and a lower recombination rate.

In general, HMHPs are a large family of semiconductors that share the same stoichiometry of  $\text{ABX}_3$ . Notably, the oxidation states of the two cations have to be equal to three ( $q^A + q^B = -3q^X = 3$ ), hence the only possible ternary mixture is I-II- $\text{X}_3$ . For example, if  $X$  is a group VII element, the cations  $A$  and  $B$  correspond to monovalent and divalent, respectively. In details,

- 1) A-sites are generally monovalent organic molecular groups  $\text{CH}_3\text{NH}_3^+$ ,  $\text{CH}(\text{NH}_2)_2^+$ ,  $\text{Cs}^+$ , and their combinations;
- 2) B denotes divalent metal cations, including lead ions ( $\text{Pb}^{2+}$ ), tins ions ( $\text{Sn}^{2+}$ ) and their combinations, or ions with dissimilar sizes;
- 3) X represents halide anions, such as  $\text{I}^-$ ,  $\text{Cl}^-$ ,  $\text{Br}^-$  and their mixtures. A different spectral response can be easily achieved via halide anion rearrangement.

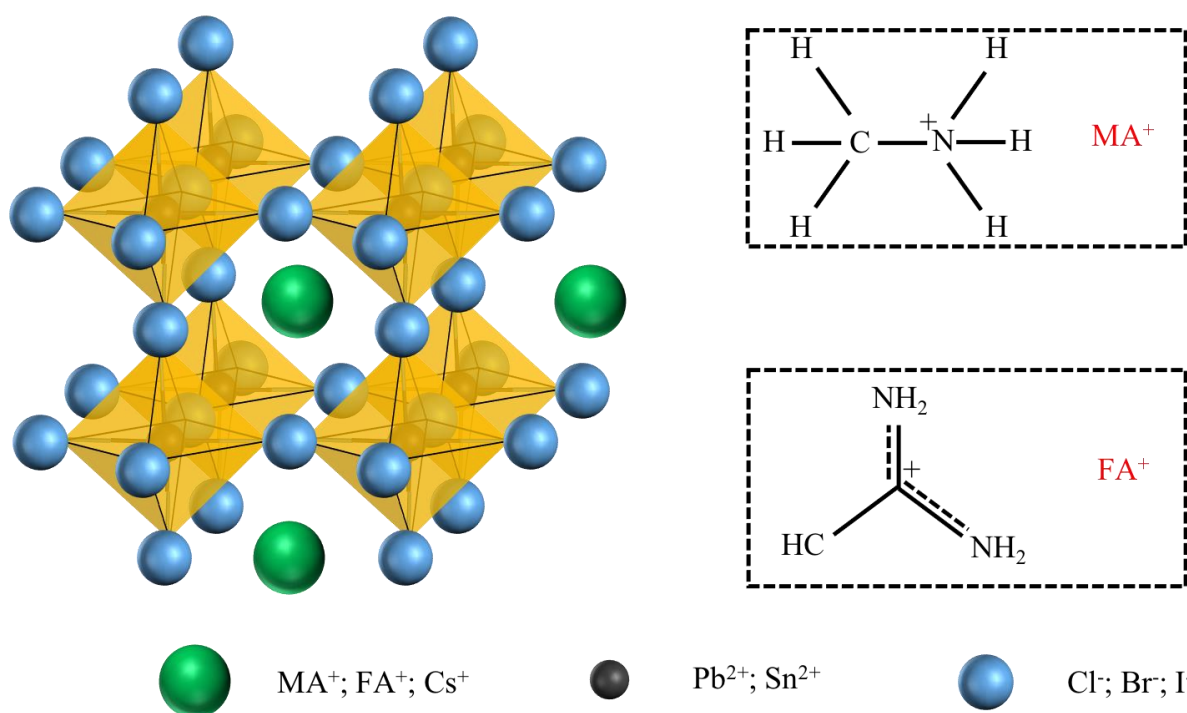


**Figure 2.1** Typical crystal structure of perovskites.

As shown in Figure 2.1,  $\text{ABX}_3$  perovskite is formed with monovalent A-site cations occupying the cavity between four adjacent corner-sharing  $\text{BX}_6$  metal halide octahedra. With the consideration of the Goldschmidt tolerance factor ( $t$ ) and the octahedral factor ( $m$ ), their crystallographic stability can be accordingly determined.<sup>[13–15]</sup> Both  $t$  and  $m$  are dependent on the ionic radii ( $r$ ) of A, B and X with the expressions:

$$t = (r_A + r_X) / [\sqrt{2}(r_B + r_X)], \text{ and } m = r_B / r_X, \text{ respectively.}$$

When  $t = 1$ , the crystal structure is the ideal body-centred cubic configuration with the best symmetry. While  $t$  is in the range of 0.89–1.0, there is a distortion in cells and crystal

structures, but good optical and electrical properties are still exhibited. It has been proven that a stable 3D perovskite structure is obtained when  $0.813 < t < 1.107$  and  $0.442 < m < 0.895$ , which provides optimum optical and electrical characteristics, owing to a high degree of ionic bonding.<sup>[16,17]</sup> On the other hand, if  $t$  is lower (A is small or B is large), the structure tends to be less symmetric, as shown in Figure 2.2.

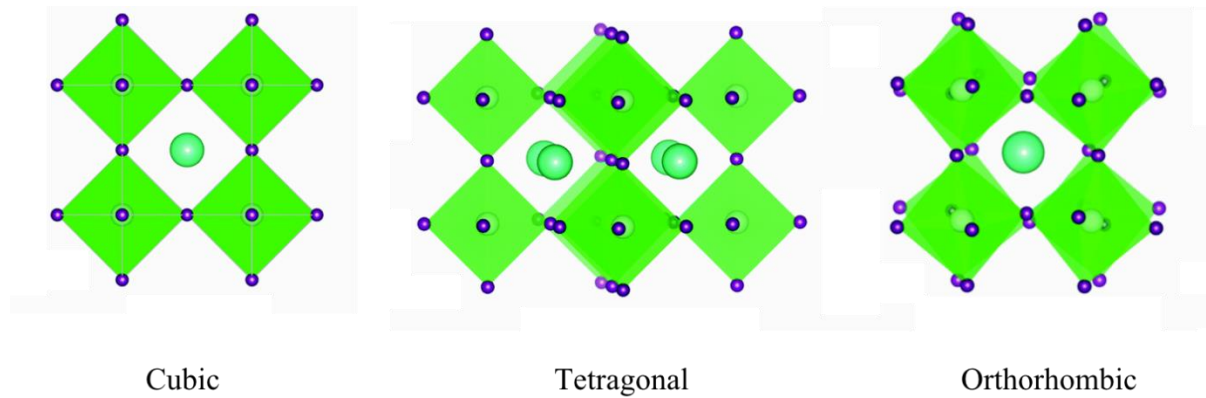


**Figure 2.2** Crystal structure of the  $\text{CsPbBr}_3$  perovskite in different phases. Reproduced from ref. [18] with permission from Royal Society of Chemistry, copyright 2020.

As mentioned previously, there are two types of HMPs, namely HMHPs and IMHPs, where the A-site is replaced with inorganic cations ( $\text{Cs}^+$ ) instead of organic groups ( $\text{MA}^+$ ,  $\text{FA}^+$  and their combinations). They can be simply obtained by rearranging the combination of A, B and X. For the most extensively investigated HMHPs,  $\text{CH}_3\text{NH}_3\text{PbI}_3$ ,  $t$  suggests that  $\text{CH}_3\text{NH}_3\text{PbI}_3$  is a tetragonal phase with given  $r$  ( $\text{CH}_3\text{NH}_3^+ = 0.21$  nm,  $\text{Pb}^{2+} = 0.119$  nm,  $\text{I}^- = 0.22$  nm). In terms of IMHPs such as  $\text{CsPbBr}_3$ ,  $r$  ( $\text{Cs}^+$ ,  $\text{Pb}^{2+}$  and  $\text{Br}^-$ ) can be determined as 0.174 nm, 0.119 nm and 0.196 nm, respectively. The detailed values of  $r$  and  $t$  are listed in Table 2.1.<sup>[16,19]</sup>

**Table 2.1** The radius of each element and the tolerance factors of  $\text{CH}_3\text{NH}_3\text{PbI}_3$  and  $\text{CsPbBr}_3$ .

Ions	$\text{MA}^+$	$\text{FA}^+$	$\text{Cs}^+$	$\text{Pb}^{2+}$	$\text{Sn}^{2+}$	$\text{Cl}^-$	$\text{Br}^-$	$\text{I}^-$
Radius (nm)	0.21	0.253	0.174	0.119	0.110	0.181	0.196	0.22
Perovskites	$\text{CH}_3\text{NH}_3\text{PbI}_3$				$\text{CsPbBr}_3$			

Tolerance factor	0.837	0.86
------------------	-------	------

In addition, perovskite phase structures are strongly dependent on the tilting and rotation of the  $BX_3$  polyhedra in the lattice.<sup>[20]</sup> Moreover, they were found to be changing with temperature, as shown in Table 2.2. For example,  $CH_3NH_3PbI_3$  transitioned from the orthorhombic to the tetragonal phase as the temperature reached 165 K, and further transformed to the cubic phase when the temperature was over 327 K.<sup>[21]</sup> On the other hand,  $CsPbBr_3$ , as an all-inorganic perovskite, transferred from the orthorhombic to the tetragonal and cubic phase as the temperature reached 328 K and 383 K, respectively.<sup>[22]</sup> The different phase transition temperature between  $CH_3NH_3PbI_3$  and  $CsPbBr_3$  suggests the better thermal stability of  $CsPbBr_3$ .

**Table 2.2** The temperature required for phase transitions of  $CH_3NH_3PbI_3$  and  $CsPbBr_3$ .

Materials	Phase transition		
$CH_3NH_3PbI_3$	Orthorhombic	→ Tetragonal 165 K	→ Cubic 327 K
$CsPbBr_3$	Orthorhombic	→ Tetragonal 328 K	→ Cubic 383 K

## 2.2 Absorption

In solid-state physics, absorption is one of the essential processes of semiconductors, which primarily determines the ability of absorbing photon energy and therefore further affects the performance of as-fabricated photodetectors. The bandgap energy ( $E_g$ ), as one of the fundamental concepts in the absorption process, can be defined as the energy gap between the conduction band minimum (CBM) and valence band maximum (VBM), where electron states are forbidden, as shown in Figure 2.3. Compared to conductors, electrons in a semiconductor have to absorb energy to cross the bandgap and reach the CB.

Generally, semiconductors can be classified into two categories, namely direct- and indirect-bandgap semiconductors. For direct-bandgap semiconductors, including InP, GaAs and perovskites, the positions of the CBM and VBM in the crystal momentum ( $k$ -vector) are the same, as depicted in Figure 2.3a. The transition of electrons from VBM to CBM only requires the absorption of incident photon energy, instead of the participation of phonons (quantised energy of lattice vibration). Accordingly, it suggests that the electrons would not be scattered by the lattice vibration.

In addition, the  $k$ -vectors of the CBM and VBM of indirect-bandgap semiconductors, such as Si and Ge, are different, as illustrated in Figure 2.3b. Different from direct-bandgap materials, the excitation process not only absorbs incident energy but also requires the participation of phonons. Initially, photons are introduced to satisfy the conversion of momentum. It is worth noting that the energy of phonons is discrete, suggesting electrons transit more easily in direct-bandgap semiconductors. Optical measurements can be used for determining the types of semiconductor bandgaps. In direct-bandgap semiconductors one can easily distinguish the absorption band edge in the absorption spectra, where the change is relatively sharp, as opposed to the slow change observed in indirect-bandgap materials.

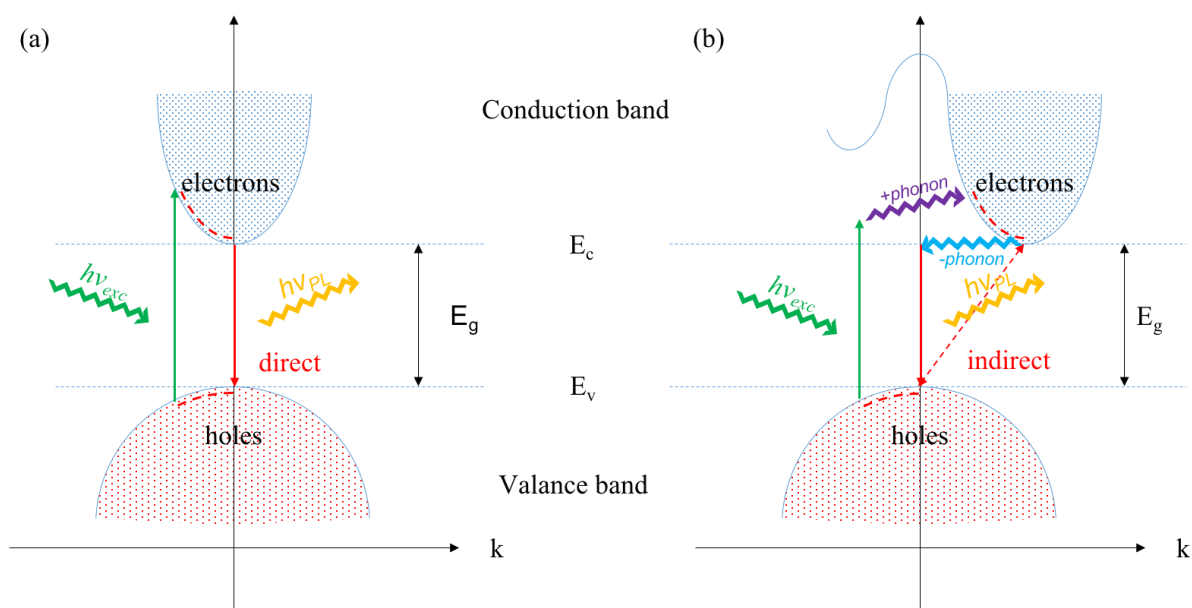


**Figure 2.3** The band diagrams of (a) direct and (b) indirect semiconductors.

The absorption coefficient ( $\alpha$ ) is another important parameter in the absorption process, determining how far the light of a particular wavelength can penetrate materials before it is absorbed. The expression can be written as

$$\alpha = 4\pi k/\lambda \quad \text{Equation 2.2}$$

where the unit of  $\alpha$  is  $\text{cm}^{-1}$ . The absorption coefficient depends on both the material and the wavelength of the incident light; therefore, different materials have different absorption coefficients at a particular wavelength. In general, a sharp edge occurs in the semiconductors' absorption coefficient spectrum, and the absorption coefficients of a variety of state-of-the-art semiconductors are further summarised over a wide range between UV and near-infrared, as illustrated in Figure 2.4.<sup>[23]</sup> It can be clearly observed that the  $\alpha$  of  $\text{CH}_3\text{NH}_3\text{PbI}_3$  is better than that of c-Si (indirect bandgap) in the visible wavelength range, and is comparable to that of a-Si:H (10% H) and GaAs (direct bandgap). Since light with a low energy below  $E_g$  has insufficient energy to excite an electron from the VB into the CB, accordingly, this light cannot be absorbed.

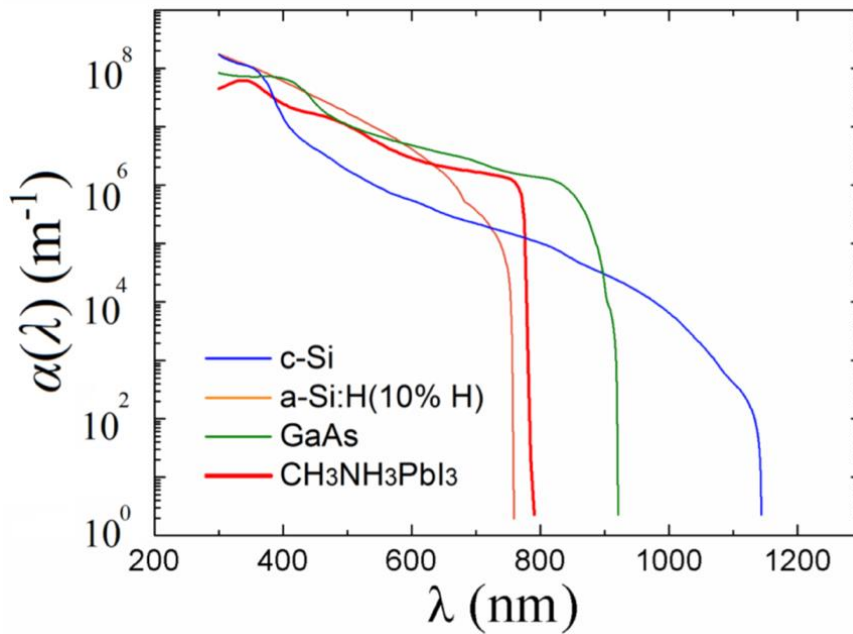


**Figure 2.4** Absorption coefficient of various semiconductor materials in a range of wavelength.<sup>[23]</sup>

To be more specific, silicon (Si), as one of the represented conventional semiconductors, is a relatively poor light harvester over the visible range, resulting in less photon absorption. Moreover, the radiative recombination efficiency is limited due to its intrinsic nature (indirect bandgap). Therefore, devices based on Si normally require a much greater (hundreds of  $\mu\text{m}$ ) thickness to compensate for the disadvantages of the low absorption coefficient, which denies the philosophy of portable and cost-effective fabrications. On the other hand, perovskite, as a promising candidate in optoelectronic devices, is a direct-bandgap semiconductor with a large absorption coefficient exceeding  $\approx 10^4 \text{ cm}^{-1}$  in a wide range. It can more readily absorb photons, suggesting that perovskite film of only a few hundred nm is able to absorb all incident illumination, which is much thinner than Si. This is one of the most important advantages of employing perovskites in optoelectronic devices. Therefore, they are more promising for achieving high-performance devices and can be further employed in portable and wearable modules.

After absorbing photons, the electrons of perovskites transit from the VBM to the CBM, and simultaneously form an exciton. In order to achieve efficient optoelectronic conversion, excitons have to migrate and be separated before recombination.<sup>[8]</sup> For perovskites, electrons and holes in excitons are distributed in the larger lattice space, where the binding energy ( $E_b$ ) is weak due to the weak Coulomb force. According to the reported literature, the  $E_b$  of  $\text{CH}_3\text{NH}_3\text{PbI}_3$  and  $\text{CsPbBr}_3$  is 20 meV and 40 meV, respectively, via time-resolved spectroscopy.<sup>[24,25]</sup> Thus, excitons are easy to separate at room temperature and become free electrons and holes, which is beneficial for photodetectors.

Moreover, the bandgap energy of perovskite determines the limit of the absorbing wavelength, which can be obtained from a Tauc plot. The typical perovskite  $\text{CH}_3\text{NH}_3\text{PbI}_3$  has a bandgap energy of  $\sim 1.6 \text{ eV}$ , which almost covers the visible spectrum, and can be considered

as a broadband photodetector. Moreover, element substitutions can be used to control the bandgap of perovskites, as shown in Figure 2.5:

- i) A-site cation substitution,
- ii) B-site substitution,
- iii) Halogen substitution.

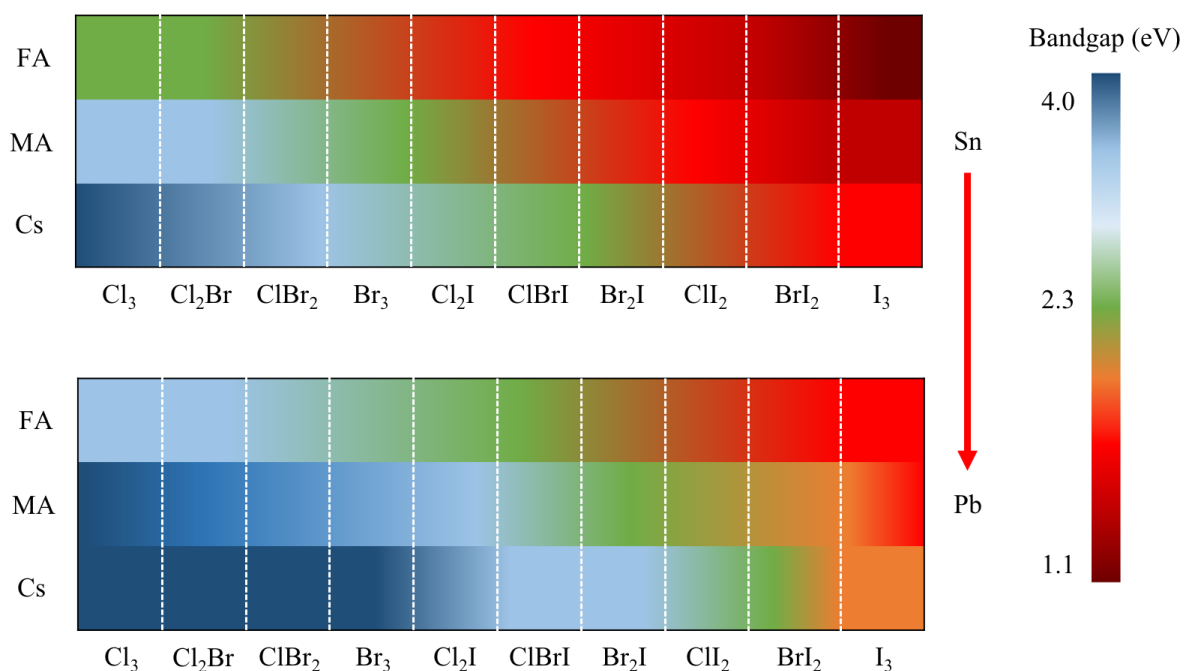


**Figure 2.5** The tuneable bandgaps with different compositions.<sup>[26]</sup>

Theoretically, A-site cation dramatically affect the material structural stability, which can adjust the Goldschmidt tolerance factor, and change the tilting of the Pb–X<sub>6</sub> octahedra.<sup>[27]</sup> For example, Gratzel *et al.* replaced CH<sub>3</sub>NH<sub>3</sub><sup>+</sup> with Cs<sup>+</sup> and CH(NH<sub>2</sub>)<sub>2</sub><sup>+</sup>, which significantly improved the stability of perovskite, resulting in record efficiencies.<sup>[28,29]</sup> Meanwhile, the bandgap energy of perovskites can be slightly tuned. The bandgap of CsPbI<sub>3</sub> can be tuned by replacing inorganic Cs<sup>+</sup> with CH<sub>3</sub>NH<sub>3</sub><sup>+</sup> and CH(NH<sub>2</sub>)<sub>2</sub><sup>+</sup>, which are slightly larger molecules, shrinking the bandgap energy from 1.7 eV to around 1.59 eV and 1.48 eV, respectively. However, the organic parts in perovskite are unstable under ambient conditions, resulting in a poor device performance.

Taking the advantage of the relationship between conduction band and the outer shell orbitals of B-site element, the optical and electrical properties can be controlled. For example, the bandgap can be adjusted by replacing  $\text{Pb}^{2+}$  with tin ( $\text{Sn}^{2+}$ ). Specifically, the bandgap energy of a Sn-Pb mixed halide perovskite ( $\text{CsSn}_{0.6}\text{Pb}_{0.4}\text{I}_3$ ) is  $\sim 1.46$  eV, and can be further reduced to  $\sim 1.3$  eV when completely substitute  $\text{Pb}^{2+}$  with  $\text{Sn}^{2+}$  (*i.e.*  $\text{CsSnI}_3$ ). Although the lead-free perovskites are more environmentally friendly,  $\text{Sn}^{2+}$  is sensitive to oxygen and moisture, resulting in a degraded performance.

Different from the B-site substitution, bandgap modification by the halogen replacement is associated with the valence band. Substitution with halide elements (bromide and chloride) has also been reported, with an  $E_g$  of 2.2 eV and 3.1 eV, respectively, enabling short-wavelength detection. Depending on the requirements of spectral response, perovskite with different bandgap energy can be designed. Wang and co-workers demonstrated tunable-bandgap perovskite ( $\text{CH}_3\text{NH}_3\text{PbX}_3$ ) NWs based photodetector via a multiple engineering controlled growth.<sup>[30]</sup> Although the as-fabricated photodetectors exhibited a good photoresponse, the stability issues has not addressed yet.

## 2.3 Recombination

Recombination is another important process that should be considered in perovskite-based optoelectronics, which is the reverse process of light absorption. It can be characterised to assess the quality of the perovskite and the performance of photodetectors. Generally, the light-induced electron-hole pairs are separated by the external or internal electrical field and collected from their respective terminals, leading to the generation of photocurrent. However, not all photocarriers can contribute to the final current due to carrier recombination. The recombination process is immediate, and some of the electrons lose their absorbed energy and fall down from the CB to the VB. Hence, only some of the carriers generated by perovskites

can directly contribute to the photocurrent. There are two pathways in the recombination process, namely radiative and non-radiative recombination, which are illustrated in Figure 2.6.

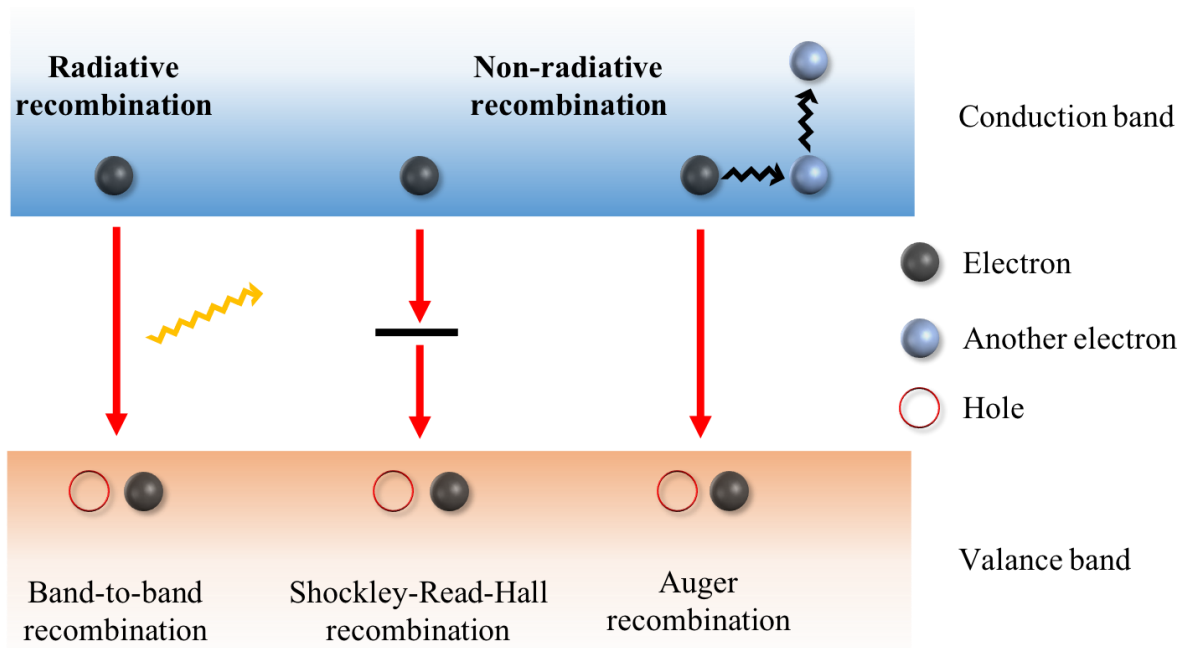


**Figure 2.6** Recombination pathways of semiconductors.<sup>[31]</sup>

High radiative recombination (band-to-band recombination) has been confirmed in perovskites. An electron from the CB can directly recombine with a hole in the VB, and efficiently release a photon. Since the energy of the photon is close to or higher than the bandgap of the semiconductor, it can only be absorbed and emitted out of the material. In some highly crystalline semiconductors, band-to-band recombination is a major contribution to the device performance.

In terms of non-radiative recombination, two types of mechanisms are involved, namely Auger recombination and Shockley-Read-Hall (SRH) recombination. There are three charge carriers participating in the Auger recombination process. Similar to band-to-band recombination, an electron recombines with a hole. However, instead of releasing a photon, the energy is given to another electron in the CB, exciting it into a higher energy level in the CB. Eventually the electron relaxes back to the CB through thermalisation, immediately dissipating its excess energy. Due to the involvement of three charge carriers, Auger

recombination is an important recombination process only where carrier densities are very high, such as in highly doped materials, at high temperature or under strong illumination.

SRH recombination, happens with defects within the crystal. Different from the aforementioned recombination pathways, an electron or a hole is initially trapped at an energy state within the forbidden region, which is caused by dopants or defects in the crystal. The trapped carrier can again be released by thermal activation. Otherwise, if the defect traps another opposite charge carrier before releasing the first trapped charge carrier, the two carriers recombine, resulting in lost energy. As the concentration of defects is high at the surface or grain boundaries due to the disruption of crystal lattices, the SRH recombination is more profound in these areas. Such strong non-radiative recombination processes are detrimental to photoelectric conversion, and further deteriorate the device performance. Therefore, it is essential to prevent non-radiative recombination as much as possible in photodetectors by controlling and minimising defects and charge traps to improve the detection capability.

## 2.4 Perovskite Morphology

A good film morphology, including good uniformity and surface coverage, is essential for constructing high-performance optoelectronics. Engineering a uniform and compact perovskite thin film with fewer defects (pinholes and grain boundaries) by fine control of the thin film over the crystallisation process benefits the electron-hole pair generation, carrier transport and/or collection, and accordingly enhances the device performance.

Polycrystalline film and single crystals are the two main forms of perovskites. To date, various fabrication methods have been used for synthesising polycrystalline films, including thermal annealing, solvent annealing and chemical vapour deposition. However, polycrystalline films generally suffer from morphological disorder, limiting the device performance.

Compared to polycrystalline films, perovskite single crystals (Figure 2.7), from bulk crystals (3D) to nanosheets (2D), nanowires (1D) and QDs (0D), possess a lower density of trap states and longer diffusion length, which is promising for rapid and sensitive photodetection.

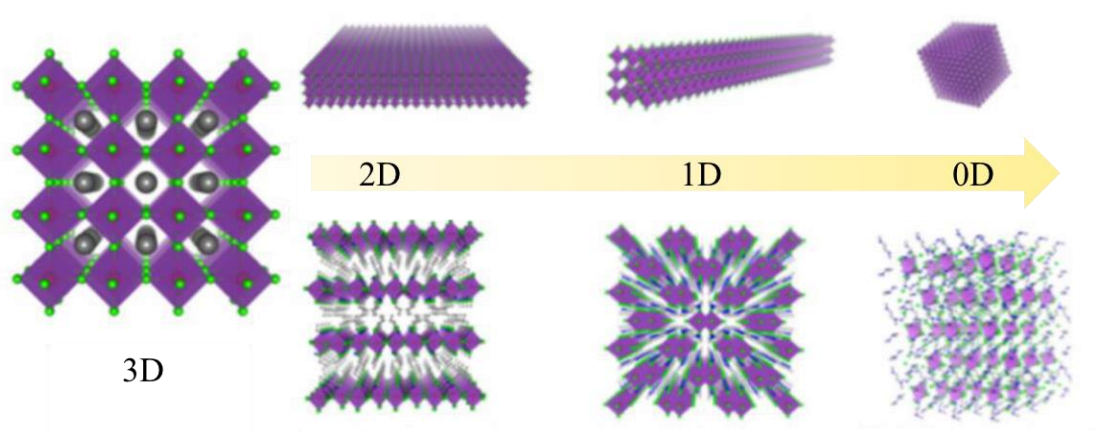


**Figure 2.7** Morphology of perovskite single crystal with different dimensions. Reproduced from ref. [32] with permission from Elsevier, copyright 2019.

#### 2.4.1 Bulk Crystals

The solution method is the main method for growing bulk perovskites. This process can be broken down into antisolvent vapour-assisted crystallisation, cooling-induced crystallisation and inverse temperature crystallisation.<sup>[33-36]</sup>

The antisolvent vapor-assisted crystallisation method uses the diffusion of antisolvents to lower the solubility of the precursor, further promoting the perovskite film growth, which does not depend on the relationship between temperature and the solubility of the solute. This method has higher freedom of operation, therefore, it is commonly used in the preparation of perovskite polycrystalline and microcrystalline films. The key is the selection of appropriate antisolvents during the process. Bakr and co-workers grew crack-free  $\text{CH}_3\text{NH}_3\text{PbX}_3$  single crystals with a volume over  $100 \text{ mm}^3$  using this method in 2015, as shown in Figure 2.8a. These single crystals exhibited an extremely low density of traps in the order of  $10^9$ – $10^{10}$  per cubic

centimetre, as well as a long diffusion length over 10 micrometres.<sup>[33]</sup> Three years later, Xu *et al.* reported centimetre-sized  $\text{CH}_3\text{NH}_3\text{PbBr}_3$  bulk crystals using a modified antisolvent vapor-assisted crystallisation method, as shown in Figure 2.8b. The resulting mobility-lifetime products achieved  $2.2 \times 10^{-4}$  and  $4.2 \times 10^{-4} \text{ cm}^2 \text{ V}^{-1}$  for electrons and holes, respectively.<sup>[34]</sup>

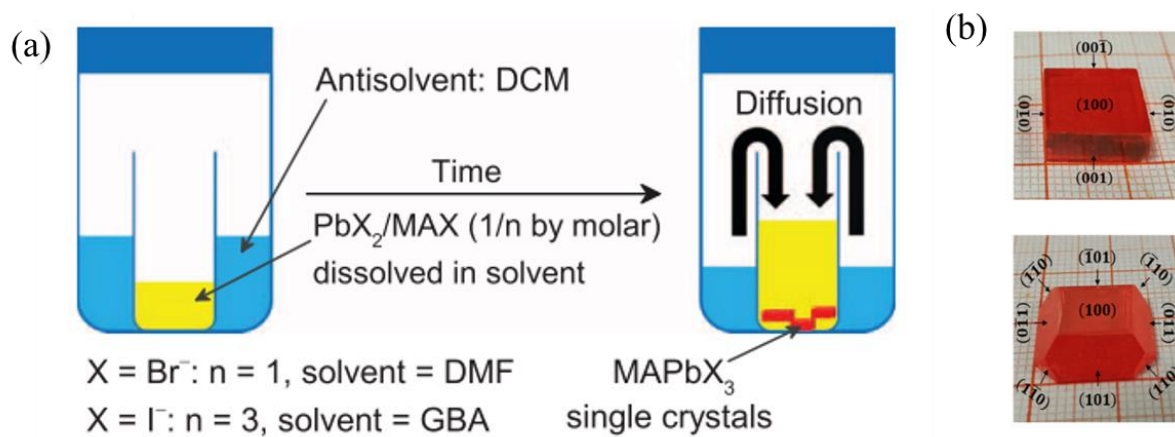


**Figure 2.8** (a) Schematic diagram of the crystallisation process. Reproduced from ref. [33] with permission from The American Association for the Advancement of Science, copyright 2015. (b) Digital images of  $\text{CH}_3\text{NH}_3\text{PbBr}_3$  bulk crystals. Reproduced from ref. [34] with permission from American Chemical Society, copyright 2018.

The cooling-induced crystallisation method uses the lowered temperature to slowly precipitate the crystals from the saturated solution of perovskite precursors, which is conventional, but time-consuming. Huang *et al.* utilised this strategy to prepare  $\text{CH}_3\text{NH}_3\text{PbI}_3$  single crystals, achieving a diffusion length of over 175 micrometres under 1 sun illumination.<sup>[35]</sup> The setup of equipment is illustrated in Figure 2.9a. Applying temperature gradients at different positions inside the vessel promotes the supersaturation of perovskite precursor, which is beneficial for growing bulk crystals. The same group also successfully synthesised  $\text{CH}_3\text{NH}_3\text{PbBr}_3$ ,  $\text{CH}_3\text{NH}_3\text{PbCl}_3$  and other hybrid perovskite bulk crystals (Figure 2.9b), and further applied them in narrowband photodetectors, resulting in an impressive photodetection performance.<sup>[36]</sup>

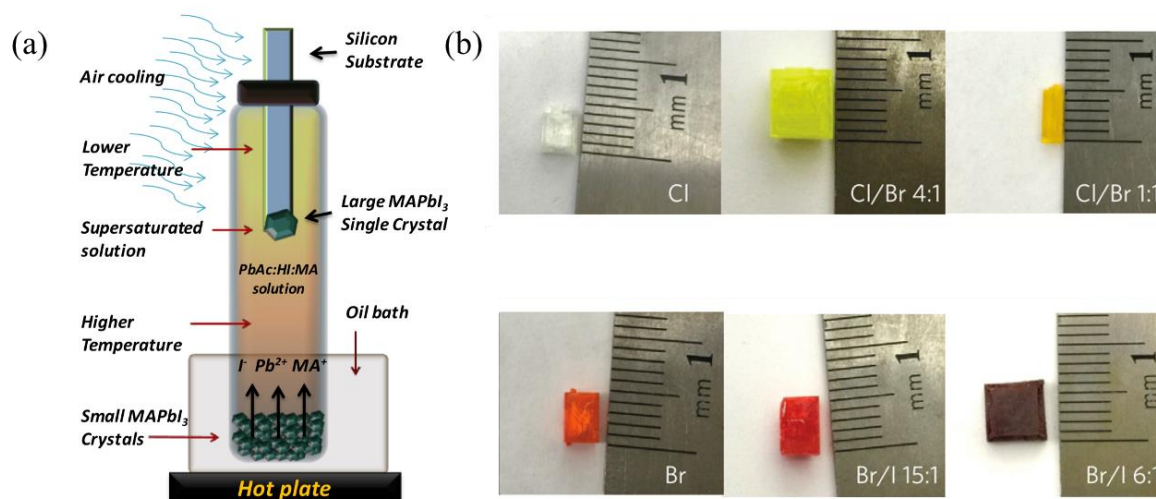


**Figure 2.9** (a) The setup for bulk single-crystal growth. Reproduced from ref. [35] with permission from The American Association for the Advancement of Science, copyright 2015. (b) Digital images of perovskite crystals with varied halide compositions. Reproduced from ref. [36] with no permission.

Different from cooling-induced crystallisation, inverse temperature crystallisation utilises the phenomenon of the decrease in the solubility of perovskites with elevated temperature to precipitate crystals. In 2015, Bakr *et al.* dissolved  $\text{CH}_3\text{NH}_3\text{Cl}$  and  $\text{PbCl}_2$  powders in a 1:1 (volume ratio) DMF and DMSO solvents, followed by heating the oil bath containing the perovskite precursor solution, as shown in Figure 2.10a.<sup>[37]</sup> With elevating temperature, the solubility of the perovskite precursor gradually decreases, resulting in a millimetre-sized perovskite bulk crystal (Figure 2.10b). Based on this method, Zhang *et al.* developed an advanced version to grow high-quality tetragonal  $\text{CH}_3\text{NH}_3\text{PbCl}_3$  single crystals, and further fabricated a high-selectivity photodetector.<sup>[38]</sup>

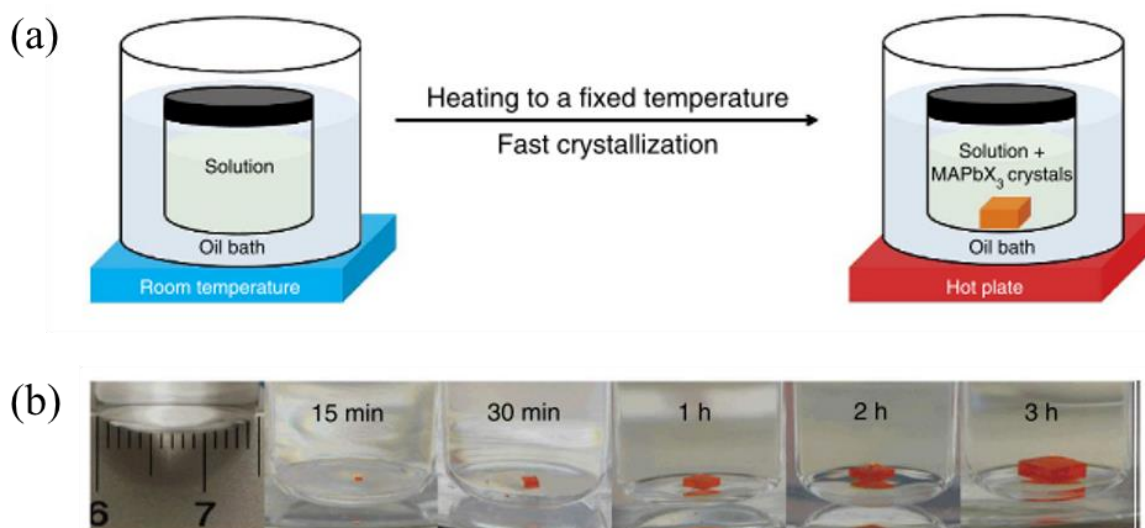


**Figure 2.10** (a) Schematic representation of the setup for crystallisation. (b)  $\text{CH}_3\text{NH}_3\text{PbBr}_3$  crystal growth at different time intervals. Reproduced from ref. [37] with permission from Nature Publishing Group, copyright 2015.

#### 2.4.2 Nanostructured Crystals

In addition to 3D bulk crystals, 2D perovskites (e.g. nanosheets and nanoplates) have recently attracted increasing attention in optoelectronics, owing to their enhanced ambient stability with respect to their 3D counterparts.

To date, the synthesis strategy of 2D perovskite crystals mainly contains solution-phase growth and a combined growth method.<sup>[39,40]</sup> As shown in Figure 2.11a, Zeng *et al.* fabricated 3.3 nm-thick 2D  $\text{CsPbBr}_3$  nanosheets through the facile solution-phase growth method.<sup>[35]</sup> The 2D nanosheets were subsequently employed as the absorber in flexible photodetectors, and demonstrated a high sensitivity, good stability and excellent flexibility after bending 10,000 cycles, as displayed in Figure 2.11b and Figure 2.11c. In 2016, Bao *et al.* reported a combined growth method, which integrated a solution process and vapour-phase conversion method, to grow ultrathin 2D  $\text{CH}_3\text{NH}_3\text{PbI}_3$  crystals with a thickness of 1.3 nm.<sup>[40]</sup> As shown in Figure 2.11d,  $\text{PbI}_2$  aqueous solution was firstly cast onto a substrate, followed by heating the substrate

at an increasing temperature. The 2D  $\text{PbI}_2$  nanosheets were subsequently nucleated, resulting in the formation of high-quality 2D  $\text{CH}_3\text{NH}_3\text{PbI}_3$  perovskite nanosheets after intercalating the vapour-phase  $\text{CH}_3\text{NH}_3\text{I}$  molecules into the interval sites of  $\text{PbI}_6$  octahedron layers. Based on these 2D crystals, a high-performance phototransistor was demonstrated with a photoresponsivity of  $22 \text{ A W}^{-1}$  under 1 V bias (Figure 2.11e).

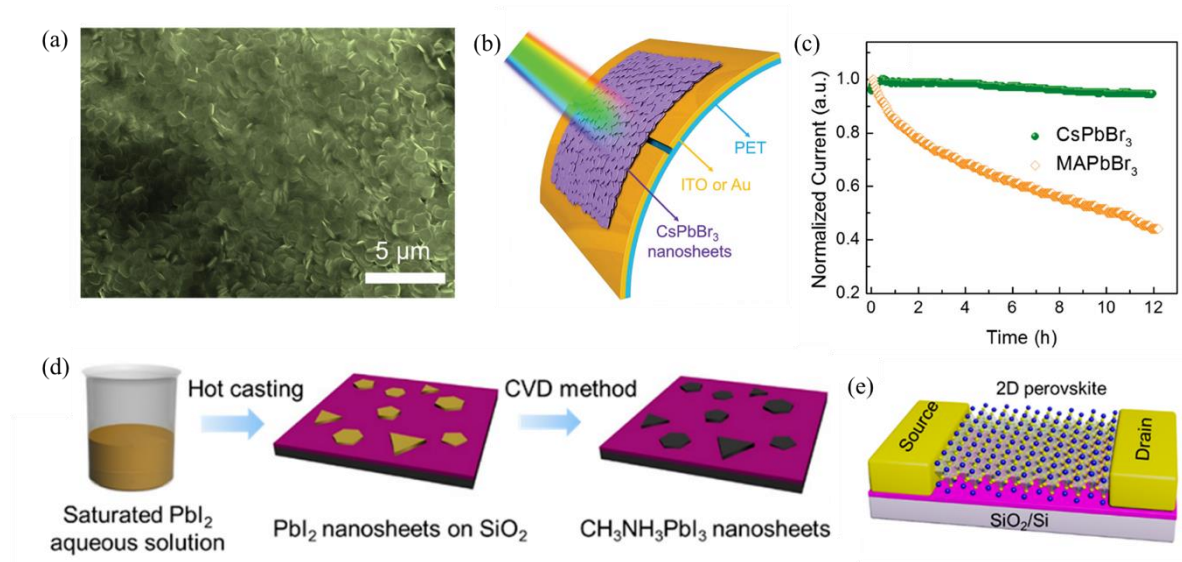


**Figure 2.11** (a) Low-magnification SEM image of 2D ultrathin  $\text{CsPbBr}_3$  nanosheets. (b) Representation of  $\text{CsPbBr}_3$  nanosheet-based photodetectors. (c) Stability comparisons between  $\text{CsPbBr}_3$  and  $\text{CH}_3\text{NH}_3\text{PbBr}_3$  detectors. Reproduced from ref. [39] with permission from The John Wiley and Sons, copyright 2016. (d) Schematic representation of growth process. (e) Illustration of a phototransistor. Reproduced from ref. [40] with permission from American Chemical Society, copyright 2016.

Perovskite nanowires, as 1D perovskite crystals, are also a hot research topic owing to their high surface-to-volume ratio and quantum size confinement, which are promising for optoelectronics and catalysis. To date, various synthesis methods have been reported, particularly the solution-phase method.<sup>[41-44]</sup> In 2015, Zhang *et al.* synthesised high-quality porous  $\text{CH}_3\text{NH}_3\text{PbBr}_3$  perovskite nanowires via the self-template directed method.<sup>[41]</sup> As shown in Figure 2.12a, Pb-containing nanowires reacted with  $\text{CH}_3\text{NH}_3\text{Br}$  and  $\text{HBr}$  in an

organic solvent, resulting in the quick formation of  $\text{CH}_3\text{NH}_3\text{PbBr}_3$  perovskite nanowires. By dissolution of the organic part of the nanowire precursor, mesopores were formed in the preserved 1D nanowires. Photodetectors based on such nanowires exhibited a reproducible photoresponse and high stability, which is beneficial for high-performance devices. Later, Mirkin's group fabricated large-area perovskite arrays oriented perpendicular to the substrate using the AAO template.<sup>[42]</sup> They simply injected precursor solution onto the AAO template, followed by dissolution and recrystallisation to realise the growth of nanowires, as shown in Figure 2.12b. In addition, other halide perovskites ( $\text{CH}_3\text{NH}_3\text{PbI}_3$ ,  $\text{CH}_3\text{NH}_3\text{PbBr}_3$  and  $\text{Cs}_2\text{SnI}_6$ ) were demonstrated using this method.

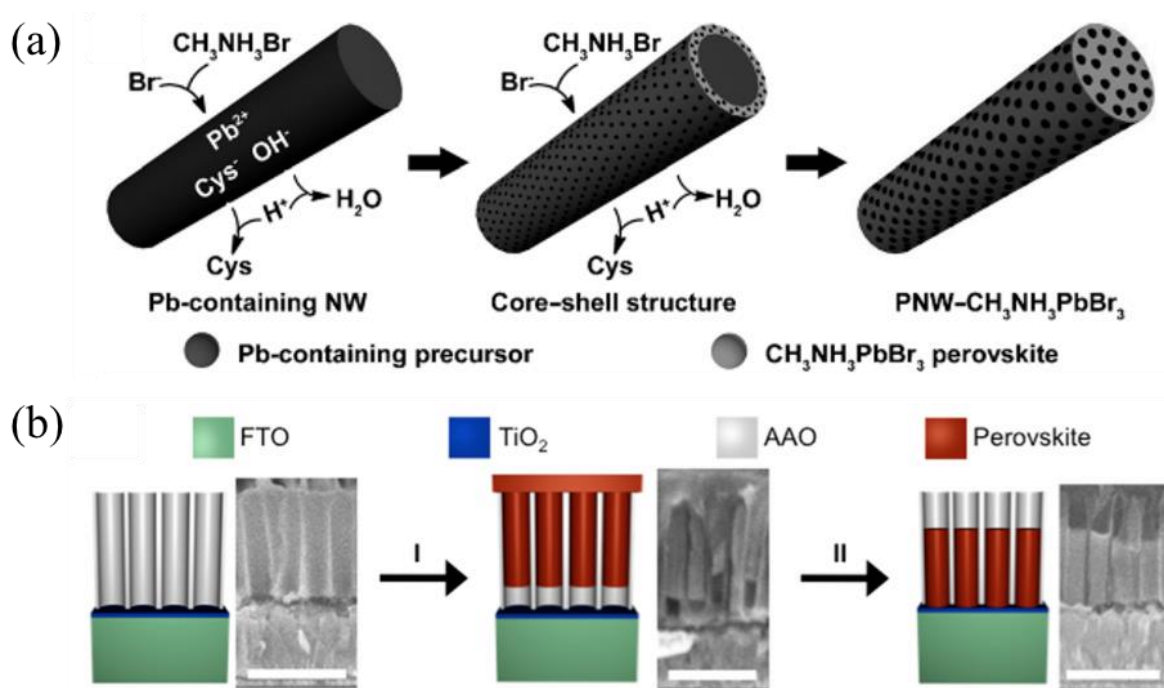


**Figure 2.12** (a) Schematic illustration of synthesis of porous  $\text{CH}_3\text{NH}_3\text{PbBr}_3$  nanowires. Reproduced from ref. [41] with permission from American Chemical Society, copyright 2016. (b) Synthesis of perovskite nanowire arrays in AAO substrate. Reproduced from ref. [42] with permission from American Chemical Society, copyright 2016.

As conventional perovskites suffer from toxicity issues due to the lead element, substituting lead with Sn is one of the efficient strategies. In 2016, Fan *et al.* fabricated lead-

free  $\text{CH}_3\text{NH}_3\text{SnI}_3$  perovskite nanowire arrays in a robust porous alumina template (PAT) via vapour-phase chemical reaction.<sup>[43]</sup> As shown in Figure 2.13a, the Sn nanoclusters were electrochemically deposited in the PAT, followed by exposing in  $\text{CH}_3\text{NH}_3\text{I}$  vapour in a tube furnace. It is worth noting that  $\text{CH}_3\text{NH}_3\text{I}$  vapour was transferred to the PAT with the help of Ar carrier gas and then reacted with the Sn nanoclusters inside the nanopores of the PAT. Moreover, the as-fabricated photodetectors exhibited an improved photoresponse compared to planar devices, as well as significantly enhanced stability, demonstrating an efficient strategy to address the stability issue. Instead of organic perovskites, all-inorganic perovskites exhibited better thermal stability. Recently, all-inorganic perovskite ( $\text{CsPbX}_3$ ) nanowires were successfully synthesised using direct vapour-liquid-solid (VLS) growth by Ho's group.<sup>[44]</sup> They used Sn NPs as catalysts, and vaporised  $\text{CsPbX}_3$  powder at an elevated temperature to initiate the VLS process (Figure 2.13b). By precise control of the structural morphology, nanowire density and chemical composition, the quality of as-grown nanowires was higher. The configured photodetectors also exhibited an excellent photoresponse, as shown in Figure 2.13c.

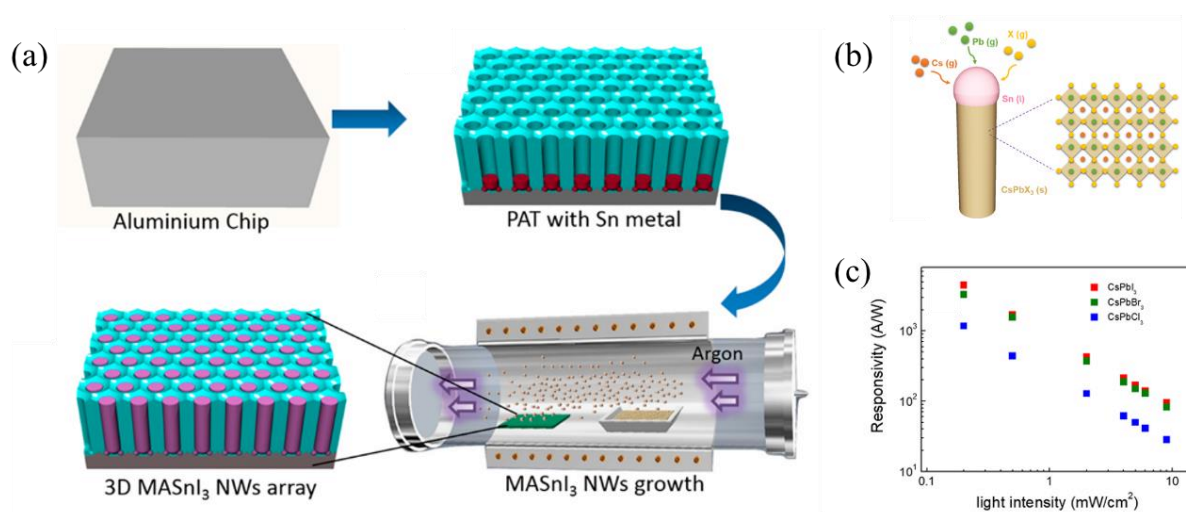


**Figure 2.13** (a) The overall process for growth of  $\text{CH}_3\text{NH}_3\text{SnI}_3$  nanowires. Reproduced from ref. [43] with permission from American Chemical Society, copyright 2016. (b) Schematic representation of VLS growth process using the Sn catalysts. (c) Responsivity of nanowire

*photodetectors under illumination with various light intensity. Reproduced from ref. [44] with permission from American Chemical Society, copyright 2019.*

Last but not least, perovskite colloidal QDs/nanocrystals exhibited unique optical and electrical properties due to their quantum-size effects with respect to their bulk counterparts. They generally possess high quantum yields with a narrow emission window, which is promising in laser and LED applications. Moreover, compared to the polycrystalline thin film, perovskite QDs have also shown multiple exciton generation, and photon upconversion tuning.<sup>[45,46]</sup> Therefore, perovskite colloidal QDs are promising to break the Shockley-Queisser limit and further improve the device performance. In addition, it has been reported that the phase stability of both CsPbI<sub>3</sub> and FAPbI<sub>3</sub> QDs were better than their bulk counterparts,<sup>[47,48]</sup> promising for future commercialisation. To date, a variety of synthesis methods for perovskite colloidal QDs/nanocrystals have been reported, such as hot injection and ligand-assisted reprecipitation.<sup>[49–51]</sup> In 2015, Song and co-workers reported the synthesis of a series of mixed-halide perovskite nanocrystals using reversible halide exchange reactions, as shown in Figure 2.14a.<sup>[49]</sup> They utilised octylamine as the capping ligand to grow plate-type nanocrystals, stirring with CH<sub>3</sub>NH<sub>3</sub>X<sub>3</sub> to prepare CH<sub>3</sub>NH<sub>3</sub>PbBr<sub>3-x</sub>Cl<sub>x</sub> or CH<sub>3</sub>NH<sub>3</sub>PbBr<sub>3-x</sub>I<sub>x</sub>, and demonstrating full-range tuneable bandgaps (1.6 eV – 3 eV). In addition, the sizes of as-synthesised NCs varies from 5 nm to 20 nm, but sizes cannot be accurately controlled. They also fabricated the thin nanocrystal film-based photodetectors, which exhibited a unique composition-dependent photoresponse. One year later, Bakr *et al.* utilised a modified hot-injection method to synthesise CsPbX<sub>3</sub> colloidal QDs, and further passivated with a two-step ligand-exchange strategy.<sup>[50]</sup> The colloidal QDs possessed an average size of 10 nm, bandgap of 2.42 eV. Moreover, the treated QD film not only exhibited an improved PLQY from 49 % to 71%, but also a higher stability, resulting in a high-efficiency LED (1.9% for blue and 3% for green). However, the hot injection method is relatively complicated, which normally

requires an elevated temperature for preparing cesium oleate solution, and an ice-water bath for growing QDs. Subsequently, Manna's group reported a facile and fast synthesis of  $\text{CsPbBr}_3$  nanocrystals via a ligand-assisted reprecipitation method at room temperature, as shown in Figure 2.14b.<sup>[51]</sup> During the synthesis process, they employed short-chain ligands with low boiling point and green solvents, resulting in 30% higher quantum yields. The size and the bandgap of the NCs were 15 nm and 2.38 eV, respectively. They further employed NCs as active layer in the solar cell, which demonstrated to an open-circuit voltage as large as 1.5 V. Among these different synthesis method, ligand-assisted reprecipitation demonstrated by Manna *et al.* are relatively simple, fast, and can be performed at room temperature.

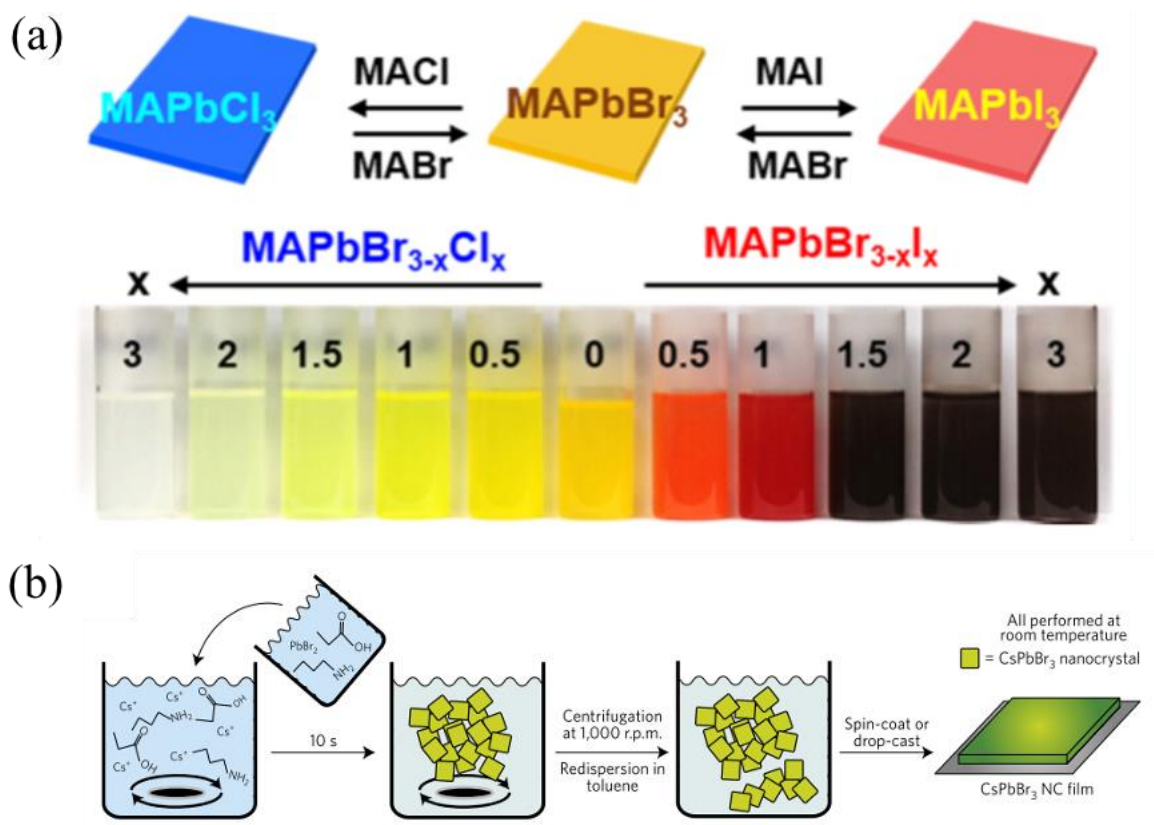


**Figure 2.14** (a) Optical images of  $\text{CH}_3\text{NH}_3\text{PbBr}_{3-x}\text{Cl}_x$  and  $\text{CH}_3\text{NH}_3\text{PbBr}_{3-x}\text{I}_x$  colloidal solutions. Reproduced from ref. [49] with permission from American Chemical Society, copyright 2016. (b) Schematic illustration of the synthesis of  $\text{CsPbBr}_3$  nanocrystals.<sup>[51]</sup> Reproduced from ref. [51] with permission from Nature Publishing Group, copyright 2017.

## 2.5 Deposition of Perovskite

Perovskite layers are employed as the light absorbers in photodetectors. The quality of perovskite film deposition is a key factor that determines the photodetector performance. Accordingly, the deposition of high-quality perovskite films has emerged as an attractive research area. Nowadays, numerous techniques for perovskite deposition have been developed, including solution deposition and chemical vapour deposition.<sup>[28,52–57]</sup> The solution deposition method is the most widely used method for perovskite film deposition, integrating the benefits of a facile process, low cost and simple equipment. It can be further divided into one-step deposition, antisolvent-assisted deposition, two-step deposition, *etc.*<sup>[28,52–56]</sup>

The one-step spin-coating deposition method is an early method for depositing perovskite layers. All chemicals and solvents are simply mixed together to form a perovskite precursor. In order to obtain the thin film, the precursor is subsequently injected onto the substrate and spin-coated at an appropriate speed and duration, followed by annealing.<sup>[52,53]</sup> It is worth noting that there are many factors affecting the quality of the film, including the substrate temperature, ambient atmosphere, annealing temperature and time, precursor concentration, *etc.* Apart from above factors, the solvents of perovskite precursor also have a significant influence on the crystallisation and film morphology.

Similar to one-step spin-coating deposition, antisolvent-assisted deposition has an extra step, which involves an antisolvent spin-coating. An antisolvent such as chlorobenzene is used to wash the solvents from the perovskite precursor, resulting in a dense and smooth perovskite film.<sup>[28,54]</sup>

Different from one-step deposition, the two-step spin-coating deposition method involves two procedures. Initially, one precursor (e.g.  $\text{PbI}_2$ ) is spin-coated on the substrate, followed by deposition of another precursor (e.g.  $\text{CH}_3\text{NH}_3\text{I}$ ). The perovskite is formed during

the deposition of the second precursor.<sup>[55,56]</sup> Noteworthy, the quality of thin film prepared by this method is highly dependent on the concentration of the CH<sub>3</sub>NH<sub>3</sub>I solution.

Chemical vapour deposition is another deposition method for growing and depositing perovskite thin film. Generally, two or more chemicals are placed into different evaporation sources, respectively, followed by heating and evaporating under high-vacuum conditions. The evaporated chemicals react in the chamber, followed by the formation of perovskite thin film on the substrate. An annealing process is finally applied to crystallise the perovskite thin film.<sup>[57]</sup> Although the quality of the film deposited using this method is very good, the equipment is expensive and the preparation process is time-consuming.

Consequently, the one-step solution deposition method is used in the presented work to grow and deposit perovskite thin film. The film quality is good and stable, the process is simple, the cost is low, and the application prospects are good.

## 2.6 Figure of Merits

It is significant for researchers to evaluate the performance of photodetectors by determining five key figures of merit, namely responsivity, specific detectivity, noise-equivalent power, linear dynamic range and response speed.

As one of the most significant parameters, the responsivity (R) represents the efficiency of a photodetector in responding to an illumination source, which can be expressed as

$$R = \frac{J_{ph}}{I_{light}} \quad \text{Equation 2.3}$$

where  $J_{ph}$  denotes the photocurrent density and  $I_{light}$  represents the power intensity.

Moreover, in order to determine the weakest level of light that can be detected by photodetectors, the specific detectivity ( $D^*$ ) is introduced, which is related to R and the noise of the photodetector, as shown below:

$$D^* = \frac{(A\Delta f)^{1/2} \cdot R}{i_n} \quad \text{Equation 2.4}$$

In this equation, A denotes the active area of the photodetector, and  $\Delta f$  and  $i_n$  represent the bandwidth and noise current, respectively. There are three noise sources contributing to the noise current, which limit the corresponding  $D^*$ ; these are the shot noise, Johnson noise and thermal noise. Among them, the shot noise is normally assumed to be the main contributor, and the expression of  $D^*$  subsequently transforms to

$$D^* = \frac{R}{(2qJ_d)^{1/2}} \quad \text{Equation 2.5}$$

where  $J_d$  is the dark current density.

Furthermore, the response time is essential for constructing fast nanotechnology, and is strongly associated with carrier recombination, transportation and collection. In general, the response time can be determined by the rise time ( $\tau_{\text{rise}}$ ) and fall time ( $\tau_{\text{fall}}$ ), which is the time between 10% and 90% of the maximum current.

Noise-equivalent power (NEP) represents the minimum incident light power that a photodetector can distinguish from the noise, which is the reciprocal of  $D^*$ :

$$\text{NEP} = \frac{(A\Delta f)^{1/2}}{D^*} = \frac{i_n}{R} \quad \text{Equation 2.6}$$

The linear dynamic range (LDR) is the linear range of photoresponse of the photodetector response to various light intensities, which is generally observed on a logarithmic scale. The typical expression of the LDR is

$$\text{LDR} = 20\log \frac{J_{\text{upper}} - J_d}{J_{\text{lower}} - J_d} \quad \text{Equation 2.7}$$

where  $J_{\text{upper}}$  and  $J_{\text{lower}}$  are the maximum and minimum current density at the limits of the linear response, respectively.

For commercial applications, it is highly desired to construct high-performance photodetectors, which integrate a large R and LDR, high  $D^*$ , fast response speed and small NEP. To date, the best figures of merit reported from perovskite-based photodetectors are

comparable or even superior to those of commercial photodetectors, including a responsivity over  $10^5 \text{ AW}^{-1}$ , detectivity up to  $10^{15} \text{ Jones}$ , response time less than 30 ns and LDR exceeding 150 dB, indicating the great potential of further commercialisation of novel photodetectors.

With the increasing demand for integrated electronics, devices tend to be miniaturised, intelligent and multifunctional. Therefore, the device area and the reliability (stability) are also important in commercial photodetectors.

## 2.7 Photodetector Architecture

As previously mentioned, perovskite photodetectors with different device architectures can be classified into photodiodes, photoconductors and phototransistors, as shown in Figure 2.15. With respect to the spatial layout of the photodetector configuration, a smaller electrode space was employed in photodiodes and vertical photoconductors ( $<600 \text{ nm}$ ). This smaller spacing can benefit the carrier transition, achieving a fast photoresponse. In contrast, lateral photoconductors and phototransistors have a relatively large spacing ( $>10 \text{ }\mu\text{m}$ ), leading to a slower response. Nevertheless, compared to the photodiode architecture, lateral photodetectors are much easier to fabricate. It is challenging to fabricate photodetectors with a simple and reproducible configuration while maintaining a good photoresponse in all aspects (R,  $D^*$ , NEP, LDR, response speed and stability).

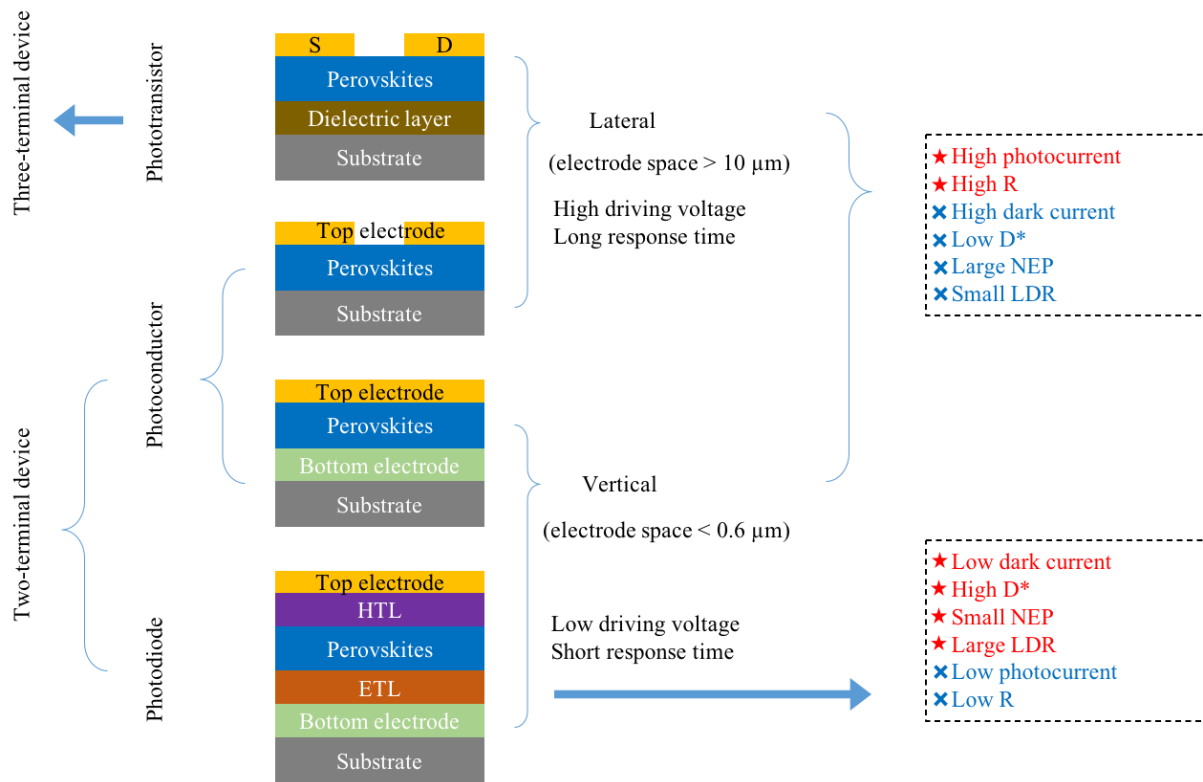


**Figure 2.15** Summary of photodetector architectures and their advantages and disadvantages.<sup>[58]</sup>

### 2.7.1 Photoconductors

Photoconductors are two-terminal devices, which enables intrinsic photocurrent amplification. The photoconductive effect is the main mechanism in photoconductors, and depends on the generation of extra free carriers in the semiconductor.<sup>[59]</sup>

Lateral and vertical perovskite-based photoconductors have been reported with impressive responsivities. In terms of lateral photoconductors, owing to the large electrode spacing ( $>10 \mu\text{m}$ ), a relatively high bias voltage is required to compensate photocurrent losses. The charge carriers are much more easily trapped by defects during the long-distance transition. In contrast, vertical photoconductors with smaller spacing ( $<0.6 \mu\text{m}$ ) require a lower driving voltage, enabled by the long diffusion length of perovskite films.

### 2.7.2 Photodiodes

The architecture of the photodiode is similar to that of solar cells, but is optimised to achieve low dark currents and a fast response speed. The main mechanism of photodiodes is the photovoltaic effect, which separates the electron-hole pair via built-in electric fields generated by materials with different work functions.<sup>[60]</sup>

Similar to vertical photoconductors, perovskite photodiodes usually employ small electrode spacing, which is beneficial for fast carrier transportation and collection. Differently, the perovskite layers in photodiodes are sandwiched by ETL and HTL to improve the device performance, i.e. lowering the dark current level.

### 2.7.3 Phototransistors

The phototransistor is a three-terminal device, including a drain, source and gate. It mainly relies on the photogating effect, and normally has a high responsivity but low response speed.<sup>[61]</sup> Perovskite phototransistors exhibit excellent carrier transport properties with ambipolar characteristics, especially when combined with 2D materials.

In the presented works, photoconductor and photodiode architectures are employed to construct high-performance photodetectors. All photodetectors exhibit an excellent photoresponse, good stability and have huge potential in the commercialisation of perovskite-based optoelectronics.

## 2.8 Challenges

Although the performance of perovskite photodetectors has been dramatically enhanced via various strategies, there are several challenges that perovskite-based photodetectors still need to overcome, including long-term stability and element toxicity.

The environmental stability of perovskites is a key challenge, as compared with conventional semiconductors. There are two types of stability in perovskite materials; one is the intrinsic structural instability and the other is the chemical instability.

The intrinsic structural instability of perovskites is mainly attributed to its own physical structure that causes thermodynamic instability. As mentioned above, the stability is significantly affected by the crystal structure. When the tolerance factor is in the range of 0.8–1.1, the perovskite structure is stable. Nevertheless, there is no direct quantitative relationship between the tolerance factor and the stability of the perovskite cubic structure. Yin *et al.* systematically studied the thermodynamic stability of 138 possible perovskite compounds using first-principles calculations, and further evaluated the thermodynamic stability of the cubic structure using the octahedral factor ( $m$ ), where  $m = r_A / r_X$ .<sup>[62]</sup> As shown in Figure 2.16, the perovskite is considered to be stable only when the decomposition energy is  $>0$ , which is more accurate than only considering tolerance factors. As one of the most studied perovskites,  $\text{CH}_3\text{NH}_3\text{PbI}_3$  also has thermodynamic instability. Sit *et al.* found that  $\text{CH}_3\text{NH}_3\text{PbI}_3$  is easily decomposed into  $\text{CH}_3\text{NH}_3\text{I}$  and  $\text{PbI}_2$ , even in the absence of external environmental factors, including water, oxygen, heat and light.<sup>[63]</sup>

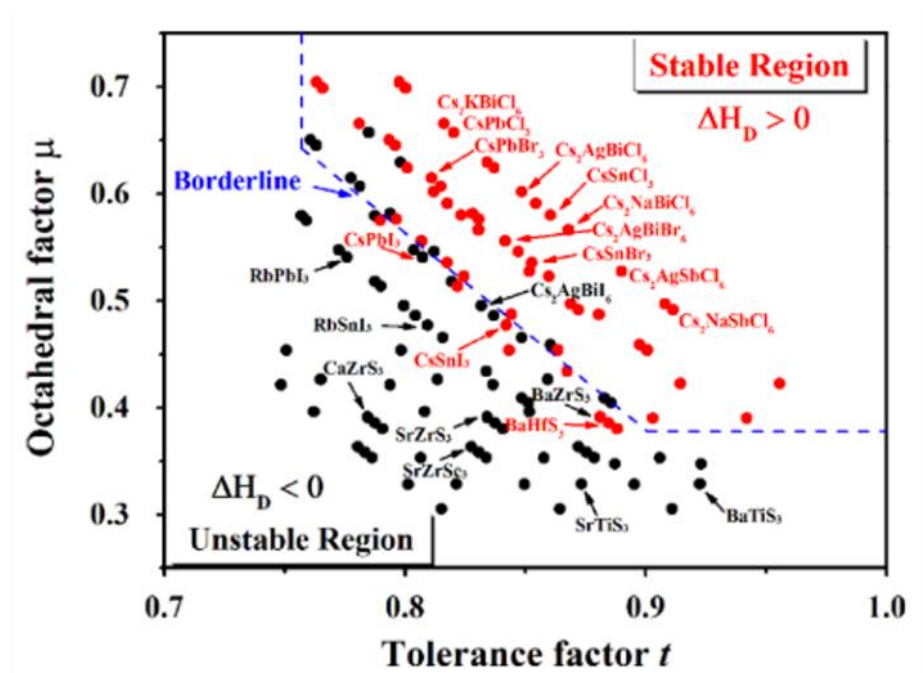


**Figure 2.16** Mapping of 138 perovskite materials. Red dots and black dots represent stable and unstable regions, respectively. Reproduced from ref. [62] with permission from American Chemical Society, copyright 2017.

Apart from the intrinsic stability of the material itself, the chemical instability of perovskites is also observed, as illustrated in Figure 2.17. Perovskites are sensitive to oxygen, moisture, heat and light, leading to irreversible decomposition and degradation.

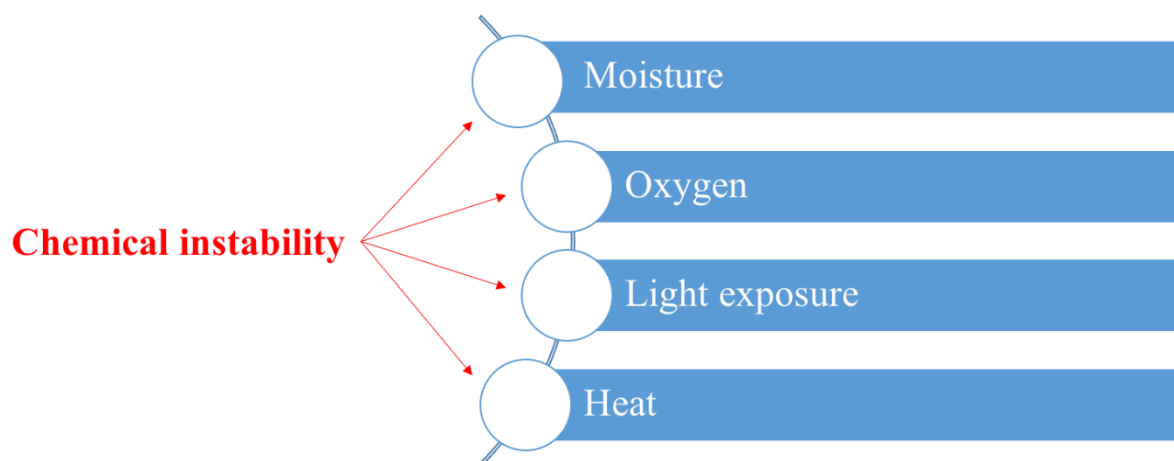
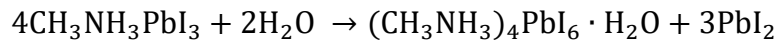


**Figure 2.17** Chemical instability of perovskites.

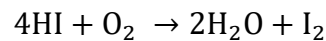
For example, when perovskite ( $\text{CH}_3\text{NH}_3\text{PbI}_3$ ) is placed under high-moisture conditions, it reacts with water, thus causing its decomposition.<sup>[64]</sup> A two-step reaction is involved in this

process. First, a water molecule combines with  $\text{CH}_3\text{NH}_3\text{PbI}_3$  and takes a hydrogen atom away from the  $\text{CH}_3\text{NH}_3^+$  group to form an intermediate product. The intermediate product is further decomposed into HI hydrates and gaseous  $\text{CH}_3\text{NH}_2$ , and finally generates  $\text{PbI}_2$ . The complete chemical reaction can be expressed as



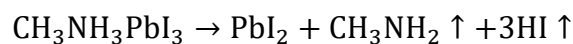
Although the halogen doping strategy can partially improve the moisture stability, phase segregation was observed under continuous light illumination, leading to chemical instability. In 2016, Ginsberg *et al.* carried out a study on the phase separation phenomenon of  $\text{CH}_3\text{NH}_3\text{PbI}_x\text{Br}_{3-x}$  via *in situ* characterisations of the cathodoluminescence and the secondary ion secondary electron.<sup>[65]</sup> The movement of I<sup>-</sup> ions was observed, and tended to be enriched at the grain boundaries of perovskite thin films after irradiating with a 405 nm laser diode for 5 min.

Meanwhile, perovskite is also sensitive to oxygen in the air, as the decomposed HI can react with oxygen:



It was reported that the unencapsulated perovskite device decomposed after being placed under ambient conditions for 24 hours, and the device performance was significantly degraded.

In addition, perovskite has been proven to have poor thermal stability. Once increasing the temperature to 85 °C, the perovskite started to decompose as follows:



The decomposed products have a strong chemical effect on  $\text{CH}_3\text{NH}_3\text{PbI}_3$ , further leading to the destruction of the material.

Overall, due to the moisture, oxygen, heat and light, the manufacture and storage of perovskite devices needs to be carried out in a strictly dry nitrogen environment glove box, which limits its application.

To date, various approaches have been explored to overcome the instability issues, including interface engineering, morphology control, perovskite passivation and architecture optimisation. In addition, encapsulation is another strategy to effectively improve the device stability. However, encapsulation is a postprocessing method, and does not originally enhance the material stability at synthesis stage. Therefore, it is of much significance to design and fabricate chemically stable perovskite materials and develop novel strategies to improve the device performance at the same time.

One effective and simple way to improve the stability of HMHP is to replace conventional organic cations (e.g.  $\text{CH}_3\text{NH}_3^+$ ) with inorganic cations (e.g.  $\text{Cs}^+$ ). For example,  $\text{CsPbBr}_3$  exhibited an extra thermal stability and moisture resistance due to their higher tolerance factor ( $\sim 0.86$ ) and larger binding energy ( $\sim 40$  meV). Although a part of spectrum response is sacrificed, the practicability of devices in detection applications is improved. On the other hand, owing to its larger bandgap energy ( $\sim 2.3$  eV), the response spectrum of photodetectors are able to entirely cover the green light. Therefore, for the green light or short-wavelength applications,  $\text{CsPbBr}_3$  is an ideal active material. Thanks for the quantum confinement, the  $\text{CsPbBr}_3$  QDs with the reduced dimension can offer unique optical and electrical properties, and this research area has not completely explored yet. Furthermore, the synthesis of these colloidal QDs is compatible with the industrial process at room temperature. By decoupling the grain crystallisation from the film deposition,<sup>[47]</sup> it can be fabricated more conveniently. Therefore, in this thesis,  $\text{CsPbBr}_3$  QDs are chosen as the active material, and are further employed into the photodetectors to extensively study the characteristics of materials as well as improve the device performance.

## 2.9 References

- [1] Z. Wu, Z. Ni, *Nanophotonics* **2017**, 6, 1219.
- [2] J. Kreiselt, A. M. Glazer, G. Jones, P. A. Thomas, L. Abello, G. Lucazeau, *J. Phys. Condens. Matter* **2000**, 12, 3267.
- [3] B. Seyfi, M. Baghalha, H. Kazemian, *Chem. Eng. J.* **2009**, 148, 306.
- [4] J. Zhu, H. Li, L. Zhong, P. Xiao, X. Xu, X. Yang, Z. Zhao, J. Li, *ACS Catal.* **2014**, 4, 2917.
- [5] D. Shi, V. Adinolfi, R. Comin, M. Yuan, E. Alarousu, A. Buin, Y. Chen, S. Hoogland, A. Rothenberger, K. Katsiev, Y. Losovyj, X. Zhang, P. A. Dowben, O. F. Mohammed, E. H. Sargent, O. M. Bakr, *Science*. **2015**, 347, 519.
- [6] J. Song, J. Li, X. Li, L. Xu, Y. Dong, H. Zeng, *Adv. Mater.* **2015**, 27, 7162.
- [7] Y. C. Kim, K. H. Kim, D. Y. Son, D. N. Jeong, J. Y. Seo, Y. S. Choi, I. T. Han, S. Y. Lee, N. G. Park, *Nature* **2017**, 550, 87.
- [8] S. D. Stranks, G. E. Eperon, G. Grancini, C. Menelaou, M. J. P. Alcocer, T. Leijtens, L. M. Herz, A. Petrozza, H. J. Snaith, *Science*. **2013**, 342, 341.
- [9] G. Xing, N. Mathews, S. Sun, S. S. Lim, Y. M. Lam, M. Gratzel, S. Mhaisalkar, T. C. Sum, *Science*. **2013**, 342, 344.
- [10] H. Wei, Y. Fang, P. Mulligan, W. Chuirazzi, H. H. Fang, C. Wang, B. R. Ecker, Y. Gao, M. A. Loi, L. Cao, J. Huang, *Nat. Photonics* **2016**, 10, 333.
- [11] E. Edri, S. Kirmayer, S. Mukhopadhyay, K. Gartsman, G. Hodes, D. Cahen, *Nat. Commun.* **2014**, 5, 3461.
- [12] Y. Bi, E. M. Hutter, Y. Fang, Q. Dong, J. Huang, T. J. Savenije, *J. Phys. Chem. Lett.* **2016**, 7, 923.
- [13] C. Li, K. C. K. Soh, P. Wu, *J. Alloys Compd.* **2004**, 372, 40.
- [14] A. E. Fedorovskiy, N. A. Drigo, M. K. Nazeeruddin, *Small Methods* **2020**, 4, 1900426.

- [15] V. M. Goldschmidt, *Naturwissenschaften* **1926**, *14*, 477.
- [16] M. A. Green, A. Ho-Baillie, H. J. Snaith, *Nat. Photonics* **2014**, *8*, 506.
- [17] G. Kieslich, S. Sun, A. K. Cheetham, *Chem. Sci.* **2014**, *5*, 4712.
- [18] D. Yang, D. Huo, *J. Mater. Chem. C* **2020**, *8*, 6640.
- [19] K. Y. Tsui, N. Onishi, R. F. Berger, *J. Phys. Chem. C* **2016**, *120*, 23293.
- [20] A. M. Glazer, *Acta Crystallogr. Sect. B Struct. Crystallogr. Cryst. Chem.* **1972**, *28*, 3384.
- [21] H. Wang, D. H. Kim, *Chem. Soc. Rev.* **2017**, *46*, 5204.
- [22] P. Cottingham, R. L. Brutchey, *Chem. Mater.* **2018**, *30*, 6711.
- [23] X. Ziang, L. Shifeng, Q. Laixiang, P. Shuping, W. Wei, Y. Yu, Y. Li, C. Zhijian, W. Shufeng, D. Honglin, Y. Minghui, G. G. Qin, *Opt. Mater. Express* **2015**, *5*, 29.
- [24] A. Miyata, A. Mitioglu, P. Plochocka, O. Portugall, J. T.-W. Wang, S. D. Stranks, H. J. Snaith, R. J. Nicholas, *Nat. Phys.* **2015**, *11*, 582.
- [25] B. Ai, C. Liu, Z. Deng, J. Wang, J. Han, X. Zhao, *Phys. Chem. Chem. Phys.* **2017**, *19*, 17349.
- [26] I. E. Castelli, J. M. García-Lastra, K. S. Thygesen, K. W. Jacobsen, *APL Mater.* **2014**, *2*, 081514.
- [27] Z. Li, M. Yang, J.-S. Park, S.-H. Wei, J. J. Berry, K. Zhu, *Chem. Mater.* **2016**, *28*, 284.
- [28] M. Saliba, T. Matsui, J. Y. Seo, K. Domanski, J. P. Correa-Baena, M. K. Nazeeruddin, S. M. Zakeeruddin, W. Tress, A. Abate, A. Hagfeldt, M. Grätzel, *Energy Environ. Sci.* **2016**, *9*, 1989.
- [29] L.-Q. Xie, L. Chen, Z.-A. Nan, H.-X. Lin, T. Wang, D.-P. Zhan, J.-W. Yan, B.-W. Mao, Z.-Q. Tian, *J. Am. Chem. Soc.* **2017**, *139*, 3320.
- [30] K. Ren, J. Wang, K. Liu, Y. Huang, Y. Sun, M. Azam, P. Jin, Z. Wang, S. Qu, Z. Wang, *RSC Adv.* **2019**, *9*, 19772.
- [31] E. Kioupakis, Q. Yan, D. Steiauf, C. G. Van de Walle, *New J. Phys.* **2013**, *15*, 125006.

- [32] C. Zhou, H. Lin, Q. He, L. Xu, M. Worku, M. Chaaban, S. Lee, X. Shi, M. H. Du, B. Ma, *Mater. Sci. Eng. R Reports* **2019**, *137*, 38.
- [33] D. Shi, V. Adinolfi, R. Comin, M. Yuan, E. Alarousu, A. Buin, Y. Chen, S. Hoogland, A. Rothenberger, K. Katsiev, Y. Losovyj, X. Zhang, P. A. Dowben, O. F. Mohammed, E. H. Sargent, O. M. Bakr, *Science* **2015**, *347*, 519.
- [34] X. Liu, H. Zhang, B. Zhang, J. Dong, W. Jie, Y. Xu, *J. Phys. Chem. C* **2018**, *122*, 14355.
- [35] Q. Dong, Y. Fang, Y. Shao, P. Mulligan, J. Qiu, L. Cao, J. Huang, *Science* **2015**, *347*, 967.
- [36] Y. Fang, Q. Dong, Y. Shao, Y. Yuan, J. Huang, *Nat. Photonics* **2015**, *9*, 679.
- [37] M. I. Saidaminov, A. L. Abdelhady, B. Murali, E. Alarousu, V. M. Burlakov, W. Peng, I. Dursun, L. Wang, Y. He, G. MacUlan, A. Goriely, T. Wu, O. F. Mohammed, O. M. Bakr, *Nat. Commun.* **2015**, *6*, 1.
- [38] Y. Chen, X. Hou, S. Tao, X. Fu, H. Zhou, J. Yin, M. Wu, X. Zhang, *Chem. Commun.* **2020**, *56*, 6404.
- [39] J. Song, L. Xu, J. Li, J. Xue, Y. Dong, X. Li, H. Zeng, *Adv. Mater.* **2016**, 4861.
- [40] J. Liu, Y. Xue, Z. Wang, Z. Q. Xu, C. Zheng, B. Weber, J. Song, Y. Wang, Y. Lu, Y. Zhang, Q. Bao, *ACS Nano* **2016**, *10*, 3536.
- [41] S. Zhuo, J. Zhang, Y. Shi, Y. Huang, B. Zhang, *Angew. Chemie* **2015**, *127*, 5785.
- [42] M. J. Ashley, M. N. O'Brien, K. R. Hedderick, J. A. Mason, M. B. Ross, C. A. Mirkin, *J. Am. Chem. Soc.* **2016**, *138*, 10096.
- [43] A. Waleed, M. M. Tavakoli, L. Gu, Z. Wang, D. Zhang, A. Manikandan, Q. Zhang, R. Zhang, Y. L. Chueh, Z. Fan, *Nano Lett.* **2016**, *17*, 523.
- [44] Y. Meng, C. Lan, F. Li, S. Yip, R. Wei, X. Kang, X. Bu, R. Dong, H. Zhang, J. C. Ho, *ACS Nano* **2019**, *13*, 6060.
- [45] M. Li, R. Begum, J. Fu, Q. Xu, T. M. Koh, S. A. Veldhuis, M. Grätzel, N. Mathews, S.

- Mhaisalkar, T. C. Sum, *Nat. Commun.* **2018**, 9, 4197.
- [46] W. Zheng, P. Huang, Z. Gong, D. Tu, J. Xu, Q. Zou, R. Li, W. You, J.-C. G. Bünzli, X. Chen, *Nat. Commun.* **2018**, 9, 3462.
- [47] T. Tormann, S. Wiemer, B. Enescu, Y. Hiramatsu, K. Obara, J. L. Hardebeck, K. C. Creager, H. Houston, A. M. Thomas, G. Savard, L. Chuang, A. M. Rubin, R. W. Clayton, W. D. Mooney, S. Detweiler, G. Zandt, N. Mcquarrie, C. Marone, Y. Fialko, K. M. Brown, M. Obata, G. Di Toro, K. Kanagawa, K. Ozawa, C. A. Trepmann, G. Hirth, H. Stunitz, E. T. Goergen, A. Plesch, J. H. Shaw, H. Gilbert, R. Clayton, R. W. Clayton, B. Energy, *Science* **2016**, 354, 92.
- [48] J. Xue, J.-W. Lee, Z. Dai, R. Wang, S. Nuryyeva, M. E. Liao, S.-Y. Chang, L. Meng, D. Meng, P. Sun, O. Lin, M. S. Goorsky, Y. Yang, *Joule* **2018**, 2, 1866.
- [49] D. M. Jang, K. Park, D. H. Kim, J. Park, F. Shojaei, H. S. Kang, J. P. Ahn, J. W. Lee, J. K. Song, *Nano Lett.* **2015**, 15, 5191.
- [50] J. Pan, L. N. Quan, Y. Zhao, W. Peng, B. Murali, S. P. Sarmah, M. Yuan, L. Sinatra, N. M. Alyami, J. Liu, E. Yassitepe, Z. Yang, O. Voznyy, R. Comin, M. N. Hedhili, O. F. Mohammed, Z. H. Lu, D. H. Kim, E. H. Sargent, O. M. Bakr, *Adv. Mater.* **2016**, 28, 8718.
- [51] Q. A. Akkerman, M. Gandini, F. Di Stasio, P. Rastogi, F. Palazon, G. Bertoni, J. M. Ball, M. Prato, A. Petrozza, L. Manna, *Nat. Energy* **2017**, 2, 16194.
- [52] S. Yuan, Z.-K. Wang, M.-P. Zhuo, Q.-S. Tian, Y. Jin, L.-S. Liao, *ACS Nano* **2018**, 12, 9541.
- [53] H. Cho, J. S. Kim, C. Wolf, Y.-H. Kim, H. J. Yun, S.-H. Jeong, A. Sadhanala, V. Venugopalan, J. W. Choi, C.-L. Lee, R. H. Friend, T.-W. Lee, *ACS Nano* **2018**, 12, 2883.
- [54] T. Zhang, J. Wu, P. Zhang, W. Ahmad, Y. Wang, M. Alqahtani, H. Chen, C. Gao, Z. D. Chen, Z. Wang, S. Li, *Adv. Opt. Mater.* **2018**, 6, 1701341.

- [55] H. Sun, K. Deng, Y. Zhu, M. Liao, J. Xiong, Y. Li, L. Li, *Adv. Mater.* **2018**, 30, 1.
- [56] J. Burschka, N. Pellet, S.-J. Moon, R. Humphry-Baker, P. Gao, M. K. Nazeeruddin, M. Grätzel, *Nature* **2013**, 499, 316.
- [57] A. Waleed, M. M. Tavakoli, L. Gu, S. Hussain, D. Zhang, S. Poddar, Z. Wang, R. Zhang, Z. Fan, *Nano Lett.* **2017**, 17, 4951.
- [58] H. Wang, D. H. Kim, *Chem. Soc. Rev.* **2017**, 46, 5204.
- [59] E. Muñoz, E. Monroy, J. A. Garrido, I. Izpura, F. J. Sánchez, M. A. Sánchez-García, E. Calleja, B. Beaumont, P. Gibart, *Appl. Phys. Lett.* **1997**, 71, 870.
- [60] A. Osinsky, S. Gangopadhyay, R. Gaska, B. Williams, M. A. Khan, D. Kuksenkov, H. Temkin, *Appl. Phys. Lett.* **1997**, 71, 2334.
- [61] S. P. Lansley, H. J. Looi, Y. Wang, M. D. Whitfield, R. B. Jackman, *Appl. Phys. Lett.* **1999**, 74, 615.
- [62] Q. Sun, W.-J. Yin, *J. Am. Chem. Soc.* **2017**, 139, 14905.
- [63] L. Zhang, P. H. L. Sit, *J. Mater. Chem. A* **2017**, 5, 23976.
- [64] T. A. Berhe, W.-N. Su, C.-H. Chen, C.-J. Pan, J.-H. Cheng, H.-M. Chen, M.-C. Tsai, L.-Y. Chen, A. A. Dubale, B.-J. Hwang, *Energy Environ. Sci.* **2016**, 9, 323.
- [65] C. G. Bischak, C. L. Hetherington, H. Wu, S. Aloni, D. F. Ogletree, D. T. Limmer, N. S. Ginsberg, *Nano Lett.* **2017**, 17, 1028.

## CHAPTER 3. EXPERIMENTAL METHODS

*In this chapter, I aim to present the comprehensive experimental procedures and methods to readers for a better understanding of this thesis. There are six sections in this chapter; namely, Perovskite Preparation, Material Characterisation, Optical Characterisation, Morphological Characterisation, Photodetector Fabrication and Device Characterisation.*

### 3.1 Perovskite Preparation

The first part introduces the chemicals used and the synthesis performed for different experiments with different purposes. The synthesis procedures were all carried out at room temperature without any protection from inert gas.

#### 3.1.1 Chemicals

All of the chemicals used for the experiments are listed in the Table 3.1. They were anhydrous and used as received without further purification.

**Table 3.1** *The list of chemicals used in experiments.*

Chemicals	Purity	Manufacturer/Product Number
Lead Bromide ( $\text{PbBr}_2$ )	99.9%	Sigma-Aldrich (398853)
Caesium Carbonate ( $\text{Cs}_2\text{CO}_3$ )	99.0%	Sigma-Aldrich (441902)
Zinc Oxide Nanoparticles ( $\text{ZnO}$ )	97.0%	Sigma-Aldrich (677450)
Particle size of ZnO NPs < 50 nm		
Potassium Bromide ( $\text{KBr}$ )	99.9%	Fisher Chemical (10714001)

<b>Caesium Bromide (CsBr)</b>	99.9%	Sigma-Aldrich (203017)
<b>Butylamine (BuAm)</b>	99.5%	Sigma-Aldrich (471305)
<b>2-Propanol (IPrOH)</b>	99.5%	Sigma-Aldrich (278475)
<b>Propionic Acid (PrAc)</b>	99.5%	Sigma-Aldrich (402907)
<b>Hexane (HEX)</b>	99.0%	Sigma-Aldrich (139386)
<b>Toluene (Tol)</b>	99.8%	Sigma-Aldrich (244511)
<b>Chloroform (CF)</b>	99.0%	Fisher Chemical (10784143)

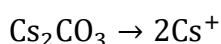
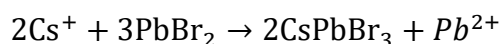
---

### 3.1.2 CsPbBr<sub>3</sub> QDs

There are five stages involved in the synthesis of CsPbBr<sub>3</sub> QDs, as shown in Figure 3.1.

#### 1) Preparing Cs<sup>+</sup> precursor solution (3.6 M):

By considering the molar ratio between Cs<sub>2</sub>CO<sub>3</sub> and Cs<sup>+</sup> as being below 1:2, once the volume of solution needing to be prepared is known, the amount of Cs<sub>2</sub>CO<sub>3</sub> and Cs<sup>+</sup> could be calculated:



First, 2 mL precursor was prepared for the experiment and future use. Cs<sub>2</sub>CO<sub>3</sub> was dissolved into 2 mL pure PrAc and stirred at room temperature overnight. The amount of Cs<sub>2</sub>CO<sub>3</sub> used could be calculated as below:

$$\text{Cs}^+ = 3.6 \frac{\text{mol}}{\text{L}} \times 2 \times 10^{-3} \text{ L} = 7.2 \text{ mmol}$$

$$\text{Cs}_2\text{CO}_3 = 7.2 \text{ mmol} \div 2 \times 326 \frac{\text{g}}{\text{mol}} = 1.1736 \text{ g}$$

#### 2) Preparing PbBr<sub>2</sub> precursor solution (0.5 M):

PbBr<sub>2</sub> was dissolved in PrAc, IPrOH and BuAm solvent at a volume ratio of 1:1:1. First, 5mL PbBr<sub>2</sub> precursor was prepared for the experiment and future use. Therefore, the volume of each solvent selected was 1.667 mL and the amount of PbBr<sub>2</sub> could be calculated as:

$$PbBr_2 = 0.5 \frac{mol}{L} \times 5 \times 10^{-3} L \times 367 \frac{g}{mol} = 0.9175 g$$

### 3) Forming CsPbBr<sub>3</sub> QDs:

10 mL HEX, 5 mL IPrOH and 25  $\mu$ L Cs<sup>+</sup> were mixed in air and at room temperature, forming a clear solution. The volume of PbBr<sub>2</sub> added could be acquired by the following calculations:

$$25 \mu L Cs^+ = 25 \mu L \times 3.6 \frac{mol}{L} = 0.09 mmol$$

$$PbBr_2 = 0.09 mmol \times 3 \div 2 = 0.135 mmol$$

$$V_{PbBr_2} = 0.135 mmol \div 0.5 \frac{mol}{L} = 270 \mu L$$

Therefore, 270  $\mu$ L PbBr<sub>2</sub> precursor was injected swiftly. This solution immediately turned yellow, and then turned turbid within seconds. The total amount of CsPbBr<sub>3</sub> obtained from the reaction could be calculated as shown below:

$$CsPbBr_3 = 0.09 mmol \times 580 g/mol = 52.2 mg$$

This solution was placed into two sealed tubes with equal amounts (7.5 mL), which meant each tube had 0.045 mmol CsPbBr<sub>3</sub>.

### 4) Collecting CsPbBr<sub>3</sub> QDs:

Each solution mentioned above was centrifuged. Only the precipitation was kept, and was dispersed in toluene to remove the residues of other solvents. Various centrifugation speeds were applied for purification, e.g. 1500 rpm for 2 min, 2000 rpm for 2 min and 1500 rpm for 2 min in the sequence.

### 5) Dissolving CsPbBr<sub>3</sub> QDs:

CsPbBr<sub>3</sub> QDs were then re-dispersed into 2 mL toluene. The concentration of the solution was

$$\text{Concentration} = 52.2 \text{ mg} \div 2 \div 2 \text{ mL} = 13.05 \text{ mg/mL}$$

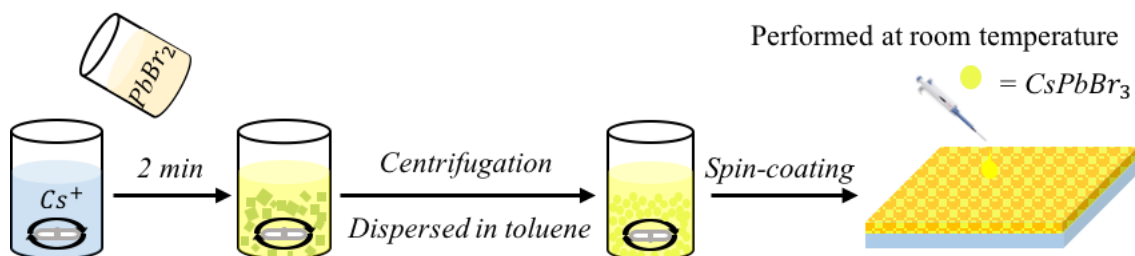


**Figure 3.1** Synthesis of CsPbBr<sub>3</sub> QDs.<sup>[1]</sup>

### 3.1.3 ZnO NPs Decorated with CsPbBr<sub>3</sub> QDs

As the procedures stated in 3.1.2, high-quality CsPbBr<sub>3</sub> QDs were initially grown after mixing, centrifugation, purification and re-dispersion. For ZnO NP-decorated CsPbBr<sub>3</sub> QDs (Figure 3.2), ZnO NP precursor (0.5 M) was firstly prepared by dissolving ZnO NPs in chloroform. The proposed volume of ZnO NP precursors from 20 μL to 100 μL was subsequently added into the as-grown CsPbBr<sub>3</sub> QDs to investigate the decoration effects.

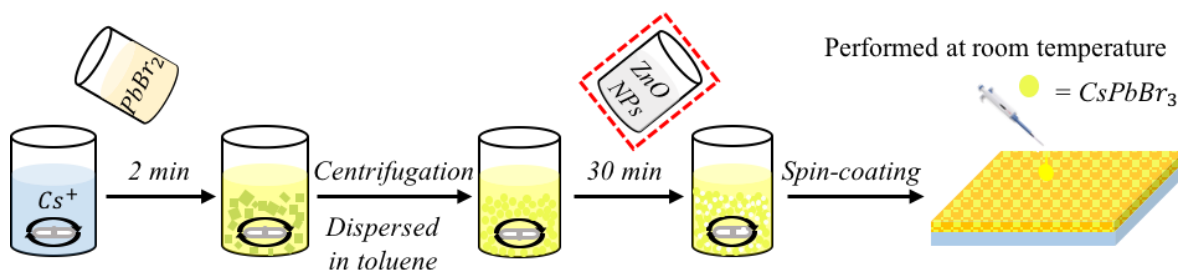


**Figure 3.2** Synthesis of ZnO NP-decorated CsPbBr<sub>3</sub> QDs. Reproduced from ref. [2] with permission from Royal Society of Chemistry, copyright 2019.

### 3.1.4 CsBr/KBr Assisted CsPbBr<sub>3</sub> Quantum Dots

For CsBr/KBr-assisted CsPbBr<sub>3</sub> QDs, the procedure is similar to that described in 3.1.2. The difference is that the CsBr/KBr precursors were prepared by dissolving CsBr/KBr

additives (22.6  $\mu\text{mol}$  / 67.1  $\mu\text{mol}$ ) in the mixture solvents (2 mL) of PrAc, IPrOH and BuAm at a volume ratio of 1:1:1, as shown in Figure 3.3. Once the perovskite precursor turned light yellow, different amounts of CsBr/KBr additives were immediately injected at a fraction from 0.025 to 0.3. High-quality CsPbBr<sub>3</sub> QDs were then obtained by centrifugation, purification and finally redispersion in toluene.

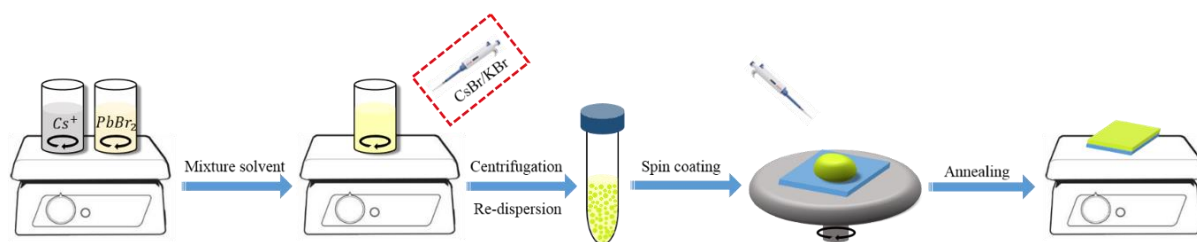


**Figure 3.3** Synthesis of CsBr/KBr-assisted CsPbBr<sub>3</sub> QDs. Reproduced from ref. [3] with permission from John Wiley and Sons, copyright 2020.

In this thesis, all-inorganic perovskite (CsPbBr<sub>3</sub>) QDs were employed as the active layer to absorb photons, owing to their better stability compared to organic perovskites. In addition, unlike DMSO or DMF, the solvents involved in all syntheses were environmentally friendly. The ligands are shorter than OE and OAm, which efficiently reduces the effects of insulating barriers caused by longer ligands.

The perovskite layers were all deposited by a spin coater, allowing facile and simple depositions. The rotating speed and time of the spin coater can be programmed depending on the specific requirements. In the presented studies, the rotating speed and duration are determined as 1000 rpm and 60 sec, respectively. Before using the spin coater, the rotating speed and time should be firstly set up. Subsequently, the substrates are placed in the rotating holder, followed by the dropping of precursors.

## 3.2 Material Characterisations

### 3.2.1 X-ray Diffraction

X-ray diffraction (XRD) was the first method developed to study the microstructure of substances, with the advantages of non-destructivity and fast operation. It has been widely applied in physics, chemistry, materials science, engineering sciences, *etc.*<sup>[4]</sup>

XRD generally comprises a stable X-ray generator, an adjustable sample stage, a sensitive X-ray detector and a precise processing system. As shown in Figure 3.4, the monochromatic X-ray is incident on the crystal, where the X-ray acts as an EM wave. It is scattered by atoms and reflected from atoms' centres. Due to the periodical arrangement of these atoms, the scattered waves have a fixed phase relationship. Accordingly, scattered X-rays reinforce each other in some directions and cancel each other in other directions, resulting in the diffraction phenomenon. Similar to fingerprints, the diffraction pattern of each crystal is unique. The distribution of the diffraction lines depends on the size, shape and orientation of the unit cell, which determines the intensity of the diffraction line, and further indicates the crystal quality. Normally, the  $\lambda$  (wavelength) of the X-ray is fixed (it can be found in the instrument manual). By applying Bragg's equation ( $2d \sin\theta = n\lambda$ ), the dimensions of the unit cell can be determined.

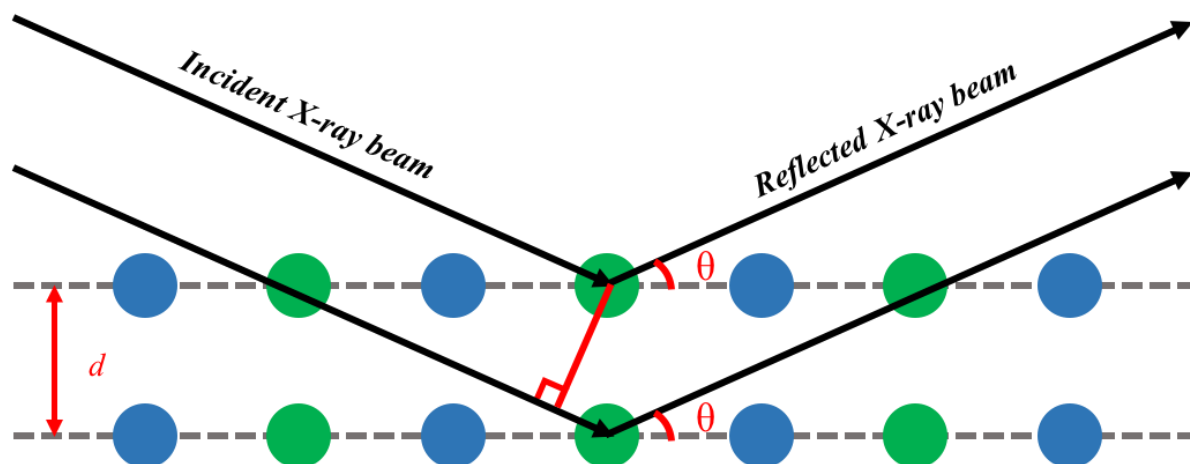


**Figure 3.4** The working mechanism of XRD.

Therefore, in this thesis, XRD is used for analysing the structures of perovskites, including phase analysis, crystallinity determination and lattice parameter measurements. The instrument used here is the PANalytical X'Pert PRO X-ray diffractometer with a Cu K $\alpha$ 1,2 excitation ( $\lambda = 1.540598 \text{ \AA}$ ) in the Institute for Materials Discovery (IMD), University College London.

### 3.2.2 Transmission Electron Microscopy

Transmission electron microscopy (TEM) is the one of the most powerful instruments to assess the precise structure of samples, or even the structures of a set of atoms, due to the short De Broglie wavelength of electrons (precision of  $\sim 0.2 \text{ nm}$ ). Accordingly, TEM has been applied in a wide range of fields, including virology, materials science, nanotechnology and semiconductor research.

Unlike XRD, TEM gives direct crystallographic information about the bulk of the perovskites. TEM employs an accelerated and concentrated electron beam to project onto an ultrathin sample. Subsequently, the collision between electrons and atoms in the sample changes the directions of electrons, leading to the scattering. The scattering angle is associated with the density and thickness of the sample, resulting in bright and dark fields in the image. Finally, the image is displayed on the imaging system after zooming and focussing.

As shown in Figure 3.5, TEM typically consists of an electron gun, condenser lenses, specimen holder, objective lenses, projector lenses and a capturing system. The electron beam is firstly generated by the electron gun, and travels through the condenser lenses in the vacuum chamber. A sharp, bright and uniform spot is subsequently formed, and illuminates the sample in the holder. After penetrating the sample, the structural information inside the sample carried by the electron beam can be detected after primary focussing and magnification of the objective

lens. Finally, the magnified electronic image is projected onto the fluorescent screen, and is converted to a visible light image for users to observe.

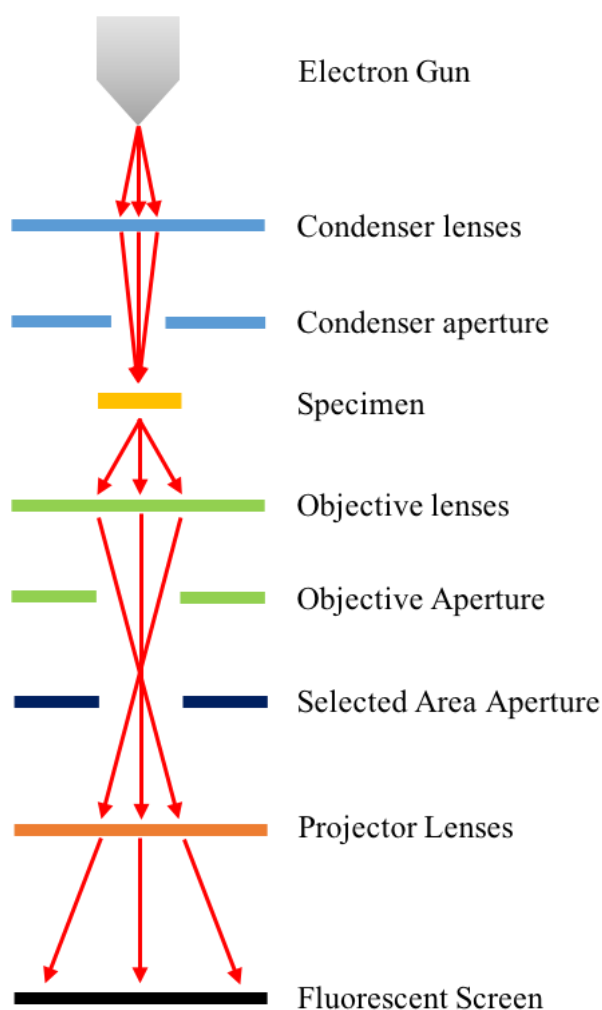


**Figure 3.5** Schematic operation mechanism of TEM.

Accordingly, TEM is essential for us to determine the crystal structure of perovskites. For the work presented in this thesis, perovskite samples were prepared on a Cu grid using a JEOL 2100 microscope attached to an X-MaxN detector (Oxford Instruments) in the Department of Chemistry, University College London.

### 3.2.3 X-ray Photoelectron Spectroscopy

X-ray photoelectron spectroscopy (XPS) is a surface-sensitive and quantitative spectroscopic technique in the microscopic analysis of materials, which not only provides

information on the elemental composition but also on the electronic state and chemical bonds of samples. However, the instrument will only probe 20 nm into a sample at most.

Briefly, XPS uses X-rays to illuminate the sample to ionise inner electrons and excite electrons, namely photoelectrons. The energy level of inner electrons is characteristic due to their unique inner electron binding energy. Accordingly, information about the sample can be obtained, where the kinetic energy of photoelectrons/binding energy ( $E_b = h\nu - E_k - \phi$ ) is assigned to the x-axis, and the relative intensity (pulse/s) is the y-axis.

The main components of the XPS system are the electron gun, X-ray anode, X-ray monochromator, high-vacuum pump, hemispherical energy analyser and multi-channel detector system. As illustrated in Figure 3.6, Al or Mg is used as the X-ray anode, which generates X-rays with a photon energy of 1486 eV or 1254 eV, respectively. The X-ray beam subsequently illuminates the sample through the monochromator, where the monochromator is installed to reduce the dispersion of photon energy. The scattered X-ray beam is then measured by the hemispherical energy analyser to obtain the distribution and the intensity of the electron energy. Therefore, the characteristics of XPS peaks can be obtained, which directly identify each element that exists on the surface of the material. By collecting and analysing the obtained information, the elemental composition can be determined.

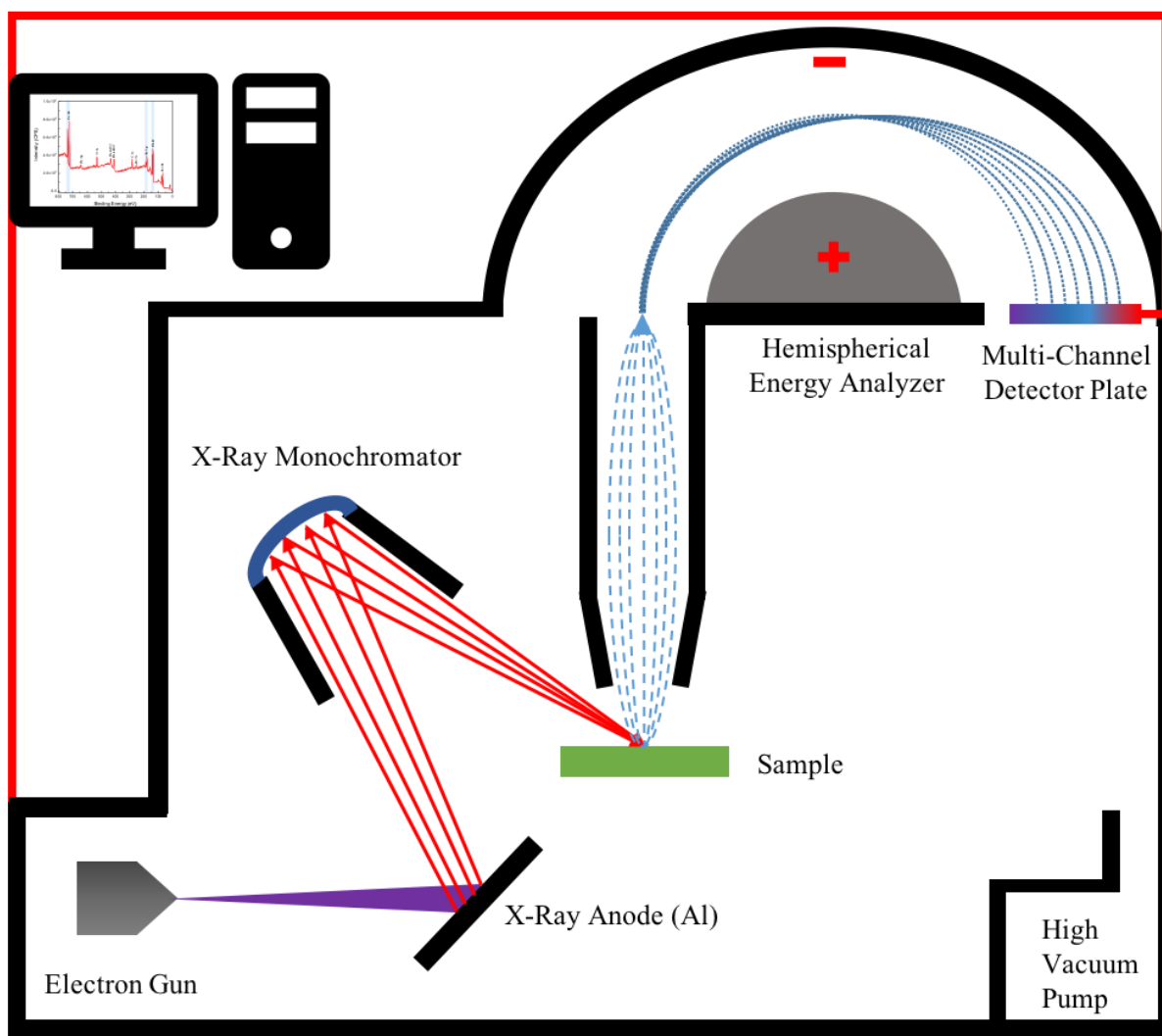


**Figure 3.6** The illustration of XPS.

For the work presented in the thesis, XPS measurements were performed using a Thermo Scientific K-alpha photoelectron spectrometer under  $\text{Al}_{K\alpha}$  radiation. The spectra were analysed with CasaXPS software. The experiment was carried out in the Department of Chemistry, University College London to assess the element content, composition and ratio of perovskites.

### 3.2.4 Element Dispersive X-ray Spectroscopy

Element dispersive X-ray spectroscopy (EDX) is used to identify and quantify elemental compositions of a solid surface. It is efficient and easy to operate. It is

realised by analysing the wavelength and intensity of X-rays emitted by characteristic elements of the sample. Accordingly, it measures the element contents and compares the intensities of different elements.

Usually, EDX is equipped with a scanning electron microscope (SEM) or TEM to perform the elemental analysis of samples. The atoms on the surface are initially excited by a high-energy X-ray beam, and emit unique wavelengths of X-rays which are characteristic of each element, detected by an energy dispersive detector. Accordingly, elements are assigned, resulting in a “fingerprint” spectrum, which allows element identification via comparison with reference spectra.

Therefore, in this thesis, EDX measurements were employed to analyse the element content and distribution of perovskites. It was conducted by an X-MaxN detector (Oxford Instruments) and performed in the Department of Chemistry, University College London.

### 3.2.5 Ultraviolet Photoelectron Spectroscopy

Ultraviolet photoelectron spectroscopy (UPS) is an effective technique for studying the structure of valence electrons within samples. It can detect the substructure of the valence electron energy level and the fine structure of the molecular vibrational energy level with a high resolution level of 10–20 meV. It has been applied in a wide range of research areas, such as catalysis, metal corrosion, adhesion and semiconductor materials.

Similar to XPS (section 3.2.3), it is based on Einstein’s photoelectric effect, the only difference being the illumination source. UPS uses UV as the excitation light source, which has a low photon energy and narrow linewidth (10 meV), such as Helium I (21.2 eV) and Helium II (30.4 eV). UPS commonly comprises a monochromator UV source, electronic energy analyser, high-vacuum chamber, electron source, sample cell and data processing

system. It measures the energy distribution of photoelectrons when UV irradiates the sample, and follows the equation below:

$$h\nu = E_b + E_k + E_r \quad \text{Equation 3.1}$$

where  $h\nu$  is the photon energy of the UV source,  $E_b$  is the binding energy,  $E_k$  represents the kinetic energy and  $E_r$  denotes the recoil energy of atoms.

Therefore, UPS was conducted to measure the work function and determine the energy band structure of perovskite QDs, and the results were recorded with a Thermo theta probe spectrometer. A base pressure of  $5 \times 10^{-10}$  mbar and He (I) UV light with a photon energy of 21.22 eV were applied. Photoelectron kinetic energy was measured using a hemispherical analyser with angular acceptance over a solid angle of  $60^\circ$  in the Department of Chemistry, University College London.

### 3.3 Optical Characterisations

#### 3.3.1 Steady-State and Time-Resolved Photoluminescence Measurements

Photoluminescence spectroscopy (PL) is a contactless and non-destructive optical characterisation instrument that is employed for quickly and easily characterising defects, impurities and luminescent properties of semiconductor materials.

PL measurement provides direct information about the optoelectronic properties of the grown sample using the fundamental principles of absorption and emission. In order to assess parameters such as the bandgap of the sample, the illumination source must have a higher photon energy than the expected bandgap of the material. In general, the PL instrument consists of a laser diode, an attenuator, a sample stage, optical lenses, a monochromator and a detector coupled with signal analyser software as shown in Figure 3.7.

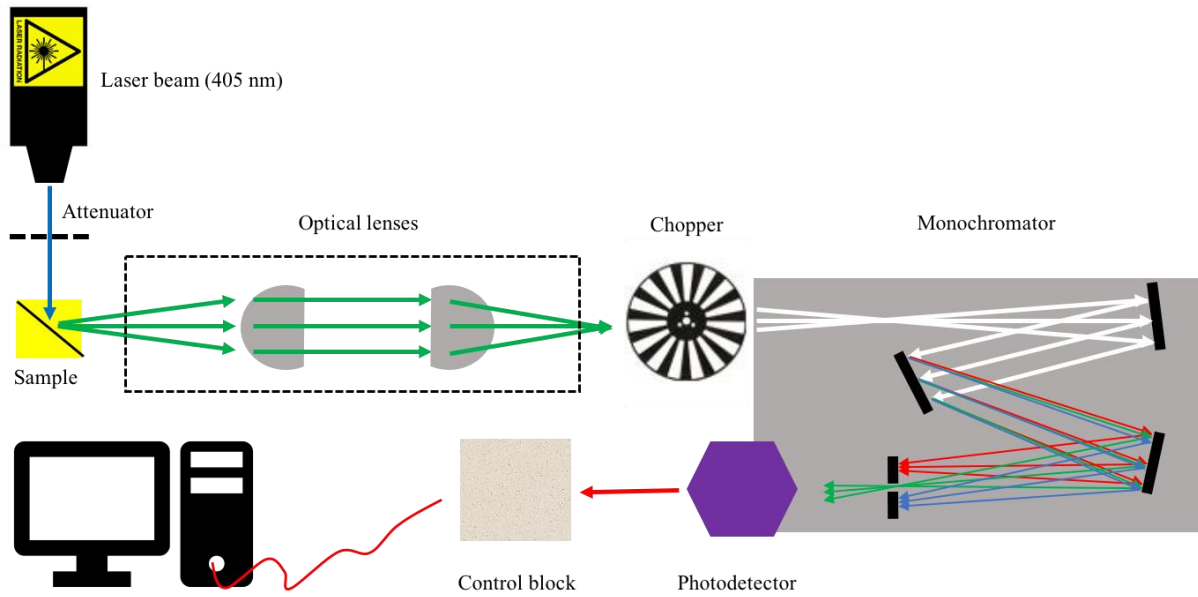


**Figure 3.7** The operation mechanism of PL.<sup>[5]</sup>

A laser with sufficient energy is employed to generate electron-hole pairs within the material. The excited electrons subsequently jump from the VB to the CB and leave holes behind. Electrons and holes relax in their respective CBs and VBs to reach the lowest unexcited state, and then recombine to release energy in the form of light. These re-emitted photons are collected by the optical system and focussed on the detector. The monochromator decomposes the incoming emitted light by wavelength and produces a spectrum of the intensity as a function of the wavelengths. The peak of the wavelength-dependent intensity of the PL spectrum gives the bandgap of the sample.

Time-correlated single-photon counting (TCSPC) is a mature and precise approach to measure the lifetime of fluorescence, which is usually in the order of ps ~  $\mu$ s. It initially emits pulsed light to the sample and subsequently detects using the ultra-fast photodetectors. Each photon-counting signal falls into a corresponding time window (the number of photons accumulated in different time channels is different), and the lifetime curve is generated by statistics and superposition after hundreds of thousands of repetitions. As radiative recombination competes with non-radiative recombination inside the photo-excited sample,

comparing the amplitude of the PL peaks and lifetimes between different samples provides information on the relative material quality and defect densities.

Therefore, for the work presented in this thesis, in order to investigate the optical properties of perovskite QDs, steady-state PL and time-resolved PL (TRPL) measurements were recorded by TCSPC (LifeSpec-ps, Edinburgh Instruments) in the Department of Electronic and Electrical Engineering, University College London. A 405 nm laser was used at  $-16^{\circ}\text{C}$ , which was further fitted with an exponential decay function in fluorescence analysis software technology (FAST).

### 3.3.2 Absorption Measurements

UV-visible spectroscopy is a powerful tool for analysing and determining the composition and content of samples with regard to the absorption of UV and visible light emitted by samples. This technique is simple and convenient while maintaining high sensitivity and good accuracy. The principle of the absorption is explained in Chapter 2.

As displayed in Figure 3.8, the UV-Vis system is mainly composed of a light source, monochromator, sample cell, optical lenses, detector and recording device. Separate dual light sources are used, wherein the xenon lamp has a wavelength of 185–395 nm and the tungsten lamp has a wavelength of 350–800 nm, to obtain light in the full wavelength range. Most instruments use a moving mirror to achieve smooth switching between the light sources, which can be smoothly scanned across the full spectral range. The light emitted by the light source is modulated into a light beam through the optical aperture and then enters the monochromator. The monochromator is composed of a dispersive prism or a diffraction grating, and the light beam emitted from the dispersion component of the monochromator becomes a multi-component monochromatic light with different wavelengths. The rotation of the grating respectively sends monochromatic light with different wavelengths into the sample cell through

the slit. It then enters the photodetector and is finally amplified by an electronic amplification circuit. The absorbance can be read from a microampere meter, digital voltage meter or driving recording device to obtain a spectrum.

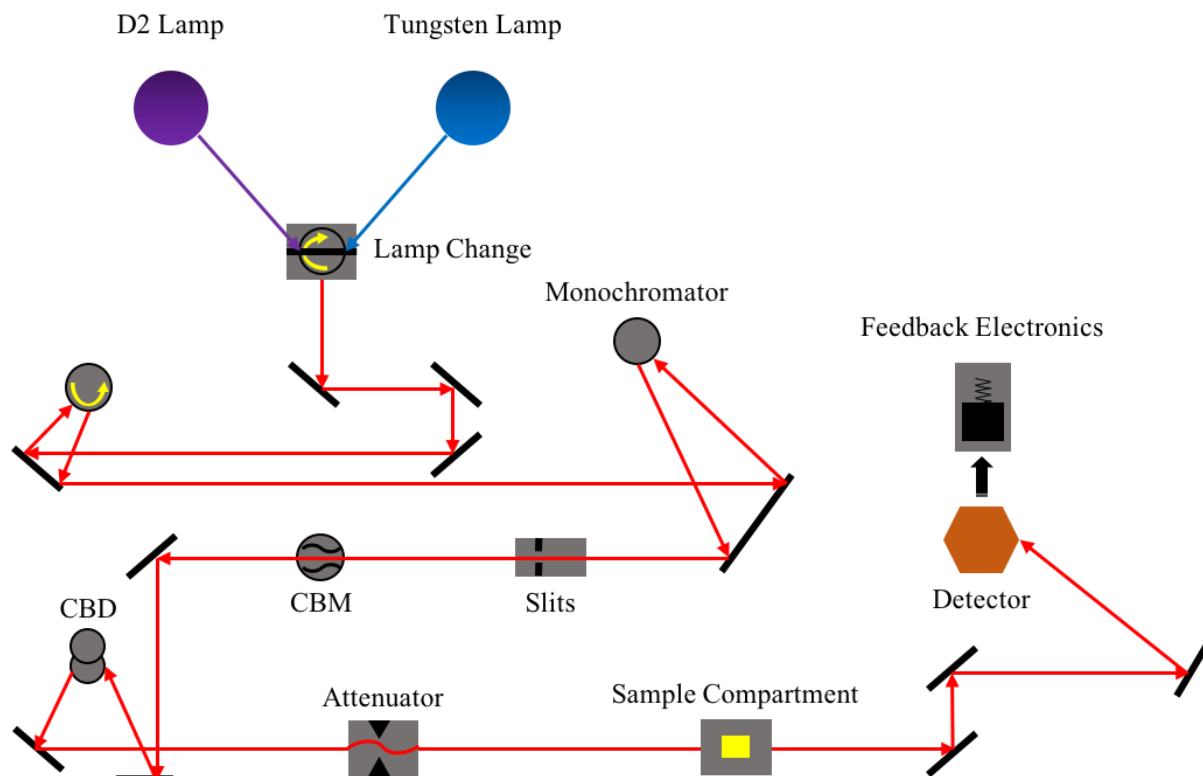


**Figure 3.8** The working principle of UV-Vis.<sup>[6]</sup>

For the work presented in this thesis, UV-Vis is used for measuring the absorbance of perovskite QDs. The absorption spectra were measured by Lambda 750S UV-Vis spectrometers (Perkin Elmer) at room temperature, in a range between 250 nm and 800 nm at IMD, University College London.

## 3.4 Morphological Characterisations

### 3.4.1 Atomic Force Microscopy

Atomic force microscopy (AFM) is an analytical equipment, which is conducted to explore the surface morphology of solid materials. It investigates the surface structures of materials by detecting the weak atomic interaction between the sample surface and cantilever.

As shown in Figure 3.9, AFM mainly consists of a tip and cantilever, laser, photodetector and feedback electronics. The key component of AFM is the cantilever with a tip attached on its head, which scans the sample surface. The cantilever is mostly made of silicon and silicon nitride materials, and its dimension ranges from tens to hundreds of micrometres. The tip carried by the cantilever has a radius of curvature in the order of nanometres. Initially, the cantilever is fixed at one end, and the back of the tip end is illuminated by a laser diode. During the sample scanning, the cantilever will bend and undulate in the direction perpendicular to the surface plane of the sample, due to the weak repulsive force between the tip and atoms on the surface of the sample. Therefore, detecting the changes in the position of the spot by photodiode, information on the surface topography of the sample can be obtained with atomic resolution.

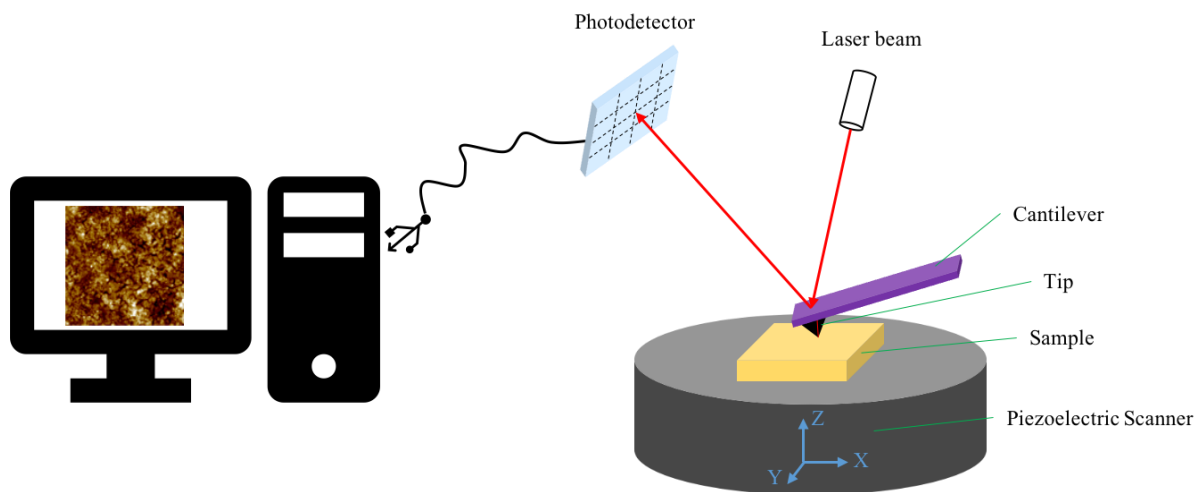


**Figure 3.9** Schematic representation of AFM.<sup>[7]</sup>

Unlike SEM and TEM, AFM provides real-time 3D surface maps, and enables the observation of non-conductive samples. Therefore, AFM is preferred in this work for investigating the surface morphology of perovskite QDs. AFM measurement was conducted by Bruker Dimension Icon with ScanAsyst under a soft tapping mode in the Department of Electronic and Electrical Engineering, University College London.

### 3.4.2 Scanning Electron Microscopy

SEM is a reliable and precise process for high-resolution morphology analysis, which has been widely employed in micro-research fields of life science, physics, chemistry, justice, earth science and materials science.

Different from the TEM imaging mechanism, SEM does not require any imaging lenses, and the SEM images are formed in a certain time and space sequence point by point, and displayed on the external imaging tube. As shown in Figure 3.10, a complete SEM is mainly composed of five units, including a high-energy electron beam generator, an imaging system that receives and processes various electronic signals, an information recording system, a vacuum system and a power supply system.

Initially, the electron gun emits the electron beam into a point by focussing and concentrating. By applying an accelerating voltage, a high-energy electron beam is further formed, and is subsequently condensed into a light spot with a smaller diameter after passing through objective lenses and objective aperture. Electronic signals with different depths are simultaneously excited, including Auger electrons, secondary electrons, back-scattered electrons, X-rays, cathodoluminescence, absorbed electrons and transmitted electrons. These electron signals are then received by different detectors above the sample cell, and are collected and amplified to formed a real-time image to achieve the purpose of characterising the surface morphology of samples. The resolution and magnification of the new SEM can reach 1 nm and 300,000-fold continuous adjustment, respectively.

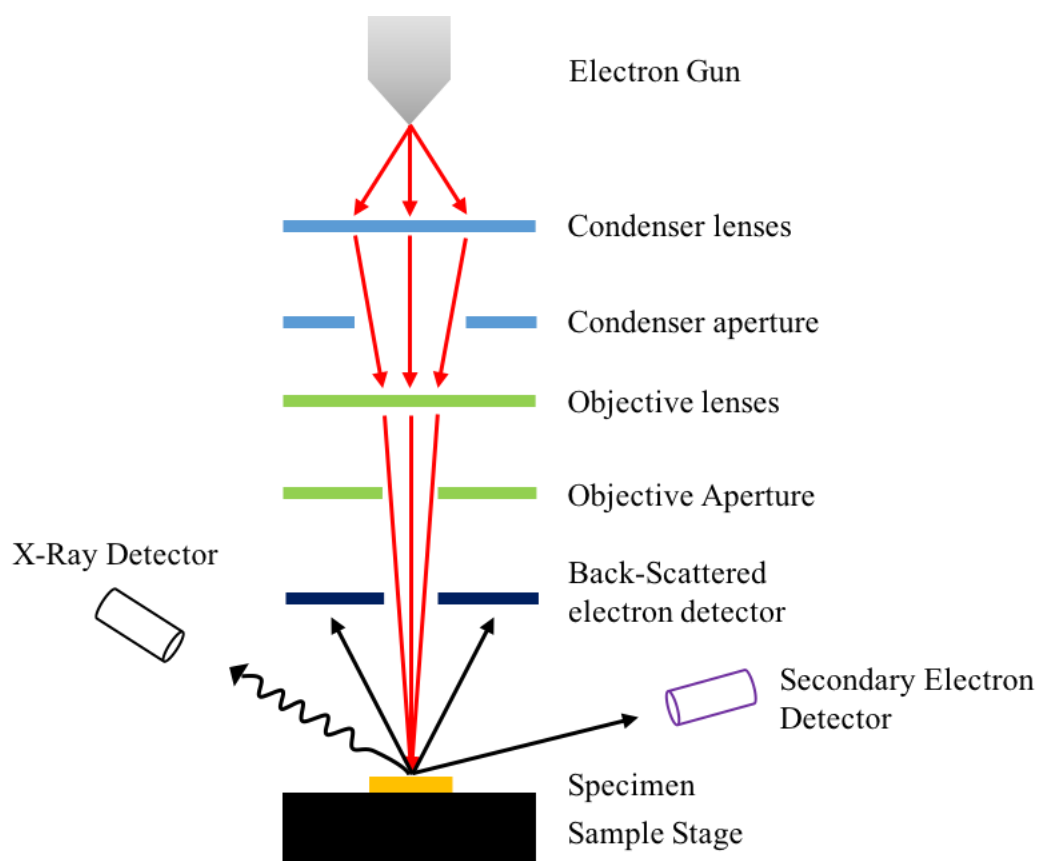


**Figure 3.10** Schematic drawing of SEM.

Therefore, SEM is essential for the investigation of surface morphology of perovskite QDs. They were examined by EVO LS15, ZEISS at IMD, University College London.

## 3.5 Photodetector Fabrications

### 3.5.1 Substrate Preparation

The substrate is one of the fundamental components in all device fabrications. A clean and smooth substrate is needed for constructing high-performance optoelectronic devices. Microscopic contaminants can introduce defects into the semiconductor-metal interface, which could potentially disrupt the surface crystallinity and increase surface recombination, further resulting in a degradation of the device performance. Therefore, all substrates, including ultra-white glass, quartz, ITO-coated glass and ITO-coated PET were cleaned sequentially in

detergent, deionised water, acetone and 2-propanol. Each step was carried out in an ultrasonic bath for 15 min, followed by oxygen plasma (UV-zone) treatment for 15 min.

### 3.5.2 Photolithography

Photolithography is a precise micro-processing technology that can transfer circuit patterns to the substrate. It has been widely used in nanotechnologies. In general, UV light is illuminated to the substrate coating with photoresist film through a photomask, which leads to a chemical reaction of the photoresist in the exposed area. The exposed photoresist is then removed by a developing technique, resulting in a circuit pattern copied onto the photoresist film. The pattern is finally transferred to the substrate by etching.

In this thesis, photolithography is used for patterning ITO electrodes. The detailed procedure is shown in Figure 3.11. ITO-coated PET was firstly prepared and cleaned in the sequence of detergent deionised water, acetone and IPA in an ultrasonic bath for 15 min each time, and subsequently dried at 115 °C for 1 min. Before each photoresist deposition process, a test was conducted to ensure the right spin-coating speed and protection from dropping out. Subsequently, the positive photoresist (S1818) was spin-coated at a speed of 4000 rpm for 30 sec to achieve the desired thickness of photoresist ( $\sim 1.8 \mu\text{m}$ ), followed by another soft baking (115 °C, 1 min). In order to obtain the desired electrode pattern, the substrate was aligned with a purpose-designed photomask and exposed to UV light for 3.5 sec by a Mask Aligner. MF319 developer solution was used to remove the photoresist from the exposing region (60 sec), followed by gently rinsing with deionised water for 2 min, and blowing with  $\text{N}_2$ . To remove the remaining ITO, the treated-substrate was immersed in an acid etchant (HCl, 37% in molar solution) for 6.5 min at an etching rate of  $20 \text{ nm min}^{-1}$ . Finally, the sample was sonicated with S1165 for 5 min (twice) to get rid of the photoresist residues. The photolithography was processed at the London Centre of Nanotechnology, University College London.

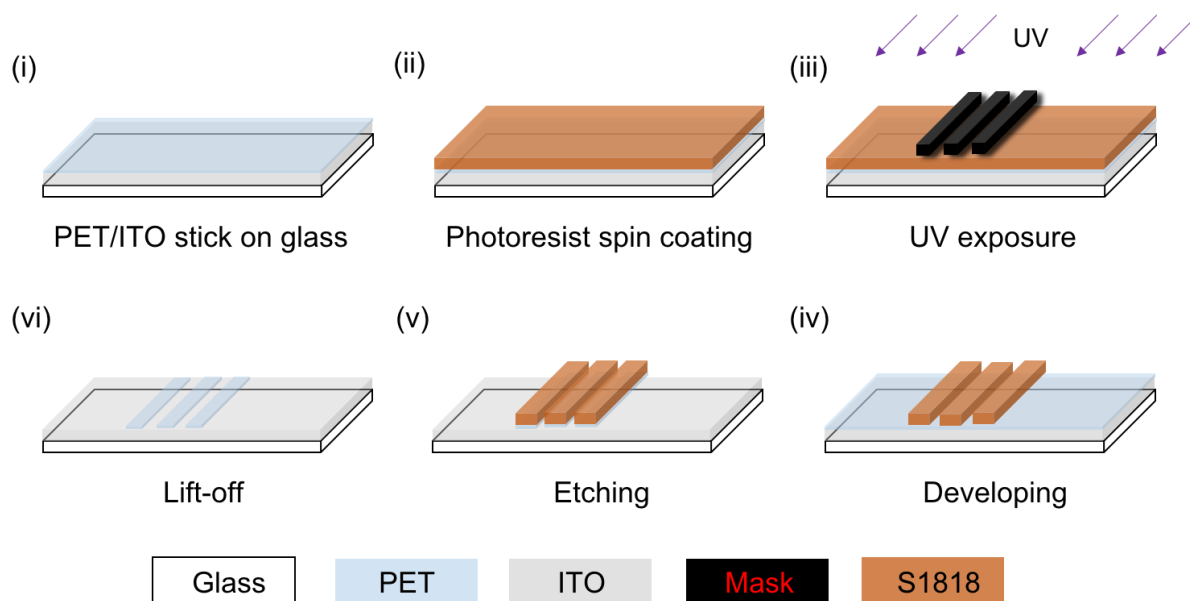


**Figure 3.11** The process of photolithography.

### 3.5.3 Anodic Aluminium Oxide Nanostructure Fabrication

As illustrated in Figure 3.12, the hybrid plasmonic nanostructures were fabricated by preparing highly ordered porous AAO and Al substrate using a two-step anodisation technique, which was done by Dr. Mingyu Li in the Wuhan University of Technology.

In preparation, each  $2 \times 2 \text{ cm}^2$  high-purity aluminium foil was polished at a 20 V constant voltage in a mixture of ethanol absolute and perchloric acid ( $V_{\text{Alcohol}}: V_{\text{Acid}} = 4:1$ ) at room temperature, and the anodisation was subsequently carried out in oxalic acid for 15 min at 60 V. To define the pores, the irregular-shaped oxidised aluminium films were etched in a mixed solution of chromic acid and phosphoric acid at 80 °C for 30 min. Uniform porous AAO membranes with a pore length of 450 nm were formed after the second anodisation in 0.3 mol  $\text{L}^{-1}$  oxalic acid under identical conditions. A fine control of the etching process (in 5%  $\text{H}_3\text{PO}_4$ ) was performed to achieve different pore sizes of AAO matrix from 120 nm to 220 nm, followed by Ag thin-film deposition (3 nm) at a rate of  $0.1 \text{ nm s}^{-1}$  under  $\sim 7 \times 10^{-4} \text{ Pa}$ . In order to investigate the impacts of different metallic NPs (including Al and Cu), 3-nm-thick Cu and Al films were thermally evaporated on AAO matrices. The metallic NPs started to aggregate

during the annealing process (rapid thermal annealing furnace, OTF-1200-4-RTP) at 400 °C for 10 min.

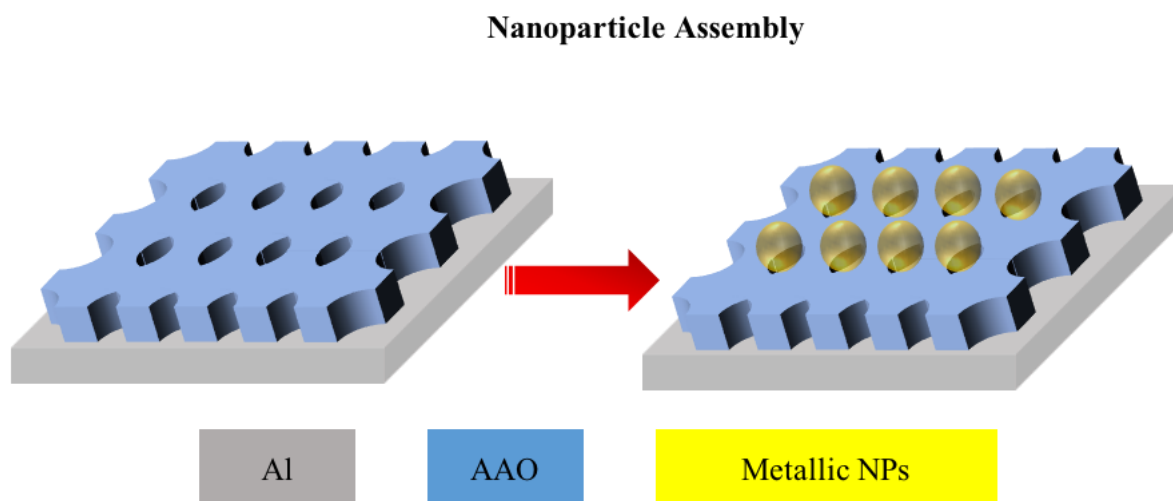


**Figure 3.12** Schematic fabrication of the metallic NP-decorated AAO plasmonic nanostructure.

### 3.5.4 Electron Transport Layer Deposition

#### 3.5.4.1 Glassy Graphene

Glassy graphene is an intermediate state between glassy carbon and graphene, which has high crystallinity but curly lattice planes.<sup>[8,9]</sup> Moreover, glassy graphene, inheriting advantages from graphene and glassy carbon, shows impressive conductivity, high transparency and good mechanical flexibility. In this work, ultra-smooth glassy graphene was fabricated via a polymer-assisted approach by Dr. Xiao Dai and Prof. Guifu Zou in the University of Soochow, China.<sup>[9]</sup>

Glucose (1 g) and PEI (0.5 g) were firstly dissolved in deionised water (5 ml) with vigorous stirring overnight at room temperature. As shown in Figure 3.13, the as-prepared precursor was subsequently deposited onto the quartz substrate by spin-coating at 8000 rpm for 30 s. The substrate was gradually annealed to 1000 °C at a rate of 2 °C min<sup>-1</sup> under Ar/H<sub>2</sub> (10/1) atmosphere. After 5 min annealing at 1000 °C, the cooling process (down to room temperature) was applied for the films. In order to obtain high-quality glassy graphene, Ni thin

film was evaporated on top of the film followed by annealing at 850 °C, and the residual Ni was removed through etching.

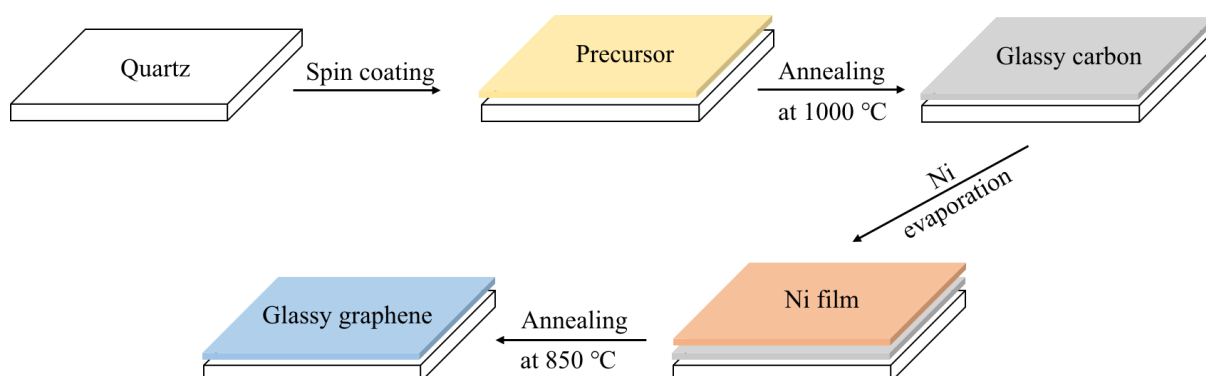


**Figure 3.13** The fabrication of glassy graphene.

#### 3.5.4.2 Titanium Dioxide

Titanium dioxide ( $\text{TiO}_2$ ) is a wide-bandgap semiconductor that is widely employed as an ETL in perovskite-based optoelectronics.<sup>[10–13]</sup> In general,  $\text{TiO}_2$  is deposited by spin-coating followed by thermal annealing. However, the annealing temperature is relatively high ( $\sim 500$  °C), which is not compatible with flexible substrate (e.g. PET  $\sim 150$  °C), as the overheating would damage the flexible substrate.<sup>[14,15]</sup>

ALD is one of the most important techniques that enables precise and uniform film formation and excellent film coverage. Two or more gas-phase precursors are periodically and alternatively introduced to the substrate surface with continuous intermediate purging in the reaction chamber. Subsequently, a gas-solid phase chemical adsorption reaction occurs on the deposited surface, leading to thin-film formation. This kind of working mechanism enables precise sub-nanometre control over the deposition thickness. In order to deposit high-quality thin film, the precursors and deposition cycle parameters should be carefully selected, considering the thermodynamics and kinetics of the involved surface reactions. More specifically, the precursors have to possess good volatility, sufficient reactivity and certain thermal stability, and cannot corrode or dissolve the substrate. The pulse time of the precursor

must ensure the single-layer saturated adsorption, and the deposition temperature should be kept within the ALD window to avoid condensation or thermal decomposition of the precursor, leading to a non-uniform film morphology.

Therefore, in this thesis,  $\text{TiO}_2$  was deposited by the ALD technique (Ultratech, Savannah G2 S200) at 100 °C, with 100 cycles, at IMD, University College London. The deposition process steps of  $\text{TiO}_2$  by  $\text{TiCl}_4$  and  $\text{H}_2\text{O}$  are shown in Figure 3.14. Firstly, short precursor pulses ( $\text{TiCl}_4$ ) are injected into the flowing carrier gas, separated by a short purge. A defined amount of the thin-film material is grown during each ALD cycle (pulse of precursor 1 – purge). Once the whole surface is covered by a monolayer of  $\text{TiCl}_4$ , self-saturation is considered to have been reached. Subsequently, the excess gas precursor is purged and a second gas-phase precursor ( $\text{H}_2\text{O}$ ) is introduced, which condenses and is chemisorbed on top of the first layer. There is a reaction or decomposition that converts the  $\text{TiCl}_4$  and  $\text{H}_2\text{O}$  precursors into the desired coating as a saturated surface reaction. After reaction, the excess gas or biproducts are pumped away, and a monolayer of  $\text{TiO}_2$  is finally formed. The whole process can be repeated to deposit more layers one by one until reaching the desired coating thickness.

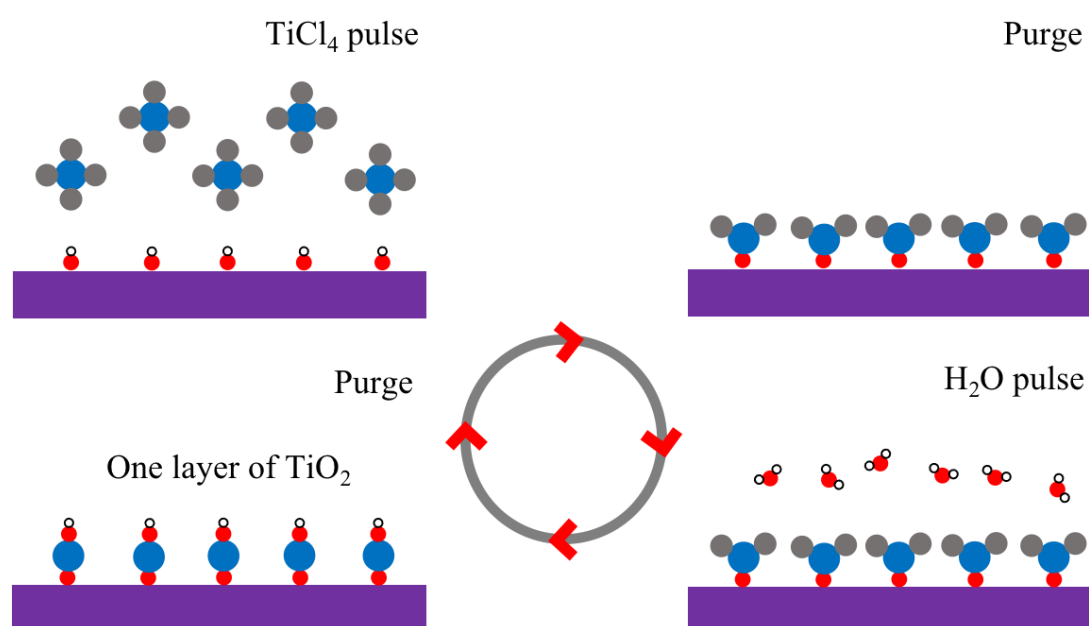


**Figure 3.14** Operation mechanism of  $\text{TiO}_2$  deposition by ALD.<sup>[16]</sup>

### 3.5.5 Active Layer Deposition

The active layer is the most important layer in photodetectors, which absorbs incident photons and generates a number of electron-hole pairs.

In the presented works, the perovskite QDs were employed as the active materials to absorb incident light signals. The corresponding perovskite QD films were obtained by spin-coating the QD precursors onto a pre-cleaned substrate at 1000 rpm for 60 sec. The number of deposition cycles applied can adjust the thickness of the QD layer. The samples were subsequently baked at 120 °C for 1 min after each coating, and annealed at 120 °C for 5 min after spinning the last layer. This gave a uniform active layer with a total thickness of ~150 nm measured by Dektak surface profilometer.

### 3.5.6 Hole Transport Layer Deposition

HTL is used for extracting and transporting holes generated in the active layer. Various hole transport materials have been employed in perovskite devices, including 2,2',7,7'-tetrakis-(N,N-di-p-methoxyphenylamine)9,9'-spirobifluorene (Spiro-OMeTAD), poly(triarylamine) (PTAA) and PEDOT:PSS.<sup>[17–20]</sup>

In this work, Spiro-OMeTAD was selected as the hole-transport material. It was deposited by spin-coating the Spiro-OMeTAD precursor at 2000 rpm for 30 s and then exposing to oxygen for 12 h. The Spiro-OMeTAD precursor was synthesised by dissolving Spiro-OMeTAD powder, 4-tert-butylpyridine and lithium bis(trifluoromethanesulfonyl)imide (Li-TFSI, 1.8 M, dissolved in acetonitrile) in chlorobenzene to form a clear Spiro-OMeTAD solution (0.056 M), where the volume ratio between 4-tert-butylpyridine, Li-TFSI and chlorobenzene (CB) was 28.8:17.5:1000.<sup>[17]</sup> Tert-butylpyridine additives assist in film formation but may also play an important role in perovskite film surface passivation.

### 3.5.7 Electrode Deposition

To fabricate a complete device, metallic electrodes are essential, as they allow the collection of charge carriers from the perovskite QD layers. Thermal evaporation is applied for electrode deposition, as shown in Figure 3.15. Basically, thermal evaporation uses the principle of resistance evaporation, which heats the metal source on the evaporating boat by applying large current under high vacuum. The vaporous metal subsequently adheres to the substrate placed on the upper side of the raw material without colliding with the background atmosphere. By controlling the magnitude of the applied current, the evaporation rate of the coating metals can be conveniently controlled.

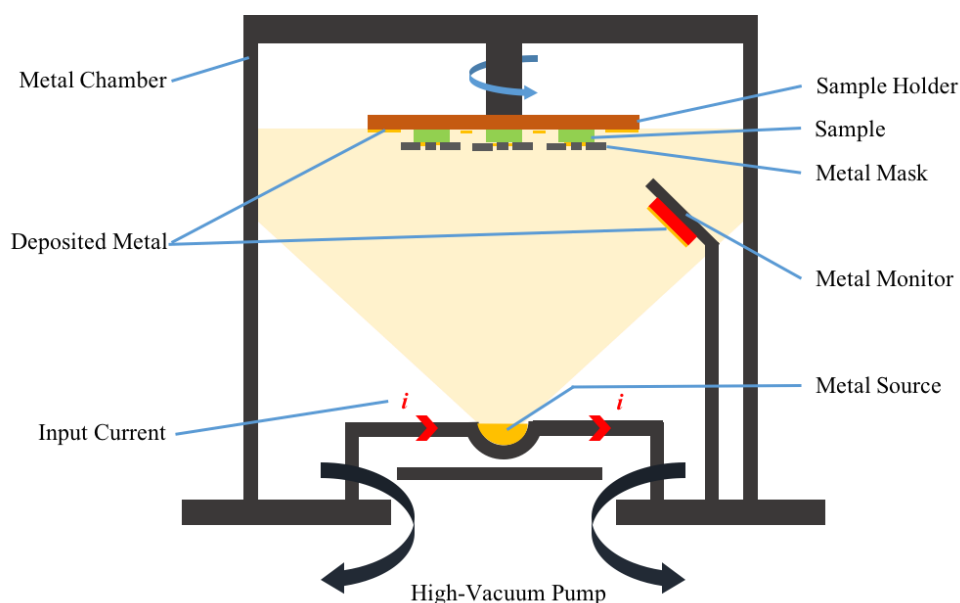


**Figure 3.15** Overview of the thermal evaporator.

Au exhibits high conductivity and an acceptable work function (5.1 eV), but a relatively weak adhesion to perovskite QDs. In addition, thermal treatment can promote the diffusion of Au atoms through the perovskite QD surface. Therefore, in the presented work, 10 nm Ni and 100 nm Au contact pads were deposited through a metal shadow mask under a vacuum of  $\sim 10^{-7}$  Torr in the thermal evaporator at a rate of 0.3 and 1 A s<sup>-1</sup>, respectively, to complete the devices. 10 nm Ni was used to increase the connection between the interface layer and metal contact, and facilitate the formation of ohmic contacts as well as prevent Au diffusion.

### 3.6 Device Characterisations

The electrical properties under illumination were explored using a Keithley 4200 semiconductor characterisation system (SCS), which was designed and manufactured by Keithley Instruments Ltd., USA. The characterising system was mainly used for analysing the electrical parameters of semiconductor devices, and was equipped with a modular, configurable and scalable architecture that allowed it to accurately meet the current measurement needs. Meanwhile, this advanced parametric analyser delivers excellent measurement sensitivity and accuracy while inheriting embedded Windows operations which can intuitively analyse the characteristics of semiconductor devices.

The core measurement components of the system are SMU (source measure unit) and PREAMP. Each SMU can realise four functions: voltage source, voltmeter, current source and ammeter. The SMU has a maximum range of 100 mA (21 V), and the 210 V (10 mA) high-power SMU option can reach 1 A (21 V). The minimum range of SMU can be resolved to 0.1 pA, 1  $\mu$ V. The SMU is installed in the main chassis of the 4200-SCS. The 4200-PA preamplifier is connected to the SMU to resolve the very weak current signal and solve noise problems. The 4200-SCS has a separate ground terminal, and all SMUs are completely independent and are fully protected four-wire measurement structures.

In this thesis, the optoelectrical performance was characterised using a Keithley 4200 SCS under ambient conditions. An anti-vibration probe stage was equipped to prevent unnecessary noise, as displayed in Figure 3.16. During the measurements, all devices were kept under ambient conditions with no encapsulation. The current–voltage ( $I$ – $V$ ) curve is essential for photodetector characterisation, measuring device current in the absence and presence of light illumination. In the absence of light, the device properties can be examined by electrically injecting carriers into the detector rather than light-induced photocarriers. By applying a range of bias voltages, a typical  $I$ – $V$  curve is formed, which would give a dark current measurement.

To determine the photoresponse, various lasers were employed as light sources to illuminate the photodetectors on the sample stage, including 405 nm, 450 nm and 520 nm laser diodes with a spot size of  $\sim 0.75$  mm in radius. The corresponding power intensity of light sources was measured by a LOT solar simulator system. Under light illumination, photocurrent can be generated via a photoconductive or photovoltaic effect, and the relationship between photocurrent and voltage can be subsequently recorded by a Keithley 4200 system. In terms of the response time measurement, the curve of photocurrent versus time was recorded as periodically turned on/off laser diodes. Aforementioned, the response time can be evaluated by measuring the duration between 10 % and 90 % of the maximum photocurrent. Moreover, the area of the photodetector is important, as it directly affects the device performance. For the photodetectors with lateral structure, the active area can be defined as the area between two electrodes. In terms of the vertical stacked photodetectors, the active area can be assigned to the overlapped region between top electrode, ETL, perovskite layer, HTL and bottom electrode.

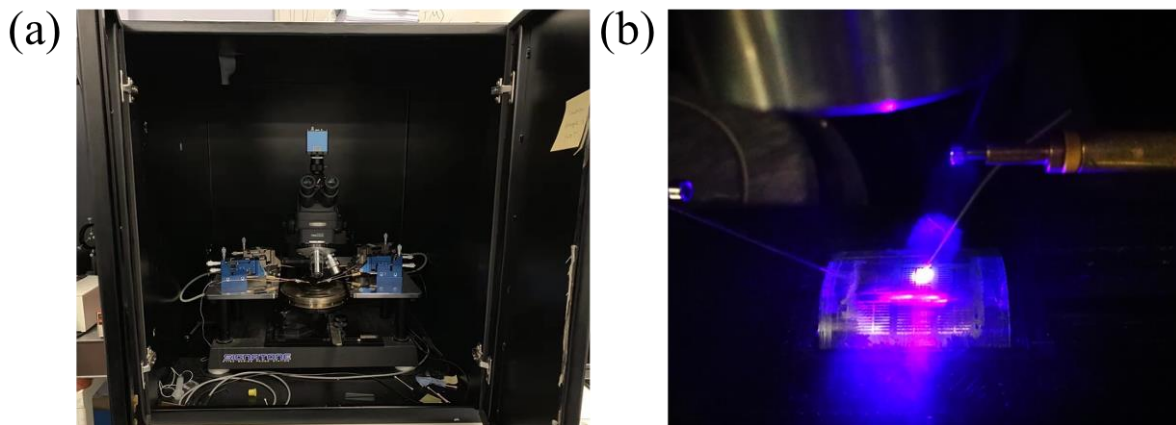


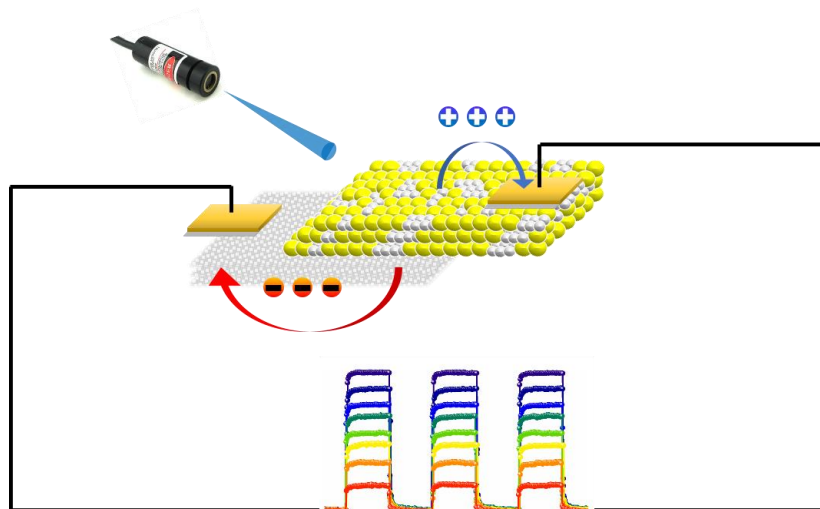
**Figure 3. 16** (a) An overview of the anti-vibration probe stage. (b) Characterising electrical properties of photodetectors under light illumination.

### 3.7 References

- [1] Q. A. Akkerman, M. Gandini, F. Di Stasio, P. Rastogi, F. Palazon, G. Bertoni, J. M. Ball, M. Prato, A. Petrozza, L. Manna, *Nat. Energy* **2017**, 2, 16194.
- [2] K. Shen, X. Li, H. Xu, M. Wang, X. Dai, J. Guo, T. Zhang, S. Li, G. Zou, K. Choy, I. P. Parkin, Z. Guo, H. Liu, J. Wu, *J. Mater. Chem. A* **2019**, 7, 6134.
- [3] K. Shen, H. Xu, X. Li, J. Guo, S. Sathasivam, M. Wang, A. Ren, K. L. Choy, I. P. Parkin, Z. Guo, J. Wu, *Adv. Mater.* **2020**, 32, 2000004.
- [4] A. Chauhan, *J. Anal. Bioanal. Tech.* **2014**, 5, 1.
- [5] I. Bayn, B. Meyler, J. Salzman, R. Kalish, *New J. Phys.* **2011**, 13, 025018.
- [6] Y. A. Gandomi, D. S. Aaron, J. R. Houser, M. C. Daugherty, J. T. Clement, A. M. Pezeshki, T. Y. Ertugrul, D. P. Moseley, M. M. Mench, *J. Electrochem. Soc.* **2018**, 165, A970.
- [7] H. O. B. Gautier, A. J. Thompson, S. Achouri, D. E. Koser, K. Holtzmann, E. Moeendarbary, K. Franze, in *Methods Cell Biol.*, **2015**, pp. 211–235.
- [8] H. Xu, X. Han, X. Dai, W. Liu, J. Wu, J. Zhu, D. Kim, G. Zou, K. A. Sablon, A. Sergeev, Z. Guo, H. Liu, *Adv. Mater.* **2018**, 30, 1706561.
- [9] X. Dai, J. Wu, Z. Qian, H. Wang, J. Jian, Y. Cao, M. H. Rummeli, Q. Yi, H. Liu, G. Zou, *Sci. Adv.* **2016**, 2, 1.
- [10] H. P. Photodetectors, J. Feng, X. Yan, Y. Liu, H. Gao, Y. Wu, B. Su, L. Jiang, *Hosp. Food Nutr. Focus* **1993**, 10, 6.
- [11] A. Mei, X. Li, L. Liu, Z. Ku, T. Liu, Y. Rong, M. Xu, M. Hu, J. Chen, Y. Yang, M. Gratzel, H. Han, *Science*. **2014**, 345, 295.
- [12] C. Liu, K. Wang, P. Du, E. Wang, X. Gong, A. J. Heeger, *Nanoscale* **2015**, 7, 16460.
- [13] L. Zhou, K. Yu, F. Yang, J. Zheng, Y. Zuo, C. Li, B. Cheng, Q. Wang, *Dalt. Trans.* **2017**, 46, 1766.

- [14] W.-H. Chung, S.-H. Park, S.-J. Joo, H.-S. Kim, *Nano Res.* **2018**, *11*, 2190.
- [15] I. G. Serrano, J. Panda, T. Edvinsson, M. V. Kamalakar, *Nanoscale Adv.* **2020**, *2*, 3156.
- [16] G. S. Oehrlein, D. Metzler, C. Li, *ECS J. Solid State Sci. Technol.* **2015**, *4*, N5041.
- [17] P. Zhang, T. Zhang, Y. Wang, D. Liu, H. Xu, L. Chen, Y. Li, J. Wu, Z. D. Chen, S. Li, *J. Power Sources* **2019**, *439*, 227091.
- [18] J. Xu, A. Buin, A. H. Ip, W. Li, O. Voznyy, R. Comin, M. Yuan, S. Jeon, Z. Ning, J. J. McDowell, P. Kanjanaboos, J.-P. Sun, X. Lan, L. N. Quan, D. H. Kim, I. G. Hill, P. Maksymovych, E. H. Sargent, *Nat. Commun.* **2015**, *6*, 7081.
- [19] C. Bao, Z. Chen, Y. Fang, H. Wei, Y. Deng, X. Xiao, L. Li, J. Huang, *Adv. Mater.* **2017**, *29*, 1.
- [20] B. R. Lee, J. C. Yu, J. H. Park, S. Lee, C. K. Mai, B. Zhao, M. S. Wong, E. D. Jung, Y. S. Nam, S. Y. Park, D. Di Nuzzo, J. Y. Kim, S. D. Stranks, G. C. Bazan, H. Choi, M. H. Song, R. H. Friend, *ACS Nano* **2018**, *12*, 5826.

## CHAPTER 4. THE STUDY OF ZnO NPs DECORATED ALL-INORGANIC PEROVSKITE PHOTODETECTORS



### 4.1 Introduction

Photodetectors, as a fundamental optoelectronic component, have been applied in various applications, including imaging, biosensing, environmental monitoring and optical communication. To date, commercial photodetectors are mainly based on conventional semiconductors, such as GaN, Si and GaAs. Various spectral responses can be achieved by employing the above semiconductors, including X-ray, UV, visible, NIR and MIR, owing to their distinct bandgaps. Although the performance of commercial photodetectors is reliable and stable, their fabrication procedure is relatively complex. Moreover, the equipment (e.g. MOCVD and MBE) used for growing conventional semiconductors is expensive, and the atmosphere is strictly controlled, which partly limits their wide use. Therefore, the demand for developing simple and cost-effective photodetectors is ever increasing. One effective approach is employing emerging materials to replace the conventional semiconductors in photodetectors.

Recently, perovskites, as novel and cost-effective semiconductors, have attracted substantial research interest due to their excellent optoelectronic characteristics. Within ten years, the PCE of single-junction hybrid perovskite solar cells has exceeded 25%. Perovskites

not only show promise in photovoltaic applications, but also in photodetectors, LEDs and lasers. However, hybrid perovskites are prone to stability issues when exposed in ambient air. Moisture, oxygen and heat have a significant impact on perovskite devices due to their sensitive organic cations, resulting in a degraded device performance. Therefore, extensive research has been undertaken to address such stability issues caused by organic cations.

In 2013, Kanatzidis *et al.* successfully prepared CsPbBr<sub>3</sub> bulk single crystals, and further demonstrated the X-ray response under a Ag radiation source.<sup>[1]</sup> Subsequently, more and more studies were carried out to investigate the characteristics of such all-inorganic perovskites and explore their applications. In addition to bulk single crystals, 2D, 1D and 0D all-inorganic perovskites have been reported, especially 0D QDs. Benefiting from quantum size confinement, the bandgaps of CsPbX<sub>3</sub> QDs can be easily tuned. In 2015, Kovalenko *et al.* designed CsPbX<sub>3</sub> colloidal QDs using the solution-phase method. The as-synthesised CsPbX<sub>3</sub> QDs exhibited a high quantum yield between 50% and 90%, showing huge potential in light-emitting devices.<sup>[2]</sup> Moreover, CsPbX<sub>3</sub> QDs are also promising in solar cells and photodetectors. In 2017, Manna *et al.* employed CsPbBr<sub>3</sub> QDs as an absorbing layer in solar cells, and exhibited an open-circuit voltage of 1.5 V and an impressive PCE exceeding 5%. Shao *et al.* demonstrated photodiodes based on CsPbBr<sub>3</sub> QDs by spray-coating.<sup>[3]</sup> A high responsivity of 3 A W<sup>-1</sup> and detectivity of 10<sup>14</sup> Jones were achieved, which is beneficial for large-scale fabrications. In addition, all-inorganic perovskites, particularly CsPbBr<sub>3</sub> QDs, share the same advantages as hybrid perovskites, but exhibit better thermal stability and can be synthesised under ambient conditions.<sup>[1,4–6]</sup> Nevertheless, similar to general colloidal QDs, CsPbBr<sub>3</sub> QDs are usually surrounded by a large number of long-chain ligands and dangling bonds. These can serve as insulating barriers, which severely hinder efficient charge transport. Moreover, CsPbBr<sub>3</sub> QDs also suffer from a large number of trap states, leading to unwanted non-radiative recombination and further deteriorating the device performance.<sup>[7,8]</sup> Although atomic-ligand and passivation

strategies have been demonstrated, they are complex and time-consuming.<sup>[9,10]</sup> Therefore, new facile schemes are highly desired to facilitate the carrier transport and lower surface states.

ZnO NPs are n-type wide-bandgap semiconductors, and are generally employed as the ETL in perovskite-based photodetectors to improve the electron extraction and transportation. Moreover, the advantage of nanoscale dimensions of NPs is also beneficial to improve the surface morphology and optical characteristics of thin film.

In this work, we propose to combine ZnO NPs with CsPbBr<sub>3</sub> QDs to improve the film morphology and provide efficient carrier transport. CsPbBr<sub>3</sub> QDs were firstly synthesised under ambient conditions, followed by injecting ZnO NPs, as explained in Chapter 3, 3.1.3. The ZnO NP-assisted QDs were then employed as absorbing layer in photodetectors. By optimising the amount of ZnO NPs and the device configuration, the photodetectors exhibited an improved photoresponse and excellent stability, making them a potential candidate for practical applications.

## 4.2 Material Characterisations

### 4.2.1 Structural Analysis

The phase purity and crystallographic structures of ZnO NP-decorated CsPbBr<sub>3</sub> QD thin films were studied and identified by XRD. As shown in Figure 4.1, all of the samples exhibited barely changed XRD peaks after blending ZnO NPs, revealing that the incorporation of ZnO NPs does not affect the crystal quality of the CsPbBr<sub>3</sub> QDs. Notably, there are three characteristic peaks indicated in the spectra, at 15.1°, 21.45° and 30.7°. Referring to the ICSD #97851, they can be assigned to the (110), (112) and (220) planes of the orthorhombic CsPbBr<sub>3</sub> perovskite, respectively.<sup>[11]</sup> It is worth noting that the full width at half-maximum (FWHM) of the dominant peaks is ~ 0.5°, which is very narrow, revealing highly uniform and crystalline QDs. However, it can be clearly seen that there is an additional peak located at 11.65°, as

compared to standard card of CsPbBr<sub>3</sub> QDs. This may be caused by the formation of CsPb<sub>2</sub>Br<sub>5</sub> or the existence of excess PbBr<sub>2</sub>.<sup>[12,13]</sup> After blending ZnO NPs, especially when the amount of ZnO NPs is 60  $\mu$ L, this additional peak tends to be eliminated with the decreasing intensity. This phenomenon can be attributed to the effective capping capability of ZnO NPs, preventing further reaction between CsPbBr<sub>3</sub> QDs and overdosed Pb<sup>2+</sup> and Br<sup>-</sup> ions.<sup>[14]</sup>

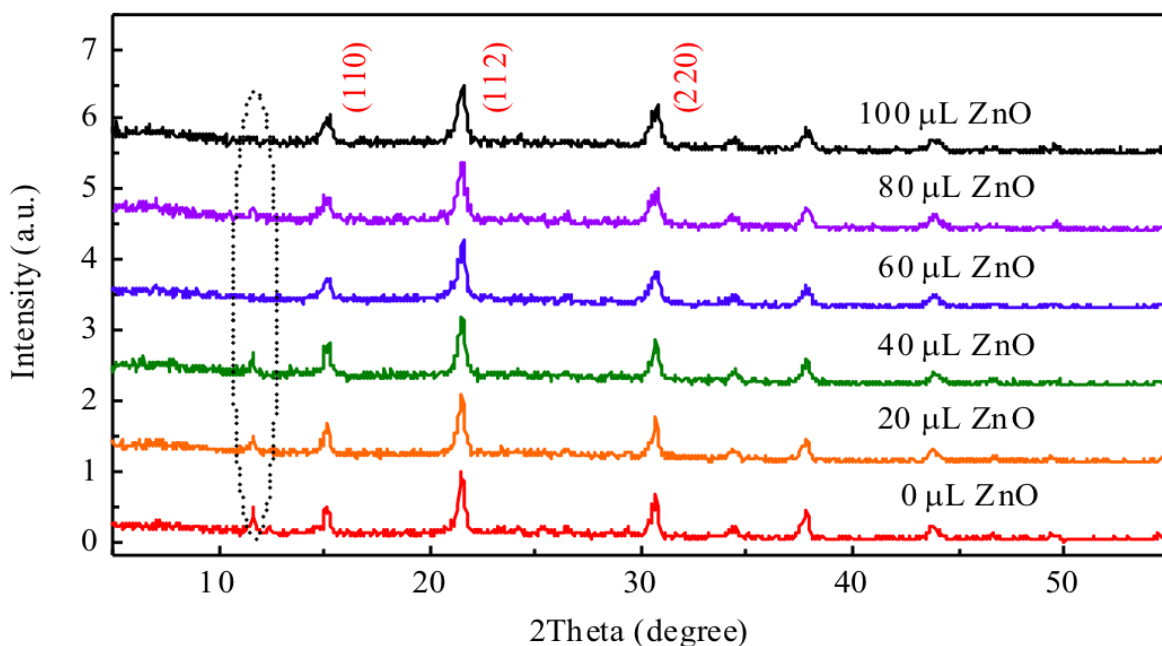


**Figure 4.1** XRD measurements for different injections of ZnO NPs from 0  $\mu$ L to 100  $\mu$ L. The black dot circle represents the peak at 11.65°.

To further acquire the structural information and investigate the crystal quality of ZnO NP-treated QDs, TEM was employed, as shown in Figure 4.2. As representations, high-resolution TEM images of pristine and 60  $\mu$ L ZnO NP-assisted CsPbBr<sub>3</sub> QDs are presented in Figures 4.2a and 4.2b, respectively. The fast Fourier transform (FFT) patterns of both samples are displayed in the insets. As indicated in the red rectangles, both QDs exhibited clear lattice fringes, confirming the high crystallinity. Taking 60  $\mu$ L ZnO NP-decorated CsPbBr<sub>3</sub> QDs as an example, the QDs were uniformly distributed on the Cu grid, as shown in Figure 4.2c. The average size was determined as ~9 nm by performing size distribution measurements (Figure 4.2d), proving the nanoscale dimension of treated QDs.

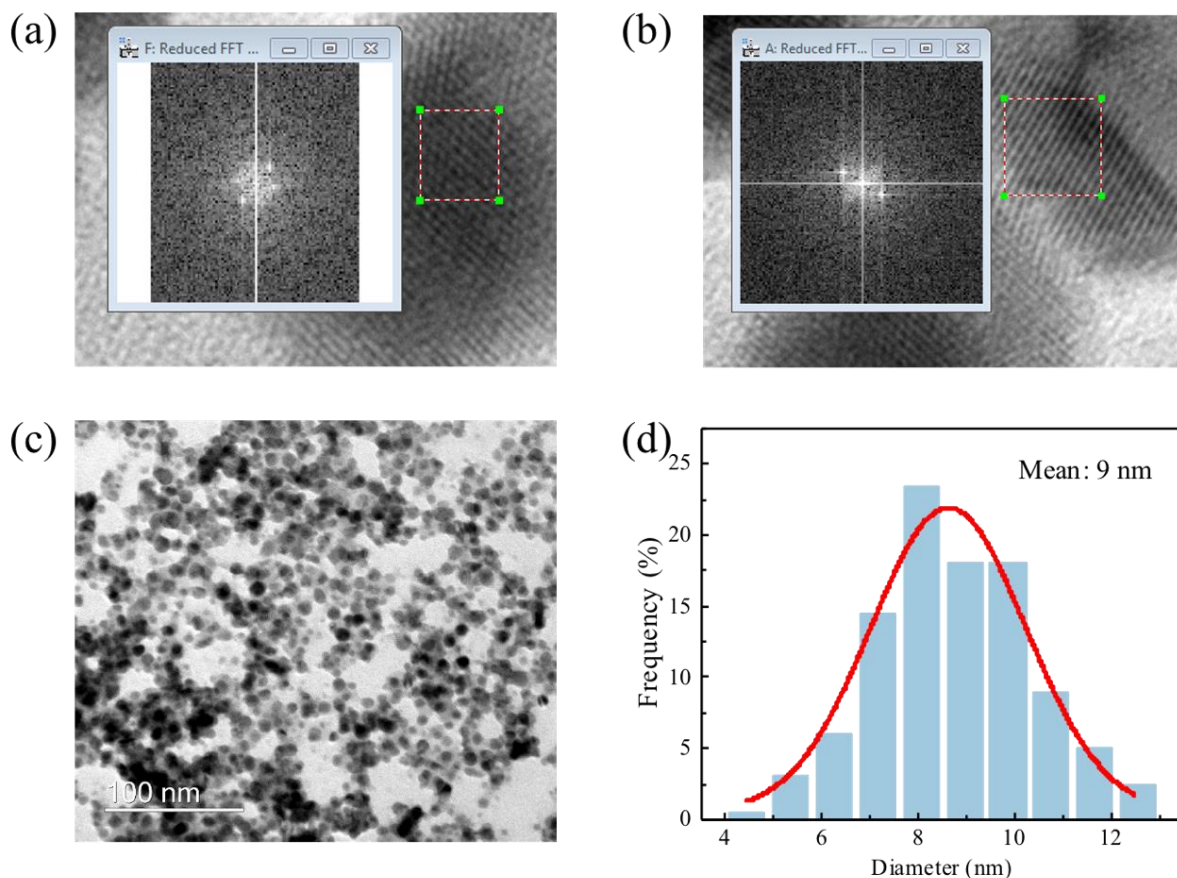


**Figure 4.2** High-resolved TEM image of (a) pristine CsPbBr<sub>3</sub> QDs and (b) 60 μL ZnO NP-assisted CsPbBr<sub>3</sub> QDs. Insets are the corresponding FFT patterns. (c) Low-magnification TEM image of 60 μL ZnO NP-assisted CsPbBr<sub>3</sub> QDs. (d) The corresponding size distribution of treated QDs.

Moreover, in order to further verify the incorporation of ZnO NPs in QDs, the as-prepared samples were subsequently examined by EDX. As displayed in Figure 4.3, the element distribution (Cs, Pb, Br, Zn and O) was consistent with the overview image, particularly for Zn and O, which strongly confirms the uniform distribution of ZnO NPs along the sample.

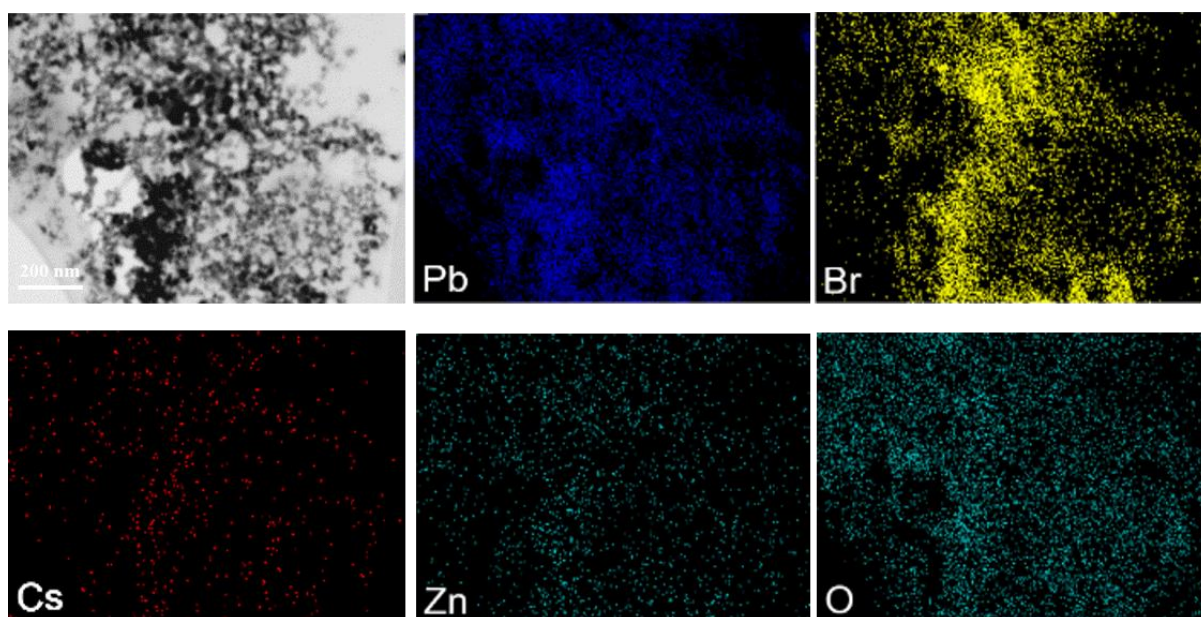


**Figure 4.3** The element mappings of ZnO NP-blended CsPbBr<sub>3</sub> QDs.

#### 4.2.2 Morphological Evolution

As mentioned, it is critical to engineer the surface morphology for high-performance photodetectors. After introducing a defined amount of ZnO NPs into CsPbBr<sub>3</sub> QDs, the surface morphologies of CsPbBr<sub>3</sub> QD thin films significantly improved, as shown in Figure 4.4. Evidently, pristine QD thin film is comprised of large grains (~1  $\mu\text{m}$ ), long grain boundaries and large pinholes, showing poor film coverage. Such poor surface morphology is caused by the aggregation or agglomeration of CsPbBr<sub>3</sub> QDs. In contrast, after blending an increased volume of ZnO NPs from 20  $\mu\text{L}$  to 100  $\mu\text{L}$  (the same concentration), the grains and pinholes started to shrink and reduce in number. In addition, the gradual increase in ZnO NP injection leads to a denser film and better surface coverage, particularly when 40  $\mu\text{L}$ , 60  $\mu\text{L}$ , 80  $\mu\text{L}$  and 100  $\mu\text{L}$  ZnO NPs were injected. Such enhancement of film morphology confirms the successful incorporation of CsPbBr<sub>3</sub> QDs by ZnO NPs, which is advantageous for reducing grain boundaries and facilitating carrier transfer.

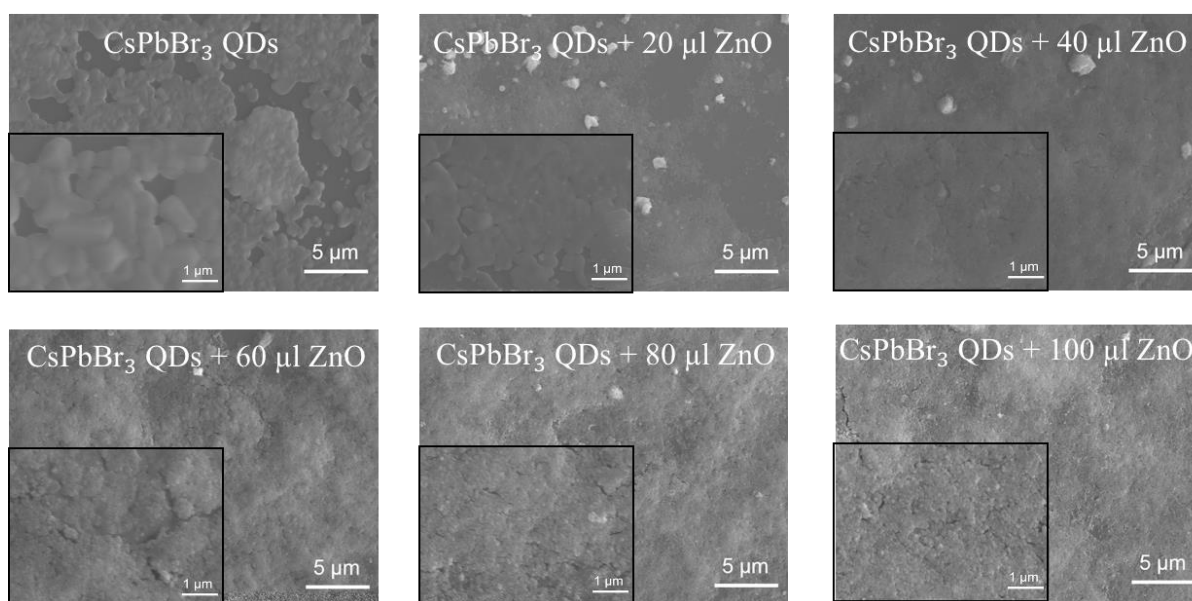


**Figure 4.4** SEM images of CsPbBr<sub>3</sub> QD thin films with increasing amount of ZnO NPs from 20  $\mu$ L to 100  $\mu$ L. Insets are the corresponding high-magnification SEM images. Samples were all deposited on the glass substrate.

The impacts of blending ZnO NPs on the surface morphology and electrical characteristics were further investigated by AFM and conductive atomic force microscopy (CAFM). Figure 4.5a shows the morphological features of thin films synthesised with 0–80  $\mu$ L ZnO NPs, respectively. It can be clearly noted that pinholes were gradually filled by ZnO NPs, resulting in much more compact thin film, which is consistent with the SEM images (Figure 4.4). In addition, the surface roughness was reduced after ZnO NP treatment, indicative of a smoother film morphology. The ZnO NP treatment-induced influences on the electrical properties of films were further evaluated by CAFM. The corresponding surface current maps are shown in Figure 4.5b. Without the inclusion of ZnO NPs, a higher current is measured in the pristine QD films. Once increasing the volume of ZnO NPs, a lower and more uniform current was observed across the scanning area, revealing a smaller leakage current across the whole surface. It is worth noting that a smaller and uniform leakage current is advantageous in photodetectors, and indicates a lower dark current.

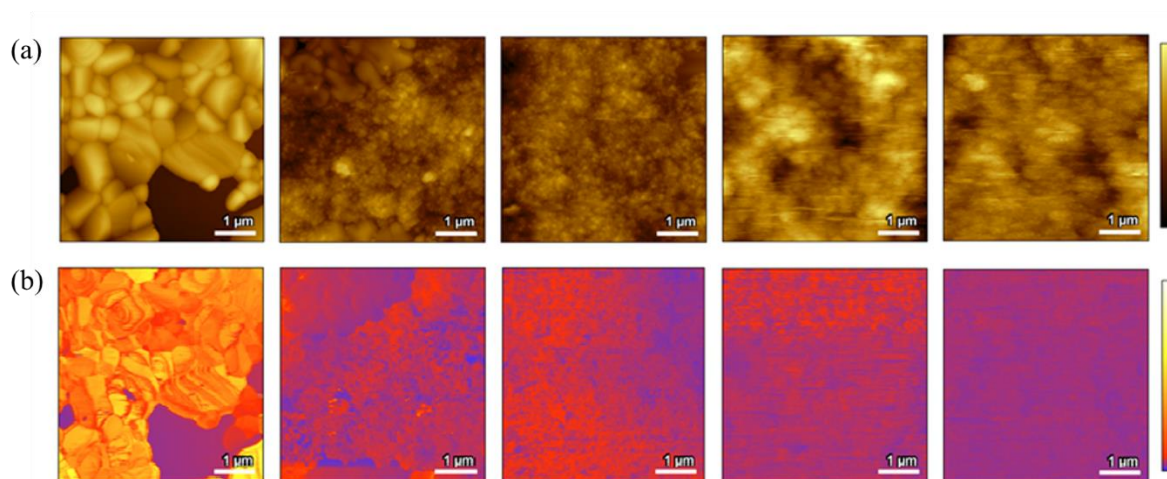


**Figure 4.5** AFM images of as-prepared CsPbBr<sub>3</sub> QD films measured under ambient condition. (a) Using soft tapping mode for measuring surface roughness. (b) Using current-sensing mode for verifying surface current. The scale bar is 1 μm. Reproduced from ref. [15] with permission from Royal Society of Chemistry, copyright 2019.

#### 4.2.3 Optical Characterisations

The optical properties of ZnO NP-assisted CsPbBr<sub>3</sub> QD films were subsequently investigated by performing UV-Vis and PL measurements. As displayed in Figure 4.6a, a sharp absorption edge located at 531 nm was observed in the pristine CsPbBr<sub>3</sub> QD thin film. Accordingly, the corresponding bandgap energy could be calculated as 2.34 eV, which is slightly larger than that of their bulk counterparts owing to the quantum size effect.<sup>[16]</sup> When starting to blend ZnO NPs from 20 μL to 100 μL, a gradual blue-shift occurred in the absorption edges from 531 nm to 521 nm. This phenomenon suggests the formation of CsPbBr<sub>3</sub> QD/ZnO NP nanocomposites, leading to a stronger quantum confinement of carriers. The PL profile of each sample is plotted in Figure 4.6b. It is clearly observed that the PL signals of all samples are symmetric and sharp, indicating high crystallinity. An evident PL peak at 526.9 nm of pristine CsPbBr<sub>3</sub> QD film was identified, as indicated in Figure 4.6c. After introducing ZnO NPs, the PL peak position started shifting to shorter wavelengths from 526.9 nm to 514 nm,

consistent with the absorption measurements. In addition, as shown in Figure 4.6d, ZnO NP-passivated CsPbBr<sub>3</sub> QD films possessed narrower FWHMs of the PL emission peak from 29.1 nm to 26.5 nm. The narrower FWHM suggests better uniformity of QDs, benefiting from the suppression of agglomerations from CsPbBr<sub>3</sub> QDs.

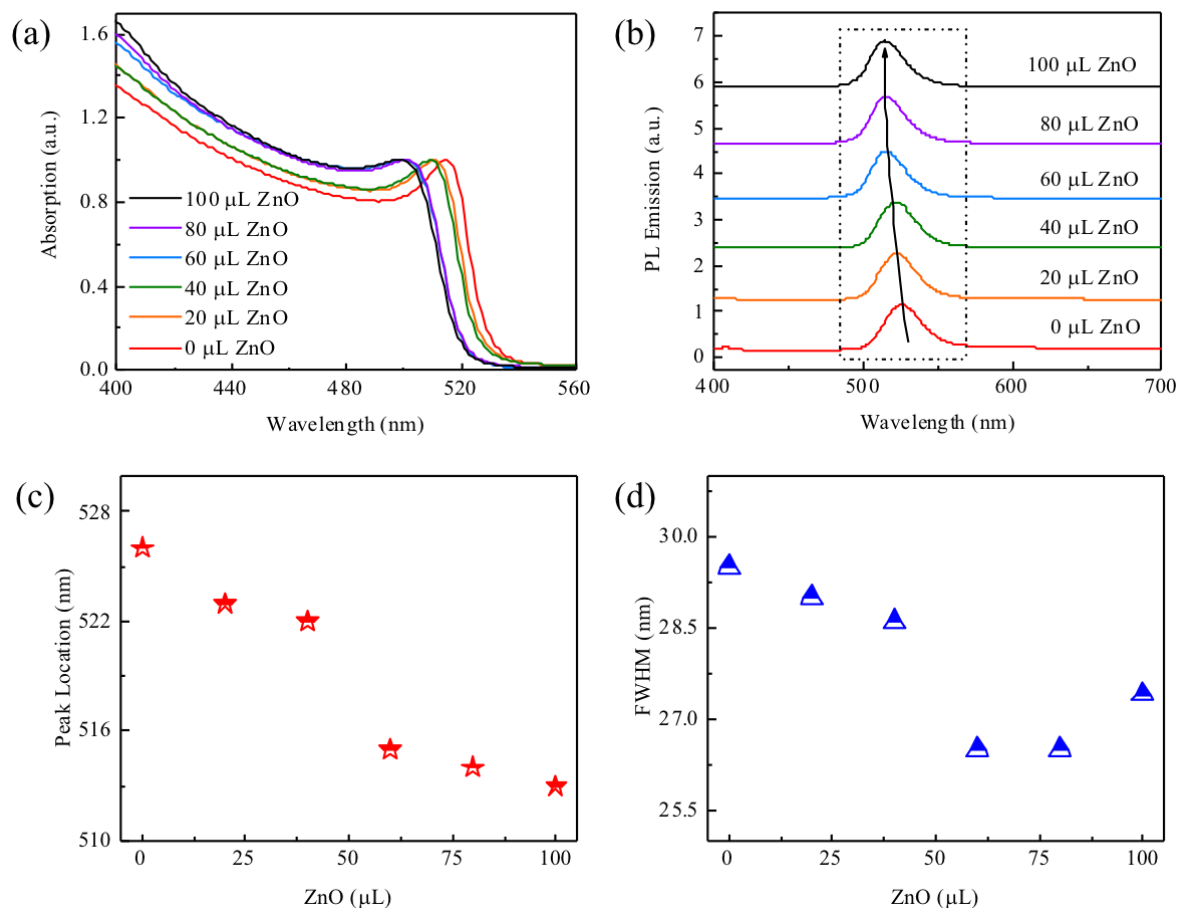


**Figure 4.6** Optical properties of ZnO NP-assisted CsPbBr<sub>3</sub> thin film with increasing amount of ZnO. (a) Steady-state absorption spectra. (b) Steady-state PL measurements. (c) The corresponding peak locations and (d) FWHMs extracted from PL spectra.

#### 4.2.4 Recombination Analysis

In order to understand the charge carrier dynamics, the TRPL spectra of CsPbBr<sub>3</sub> QDs were measured, as shown in Figure 4.7a. A three-decay-component-exponential function was applied to fit the curves. The detailed values of time constants ( $\tau_1$ ,  $\tau_2$  and  $\tau_3$ ) and their

corresponding fractions ( $f_1$ ,  $f_2$  and  $f_3$ ) are summarised in Table 4.1. It is known that a shorter lifetime is critical for fast photodetection owing to the reduced carrier trapping by surface states. Therefore, the average decay lifetimes of ZnO NP-decorated QD film were subsequently calculated as 13.431 ns, 13.921 ns, 16.530 ns, 11.006 ns, 11.536 ns and 11.724 ns, respectively, following Equation 4.1:

$$\tau_{ave} = (\tau_1 \times f_1 + \tau_2 \times f_2 + \tau_3 \times f_3) / (f_1 + f_2 + f_3) \quad \text{Equation 4.1}$$

In addition to the carrier lifetimes, the decay components and their ratios are also important to clearly understand the carrier dynamics of modified QDs. These are plotted in Figure 4.7b and 4.7c, respectively. It can be observed that the fastest decay constant ( $\tau_1$ ) and its fraction barely changed. This decay time could be ascribed to the non-radiative recombination. As the fraction of this decay is the lowest, it again reveals the high crystal quality of the CsPbBr<sub>3</sub> QDs. However, the time constants  $\tau_2$  and  $\tau_3$  have a distinct dependence on the amount of ZnO NP blending. The former,  $\tau_2$  (1 ~ 2 ns), is most likely associated with typical radiative recombination.<sup>[17]</sup> It is worth noting that the increase of ZnO NPs (>40  $\mu$ L) leads to an increase in  $\tau_2$  but relatively low ratio of radiative combination. This is mainly because electrons transfer from CsPbBr<sub>3</sub> QDs to ZnO NPs due to type-II CsPbBr<sub>3</sub>/ZnO band alignment. The slow decay component,  $\tau_3$  (over 10 ns), could be assigned to the band edge trap state-assisted processes. A reduction of  $\tau_3$  and  $f_3$  of surface trap state-related decay was observed as the amount of ZnO NPs exceeded 40  $\mu$ L. Accordingly, the radiative recombination was improved, suggesting positive surface passivation of CsPbBr<sub>3</sub> QD films by ZnO NPs.

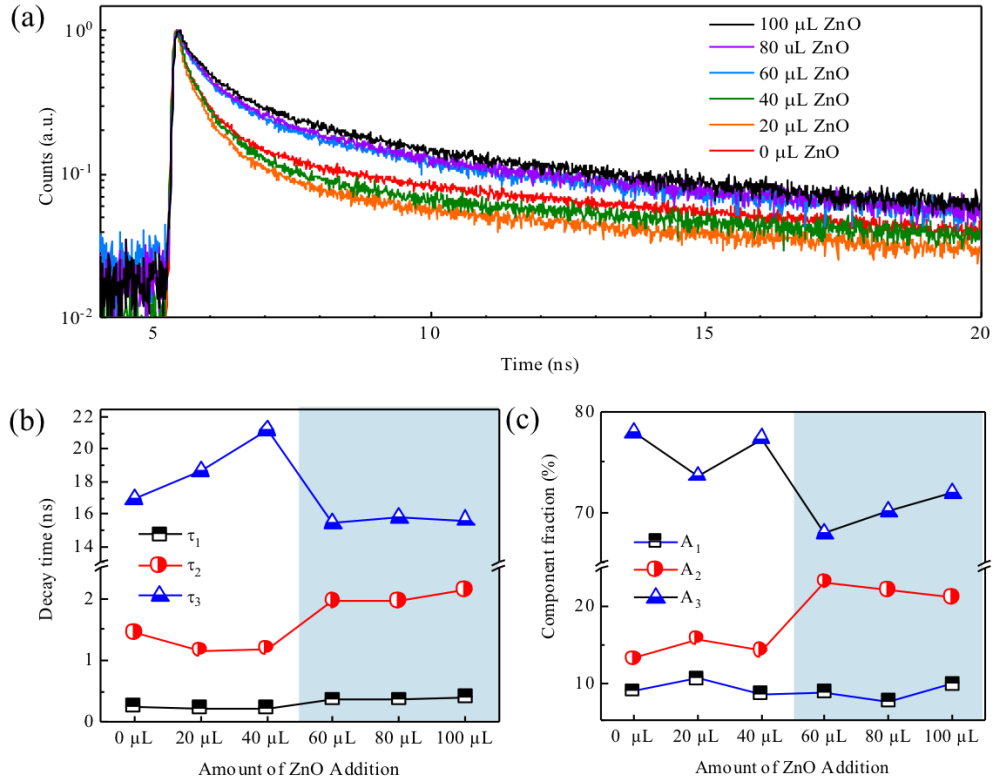


**Figure 4.7** (a) TRPL spectra of QDs with ZnO NP decoration. (b) The corresponding decay time and (c) decay component fractions extracted from TRPL as a function of amount of ZnO addition.

**Table 4.1** The values of decay components and fractions obtained by fitting with decay function.

Samples	$\tau_1$ (ns)	$\tau_2$ (ns)	$\tau_3$ (ns)	$f_1$ (%)	$f_2$ (%)	$f_3$ (%)	$\tau_{\text{average}}$ (ns)
Pristine	0.256	1.449	16.955	8.89	13.151	77.96	13.43
20 $\mu\text{L}$	0.229	1.168	18.623	10.561	15.809	73.63	13.92
40 $\mu\text{L}$	0.224	1.197	21.142	8.513	14.196	77.291	16.53
60 $\mu\text{L}$	0.368	1.972	15.462	8.731	23.263	68.006	11.01
80 $\mu\text{L}$	0.365	1.962	15.782	7.578	22.27	70.153	11.54
100 $\mu\text{L}$	0.408	2.140	15.607	9.809	21.242	71.949	11.72

Overall, use of the ZnO NP passivation strategy created an improved surface morphology and higher crystal quality with fewer trap states. It not only balanced charges on the surface of the QD film and improved the carrier transport, but also passivated trap states

that are inaccessible to much larger organic ligands. These results show a huge potential in low-cost and solution-processed optoelectronics.

### 4.3 Device Performance

As comprehensively investigated above, CsPbBr<sub>3</sub> QD film is improved by embedding ZnO NPs, especially when blending 60  $\mu$ L ZnO NPs. Therefore, optimised CsPbBr<sub>3</sub> QD nanocomposite-based photodetectors were fabricated to further verify the positive impact of blending ZnO NPs. The device configuration is illustrated in Figure 4.8a; we employed quartz as the substrate, glassy graphene ( $\sim 0.7$  nm) as the transparent electrode, QD nanocomposites (150 nm – 200 nm) as the active layer, and Ni/Au (10 nm / 100 nm) as contact pads. It is worth noting that glassy graphene thin film has been proven to have good chemical and thermal inertness, excellent conductivity and flexibility.<sup>[18]</sup> Meanwhile, ultrathin glassy-graphene possessed a high transmittance ( $>90\%$ ) that avoids extra light losses, and also enables a much thinner device compared with ITO based devices. The overview of as-fabricated photodetectors were shown in Figure 4.8b. The detailed fabrication procedures are described in Chapter 3.

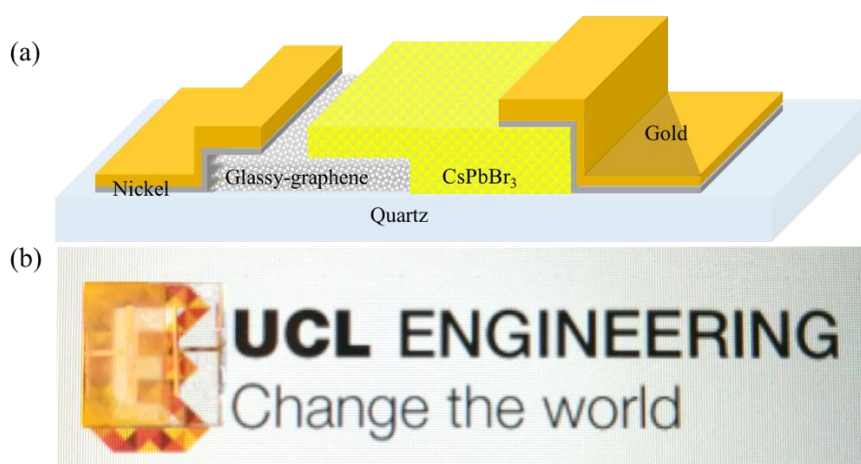


**Figure 4.8** (a) Schematic device configuration. (b) Digital photograph of as-fabricated photodetector. Reproduced from ref. [15] with permission from Royal Society of Chemistry, copyright 2020.

## 4.4 Device Characterisations

### 4.4.1 Performance Evolution

In this work, two devices were studied. One is based on 60  $\mu\text{L}$  ZnO NP-treated QDs (PGH\_1) and the other is based on pristine QDs (PGH\_2). The  $I$ - $V$  curves of both photodetectors are presented in Figure 4.9. Both were measured in the absence of light, and under illumination with white light, 405 nm and 520 nm laser diodes, respectively. Both devices exhibited a clear photoresponse, suggesting efficient carrier transfer between CsPbBr<sub>3</sub> QDs and glassy graphene thin film. When increasing the incident photon energy, the generated current obviously increased in both devices, indicating the wavelength selectivity. This is consistent with the bandgap information obtained from UV-Vis and PL spectra. In contrast to PGH\_2, PGH\_1 exhibited a linear photoresponse, which implies good ohmic contact and more efficient carrier transport. In addition, it is clearly seen that there is an intersection with the  $x$ -axis when the PGH\_1 photodetector was under light excitation, as shown in Figure 4.9b. Such an intersection can be assigned to the open-circuit voltage, which is measured as 150 mV, indicating the self-powered characteristic of the PGH\_1 device. However, this phenomenon was not observed in the PGH\_2 photodetector, which can be attributed to the built-in electric field generated by ZnO NPs and CsPbBr<sub>3</sub> QDs.

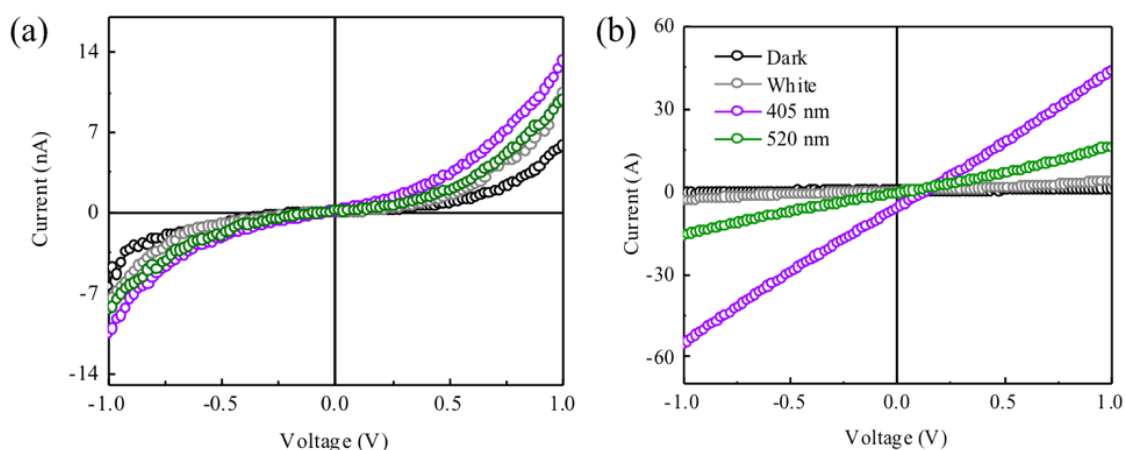


**Figure 4.9** Typical  $I$ - $V$  curves of (a) PGH\_2 and (b) PGH\_1 in dark and illuminated by white light, 405 nm and 520 nm laser diodes.

Although both photodetectors showed a good photoresponse, it is obvious that PGH\_1 possessed better light-converting ability than PGH\_2. The dark current and photocurrent of both devices were subsequently extracted from Figure 4.9 to be compared, as shown in Figure 4.10a. It is clear that PGH\_1 delivered a much higher photocurrent of  $\sim 55$  nA, while PGH\_2 only exhibited a low photocurrent of  $\sim 11$  nA, showing a five-fold improvement in photocurrent. On the other hand, the dark current measured in PGH\_1 was  $\sim 0.8$  nA, which is ten times lower than that of PGH\_2 ( $\sim 8$  nA).

Responsivity ( $R$ ), as one of the key parameters, was calculated and is plotted in Figure 4.10b. Under the same condition, it is clearly seen that the PGH\_1 photodetector possessed a higher responsivity than PGH\_2, with one order of magnitude enhancement. Specifically, with the illumination of 405 nm and 520 nm lasers, the largest  $R$  achieved in PGH\_1 was  $0.4 \text{ mA W}^{-1}$  and  $0.03 \text{ mA W}^{-1}$ , respectively, under 1 V bias. The lower response at 520 nm is due to the lower absorption of photons with energy close to the band edge (Figure 4.6a). These comparisons not only indicate a lower density of trap states in the perovskite after ZnO NP treatment, but also efficient interfacial charge transfer that lowers the carrier concentration in the depletion region.

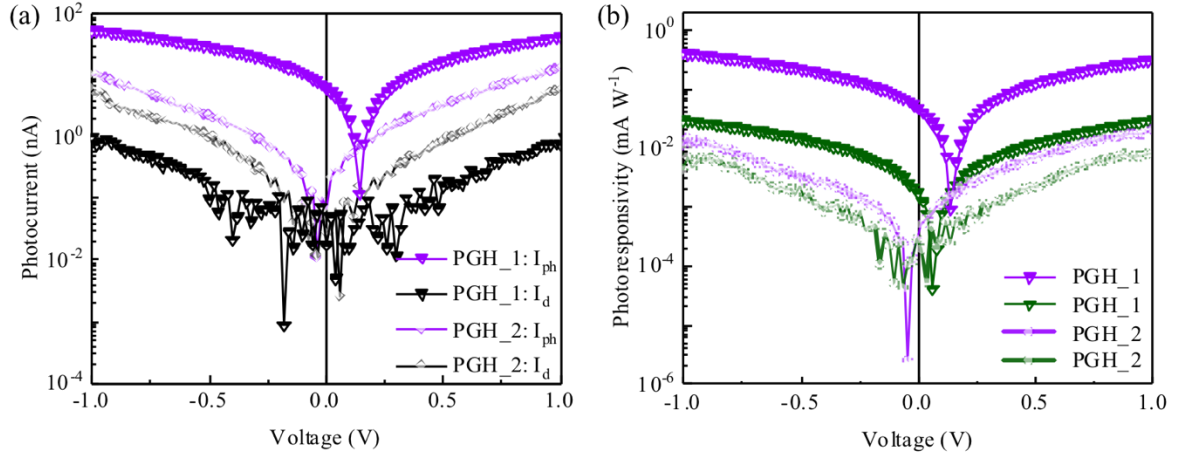


**Figure 4.10** (a) The current comparison between PGH\_1 and PGH\_2 photodetectors. (b) Their corresponding responsivity under violet and green light.

The response speed is another key figure of merit, which determines the speed of the photodetectors' response to the light source. By performing time-dependent measurements, the  $\tau_{\text{rise}}$  and  $\tau_{\text{fall}}$  of PGH\_1 can be measured as  $<76.5$  ms and  $<73.5$  ms, respectively, as plotted in Figure 4.11. Meanwhile, the pristine device possessed a  $\tau_{\text{rise}}$  of  $>76.8$  ms and a  $\tau_{\text{fall}}$  of  $\sim 188$  ms, which are both slightly longer than the values of ZnO NP-decorated devices. As a result, the improved photoresponse and response speed again confirm the superiorities of the novel NP-assisted scheme.

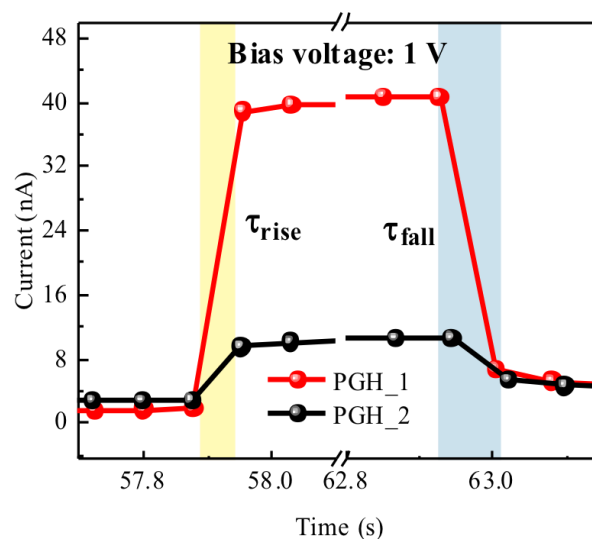


**Figure 4.11** The response time of PGH\_1 and PGH\_2 under 405 nm laser illumination with an applied bias of 1 V.

#### 4.4.2 Mechanism

The enhanced photoresponsive behaviour can be explained by Figure 4.12. Without decoration, CsPbBr<sub>3</sub> QDs are easily aggregated or agglomerated, leading to a rough surface with a large number of pinholes. These pinholes introduce a negative impact on the carrier transport and collection. Moreover, a high leakage current can be deduced in the defective thin film, as confirmed in CAFM measurement (Figure 4.5b). Both of them resulted in a lower photocurrent in the pristine QD photodetector, as supported by the  $I$ - $V$  characteristics in Figure 4.9. In contrast, the serious aggregation of QDs was effectively reduced after introducing ZnO NPs in the CsPbBr<sub>3</sub> QDs, and further promoted the formation of a much smoother and denser film. Owing to this improved surface morphology, the generated charge carriers are efficiently transported and collected by electrodes. The ZnO NPs enable a passivation function and act as bridges between QDs. Accordingly, the ZnO NP-assisted photodetectors were able to deliver a higher photocurrent while maintaining a low level of dark current.

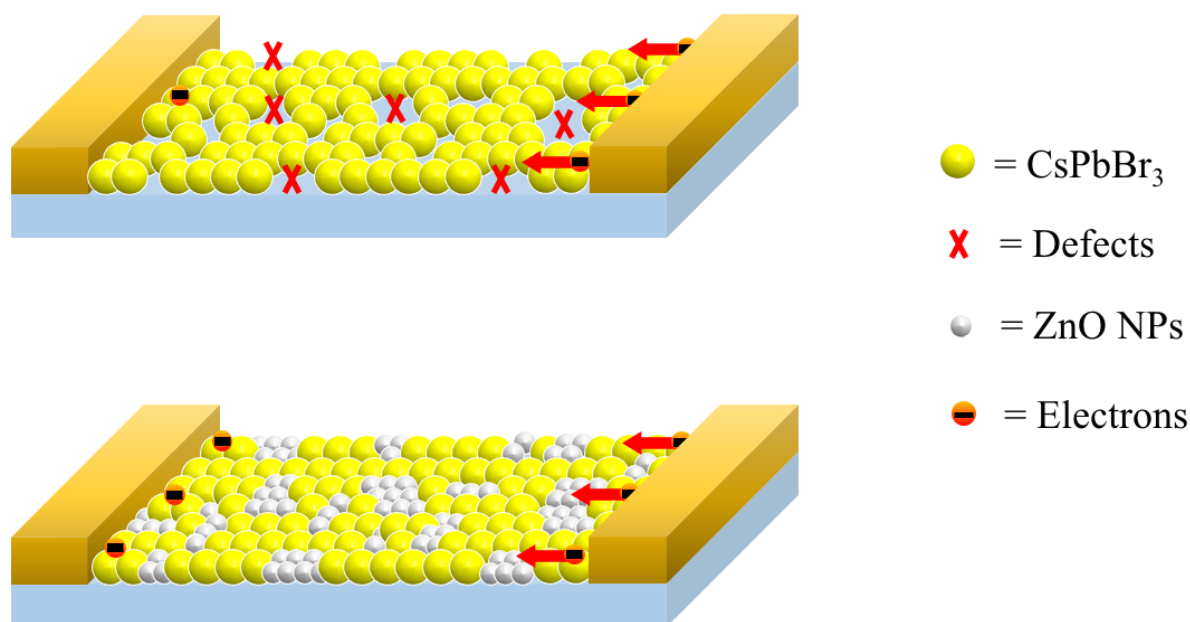


**Figure 4.12** Schematic illustration of impact of decorating ZnO NPs on photodetectors. Reproduced from ref. [15] with permission from Royal Society of Chemistry, copyright 2019.

#### 4.4.3 Photoresponse of ZnO NPs Decorated QDs Photodetector

The photoresponsive dynamics of the 60  $\mu\text{L}$  ZnO NP-decorated QD photodetector (PGH\_1) were further explored. A typical  $I$ - $V$  curve as a function of light intensity was examined under 405 nm laser illumination, as shown in Figure 4.13a. The PGH\_1 photodetector exhibited an apparent intensity dependence, with the photocurrent improved from  $\sim 10$  nA to  $\sim 40$  nA when gradually increasing the intensity from  $1.3 \text{ mW cm}^{-2}$  to  $22.8 \text{ mW cm}^{-2}$ . This increased photocurrent originated from the larger population of photogenerated carriers. Moreover, the corresponding time-resolved photoresponse is measured in Figure 4.13b. It is clear that PGH\_1 exhibited a sensitive and reproducible photoresponse while varying the incident light intensity.

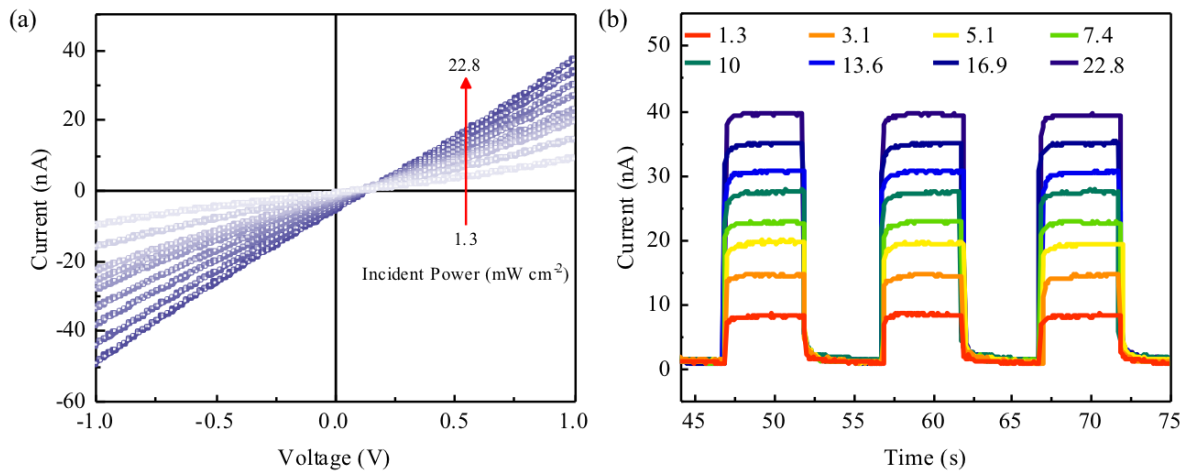


**Figure 4.13** (a)  $I$ - $V$  curves and (b)  $I$ - $t$  curves of the photodetectors excited by a 405 nm laser as a function of the light intensity.

Figure 4.14 shows the light intensity-dependent photocurrent, which was fitted by the power law. The power law can be expressed as  $I_p \propto P^\beta$ , where  $I_p$  represents the photocurrent and  $\beta$  is the exponent. Notably, the exponent is related to the carrier generation and recombination process. It can be seen that the best fitting curve suggests a non-linear behaviour of  $\beta = 0.502$ , implying the existence of recombination centres in the crystals.<sup>[19,20]</sup>

As stated before (Figure 4.7), the non-radiative recombination time constant,  $\tau_1$ , barely changed after adding ZnO NPs, and requires further optimisation of QD synthesis.

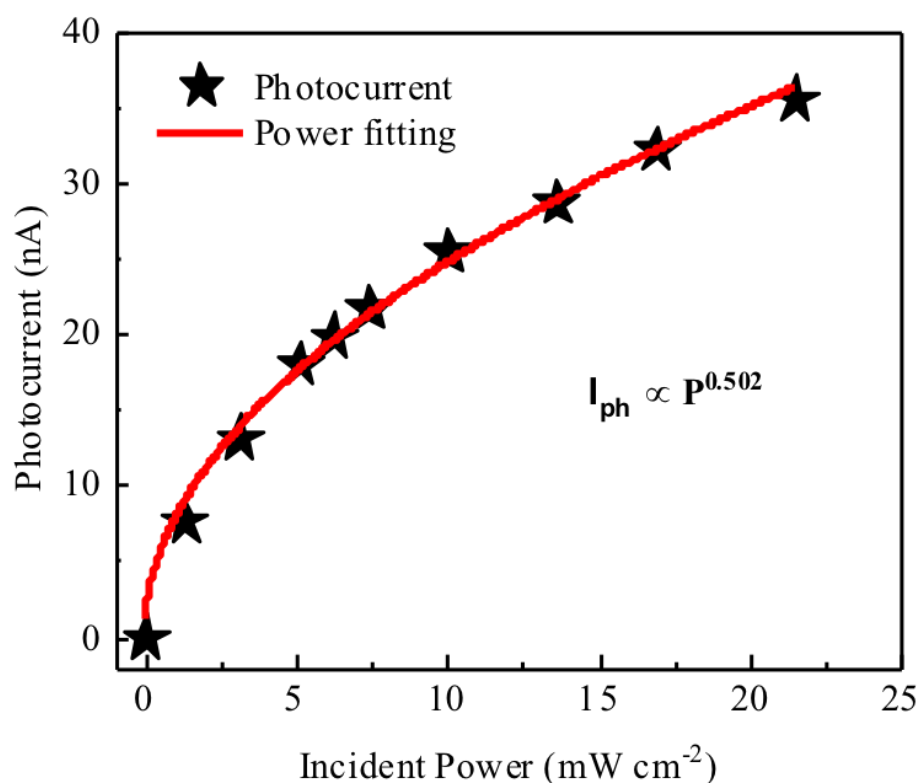


**Figure 4.14** The fitted intensity-dependent photocurrent.

The photoresponse of the PGH\_1 photodetector was measured with 405 nm and 520 nm light excitation under a -1 V and 1 V bias, respectively (Figure 4.15a). Owing to the built-in electric field, the photocurrent obtained at -1 V was higher than that at 1 V, showing an increment of 18 nA. It is worth noting that the PGH\_1 photodetector additionally exhibited an obvious response without external power supply, as shown in Figure 4.15b. Such self-powered characteristic is due to the built-in electric field generated by the ZnO NP / CsPbBr<sub>3</sub> QD heterostructure. The response time was subsequently determined with and without applied bias. As shown in Figure 4.15c,  $\tau_{\text{rise}}$  and  $\tau_{\text{fall}}$  were measured as <76.5 ms and 73.5 ms at a bias voltage of 1 V, respectively, indicating fast carrier separation and efficient charge transport. Notably, this response time is shorter than that in the PGH\_2 device, again confirming the benefits of

ZnO NP passivation. Compared to previous work, the response speed of ZnO NP-blended CsPbBr<sub>3</sub> QDs is much faster than that of photodetectors with similar material systems and architectures.<sup>[21–23]</sup> The fast response speed also implies excellent light-switching properties of PGH\_1 photodetectors. Under self-powered operation mode (Figure 4.15d),  $\tau_{\text{fall}}$  barely changed while  $\tau_{\text{rise}}$  was slightly longer, which can be attributed to the built-in electric field not being strong enough to collect the electrons and holes efficiently.

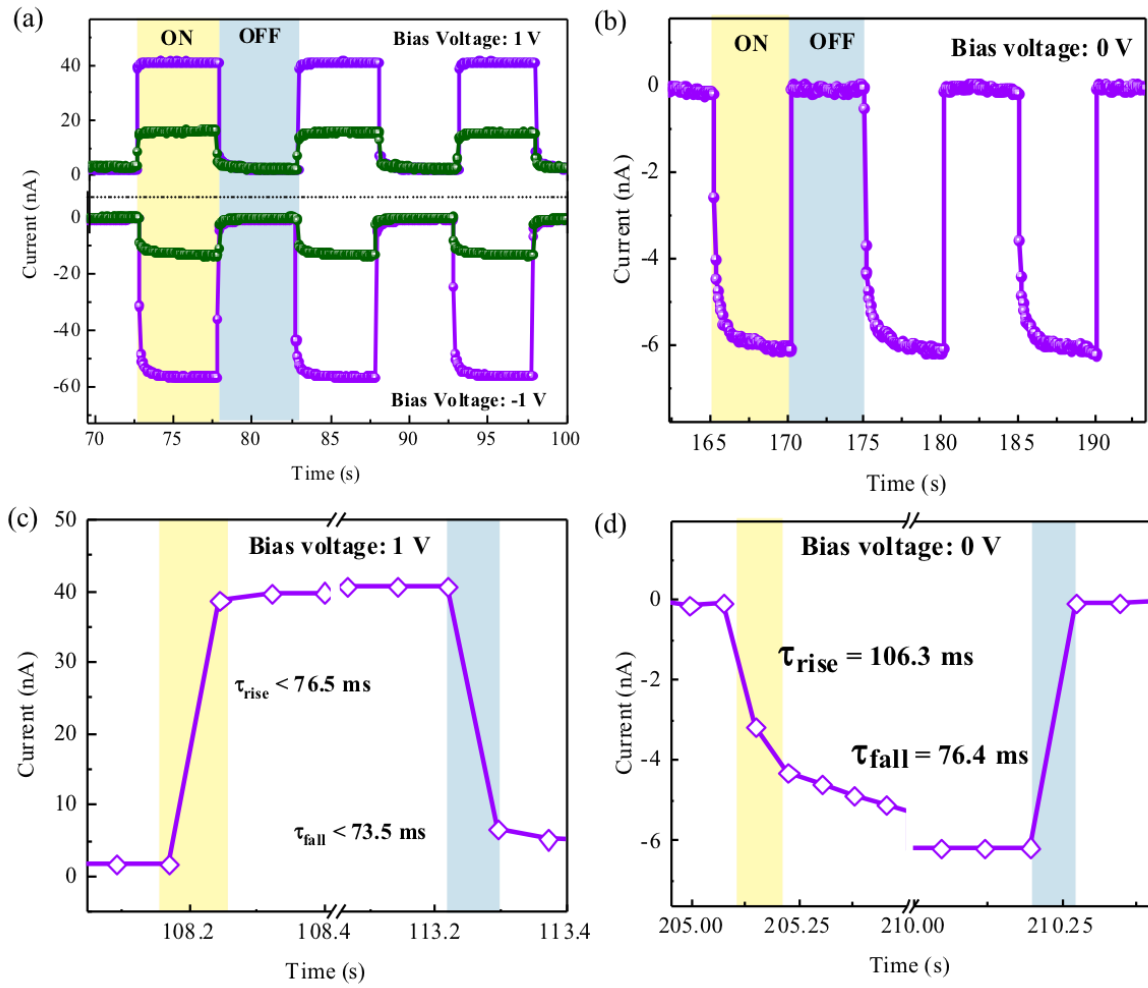


**Figure 4.15** (a) The  $I$ - $t$  curves of PGH\_1 photodetector employing 405 nm and 520 nm lasers as light source ( $22.8 \text{ mW cm}^{-2}$ ) at 1 V and -1 V, respectively. (b) The time-resolved photocurrent of PGH\_1 device under self-powered mode. The corresponding rise and fall time under (c) 1 V and (d) 0 V bias.

#### 4.4.4 Stability

The stability of perovskite-based optoelectronics is a key challenge for practical applications. In order to perform stability tests, the photoresponse measurements of ZnO NP-decorated QD photodetectors were recorded, as shown in Figure 4.16a. Notably, the as-fabricated photodetectors were stored under ambient conditions for 7 months, with no encapsulation or gas protection. There is a small variation in both dark current and photocurrent, but they remain at a similar level. The dark current varied between 0.8 nA and 4.8 nA, and the photocurrent maintained its initial value with negligible degradation after storing for 7 months. Moreover, as shown in Figure 4.16b, the PGH\_1 device still exhibited good reproducibility without sacrificing the response speed, indicating an outstanding stability. Benefiting from the efficient treatment of ZnO NPs, the stability of this device is much better than that shown in other reported works.<sup>[24–27]</sup> The corresponding device performance was summarised in Table 4.2

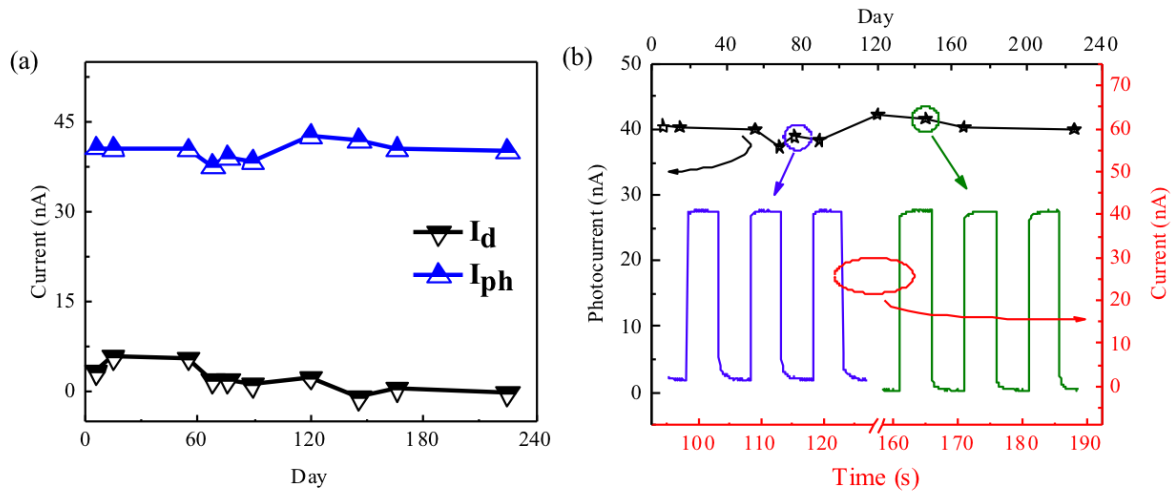


**Figure 4.16** (a) Stability test of PGH\_1 device over 7 months. (b) Time-resolved current in the middle of the stability test.

**Table 4.2** Summarised device performance of metal halide perovskite based photodetectors reported in recent works.

Active Materials	$\tau_{\text{rise}}$ (ms)	$\tau_{\text{fall}}$ (ms)	Stability
$\text{CH}_3\text{NH}_3\text{PbI}_3^{[21]}$	6170	4500	200 hour
$\text{CsPbBr}_3 : \text{ZnO}^{[22]}$	> 8000	> 10000	-
$\text{CsPbBr}_3^{[23]}$	300	5000	-
$\text{CH}_3\text{NH}_3\text{PbI}_3^{[24]}$	1200	200	2 week
$\text{CsPbBr}_3^{[25]}$	0.062	0.062	> 2000 hour
$\text{CH}_3\text{NH}_3\text{PbI}_3^{[26]}$	340	590	> 1 hour
$\text{CH}_3\text{NH}_3\text{PbI}_3 \text{ NWs}^{[27]}$	0.3	0.4	4 week
$\text{CsPbBr}_3 : \text{ZnO}$ (this work)	76	73	7 month

## 4.5 Summary

In conclusion, ZnO NPs were employed to decorate  $\text{CsPbBr}_3$  QDs via a facile non-vacuum synthesis method. The introduction of ZnO NPs was confirmed with an improved surface morphology with fewer defects, as well as enhanced optical properties. Photodetectors based on optimised QDs were subsequently fabricated. Benefiting from the above improvements, the as-fabricated devices exhibited an excellent photoresponse, including good switching behaviour, fast response speed and self-powered characteristic with a large open-circuit voltage of 150 mV. Most importantly, an impressive device stability and photoresponse with negligible degradation were achieved over 7 months, paving the way for future industrialisation of perovskite optoelectronics.

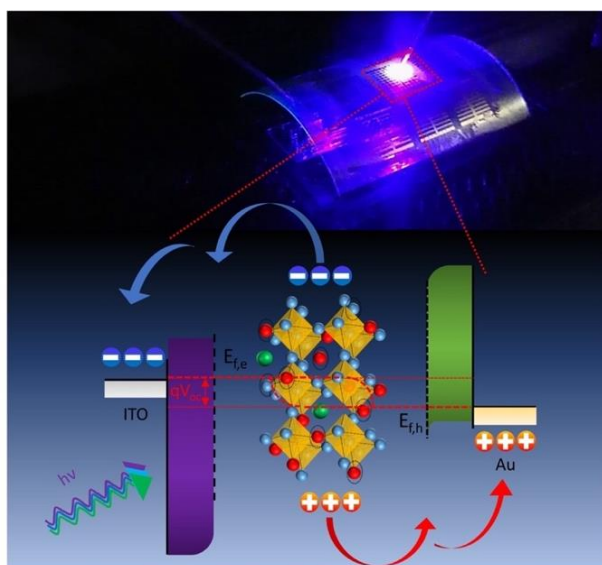
## 4.6 References

- [1] C. C. Stoumpos, C. D. Malliakas, J. A. Peters, Z. Liu, M. Sebastian, J. Im, T. C. Chasapis, A. C. Wibowo, D. Y. Chung, A. J. Freeman, B. W. Wessels, M. G. Kanatzidis, *Cryst. Growth Des.* **2013**, *13*, 2722.
- [2] L. Protesescu, S. Yakunin, M. I. Bodnarchuk, F. Krieg, R. Caputo, C. H. Hendon, R. X. Yang, A. Walsh, M. V. Kovalenko, *Nano Lett.* **2015**, *15*, 3692.
- [3] Z. Yang, M. Wang, J. Li, J. Dou, H. Qiu, J. Shao, *ACS Appl. Mater. Interfaces* **2018**, *10*, 26387.
- [4] J. Song, J. Li, X. Li, L. Xu, Y. Dong, H. Zeng, *Adv. Mater.* **2015**, *27*, 7162.
- [5] J. Song, J. Li, L. Xu, J. Li, F. Zhang, B. Han, Q. Shan, H. Zeng, *Adv. Mater.* **2018**, *30*, 1800764.
- [6] X. Zhang, Q. Wang, Z. Jin, J. Zhang, S. (Frank) Liu, *Nanoscale* **2017**, *9*, 6278.
- [7] M. V. Kovalenko, M. Scheele, D. V. Talapin, *Science* **2009**, *324*, 1417.
- [8] R. Wang, Y. Shang, P. Kanjanaboos, W. Zhou, Z. Ning, E. H. Sargent, *Energy Environ. Sci.* **2016**, *9*, 1130.
- [9] J. Tang, K. W. Kemp, S. Hoogland, K. S. Jeong, H. Liu, L. Levina, M. Furukawa, X. Wang, R. Debnath, D. Cha, K. W. Chou, A. Fischer, A. Amassian, J. B. Asbury, E. H. Sargent, *Nat. Mater.* **2011**, *10*, 765.
- [10] A. H. Ip, S. M. Thon, S. Hoogland, O. Voznyy, D. Zhitomirsky, R. Debnath, L. Levina, L. R. Rollny, G. H. Carey, A. Fischer, K. W. Kemp, I. J. Kramer, Z. Ning, A. J. Labelle, K. W. Chou, A. Amassian, E. H. Sargent, *Nat. Nanotechnol.* **2012**, *7*, 577.
- [11] Q. A. Akkerman, M. Gandini, F. Di Stasio, P. Rastogi, F. Palazon, G. Bertoni, J. M. Ball, M. Prato, A. Petrozza, L. Manna, *Nat. Energy* **2017**, *2*, 16194.
- [12] X. Zhang, Z. Jin, J. Zhang, D. Bai, H. Bian, K. Wang, J. Sun, Q. Wang, S. F. Liu, *ACS Appl. Mater. Interfaces* **2018**, *10*, 7145.

- [13] Z. Zhang, Y. Zhu, W. Wang, W. Zheng, R. Lin, F. Huang, *J. Mater. Chem. C* **2018**, *6*, 446.
- [14] J. Li, H. Zhang, S. Wang, D. Long, M. Li, Y. Guo, Z. Zhong, K. Wu, D. Wang, T. Zhang, *RSC Adv.* **2017**, *7*, 54002.
- [15] K. Shen, X. Li, H. Xu, M. Wang, X. Dai, J. Guo, T. Zhang, S. Li, G. Zou, K. Choy, I. P. Parkin, Z. Guo, H. Liu, J. Wu, *J. Mater. Chem. A* **2019**, *7*, 6134.
- [16] J. A. Sichert, Y. Tong, N. Mutz, M. Vollmer, S. Fischer, K. Z. Milowska, R. García Cortadella, B. Nickel, C. Cardenas-Daw, J. K. Stolarczyk, A. S. Urban, J. Feldmann, *Nano Lett.* **2015**, *15*, 6521.
- [17] K. Wei, Z. Xu, R. Chen, X. Zheng, X. Cheng, T. Jiang, *Opt. Lett.* **2016**, *41*, 3821.
- [18] X. Dai, J. Wu, Z. Qian, H. Wang, J. Jian, Y. Cao, M. H. Rummeli, Q. Yi, H. Liu, G. Zou, *Sci. Adv.* **2016**, *2*, 1.
- [19] Y. Li, Z. F. Shi, S. Li, L. Z. Lei, H. F. Ji, D. Wu, T. T. Xu, Y. T. Tian, X. J. Li, *J. Mater. Chem. C* **2017**, *5*, 8355.
- [20] S.-C. Kung, W. E. van der Veer, F. Yang, K. C. Donovan, R. M. Penner, *Nano Lett.* **2010**, *10*, 1481.
- [21] D. H. Kang, S. R. Pae, J. Shim, G. Yoo, J. Jeon, J. W. Leem, J. S. Yu, S. Lee, B. Shin, J. H. Park, *Adv. Mater.* **2016**, *28*, 7799.
- [22] L. Zhou, K. Yu, F. Yang, J. Zheng, Y. Zuo, C. Li, B. Cheng, Q. Wang, *Dalt. Trans.* **2017**, *46*, 1766.
- [23] J. H. Cha, J. H. Han, W. Yin, C. Park, Y. Park, T. K. Ahn, J. H. Cho, D. Y. Jung, *J. Phys. Chem. Lett.* **2017**, *8*, 565.
- [24] H. Lu, W. Tian, F. Cao, Y. Ma, B. Gu, L. Li, *Adv. Funct. Mater.* **2016**, *26*, 1296.
- [25] C. Bao, J. Yang, S. Bai, W. Xu, Z. Yan, Q. Xu, J. Liu, W. Zhang, F. Gao, *Adv. Mater.* **2018**, *30*, 1803422.

- [26] H. Zhou, J. Mei, M. Xue, Z. Song, H. Wang, *J. Phys. Chem. C* **2017**, *121*, 21541.
- [27] H. Deng, X. Yang, D. Dong, B. Li, D. Yang, S. Yuan, K. Qiao, Y.-B. Cheng, J. Tang, H. Song, *Nano Lett.* **2015**, *15*, 7963.

# CHAPTER 5. THE STUDY OF FLEXIBLE AND SELF-POWERED ALL-INORGANIC CsPbBr<sub>3</sub> QDs PHOTODETECTOR ARRAYS



## 5.1 Introduction

With the rapid development of the "Internet of Things" (IoT), the demand for wearable electronics is ever-increasing. Accordingly, as one type of fundamental wearable electronics, flexible optoelectronics, including solar cells (power supply), LEDs (display and lighting) and photodetectors (light sensing), have attracted great interest.<sup>[1,2]</sup> As mentioned earlier, photodetectors have been widely used in a variety of fields, and play an important role. However, these detectors are usually fabricated on rigid substrates, and are not compatible with flexible systems. In addition, their high cost of fabrication is not suitable for low-cost manufacturing. Therefore, it is highly desired to develop low-cost flexible photodetectors while maintaining their high performance.

To date, there are many materials that can be assembled on flexible substrates, such as low-dimensional semiconductors, perovskite materials, *etc.*<sup>[3–5]</sup> In addition to growing on rigid substrates, they can also be easily grown or transferred to other substrates, which is beneficial for fabricating flexible electronics. Thanks to their excellent optical and electrical characteristics, metal halide perovskites show great potential in photodetection. Moreover, owing to their solution-processed property, perovskites can be directly deposited on flexible substrates. However, the organic parts of metal halide perovskites are sensitive to moisture and oxygen, limiting the device performance and reliability.

Fortunately, all-inorganic CsPbBr<sub>3</sub> QDs, as the research focus in this thesis, are proven to have better thermal and environmental stability than hybrid perovskites. Therefore, CsPbBr<sub>3</sub> QDs are continuously employed as the absorbing layer in photodetectors. Nevertheless, as investigated in the previous chapter, pristine CsPbBr<sub>3</sub> QDs suffer from intrinsic weaknesses, such as the large number of trap states and insulating ligands. In addition, pristine QD film exhibits a poor surface morphology, which further limits efficient light detection. On the other hand, all-inorganic CsPbBr<sub>3</sub> QDs were prepared by simply mixing Cs<sup>+</sup> precursor and PbBr<sub>2</sub> precursor (Section 3.1.1). The entire chemical reaction is given in Figure 5.1. After balancing the equation, it can be seen that the Pb<sup>2+</sup> is exceeded, which would cause lead disclosure and the formation of its derivatives. Although the ZnO NP passivation strategy has confirmed benefits in improving the morphology and photoresponse, the responsivity and detectivity are not good enough to meet the requirement of commercial photodetectors. Therefore, it is essential to develop another efficient strategy to address the above issues.

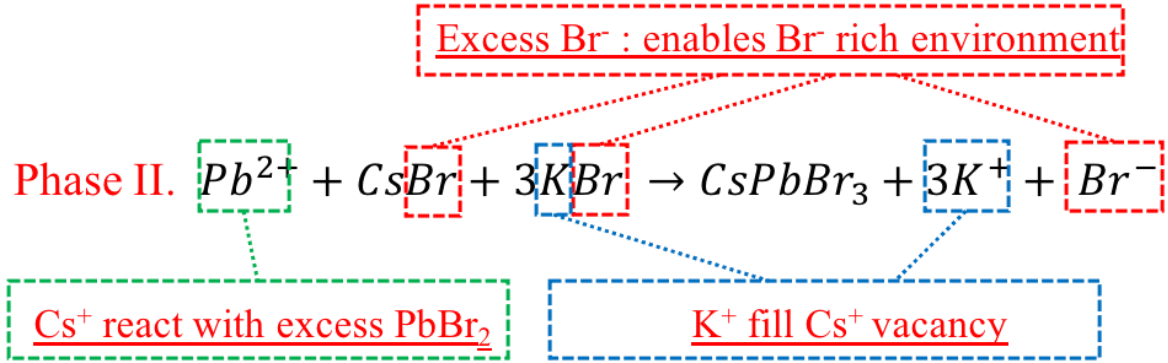
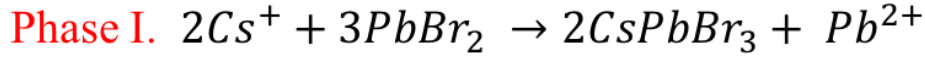


**Figure 5.1** The chemical reaction during the synthesis.

In this work, a CsBr/KBr doping strategy is firstly proposed and demonstrated to improve the material quality. As shown in Phase II, Figure 5.1, CsBr/KBr mixtures initially provide Cs<sup>+</sup> to react with excess PbBr<sub>2</sub>, eliminating the possibility of lead disclosure and the formation of other derivatives. Secondly, the mixed additives enable a Br<sup>-</sup>-rich environment, promoting the nucleation of CsPbBr<sub>3</sub> QDs. Moreover, potassium (K<sup>+</sup>) could partially fill the Cs<sup>+</sup> vacancies, and further address the non-radiative recombination issues. It is worth noting that the amount of CsBr/KBr is carefully determined. Excess additives would deteriorate the materials and device, while insufficient additives would not be effective enough. Therefore, 0.025, 0.075, 0.2 and 0.3 CsBr/KBr were used in this synthesis, where the numerical number is the molar ratio (F), which can be defined as  $F = [Cs^{+}/K^{+}] / ([Cs^{+}/K^{+}] + [Cs^{+}])$  in mol, representing [Cs<sup>+</sup>/K<sup>+</sup>] in the CsBr/KBr precursor out of the total amount of monovalent cations in the solution. Comprehensive characterisations confirm the benefits of CsBr/KBr mediation, including the improved surface morphology and crystal quality, enhanced carrier transport, boosted photoluminescence efficiency and prolonged carrier lifetime. Moreover, by adopting a sandwich configuration, the flexible photodetector arrays based on CsPbBr<sub>3</sub> QDs with the optimal fraction of CsBr/KBr exhibit an outstanding photoresponse and self-powered

characteristics, obeying the philosophy of energy saving. Furthermore, the photodetector arrays present noticeable folding endurance, uniform photoresponse and long-term stability.

## 5.2 Material Characterisations

### 5.2.1 Crystal Structure

TEM was first employed to acquire structural information and examine the crystal quality of as-synthesised CsPbBr<sub>3</sub> QDs. TEM images with different magnifications of both pristine QDs and 0.025 CsBr/KBr-assisted QDs are shown in Figure 5.2. Both the pristine and the 0.025 Cs<sup>+</sup>/K<sup>+</sup>-assisted CsPbBr<sub>3</sub> QDs are uniformly distributed in the overviews of the TEM images.

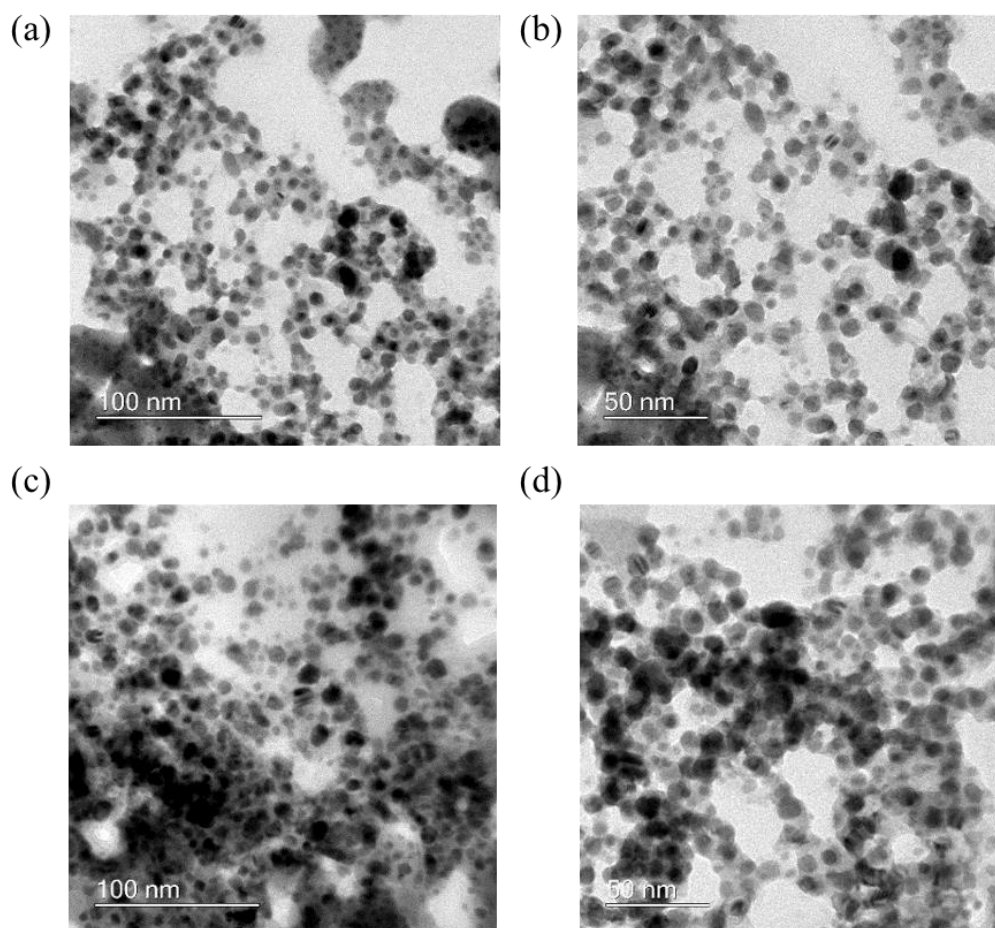


**Figure 5.2** TEM images of (a), (b) pristine CsPbBr<sub>3</sub> QDs and (c), (d) 0.025 CsBr/KBr-doped CsPbBr<sub>3</sub> QDs with different magnifications, respectively. The scale bars are 100 nm and 50 nm.

Clear lattice fringes of both QDs are observed in the corresponding high-resolution TEM images (Figure 5.3). Their lattice constants are slightly different, and can be measured as  $\sim 2.91$  Å and  $\sim 2.72$  Å, respectively, by averaging spacings in the selected areas. The origin of the reduced lattice constants can be deduced as the incorporation of CsBr/KBr additives, introducing lattice compression.

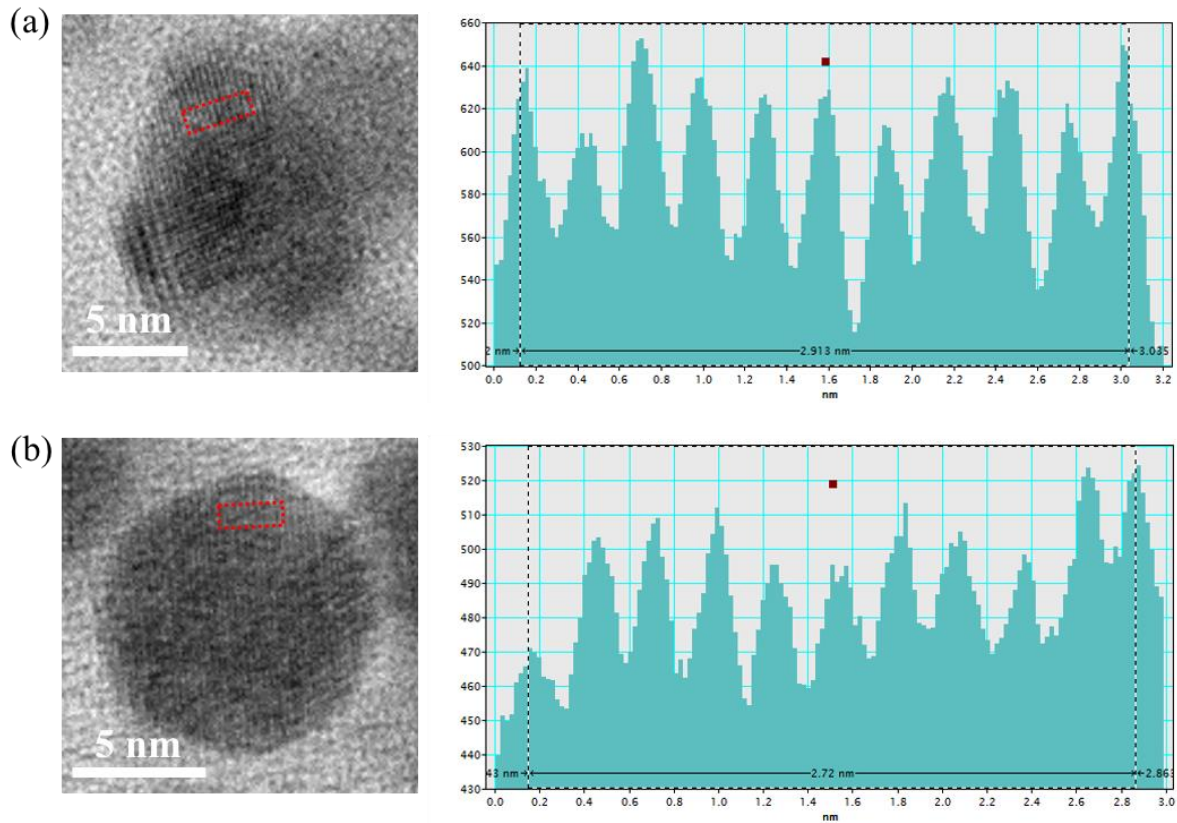


**Figure 5.3** High-resolution TEM and corresponding lattice parameters. (a) Pristine QDs, (b) 0.025 CsBr/KBr-assisted QDs.

Moreover, as shown in Figure 5.4, the average size of both QDs can be determined as 7.67 nm and 7.45 nm, respectively, by measuring the size distribution. The slightly reduced average size suggests smaller colloids after mixing with CsBr/KBr additives, which could have a certain influence on the surface morphology of samples and even the photoresponse of detectors.

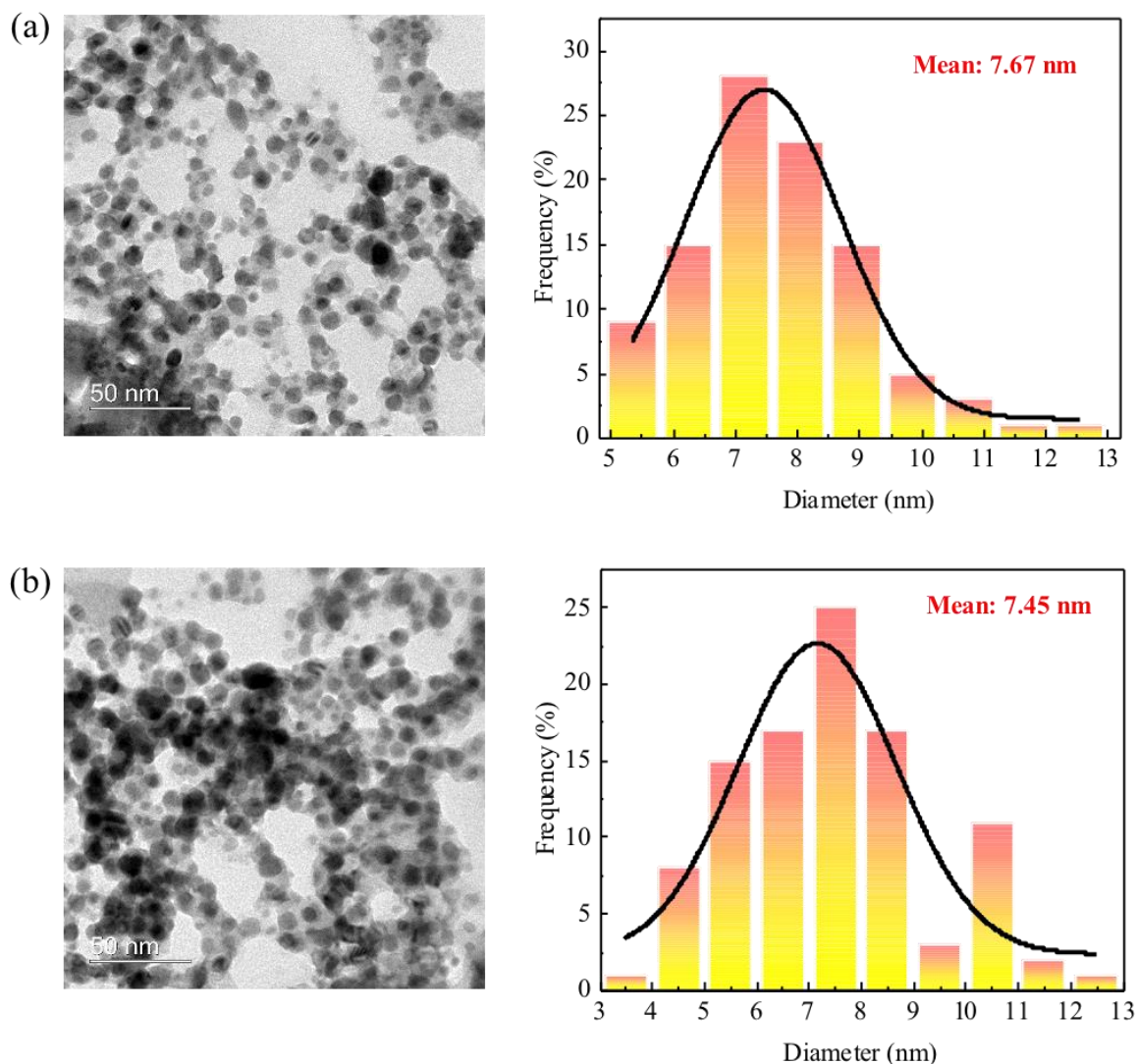


**Figure 5.4** Size distribution of (a) pristine and (b) 0.025 CsBr/KBr-treated CsPbBr<sub>3</sub> QDs.

The crystal structural features of a series of perovskite QDs were further examined by performing XRD. As shown in Figure 5.5a, all of the samples exhibited similar features after CsBr/KBr treatment, and no additional peaks were observed, implying that the introduction of CsBr/KBr would not disrupt the original crystallinity. The three characteristic peaks located at 15.0°, 21.5° and 31.1° can be assigned to the (110), (112) and (220) plane of the orthorhombic CsPbBr<sub>3</sub> structure, respectively. However, the position of the (112) peaks evidently increased from 21.475° to 21.534°, as shown in Figure 5.5b. This right shift can be attributed to the interplanar spacing transition, which further suggests reduced d-spacing with the increment of

additive blending by considering Bragg's equation ( $2d\sin\theta = n\lambda$ ).<sup>[6]</sup> This phenomenon is consistent with TEM results.

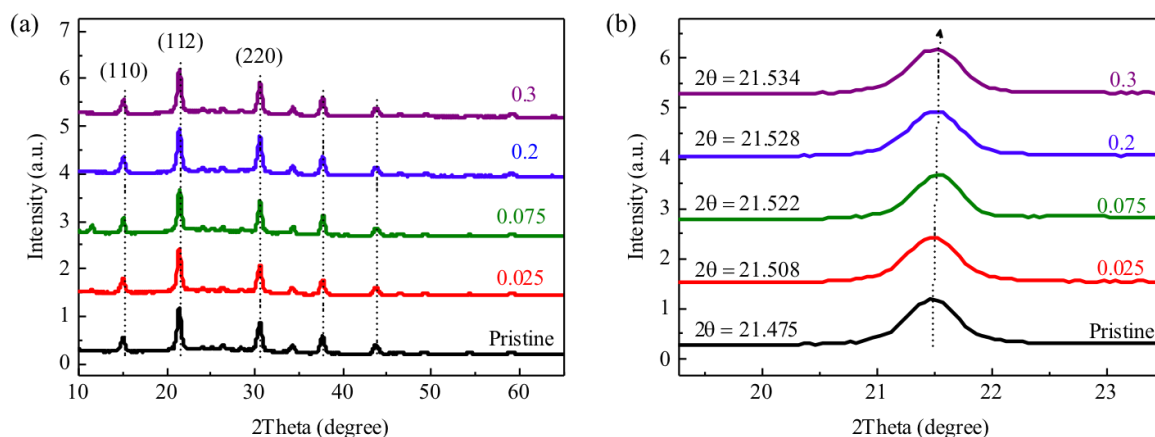


**Figure 5.5** (a) XRD measurements with different ratios of CsBr/KBr treatment from 0.025 to 0.3. (b) The enlarged XRD measurement results.

### 5.2.2 Element Distribution and Composition

In order to verify the presence of CsBr/KBr in the as-prepared QD films, the elemental distribution was subsequently measured by EDX, as shown in Figure 5.6. Obviously, potassium (K) was uniformly distributed where CsPbBr<sub>3</sub> QDs were located with the incorporation of Cs<sup>+</sup>/K<sup>+</sup>, indicating the successful incorporation of additives.

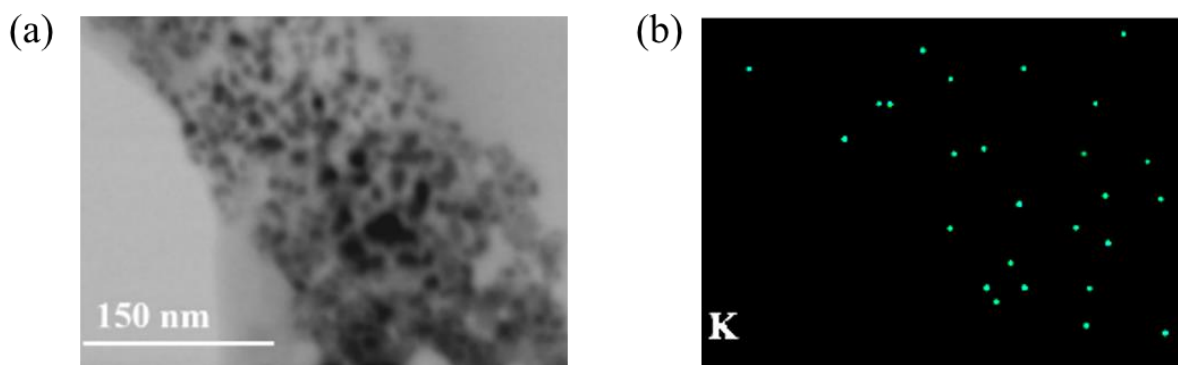


**Figure 5.6** (a) Overview of TEM image and (b) the corresponding mapping of K element.

Moreover, XPS analysis of the full spectra was subsequently performed to explore the effect of the CsBr/KBr additive strategy, as shown in Figure 5.7a. The analysis emphasises the

core levels of Cs 3d, Pb 4f, Br 3d and K 2p, with the high-resolution scans shown in Figure 5.7b–d. Notably, the peaks of Cs 3d, Pb 4f and Br 3d all initially moved to the higher binding energy when introducing CsBr/KBr at a fraction of 0.025, but to the lower binding energy when blending more additives. As investigated in previous reports, the binding energies of lead cations and halides were not changed by the slight perturbation of CsBr/KBr.<sup>[7,8]</sup> The increased binding energy, when a sufficient amount of CsBr/KBr ( $x = 0.025$ ) was added, implied a stronger interaction between Pb-Br and Cs-Br, which reasonably enables more stable crystal structures.<sup>[9–12]</sup>

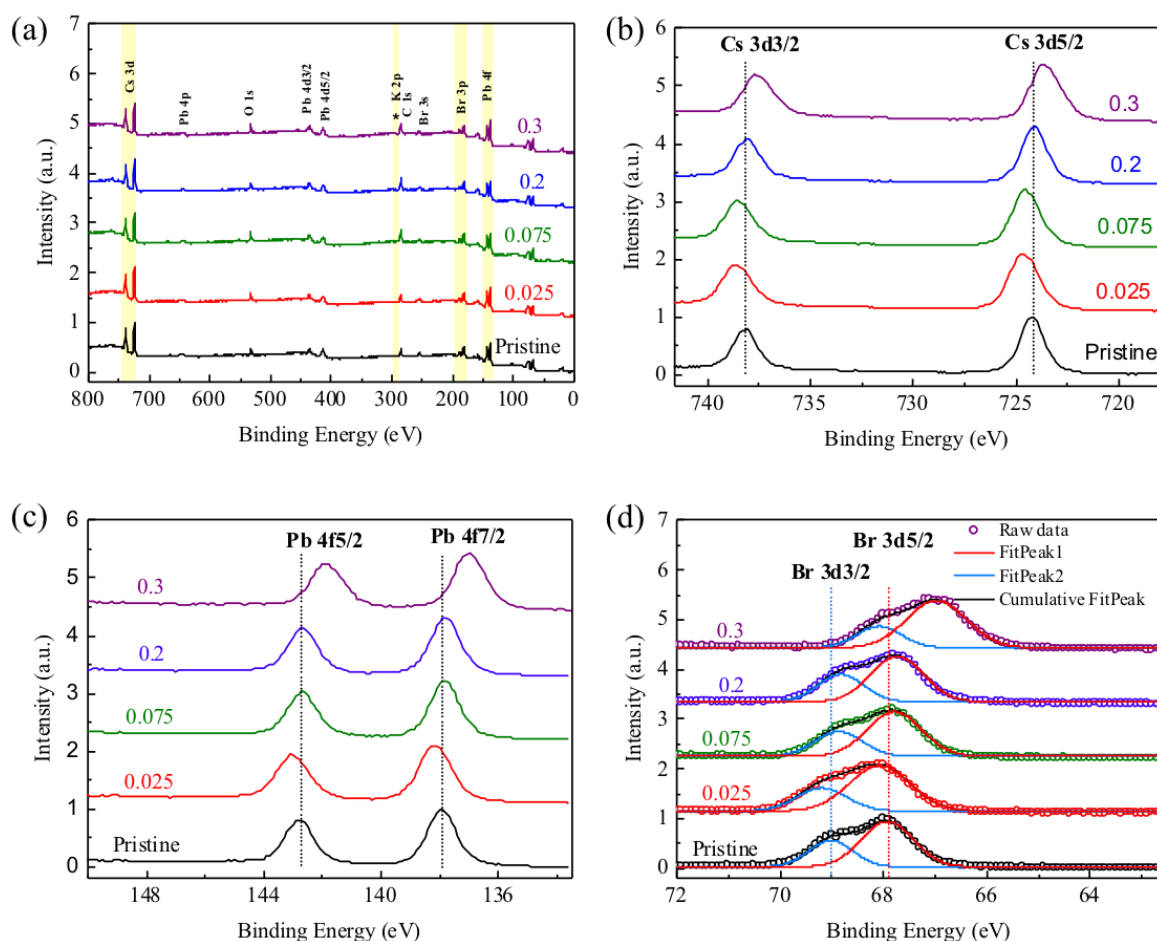


**Figure 5.7** XPS measurements of CsPbBr<sub>3</sub> QD films with different fractions of CsBr/KBr incorporation. (a) Survey spectra and high-resolved scans of the core energy level of (b) Cs 3d, (c) Pb 4f and (d) Br 3d.

Notably, there are two additional peaks clearly observed in the optimised CsPbBr<sub>3</sub> QD films compared with the pristine one, as shown in Figure 5.8. These two peaks are located at 295.8 eV and 292.8 eV, and can be assigned to the K 2p<sub>1/2</sub> and K 2p<sub>3/2</sub> states, respectively.<sup>[13]</sup> Similar to that in previously reported work, the noise of the XPS spectrum is relatively large.<sup>[8,12]</sup> Although XPS was conducted a few times to obtain a low-noise spectrum, the noise still existed. This can be attributed to the following:

- 1) The amount of injected CsBr/KBr is very small ( $K = 0.86 \mu\text{mol}$ ), and reached or even exceeded the detection resolution of our equipment (Thermo Scientific K-alpha photoelectron spectrometer).
- 2) On the other hand, the intensity of C 1s was very high, which can unavoidably level up the overall background noise. Accordingly, given that the signal of the K 2p peak (292.5 eV) was weak, it can be overlapped and confused by C 1s (284.8 eV).

The main purpose of conducting XPS was to provide additional evidence of the successfully incorporated potassium, which was further examined by EDX mappings. In addition, after calibrating the background and fitting peaks using CasaXPS software (Figure 5.8a), two evident peaks could be resolved in the spectrum. This clearly confirmed the existence of potassium.

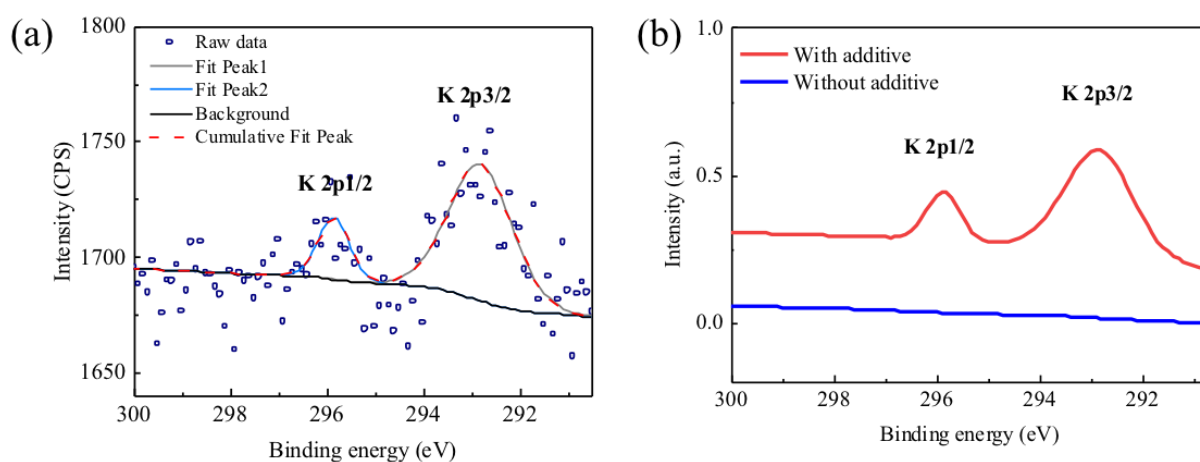


**Figure 5.8** (a) XPS measurements of K 2p in additive-treated QD thin film. (b) K 2p core level of as-prepared pristine and treated perovskite thin film. Peaks were fitted by CasaXPS.

For the CsBr/KBr-mediated CsPbBr<sub>3</sub> QDs, the amount of CsBr/KBr introduced into the standard QD precursor was 1.15 μmol, 3.65 μmol, 11.25 μmol and 19.28 μmol, respectively, corresponding to a molar fraction (F) of 0.025, 0.075, 0.2 and 0.3. As mentioned previously, the molar fraction was defined as  $F = [\text{Cs}^+/\text{K}^+] / ([\text{Cs}^+/\text{K}^+] + [\text{Cs}^+])$  in mols, representing  $[\text{Cs}^+/\text{K}^+]$  in the CsBr/KBr precursor out of the total amount of monovalent cations in the solution. The molar ratio between CsBr and KBr was controlled as 1:3. Therefore, the corresponding molar ratio of Cs and K was calculated as 1:0.0190, 1:0.060, 1:0.177 and 1:0.290. Accordingly, the atomic ratio of potassium in each sample can be estimated as 0.373%, 1.13%, 3.01% and 4.50%. As we verified from the XPS spectra (Figure 5.8 and Table 5.1), the atomic ratio of potassium in the CsPbBr<sub>3</sub> film is 3.03% and 4.31% for the fraction of 0.2 and 0.3, respectively, which is very close to our estimation. In terms of the 0.025 and 0.075 CsBr/KBr-treated film, there is no sufficient data due to the very light quantity of involved potassium and the detection limitation of the XPS instrument. Given the good consistency of the 0.2 and 0.3-treated QD films, it is reasonable to deduce that the actual ratio of potassium in each film will be similar to our estimations, *i.e.* 0.37%, 1.13%, 3.03% and 4.31%.

**Table 5.1** The quantified atomic ratio of Cs:Pb:Br:K from CsPbBr<sub>3</sub> QD film with various amounts of CsBr/KBr treatment.

Content	Pristine	0.025	0.075	0.2	0.3
Cs (at.%)	20.47	21.28	22.19	17.61	19.05
Pb (at.%)	20.52	19.36	19.55	17.67	18.79
Br (at.%)	59.02	59.36	58.27	61.68	57.85
K (at.%)	0.00	0.00	0.00	3.03	4.31
Cs:Pb:Br:K	1:1:2.88:0	1:0.91:2.79:0	1:0.88:2.63:0	1:1:3.50:0.17	1:0.99:3.04:0.23

### 5.2.3 Morphological Evolution

In order to deeply investigate the effect of blending CsBr/KBr additives, the morphological characteristics of QDs with increasing  $F = 0.025$  to  $0.3$  were measured by SEM. The results are shown in Figure 5.9. It is clearly seen that there are large pinholes in the pristine QD film (indicated by the red outlines), indicating a poor film coverage. Nevertheless, after CsBr/KBr mixture treatment, the QD thin film exhibited a much denser surface with fewer and smaller pinholes, particularly for  $F = 0.025$ . This is due to the distribution of smaller colloids in  $0.025$  CsBr/KBr-doped QDs, as confirmed in Figure 5.4.<sup>[14]</sup> However, as the amount of additives increased, the film gradually deteriorated with more defects, resulting in a poor film coverage and continuity.

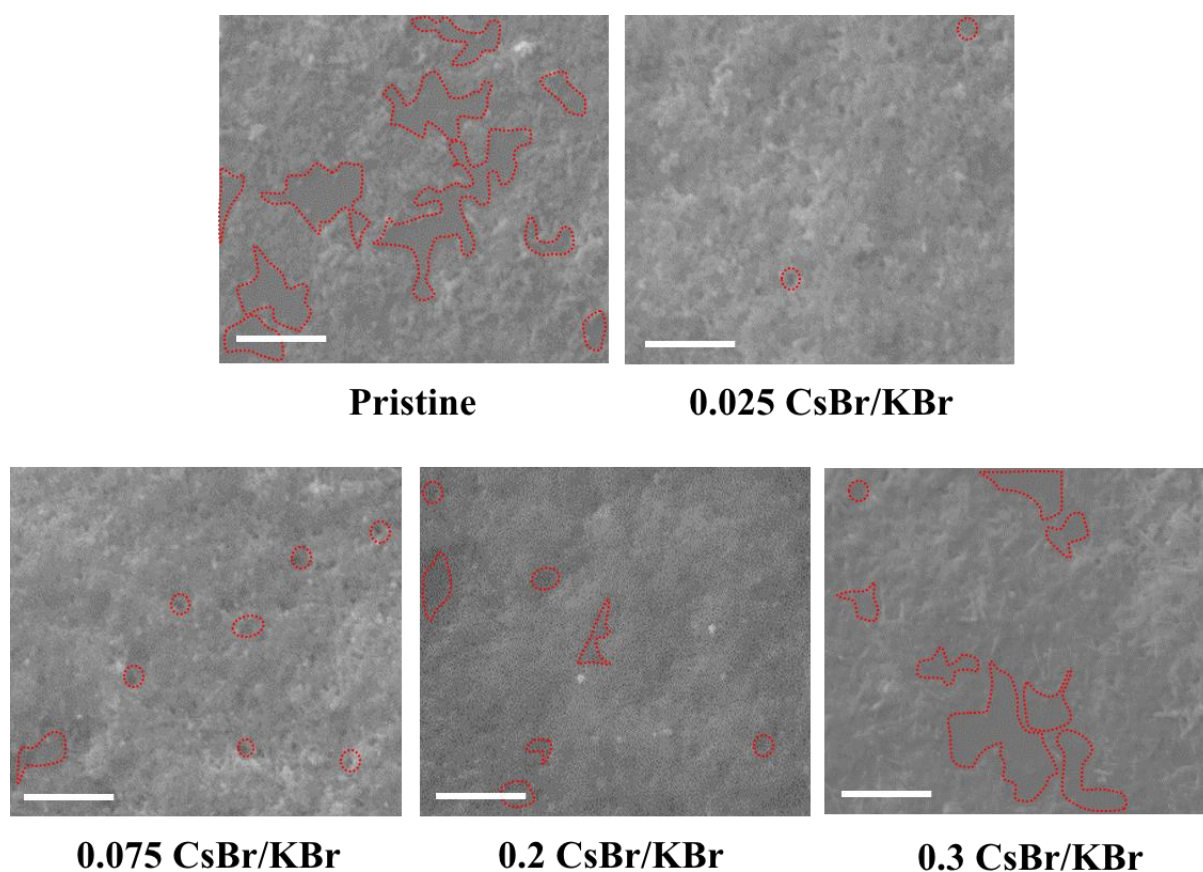


**Figure 5.9** SEM images of pristine and CsBr/KBr-assisted CsPbBr<sub>3</sub> QD films. Scale bar is  $3\ \mu\text{m}$ .<sup>[15]</sup>

Such findings were further verified by conducting contact angle measurements. As shown in Figure 5.10, the contact angles started to decrease when the fraction was 0.025, and further increased as more additives were introduced. The smallest contact angle obtained in the 0.025 CsBr/KBr treatment suggested a better substrate philicity, leading to a compact and dense thin film.<sup>[16]</sup>

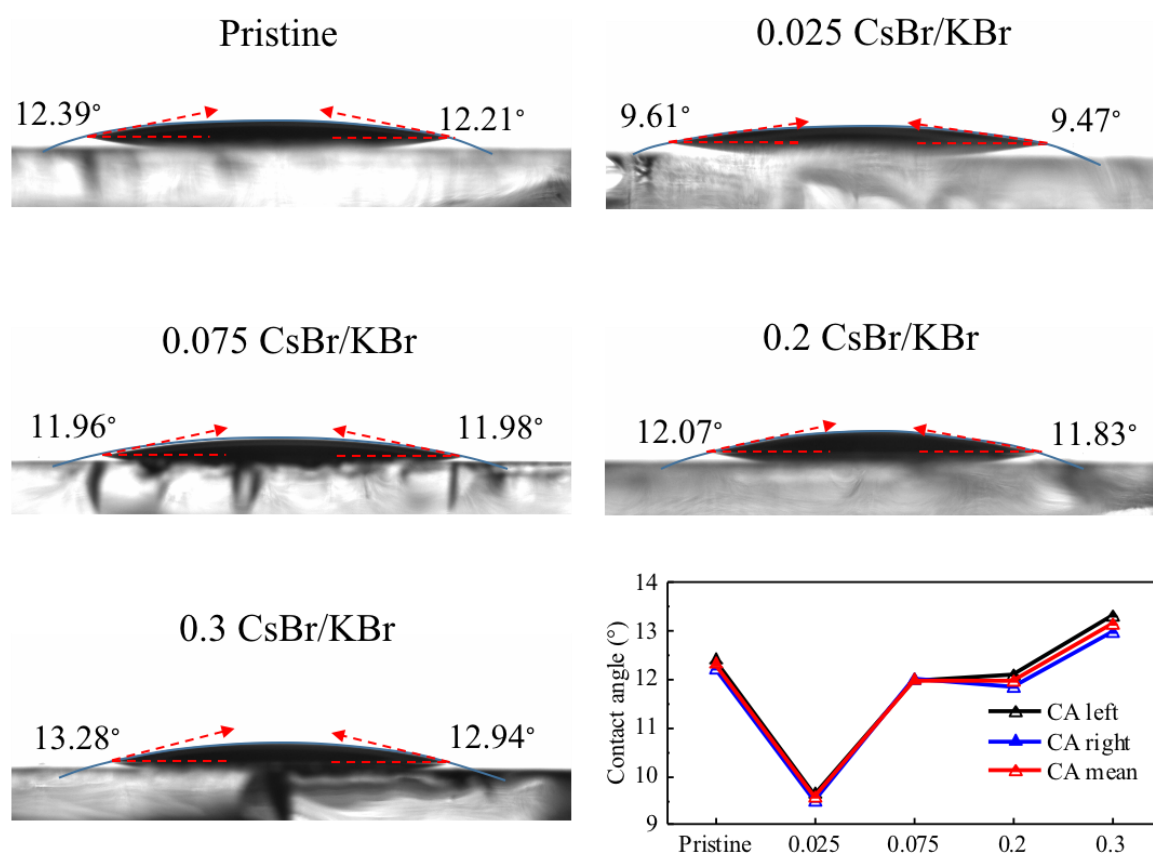


**Figure 5.10** Contact angle measurements for different colloidal perovskite solutions.

The surface morphologies were further explored by AFM, as shown in Figure 5.11. Similar to the SEM images, the number of small pinholes in the pristine film tended to decrease when blending CsBr/KBr ( $F = 0.025$ ), but increase again since introducing more additives. Similarly, the excess additives aggravated the agglomerations of CsPbBr<sub>3</sub> QDs and hence resulted in a gradually roughened surface. Notably, the CsBr/KBr ( $F = 0.025$ )-mediated thin film exhibited a relatively smooth surface with the smallest surface roughness of  $\sim 17.6$  nm (as summarised in Table 5.2), benefiting from the inhibited agglomerations. This improvement in

surface morphology indicated the effective additive mediation for CsPbBr<sub>3</sub> QDs, which can potentially facilitate carrier transport and reduce leakage current.

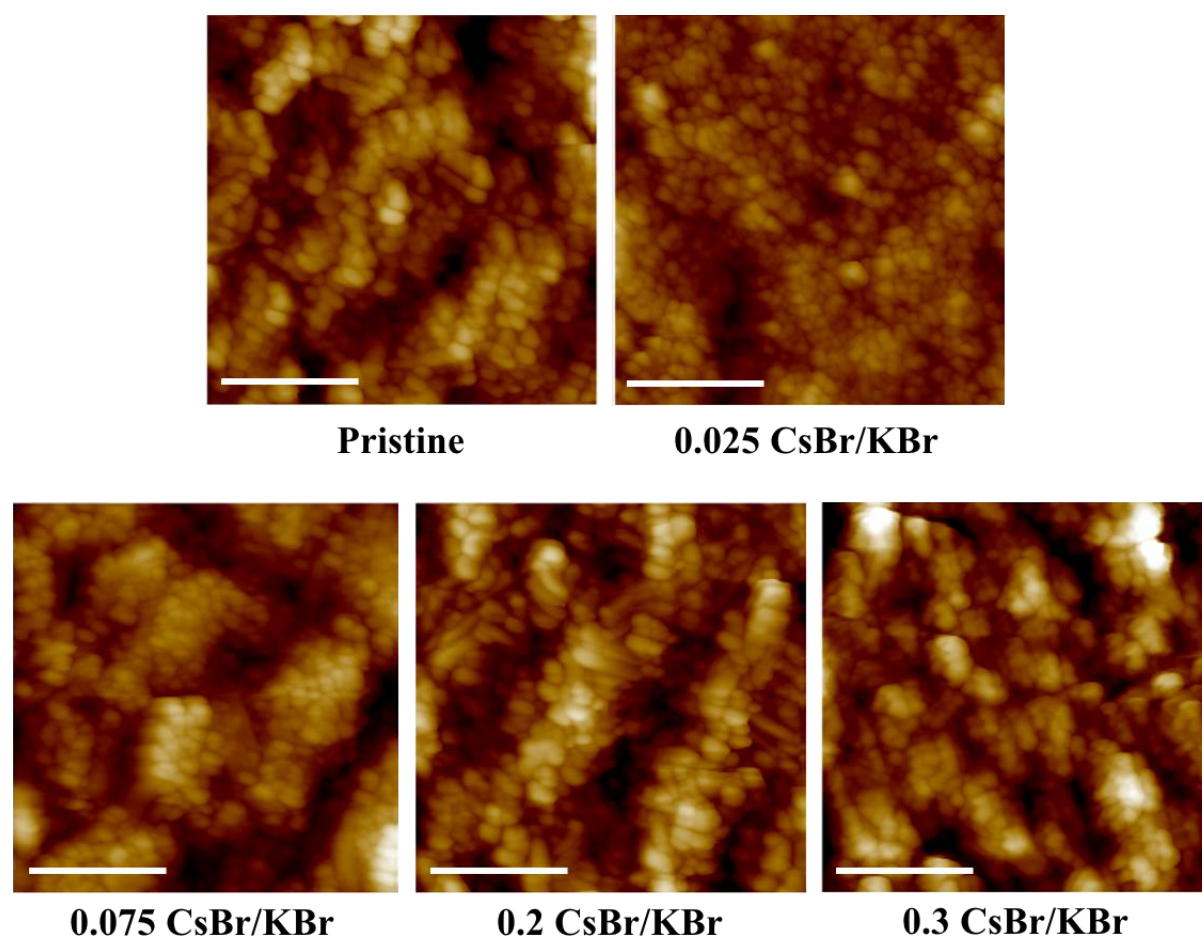


**Figure 5.11** The corresponding AFM images of each sample. The scale bar is 700 nm.<sup>[15]</sup>

**Table 5.2** Surface roughness extracted from AFM results, where  $R_q$  is the root mean square of surface roughness,  $R_a$  represents the average value of surface roughness and  $R_{max}$  denotes the maximum peak height of surface roughness.

Sample	$R_q$ (nm)	$R_a$ (nm)	$R_{max}$ (nm)
Pristine	28.4	22.4	227
0.025 CsBr/KBr	17.6	13.4	139
0.075 CsBr/KBr	29.2	23.5	203
0.2 CsBr/KBr	30.9	24.9	185
0.3 CsBr/KBr	36.0	27.5	262

#### 5.2.4 Optical Properties

In order to gain more insights into the impacts of introducing additives into QD films, the optical properties were systematically characterised by UV-Vis spectroscopy, PL and TRPL. As shown in Figure 5.12, a sharp rise was observed at the absorption edge at 530 nm in the absorption spectra of the QD film. In order to determine the bandgap energy ( $E_g$ ) of each sample, the Tauc method was applied, as shown in Figures 5.12b–f. Noteworthy, the CsBr/KBr passivation scheme introduced a slight blue-shift from 2.340 eV to 2.348 eV due to the aforementioned compressed lattice and reduced colloid size,<sup>[17]</sup> indicating the effects induced by incorporation of the CsBr/KBr mixture.

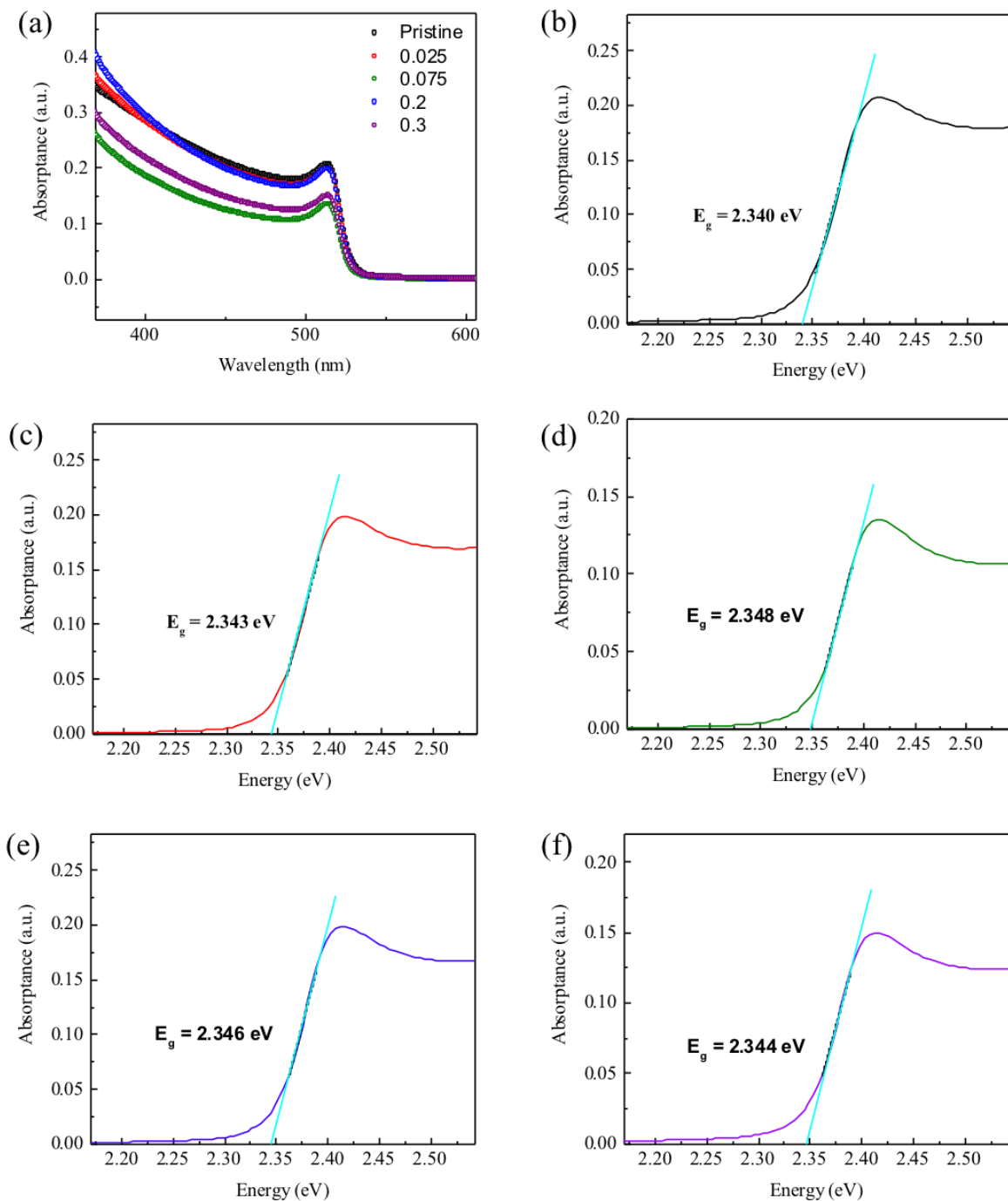


**Figure 5.12** (a) Absorbance of each QD film. Absorptions plotted using the Tauc method for the (b) pristine, (c) 0.025, (d) 0.075, (e) 0.2 and (f) 0.3 CsBr/KBr-assisted perovskite QD films.

Figure 5.13a shows the emission characteristics of QD films with excitation of the 405 nm laser. It is clearly seen that the emission peaks of all samples remained symmetric and sharp on incorporation with CsBr/KBr. By extracting the peak positions from the PL spectra, as plotted in Figure 5.13b, there is a slight blue-shift (from 524.5 nm to 522 nm) after additive

treatment, well agreed with the absorption measurements. The narrowest FWHM of  $\sim 26$  nm was obtained in 0.025 CsBr/KBr-assisted QD film (Table 5.3), suggesting an improved emission efficiency and better crystal quality. This impressive improvement can be ascribed to the effective suppression of aggregation, and shows the potential benefit for light-emitting applications.

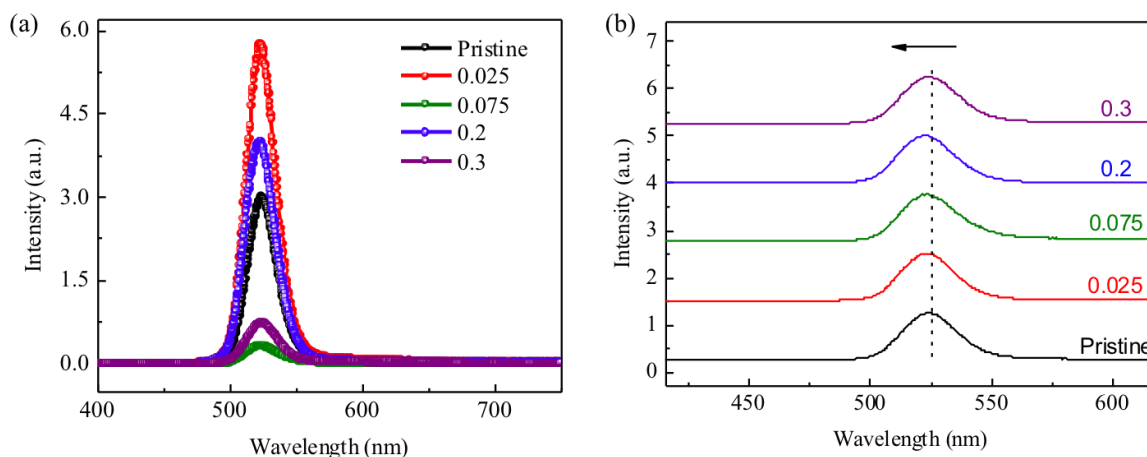


**Figure 5.13** (a) Steady-state PL spectra along with CsBr/KBr treatment. (b) PL peak positions with slight blue-shift.

**Table 5.3** Summarised peak positions, bandgaps, peak intensities and FWHM from PL spectra, along with QDs containing different fractions of CsBr/KBr injection.

Sample	Peak (nm)	E <sub>g</sub> (eV)	Peak intensity	FWHM (nm)
Pristine	524	2.366	298700	26.5
0.025 CsBr/KBr	523	2.371	575300	26
0.075 CsBr/KBr	523.5	2.369	32800	27.5
0.2 CsBr/KBr	522.5	2.373	397900	27
0.3 CsBr/KBr	523.5	2.369	73310	27.5

### 5.2.5 Carrier Dynamics

Next, the carrier dynamics were explored by performing TRPL measurements, as plotted in Figure 5.14a. A bi-exponential decay function was applied to fit the decay curves, as shown in Figures 5.14b–f. Two decay components were involved in the decay process, namely the time constants ( $\tau_1$  and  $\tau_2$ ) and the corresponding fractions ( $f_1$  and  $f_2$ ), which were summarised in Table 5.4. The average lifetime is a critical parameter associated with the recombination process, which can be determined as 4.95 ns, 7.53 ns, 7.95 ns, 4.24 ns and 1.81 ns, respectively, for samples with different fractions of additives. It is worth noting that the carrier lifetimes of CsBr/KBr-assisted QD film were prolonged over 50% when the fraction was 0.025 and 0.075. This extended lifetime could originate from the intermediate energy states introduced by the interstitial cations and deep trap states.<sup>[18]</sup> Nevertheless, similar to the tendency of PL and UV-Vis measurements, the average lifetimes reduced to 1.81 ns with excess introduction of CsBr/KBr. The excess additives acted as impurities, which could introduce more surface defects and generate non-radiative recombination centres. Therefore, it is reasonable to believe that the CsBr/KBr passivation scheme effectively suppressed the non-radiative recombination, resulting in an improved crystal quality.

As a result, CsBr/KBr treatment enabled the formation of uniform and compact film, as well as maintaining high crystallinity. The compressive characterisations confirmed the benefits of 0.025 CsBr/KBr-assisted CsPbBr<sub>3</sub> QDs, including prolonged carrier lifetimes and efficient emission features. The treatment shows promise in flexible photodetectors.

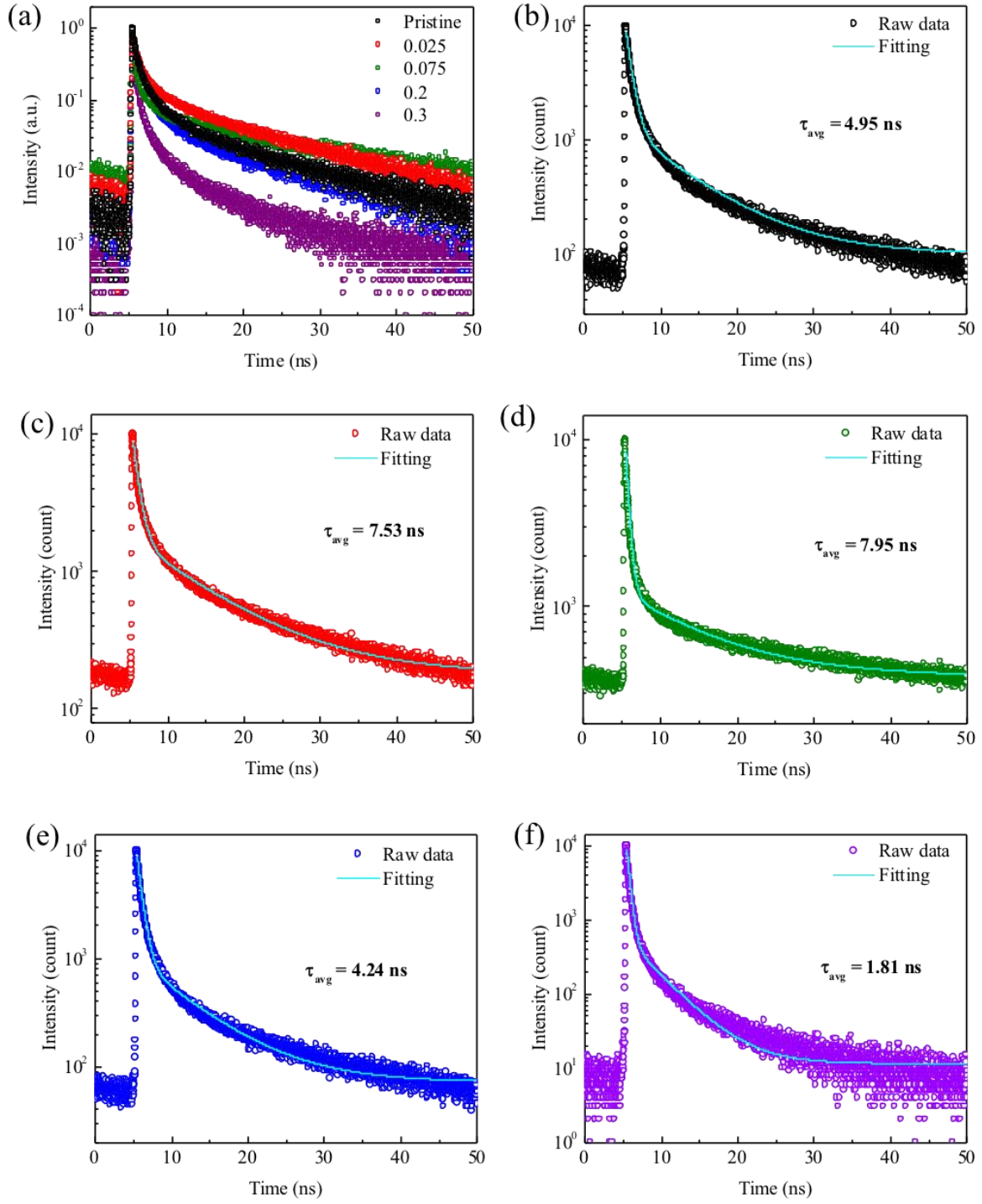


**Figure 5.14** (a) TRPL decay curves of each film. The bi-exponential function fitted TRPL decays of (b) pristine, (c) 0.025, (d) 0.075, (e) 0.2, and (f) 0.3 CsBr/KBr doped CsPbBr<sub>3</sub> QDs film.

**Table 5.4** Decay constants and their fractions as extracted from the TRPL measurements, using bi-exponential decay fitting:  $I(t) = A_1 \exp(-t/\tau_1) + A_2 \exp(-t/\tau_2)$ .

Sample	$\tau_1$ (ns)	$\tau_2$ (ns)	$f_1$ (%)	$f_2$ (%)	$\tau_{ave}$ (ns)
Pristine	0.771	7.845	40.864	59.136	4.954
0.025 CsBr/KBr	0.782	10.044	27.176	72.824	7.526
0.075 CsBr/KBr	0.448	10.852	27.862	72.138	7.953
0.2 CsBr/KBr	0.660	7.262	45.684	54.316	4.245
0.3 CsBr/KBr	0.379	4.013	60.595	39.405	1.811

### 5.2.6 Mechanism of Improvements

The mechanisms of the CsBr/KBr optimisation strategy were further explored by the schematic representation illustrated in Figure 5.15. Initially, there was competition between halide ions and ligands or solvent molecules during the synthesis procedure. Such competition enabled the formation of distorted octahedra (where electron-hole pair generation and recombination happened), leading to numerous  $\text{Br}^-$  vacancies.<sup>[19,20]</sup> Owing to the fast nucleation rate, these  $\text{Br}^-$  vacancies could not be fully compensated, and further introduced a high density of traps into the energy band.<sup>[21]</sup> The presence of these trap states has a negative impact on the recombination process, hence degrading the optical properties and photoresponse. Therefore, as presented in Figure 5.1, the additive passivation strategy initially provided a large number of Br ions in the QD precursors not only to generate a Br-rich environment but also to partially compensate halide vacancies, which is beneficial for growing highly crystalline QDs.<sup>[22]</sup> Moreover, the size of  $\text{K}^+$  ( $r = 0.138$  nm) is smaller than that of  $\text{Cs}^+$  ( $r = 0.167$  nm), which enabled  $\text{K}^+$  to more easily enter the interstitial or substitual sites of the perovskite lattice, as supported by previous studies.<sup>[23,24]</sup> Accordingly, the introduction of  $\text{K}^+$  can to lower the defect densities. Therefore, it is reasonable to believe that the introduction of CsBr/KBr additives can

efficiently inhibit halide migration and suppress non-radiative recombination. This can improve the emission efficiency and prolong carrier lifetimes, consistent with the PL and TRPL results (Figures 5.13 and 5.14). Thanks to the smaller radius,  $K^+$  was also able to compensate partial  $Cs^+$  vacancies by occupying the cavity of the Pb-Br framework. Notably, the substitution of A-site cations with smaller ions would cause a compressed lattice and hence a blue-shift, a result which is strongly supported by the TEM and PL measurements (Figures 5.3 and 5.13). Furthermore, the additive scheme additionally provided  $Cs^+$ , which reacted easily with the excess  $PbBr_2$  to prevent the formation of its derivatives, including  $CsPb_2Br_5$ , as well as achieving a higher yield.<sup>[25]</sup> As mentioned previously, the excess introduction of CsBr/KBr degrades the film quality and optical properties, and further affects the device performance. Therefore, based on the characterisation, the optimal fraction of CsBr/KBr was determined to be 0.025. This value is expected to exhibit a better photoresponse in the photodetectors.

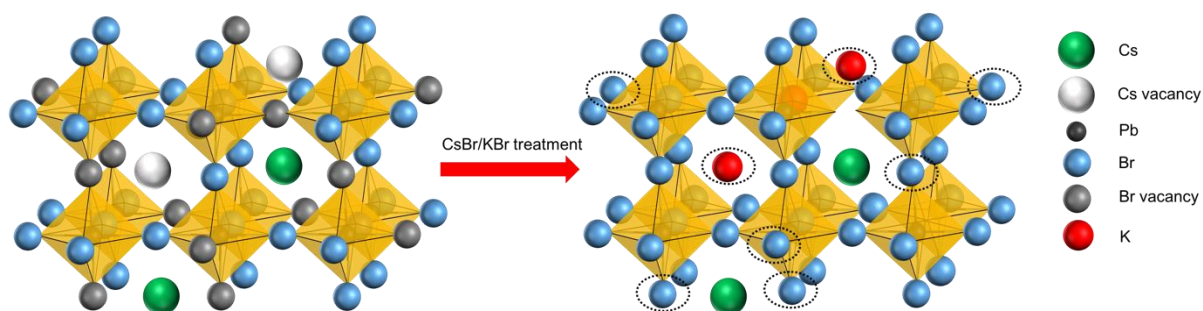


**Figure 5.15** Schematic representation of mediating  $CsPbBr_3$  QDs with CsBr/KBr additives. Reproduced from ref. [15] with permission from John Wiley and Sons, copyright 2020.

### 5.3 Device Architecture

In order to validate the impacts of the CsBr/KBr doping scheme on device performance, flexible photodetector arrays were subsequently fabricated. As shown in Figure 5.16a, a  $TiO_2$  layer was deposited on the ITO-coated PET substrate by ALD, which was employed as an ETL to extract and transport electrons. All-inorganic  $CsPbBr_3$  QDs with CsBr/KBr (from 0.025 to 0.3) were used as the active layer to absorb light and generate electron-hole pairs. Spiro-

OMeTAD was used as the HTL to transport light-induced holes and collected by Ni/Au electrodes. The details of fabrication were explained in Chapter 3. A digital image of the flexible photodetector arrays is shown in Figure 5.16a, with the arrays demonstrating good flexibility. Figures 5.16b and 5.16c present the arrays placed on a purpose-designed stage without and with illumination, respectively. It is worth noting that the bottom contact (ITO) is shared for all of pixels, and top electrodes (Ni/Au) are individual.

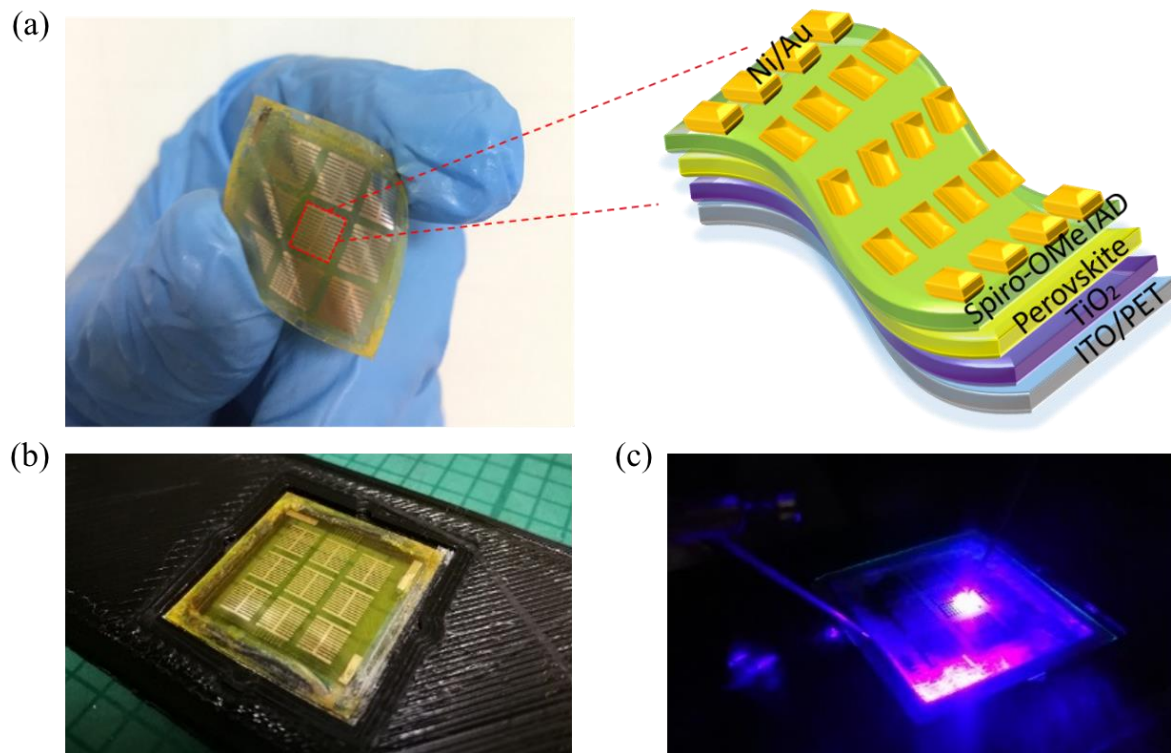


**Figure 5.16** (a) Digital photographs of flexible photodetector arrays with schematic illustration of device configuration. Images of the flexible devices (b) without and (c) with laser illumination. Reproduced from ref. [15] with permission from John Wiley and Sons, copyright 2020.

## 5.4 Device Characterisations

### 5.4.1 Photoresponse Comparison

The photoresponse of the photodetectors was measured with the excitation of 405 nm, 450 nm and 520 nm lasers, respectively. In order to clearly observe the difference in

photoresponse between each device, the dark current and photocurrent were evaluated and are plotted in Figure 5.17. As shown in Figure 5.17a, a low level of dark current of  $\sim 0.1 \mu\text{A}$  was obtained at  $-1.5 \text{ V}$  bias voltage when  $F = 0.025$  and  $0.075$ , which is five-fold lower than the pristine device. Benefiting from the direct bandgap transition, an evident photoresponse was observed in each photodetector. Noteworthily, the photodetector with  $0.025 \text{ CsBr/KBr}$  treatment exhibited the highest current at reversed bias under  $405 \text{ nm}$  laser illumination (Figure 5.17b). Specifically, the current reached  $223 \mu\text{A}$  at  $-1.5 \text{ V}$ , which was improved by  $\sim 90\%$  compared with the pristine photodetector. A similar phenomenon was also observed when illuminated with  $450 \text{ nm}$  and  $520 \text{ nm}$  laser diodes, as shown in Figures 5.17c and 5.17d. The dominant light current and lowest dark current achieved in the  $0.025 \text{ CsBr/KBr}$ -doped device suggested more efficient carrier generation, transport and collection. This enhancement was in good agreement with the morphological (SEM and AFM) and optical (PL and TRPL) evolution, revealing the advantages of blending the correct fraction of additives.

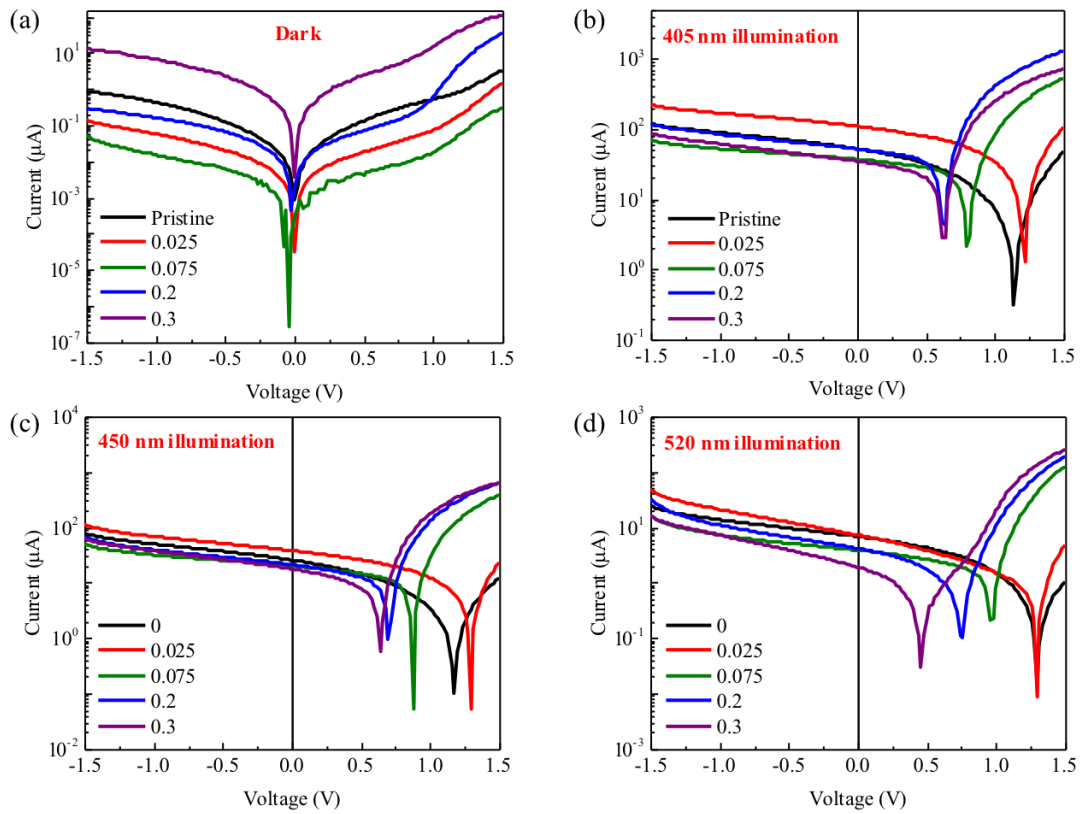


**Figure 5.17** *The photoresponse of as-prepared photodetector arrays with different fractions of CsBr/KBr, including pristine (black), 0.025 (red), 0.075 (green), 0.2 (blue) and 0.3 (violet). They were measured (a) in dark, and under (b) 405nm, (c) 450 nm and (d) 520 nm laser illumination, respectively.*

Notably, there are some valleys when different illumination sources are involved, which can be assigned to the open-circuit voltage ( $V_{oc}$ ). The  $V_{oc}$  of each device was extracted from Figure 5.17 and is plotted in Figure 5.18a. It is evident that the additive-treated device ( $F = 0.025$ ) exhibited a dominant  $V_{oc}$  over others under different light illumination. The value of  $V_{oc}$  was measured as 1.22 V, 1.30 V and 1.30 V under 405 nm, 450 nm and 520 nm laser excitation, respectively. Such strong photovoltaic effect can be attributed to the suitable device configuration and optimal doping process. The mechanism of device operation and improved  $V_{oc}$  will be explained later. Similar to the observations in the  $V_{oc}$  diagram, the largest ratio of light current ( $I$ ) and dark current ( $I_d$ ) was achieved in the 0.025 CsBr/KBr-assisted photodetectors. Compared to the pristine device, the photodetector with  $F = 0.025$  exhibited at least one order of magnitude improvement in  $I/I_d$ . Notably, the improvement was significant when operated under the self-powered mode (0 V bias). The  $I/I_d$  of the 0.025 CsBr/KBr-assisted photodetectors was as high as  $\sim 3.5 \times 10^6$  under illumination with the 405 nm diode. This value was two orders of magnitude higher than in the pristine photodetector, which was even competitive with commercial photodetectors.

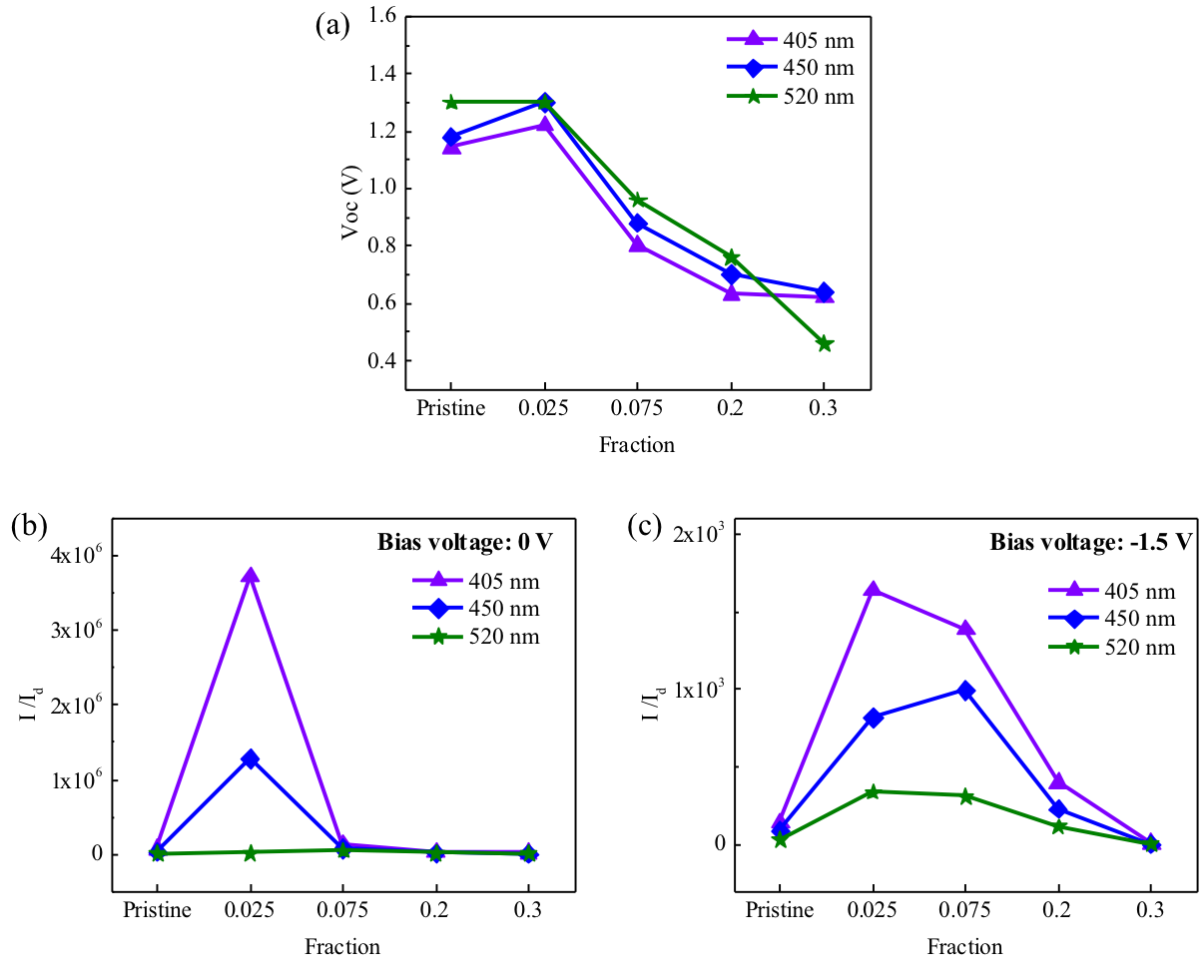


**Figure 5.18** (a) Open-circuit voltage variation under different light illuminations. The corresponding  $I/I_d$  extracted from the I–V curves under different illuminations (405 nm, 450 nm and 520 nm) at a bias voltage of (b) 0 V and (c) -1.5 V.

In addition, the 0.025 CsBr/KBr-assisted QD device exhibited an impressive external quantum efficiency (EQE) of 6400%, which is comparable to or even higher than other photodetectors. The EQE, representing the ability of light conversion response to incident light, can be expressed as<sup>[26]</sup>

$$EQE = \frac{h \times c \times R}{\lambda \times e} \times 100\% \quad \text{Equation 5.1}$$

where  $\lambda$  is the illumination wavelength (405 nm).

### 5.4.2 Band Structure

In order to gain more insight into the improved  $V_{oc}$ , the band structures of the as-fabricated photodetectors are illustrated in Figure 5.19, with explanations of the operation principles. In Figure 5.19a, the Fermi level ( $E_f$ ) of each material is indicated by a red dashed line, e.g.  $E_{f,1}$  of  $TiO_2$  and  $E_{f,2}$  of  $CsPbBr_3$  QDs. When they contacted in the absence of light,  $E_f$  started to align at the interface until reaching thermal equilibrium (Figure 5.19b). Notably, as one of the critical factors involved in band structures, the built-in potential ( $V_{bi}$ ) needs to be identified to understand the working principles of the device. It is induced by the  $E_f$  offset, and has a strong influence on  $V_{oc}$  as well as carrier separation and transport.<sup>[27–29]</sup> With respect to the as-fabricated device, the value of  $V_{bi}$  is equal to the difference between  $E_{f,1}$  and  $E_{f,2}$ .<sup>[28]</sup>  $E_{f,2}$  was subsequently measured by UPS, and the values can be calculated as 5.54 eV, 5.71 eV, 5.18 eV, 5.13 eV and 5.06 eV for their respective fractions, as shown in Figure 5.20.

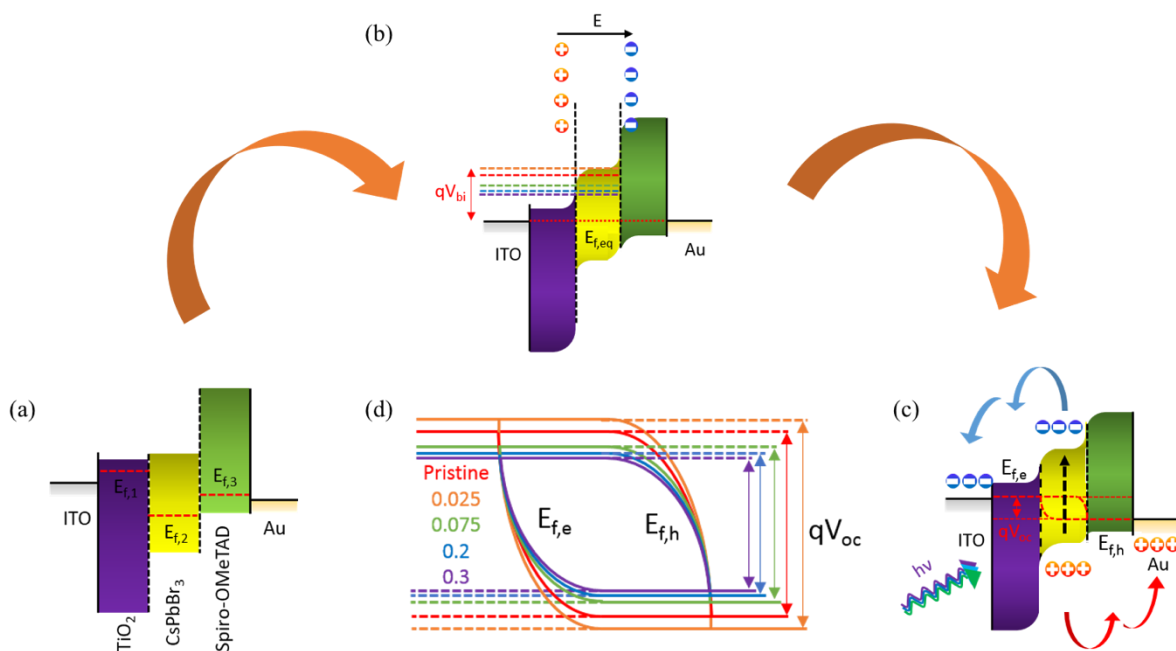


**Figure 5.19** Schematic band structure of devices. (a) Before contact. (b) After contact. (c) Operation in self-powered mode. (d)  $V_{oc}$  distribution.

Considering the reported value of  $E_{f,1}$ ,<sup>[30]</sup> the theoretical  $V_{bi}$  was estimated as 1.23 eV, 1.40 eV, 0.88 eV, 0.82 eV and 0.75 eV, respectively, which shows a similar tendency to  $V_{oc}$ .

Obviously, the introduction of 0.025 CsBr/KBr resulted in the strongest  $V_{bi}$ , implying the better capability of separating, transporting and collection of charge carriers.

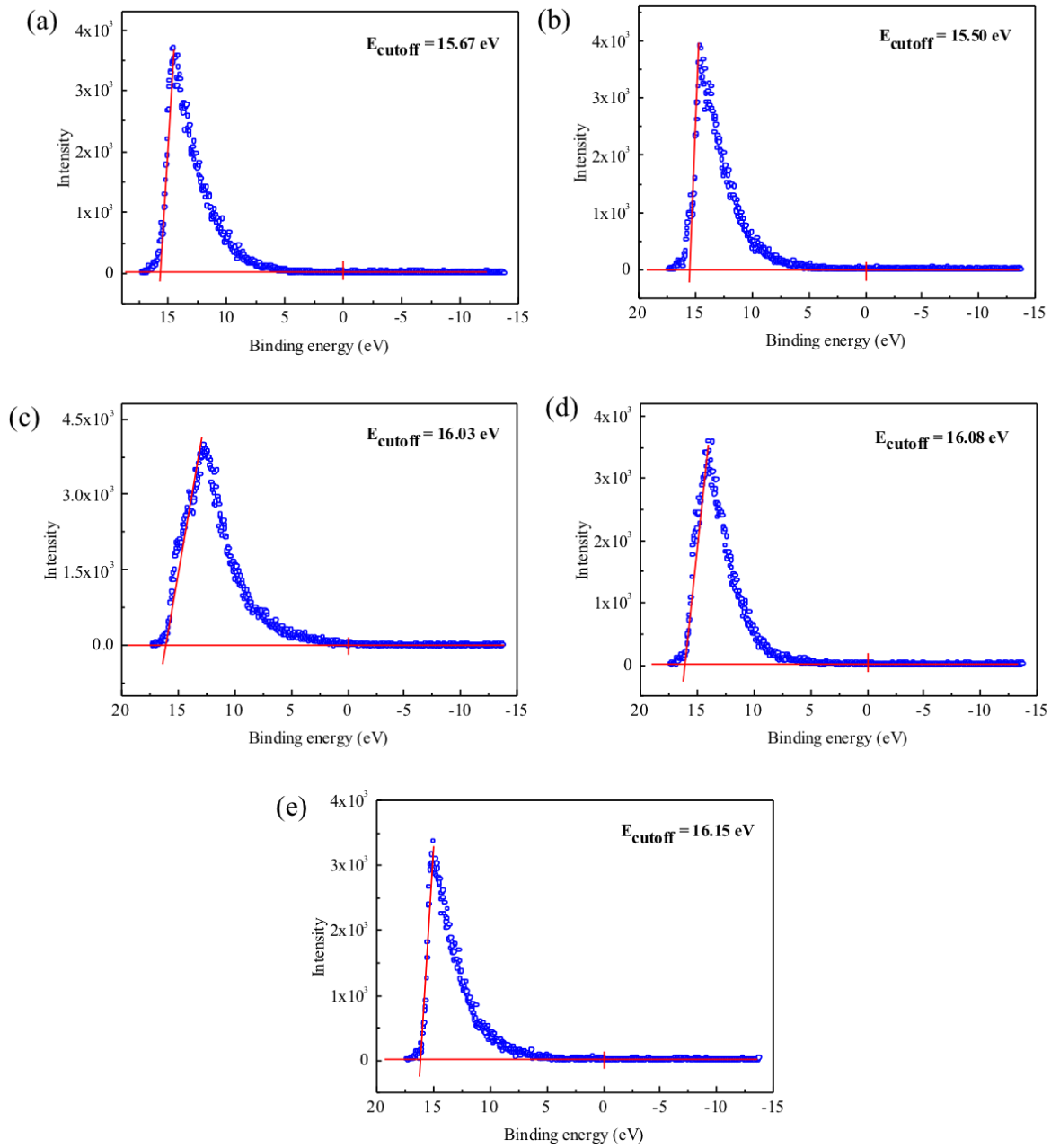


**Figure 5.20** UPS measurements for each sample, showing the binding energy secondary electron cutoffs. (a) Pristine, (b) 0.025 CsBr/KBr, (c) 0.075 CsBr/KBr, (d) 0.2 CsBr/KBr, (e) 0.3 CsBr/KBr. The corresponding work function ( $W_F$ ) can be determined by taking the difference between the photon energy (21.22 eV) and secondary electron cutoff ( $E_{cutoff}$ ).  $E_{Fermi} = 0$  eV, using Ag as the metal sample for calibration.

Under illumination, the electron-hole pairs are excited in the perovskite layer by incident photons, as illustrated in Figure 5.19c. Benefiting from the large  $V_{bi}$ , electron-hole pairs are efficiently separated. The electrons transfer from  $\text{CsPbBr}_3$  to  $\text{TiO}_2$  and are collected by the ITO. For holes, they transport from  $\text{CsPbBr}_3$  to spiro-OMeTAD and are ultimately collected by Ni/Au. Therefore, it is reasonable to deduce that the improvement in carrier separation, transportation and collection produce a larger light current in the photodetector with  $F = 0.025$ , owing to it having the largest  $V_{bi}$ . It is known that the movement of electrons and holes can introduce the split of  $E_{f,eq}$ . The resulting electron quasi-Fermi level ( $E_{f,e}$ ) and the hole quasi-Fermi level ( $E_{f,h}$ ) are the foundation of forming  $V_{oc}$ , enabling self-powered operation. The corresponding  $V_{oc}$  distribution is shown in Figure 5.19d, and the trend is in good agreement with the experimental results (Figure 5.18a).

#### 5.4.3 Performance Comparison

Responsivity ( $R$ ) and specific detectivity ( $D^*$ ) are the two important figures of merit in photodetectors. As shown in Figure 5.21,  $R$  and  $D^*$  were calculated based on dark current and light current measurements (Figure 5.17), and plotted as a function of biased voltages. When the devices were measured under 405 nm laser excitation, they exhibited an acceptable performance, demonstrating an  $R$  of at least  $3.2 \text{ A W}^{-1}$  and  $D^*$  exceeding  $10^{11}$  Jones (Figure 5.21a). It is worth noting that the highest  $R$  and  $D^*$  were obtained in the 0.025 CsBr/KBr-mediated photodetector, reaching up to  $21 \text{ A W}^{-1}$  at  $-1.5 \text{ V}$  bias and  $9.35 \times 10^{13}$  Jones under self-powered mode, respectively. The dominant state of performance was still maintained for 450 nm and 520 nm radiation as shown in Figures 5.21b and 5.21c. It is worth noting that the maximum  $R$  and  $D^*$  obtained under self-powered mode are over two-fold and ten-fold higher than the pristine photodetectors, respectively, as shown in Figure 5.21d. Compared to other

perovskite-based photodetectors, our device exhibited a competitive or even superior performance, as summarised in Table 5.5.

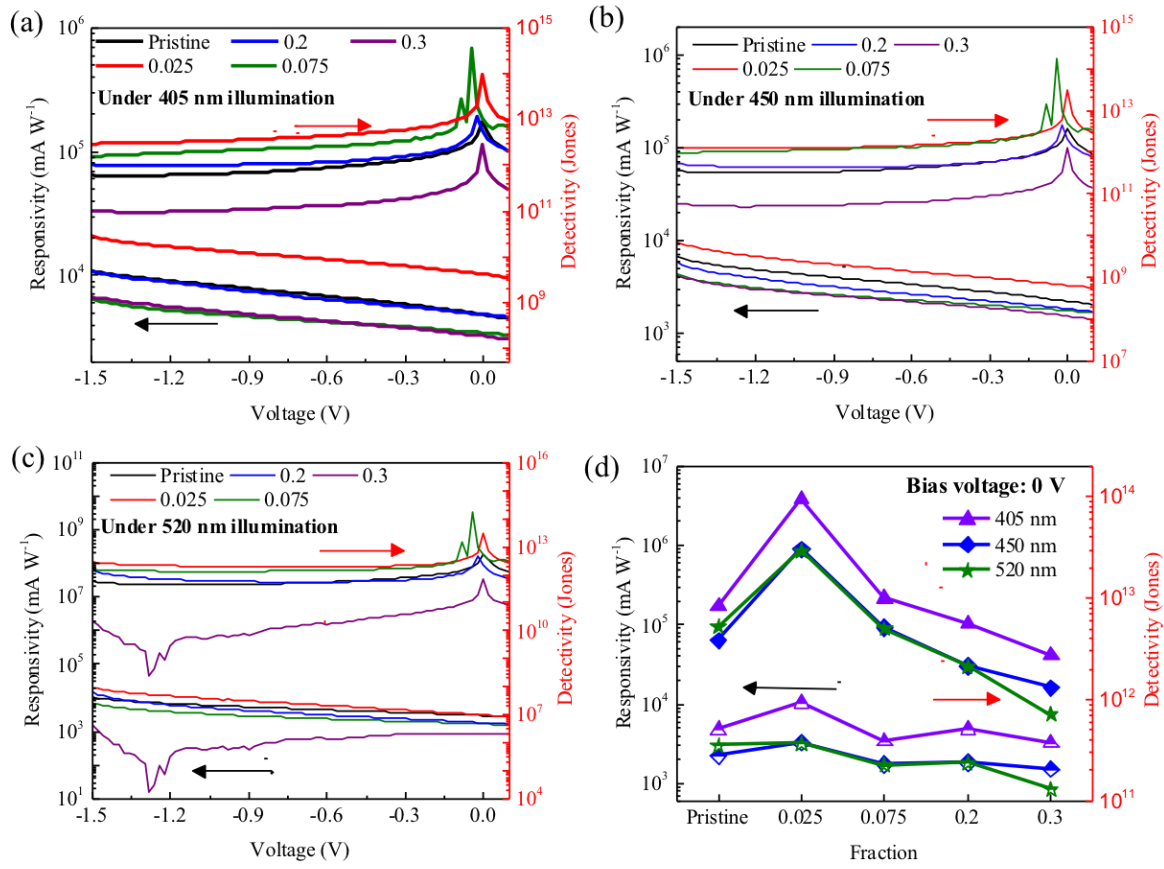


**Figure 5.21** Responsivity and detectivity of CsBr/KBr-assisted devices under (a) 405 nm, (b) 450 nm and (c) 520 nm light illumination. (d) Summary of performance at a bias voltage of 0 V.

**Table 5.5** Summary of device performance of reported perovskite photodetectors.

Active Materials	R (A W <sup>-1</sup> )	D* (Jones)	On/off
CsPbBr <sub>3</sub> :ZnO <sup>[31]</sup>	0.0115	-	12.86
CsPbBr <sub>3</sub> microcrystals <sup>[32]</sup>	6 (3 V)	~10 <sup>13</sup> (3 V)	<10
CsPbBr <sub>3</sub> nanosheets/CNTs <sup>[33]</sup>	31.1 (10 V)	-	90
CsPbBr <sub>3</sub> single crystals <sup>[34]</sup>	0.028	1.7×10 <sup>11</sup>	10 <sup>5</sup>
MAPbI <sub>3</sub> /CdS <sub>10</sub> <sup>[35]</sup>	0.48	2.1×10 <sup>13</sup>	750
MAPbI <sub>3-x</sub> Cl <sub>x</sub> <sup>[36]</sup>	2.17 (5 V)	9.4×10 <sup>11</sup> (5 V)	1.2×10 <sup>3</sup>
MAPbI <sub>3</sub> /Spiro <sup>[37]</sup>	21.5	3×10 <sup>12</sup>	79.1
CsPbBr <sub>3</sub> QDs (this work)	10.1	9.35×10 <sup>13</sup>	2.1×10 <sup>4</sup>

These impressive photoresponses may originate from the integration of enhanced film formation and crystal quality, and efficient carrier generation, extraction and transportation. These results further validate the advantages of treating with proper CsBr/KBr additives, which is beneficial for constructing high-performance photodetectors.

#### 5.4.4 Photoresponse of CsBr/KBr Doped CsPbBr<sub>3</sub> QDs Photodetector

As discussed and summarised above, the optimal fraction of additives is 0.025, and the optimised photodetector demonstrated an enhanced device performance compared to photodetectors with other ratios. Therefore, in this section, studies were carried out to obtain a comprehensive photoresponse. Figure 5.22a shows the *I*-*V* curve as a function of power intensity under excitation of the 405 nm laser diode. When increasing the incident light intensity from 0.7 mW cm<sup>-2</sup> to 13.4 mW cm<sup>-2</sup>, the current was amplified accordingly. The same

tendency is also witnessed under 450 nm and 520 nm laser illumination (Figures 5.22b and 5.22c).

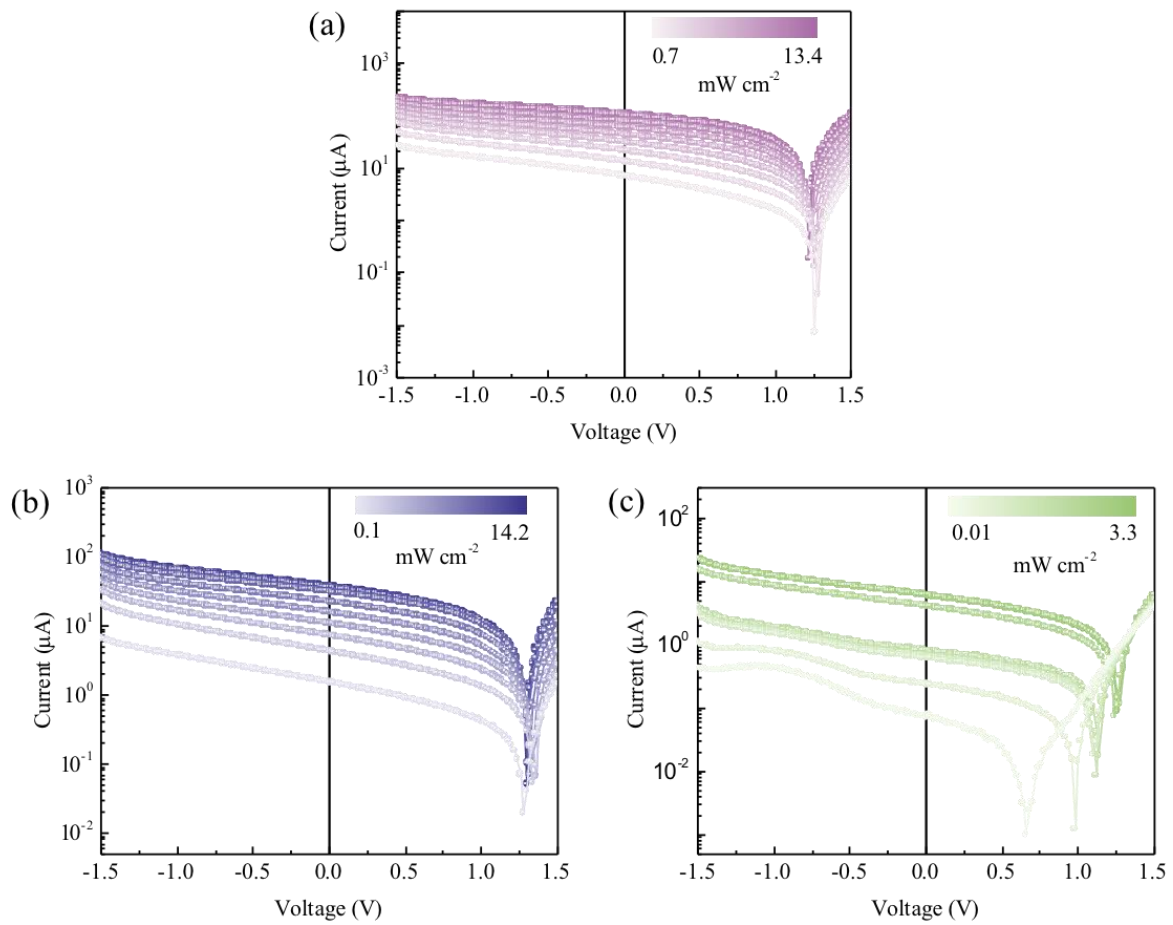


**Figure 5.22** Typical  $I$ - $V$  curves as a function of intensity in logarithmic scale with excitation of (a) 405 nm, (b) 450 nm and (c) 520 nm laser diodes.

The corresponding fitted power-dependent photocurrent at various applied biases are plotted in Figure 5.23. Without an external power supply, the power exponent was calculated as 1.076 and 0.805 for illumination with the 405 nm and 450 nm lasers, respectively, as shown in Figure 5.23a. Such linear exponents suggested a low recombination rate and efficient carrier extraction. The non-unity exponent was also obtained for the biased devices as -0.5 V (Figure 5.23b), -1 V (Figure 5.23c) and -1.5 V (Figure 5.23d). Notably, the power exponent at 0 V is the closest to unity, indicating an efficient carrier generation and recombination process.

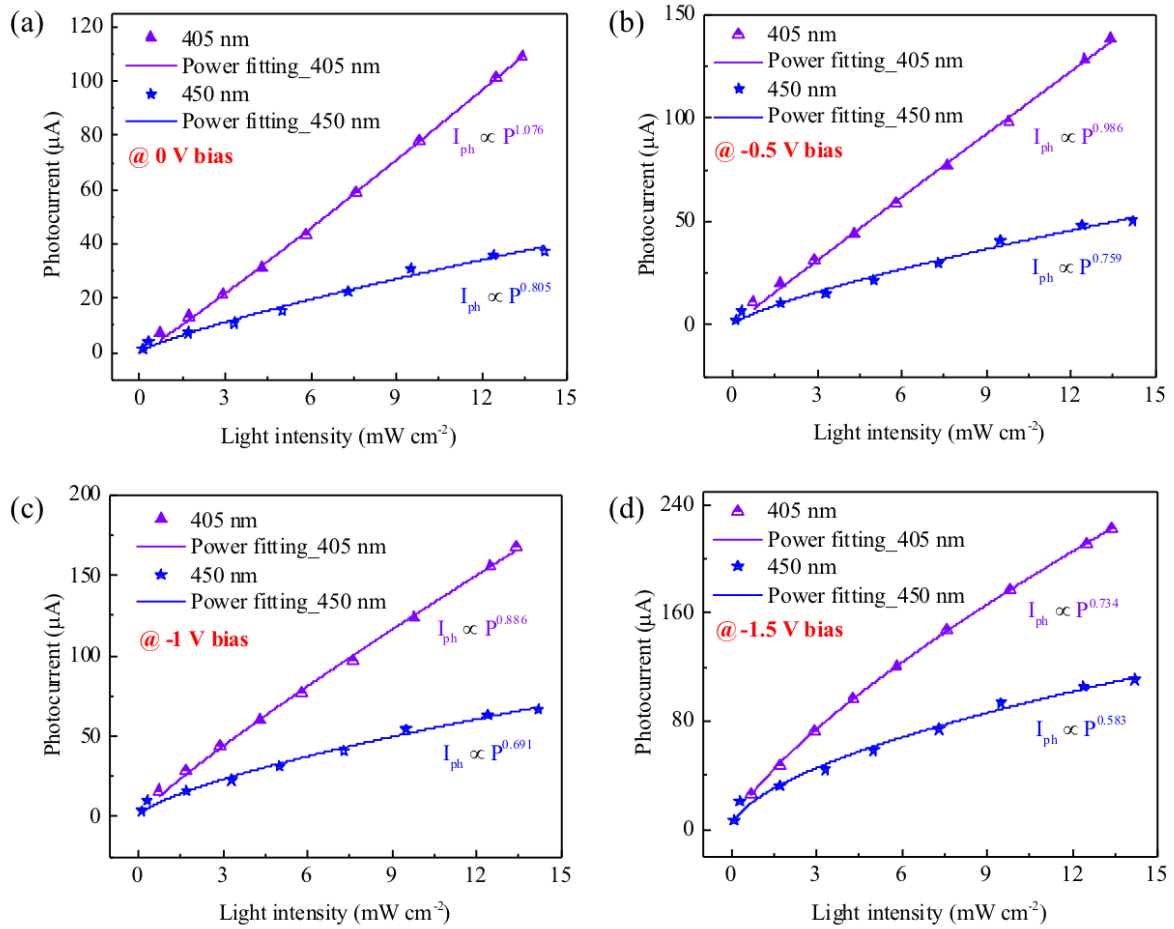


**Figure 5.23** The fitted power-dependent photocurrent under 405 nm and 450 nm light illumination at (a) 0 V, (b) -0.5 V, (c) -1 V and (d) -1.5 V bias.

The time-dependent photoresponse at different bias voltages is shown in Figure 5.24. By providing periodical on/off cycles on the illumination source, the current rose/fell immediately when the laser was turned on/off, demonstrating reproducible cycles and a good on/off switching behaviour with a large on/off ratio of  $\sim 2.1 \times 10^4$ . It is evident that the steady state of the photocurrent was amplified when increasing the bias, which is attributed to the more efficient separation of electron-hole pairs by the stronger electric field. Similar findings were also observed when the 450 nm light source was employed, as shown in Figure 5.24b. It is worth noting that the current generated by the 405 nm laser is higher than that by the 450 nm laser, showing a distinctive wavelength selectivity.

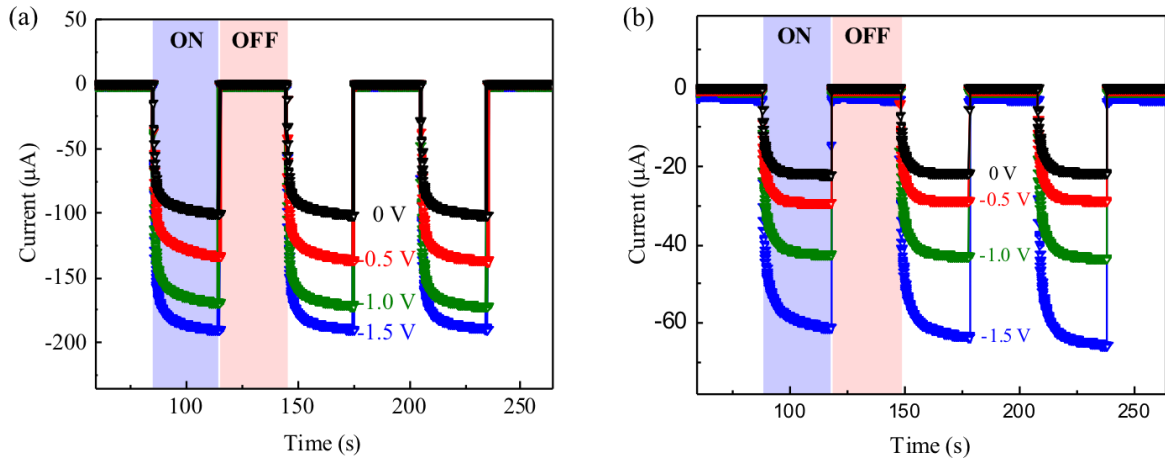


**Figure 5.24** Transient photoresponse at different bias voltages under (a) 405 nm and (b) 450 nm laser diode excitation with a power intensity of  $13.4 \text{ mW cm}^{-2}$ .

Compared with the pristine photodetector under self-powered mode, it is clear that the optimised device exhibited a larger current of 101 nA than the pristine device, which is a ~40% improvement (Figure 5.25a). Moreover, as shown in Figure 5.25b, the response time is also shortened by ~248%. Both comparisons confirm the benefits of the CsBr/KBr passivation strategy for enhancing the device performance.

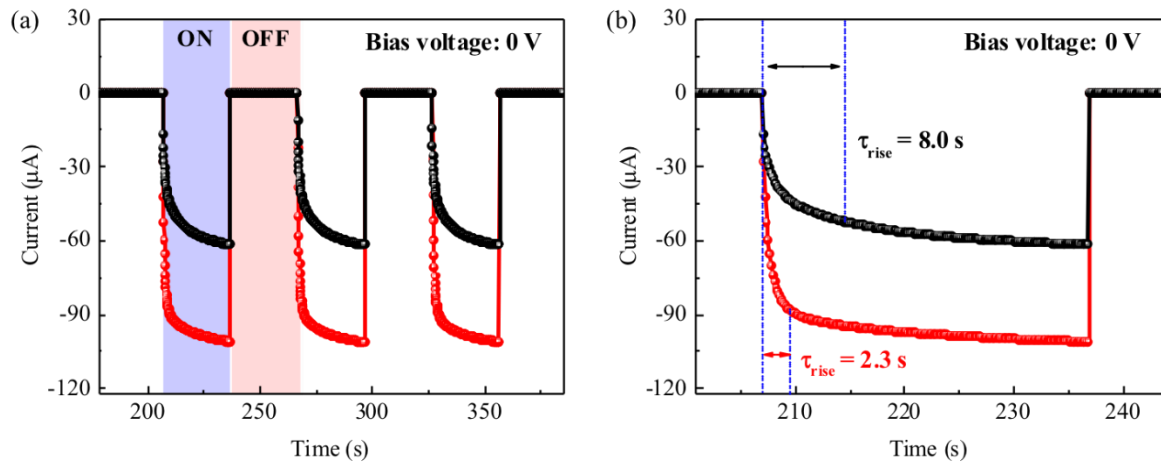


**Figure 5.25** Photoresponse comparison between pristine (black line) and 0.025 Cs<sup>+</sup>/K<sup>+</sup>-treated (red line) photodetectors at 0 V under 405 nm laser illumination. (a) Time-resolved photoresponse. (b) The corresponding response time.

### 5.4.5 Bending Test

Aside from the excellent photoresponse, CsPbBr<sub>3</sub> QD-based photodetectors with optimal ratio additionally exhibited obvious mechanical flexibility. The wavelength-dependent transient electrical characteristics of the devices were assessed with bending angles of 0° and 60°, as shown in Figure 5.26a. The light current of the flexible photodetector maintained ~94% of its initial value after bending, while the dark current retained the same level with negligible degradation. Moreover, the optimised photodetector was further investigated by applying various bending cycles from 0 to 1600 under self-powered mode. The resulting time-resolved photoresponse is illustrated in Figure 5.26b. It can be clearly observed that the light current was slightly degraded by ~7% after 1600 bending cycles, suggesting a strong folding endurance and good electrical stability. Meanwhile, the as-fabricated device still exhibited a sensitive and reproducible photoresponse after bending.

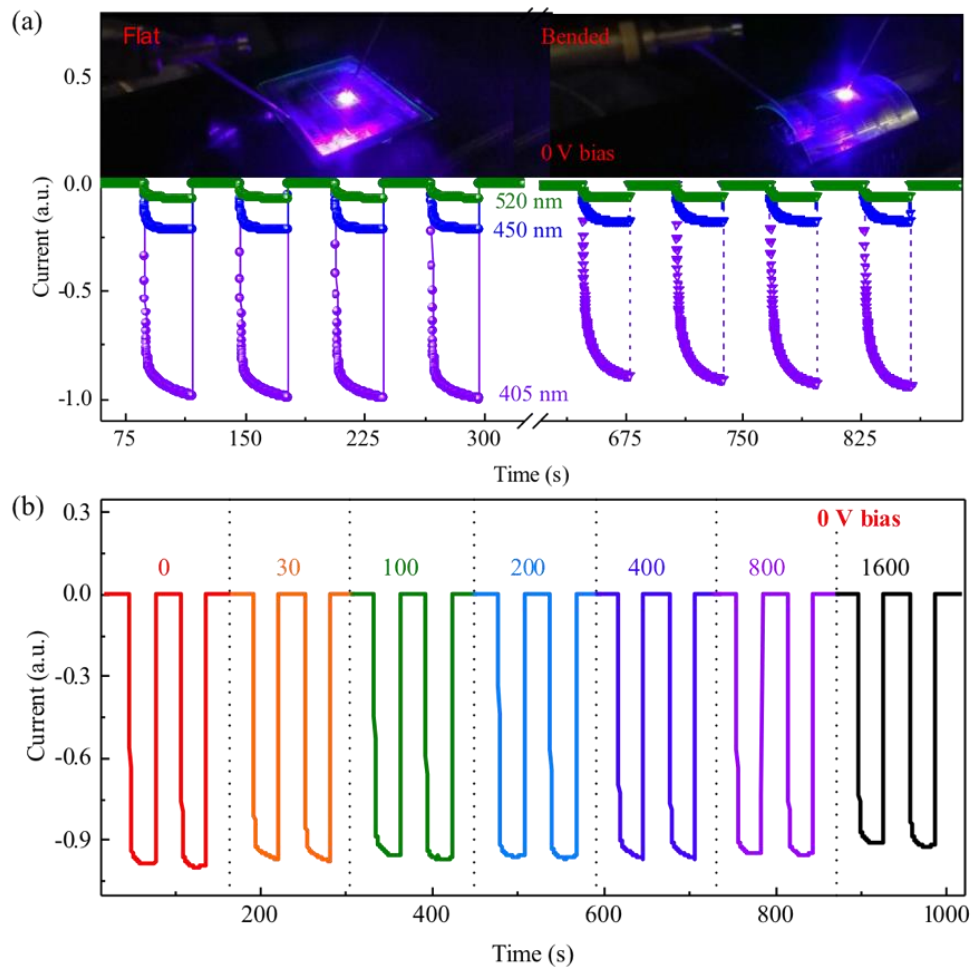


**Figure 5.26** (a) The switching photoresponse at  $0^\circ$  (solid line) and  $60^\circ$  (dashed line), employing a 405 nm, 450 nm and 520 nm laser as light source, respectively. The insets are digital images of the device when tested. (b) The normalised transient photoresponse under up to 1600 bending cycles, with excitation of 405 nm laser diode ( $13.2 \text{ mW cm}^{-2}$ ).<sup>[15]</sup>

The long-term stability was subsequently examined after storing the device in ambient atmosphere for 7 months. The typical  $I$ - $V$  features are shown in Figure 5.27a, revealing a good response to the light illumination. Comparing the photoresponse before and after under different wavelengths of illumination at 0 V, it is found that  $\sim 91\%$  of photocurrent was achieved after 7 months of storage, as shown in Figure 5.27b. Figure 5.27c demonstrates the  $I$ - $t$  curves applied with different bias voltages after 7 months, suggesting outstanding environmental stability.

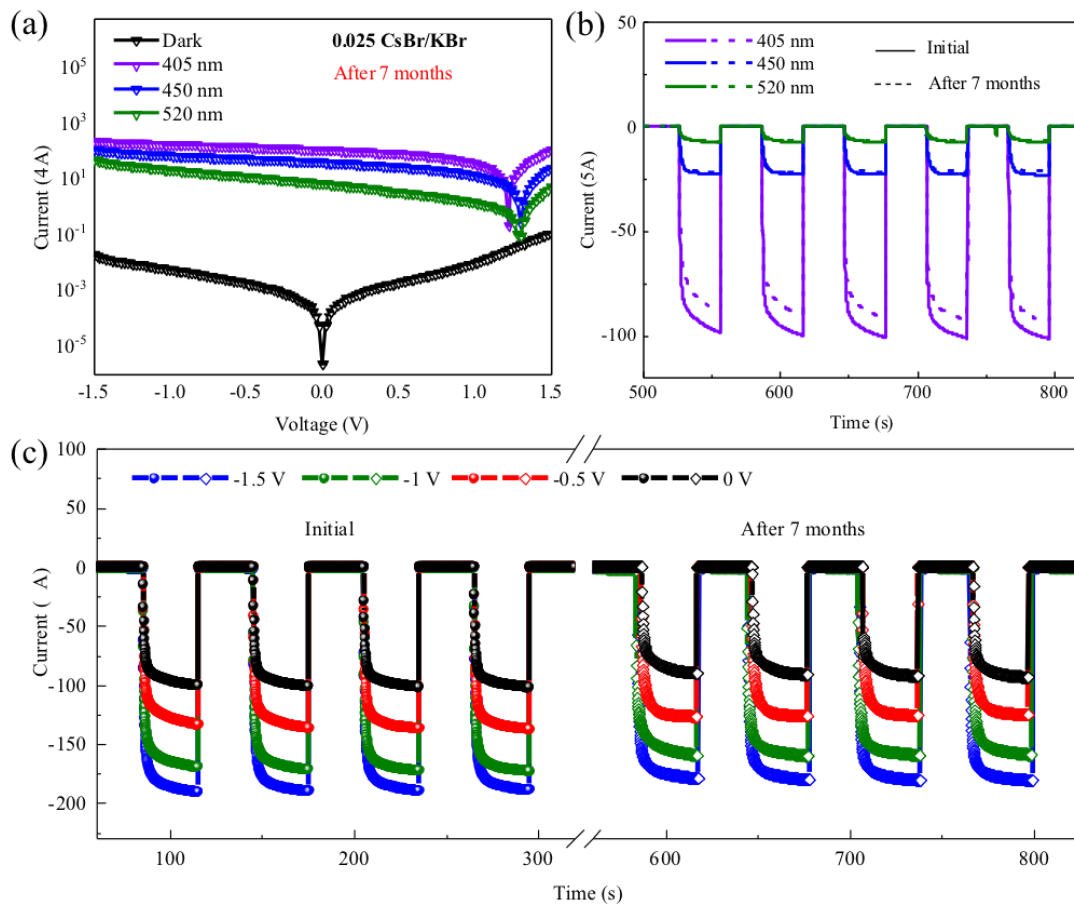


**Figure 5.27** The long-term stability characterisations of  $\text{CsPbBr}_3$  QD photodetector with assistance of 0.025 CsBr/KBr. (a)  $I$ - $V$  curves under illumination of 405 nm (purple), 450 nm

(blue) and 520 nm (green) lasers. (b) The transient photoresponse under self-powered mode. (c) Time-dependent photoresponse at different biases under 405 nm laser illumination.

#### 5.4.6 Performance Uniformity

Last but not least, the uniformity of device performance of the flexible photodetector arrays was examined. Figure 5.28a shows an optical image of an individual section, which comprises 8 x 11 pixels as marked by the dashed lines. The optimal photodetector arrays were characterised under the self-powered mode employing the 405 nm laser as the light source. Figures 5.28b–d show the performance distributions (including  $R$ ,  $D^*$  and  $V_{oc}$ ) of each pixel. Based on the colour variation in the map, over 80% of devices exhibited a similar performance, revealing a uniform photoresponse.

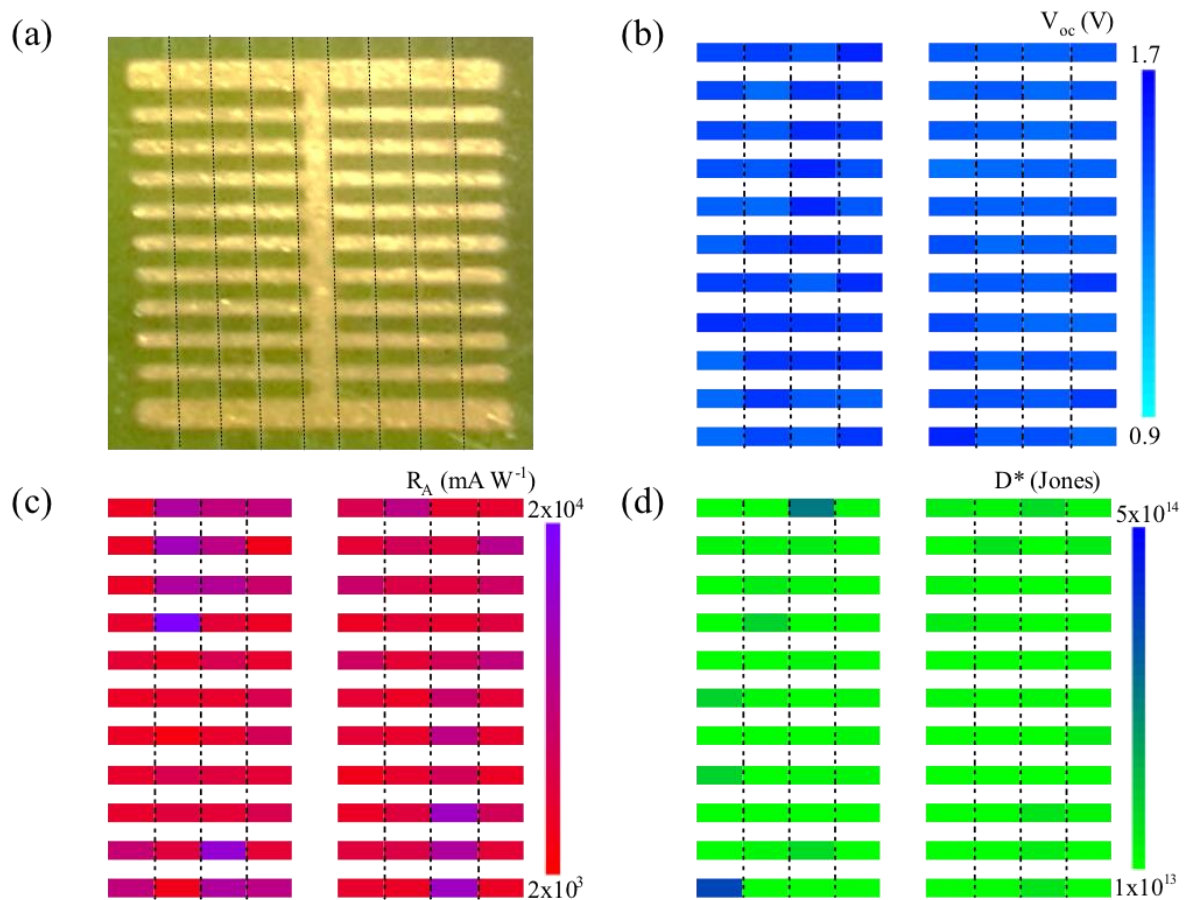


**Figure 5.28** (a) Optical image of a single section in photodetector arrays. The performance mapping for the corresponding section, including (b) open-circuit voltage, (c) responsivity and (d) detectivity.

## 5.5 Summary

In summary, the CsPbBr<sub>3</sub> QDs were effectively optimised by introducing CsBr/KBr additives, especially when the fraction was 0.025. The mediated QD film exhibited improved morphological characteristics of smooth surface and dense film. In addition, a higher crystallinity with reduced defect densities and better optical properties was achieved, resulting in a more efficient carrier transport. An open-circuit voltage as high as 1.3 V, responsivity of 10.1 A W<sup>-1</sup>, specific detectivity reaching up to  $9.35 \times 10^{13}$  Jones and a large on/off ratio were demonstrated in the flexible photodetector arrays with the optimal fraction of CsBr/KBr, with no external power supply. Meanwhile, an excellent mechanical flexibility and electrical stability with marginal degradation were observed when testing after 1600 bending cycles. A uniform distribution of device performance was also achieved, which is promising for practical imaging systems.

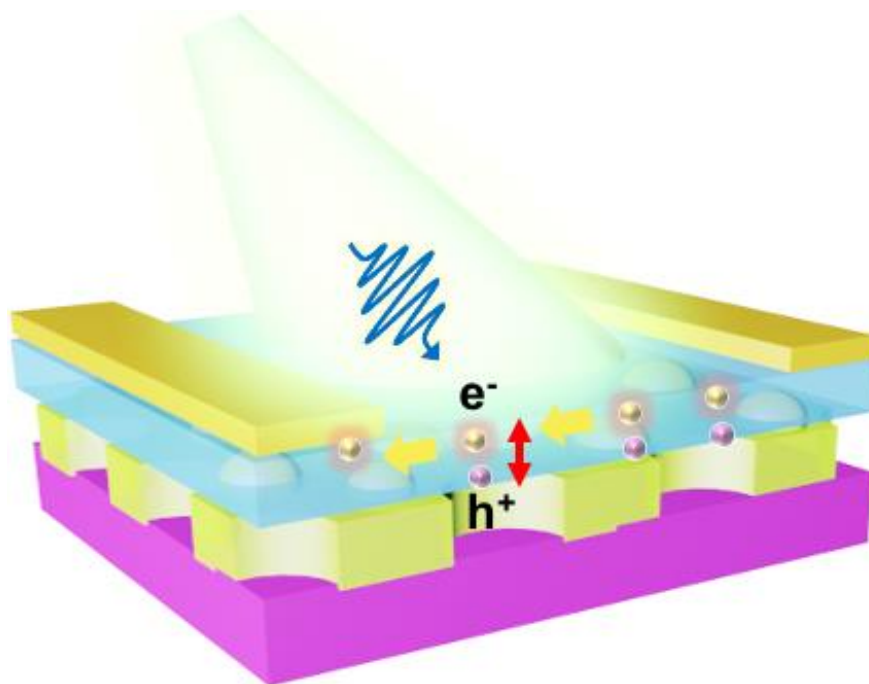
## 5.6 References

- [1] K. Xu, Y. Lu, K. Takei, *Adv. Mater. Technol.* **2019**, *4*, 1800628.
- [2] Z. Bao, X. Chen, *Adv. Mater.* **2016**, *28*, 4177.
- [3] T. Zhang, F. Wang, P. Zhang, Y. Wang, H. Chen, J. Li, J. Wu, L. Chen, Z. D. Chen, S. Li, *Nanoscale* **2019**, *11*, 2871.
- [4] G. Azzellino, A. Grimoldi, M. Binda, M. Caironi, D. Natali, M. Sampietro, *Adv. Mater.* **2013**, *25*, 6829.
- [5] G. Konstantatos, E. H. Sargent, *Nat. Nanotechnol.* **2010**, *5*, 391.
- [6] D. J. Gundlach, T. N. Jackson, D. G. Schlom, S. F. Nelson, *Appl. Phys. Lett.* **1999**, *74*, 3302.
- [7] C. Yi, J. Luo, S. Meloni, A. Boziki, N. Ashari-Astani, C. Grätzel, S. M. Zakeeruddin, U. Röthlisberger, M. Grätzel, *Energy Environ. Sci.* **2016**, *9*, 656.
- [8] J. K. Nam, S. U. Chai, W. Cha, Y. J. Choi, W. Kim, M. S. Jung, J. Kwon, D. Kim, J. H. Park, *Nano Lett.* **2017**, *17*, 2028.
- [9] H. Wang, X. Zhang, Q. Wu, F. Cao, D. Yang, Y. Shang, Z. Ning, W. Zhang, W. Zheng, Y. Yan, S. V Kershaw, L. Zhang, A. L. Rogach, X. Yang, *Nat. Commun.* **2019**, *10*, 665.
- [10] M. Liu, G. Zhong, Y. Yin, J. Miao, K. Li, C. Wang, X. Xu, C. Shen, H. Meng, *Adv. Sci.* **2017**, *4*, 1700335.
- [11] C. Liu, W. Li, H. Li, H. Wang, C. Zhang, Y. Yang, X. Gao, Q. Xue, H. Yip, J. Fan, R. E. I. Schropp, Y. Mai, *Adv. Energy Mater.* **2019**, *9*, 1803572.
- [12] J.-N. Yang, Y. Song, J.-S. Yao, K.-H. Wang, J.-J. Wang, B.-S. Zhu, M.-M. Yao, S. U. Rahman, Y.-F. Lan, F.-J. Fan, H.-B. Yao, *J. Am. Chem. Soc.* **2020**, *142*, 2956.
- [13] Q. D. Ling, S. Li, E. T. Kang, K. G. Neoh, B. Liu, W. Huang, *Surf. Interface Anal.* **2002**, *33*, 552.
- [14] K. Yan, M. Long, T. Zhang, Z. Wei, H. Chen, S. Yang, J. Xu, *J. Am. Chem. Soc.* **2015**,

- 137, 4460.
- [15] K. Shen, H. Xu, X. Li, J. Guo, S. Sathasivam, M. Wang, A. Ren, K. L. Choy, I. P. Parkin, Z. Guo, J. Wu, *Adv. Mater.* **2020**, 32, 2000004.
  - [16] L. Zhang, X. Yang, Q. Jiang, P. Wang, Z. Yin, X. Zhang, H. Tan, Y. (Michael) Yang, M. Wei, B. R. Sutherland, E. H. Sargent, J. You, *Nat. Commun.* **2017**, 8, 15640.
  - [17] S. Tsunekawa, T. Fukuda, A. Kasuya, *J. Appl. Phys.* **2000**, 87, 1318.
  - [18] P. Zhao, W. Yin, M. Kim, M. Han, Y. J. Song, T. K. Ahn, H. S. Jung, *J. Mater. Chem. A* **2017**, 5, 7905.
  - [19] X. Li, Y. Wu, S. Zhang, B. Cai, Y. Gu, J. Song, H. Zeng, *Adv. Funct. Mater.* **2016**, 26, 2435.
  - [20] Y. Wu, C. Wei, X. Li, Y. Li, S. Qiu, W. Shen, B. Cai, Z. Sun, D. Yang, Z. Deng, H. Zeng, *ACS Energy Lett.* **2018**, 3, 2030.
  - [21] I. Lignos, S. Stavrakis, G. Nedelcu, L. Protesescu, A. J. Demello, M. V. Kovalenko, *Nano Lett.* **2016**, 16, 1869.
  - [22] P. Liu, W. Chen, W. Wang, B. Xu, D. Wu, J. Hao, W. Cao, F. Fang, Y. Li, Y. Zeng, R. Pan, S. Chen, W. Cao, X. W. Sun, K. Wang, *Chem. Mater.* **2017**, 29, 5168.
  - [23] J. Cao, S. X. Tao, P. A. Bobbert, C.-P. Wong, N. Zhao, *Adv. Mater.* **2018**, 30, 1707350.
  - [24] M. Abdi-Jalebi, Z. Andaji-Garmaroudi, S. Cacovich, C. Stavrakas, B. Philippe, J. M. Richter, M. Alsari, E. P. Booker, E. M. Hutter, A. J. Pearson, S. Lilliu, T. J. Savenije, H. Rensmo, G. Divitini, C. Ducati, R. H. Friend, S. D. Stranks, *Nature* **2018**, 555, 497.
  - [25] Z. Zhang, Y. Zhu, W. Wang, W. Zheng, R. Lin, F. Huang, *J. Mater. Chem. C* **2018**, 6, 446.
  - [26] C. H. Kang, I. Dursun, G. Liu, L. Sinatra, X. Sun, M. Kong, J. Pan, P. Maity, E.-N. Ooi, T. K. Ng, O. F. Mohammed, O. M. Bakr, B. S. Ooi, *Light Sci. Appl.* **2019**, 8, 94.
  - [27] V. D. Mihailetschi, P. W. M. Blom, J. C. Hummelen, M. T. Rispens, *J. Appl. Phys.* **2003**,

- 94, 6849.
- [28] G. G. Malliaras, J. R. Salem, P. J. Brock, J. C. Scott, *J. Appl. Phys.* **1998**, *84*, 1583.
  - [29] Q. Chen, L. Mao, Y. Li, T. Kong, N. Wu, C. Ma, S. Bai, Y. Jin, D. Wu, W. Lu, B. Wang, L. Chen, *Nat. Commun.* **2015**, *6*, 7745.
  - [30] W. Ye, J. Xiang, F. Huang, D. Zhong, *Mater. Res. Express* **2018**, *5*, 085506.
  - [31] C. Li, C. Han, Y. Zhang, Z. Zang, M. Wang, X. Tang, J. Du, *Sol. Energy Mater. Sol. Cells* **2017**, *172*, 341.
  - [32] B. Yang, F. Zhang, J. Chen, S. Yang, X. Xia, T. Pullerits, W. Deng, K. Han, *Adv. Mater.* **2017**, *29*, 1703758.
  - [33] X. Li, D. Yu, J. Chen, Y. Wang, F. Cao, Y. Wei, Y. Wu, L. Wang, Y. Zhu, Z. Sun, J. Ji, Y. Shen, H. Sun, H. Zeng, *ACS Nano* **2017**, *11*, 2015.
  - [34] M. I. Saidaminov, M. A. Haque, J. Almutlaq, S. Sarmah, X.-H. Miao, R. Begum, A. A. Zhumeckenov, I. Dursun, N. Cho, B. Murali, O. F. Mohammed, T. Wu, O. M. Bakr, *Adv. Opt. Mater.* **2017**, *5*, 1600704.
  - [35] F. Cao, L. Meng, M. Wang, W. Tian, L. Li, *Adv. Mater.* **2019**, *31*, 1806725.
  - [36] W. Wu, X. Wang, X. Han, Z. Yang, G. Gao, Y. Zhang, J. Hu, Y. Tan, A. Pan, C. Pan, *Adv. Mater.* **2019**, *31*, 1805913.
  - [37] H. Sun, T. Lei, W. Tian, F. Cao, J. Xiong, L. Li, *Small* **2017**, *13*, 1701042.

# CHAPTER 6. THE STUDY OF HYBRID PLASMONIC NANOSTRUCTURE-BASED ALL-INORGANIC PEROVSKITE PHOTODETECTORS



## 6.1 Introduction

All-inorganic perovskites,  $\text{CsPbBr}_3$  QDs, have been proven to have improved stability and have demonstrated an excellent performance in solar cells, photodetectors and LEDs.<sup>[1–5]</sup> In addition, they can be fabricated on a large scale, which is beneficial for the potential commercialisation of photodetectors.<sup>[6,7]</sup> In order to address the issues of high trap densities and poor carrier transport in  $\text{CsPbBr}_3$  QDs,<sup>[8]</sup> a ZnO NP decoration strategy and CsBr/KBr additive treatment have been explored, as explained in Chapters 4 and 5. Although these two schemes effectively improved the device performance, additional challenges still exist, such as extra light consumption or limited absorption volume.<sup>[9]</sup>

It has been demonstrated that the introduction of metallic NPs can effectively strengthen the near-surface EM fields, leading to a spontaneous concentration of light beams on the active layer. This strategy has potential in enhancing the photoresponse of CsPbBr<sub>3</sub> QD photodetectors. To date, various metallic NPs have been employed in perovskite-based photodetectors, e.g. Au NPs/ CsPbBr<sub>3</sub> QDs.<sup>[10,11]</sup> Moreover, Ag NPs are expected to exhibit a more radical light-matter interaction, owing to their high-quality-factor plasmonic property.<sup>[12]</sup> Apart from the aforementioned metals, excellent resonant EM features can also be demonstrated on non-noble metals (e.g. Al and Cu).<sup>[13]</sup> However, a large quantity of light easily escapes, as the light can only be confined to the near-field of metallic NPs.

Therefore, in order to improve the device performance, an AAO structure was employed in the CsPbBr<sub>3</sub> QD photodetectors. AAO was initially proposed to reduce the light consumption during the transmission. With the participation of metallic NPs, the cyclic utilisation of incident light can be expected. With the help of both geometrical and metallic NP control, the optimal photodetectors exhibited an improved photoresponse.

## 6.2 Pore-Size Dependence of Ag/AAO Nanostructure

The pore size of AAO nanostructures is important for light confinement, and significantly affects the device performance. Therefore, Ag/AAO nanostructures with various pore sizes of 120 nm, 170 nm and 220 nm ( $\pm 5$  nm) were demonstrated to investigate the induced size effects. When performing SEM measurements (Figure 6.1), it could be seen that Ag NPs were uniformly distributed on each AAO nanostructure. Meanwhile, the average diameters of Ag NPs exhibited an inverse proportional dependence on the pore sizes. Specifically, the average diameters of Ag NPs were observed to be reduced from 29.6 nm to 23.3 nm when increasing the pore size, as shown in the insets.

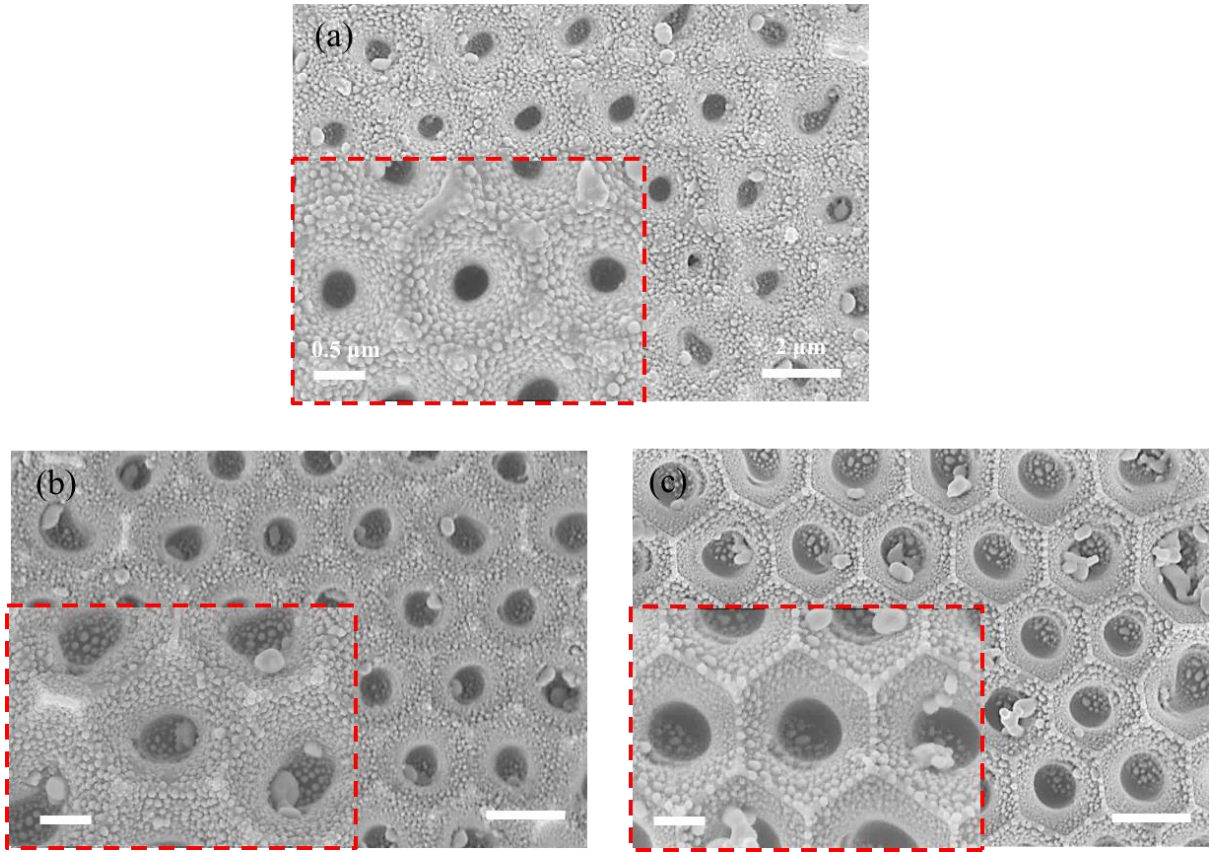


**Figure 6.1** SEM images of the Ag/AAO structures with varied pore sizes. (a) 120 nm, (b) 170 nm and (c) 220 nm. Insets are enlarged SEM images.

This reduced dimension can be attributed to the aggregation of Ag NPs. By applying the diffusion-limited agglomeration model, the diffusion length of Ag NPs ( $l_{Ag}$ ) can be expressed as<sup>[14]</sup>

$$l_{Ag} = \sqrt{D_0 \times \exp(-\gamma_{Ag}/kT) \times \tau} \quad \text{Equation 6.1}$$

where  $D_0$  denotes the ideal diffusivity,  $\gamma_{Ag}$  represents the activation energy of Ag,  $k$  is the Boltzmann constant,  $T$  is the annealing temperature, and  $\tau$  is the residence time.<sup>[15]</sup> In this case,  $T$  and  $\tau$  are kept the same for each matrix, and  $l_{Ag}$  is accordingly dependent on  $\gamma_{Ag}$ . Owing to the enlarged pore size, the interaction between AAO and Ag NPs was weakened, as well as introducing additional vacancies, which resulted in a prolonged  $l_{Ag}$ . Therefore, Ag atoms were likely aggregated on the sidewalls of AAO nanostructures.

Figure 6.2a shows the reflectance of AAO nanostructures in the absence and presence of Ag NPs as a function of the pore size. It is worth noting that the reflectance was gradually inhibited when increasing the pore size, and further reduced after the decoration of Ag NPs. This is explained by Figure 6.2c. With the larger pore size, the reflected light waves from the Al back-reflecting layers are easily overlapped, resulting in multiple interferences. With the help of multiple interferences the light loss during transmission can be effectively suppressed. Therefore, the light can be re-utilised, which is favourable for constructing high-performance photodetectors. Taking into account the negligible contribution of the reflected light beams, the overall reflectance ( $R(\lambda)$ ) can be simply expressed as<sup>[16]</sup>

$$R(\lambda) = \left( R_1 + R_2 + 2\sqrt{R_1 R_2} \cos \frac{4\pi d n_{AAO} \cos \theta_1}{\lambda} \right) \times \exp(-\alpha) \quad \text{Equation 6.2}$$

where  $R_1$  and  $R_2$  denote the reflected light,  $d$  is the thickness of the AAO layers, and  $\theta_1$  and  $n_{AAO}$  represent the angle of incident light and refractive index, respectively. The  $\exp(-\alpha)$  is the scattering-induced light loss factor, which can be displayed as  $\alpha = \rho \times \delta/\lambda$ .<sup>[17]</sup> Here,  $\rho$  is the fitting constant and  $\delta$  is the surface roughness, which gradually increased along with the extended pore size. Originating from the increased light scattering, the average reflectance fell from 6.8% to 2.1% with the expansion of pore size (Figure 6.2b). As mentioned previously, the reflectance was further reduced with the incorporation of Ag NPs, which can be attributed to the enhanced localised surface scattering, as illustrated in Figure 6.2d. Meanwhile, the existence of Ag NPs resulted in further reduction of the reflectance for each sample, as a result of the enhanced localised surface scattering (Figure 6.2d).<sup>[18]</sup>

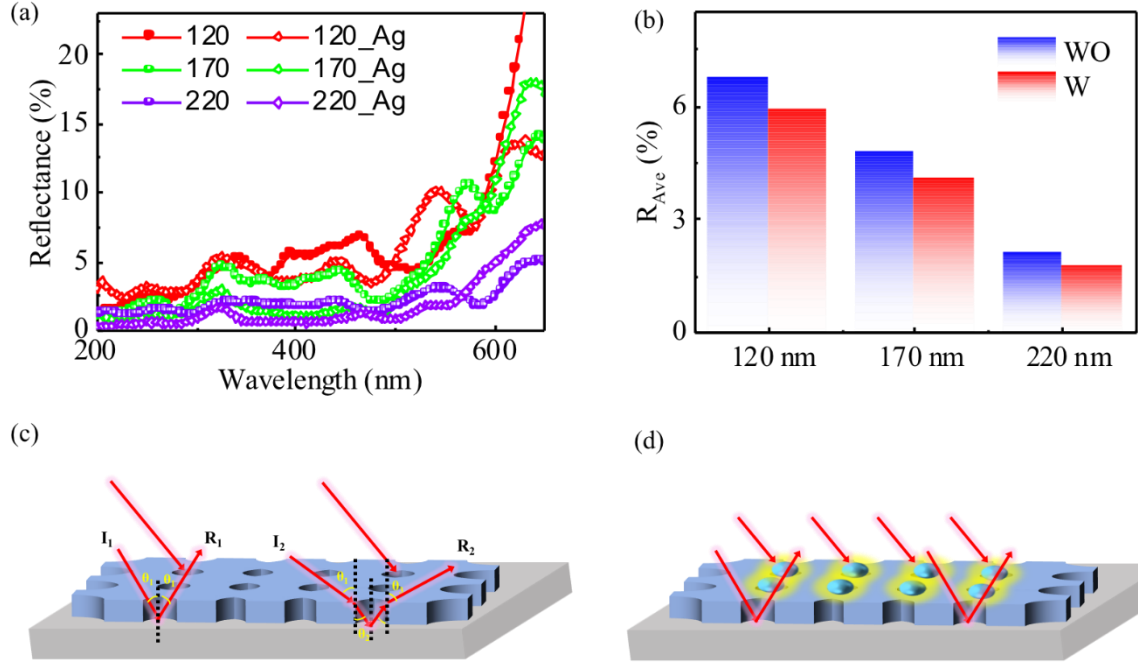


**Figure 6.2** (a) Reflectance spectra and (b) average reflectance of the AAO matrices with and without Ag NP decoration. The corresponding schematic diagrams of light-matter interaction within the AAO matrices (c) without and (d) with metallic NPs.

All-inorganic CsPbBr<sub>3</sub> QDs, as an emerging photoelectric material, were employed in this work to explore the enhancement of pore size adjustment. Accordingly, 450 nm QD thin films were deposited on Ag NP-decorated AAO nanostructures with various pore sizes. It is worth noting that CsPbBr<sub>3</sub> QDs were synthesised under ambient conditions, as described in Chapter 3. As shown in Figure 6.3, the QD films were compact and exhibited a good morphological continuity in all samples, suggesting the negligible impact of the AAO geometry on the film morphology.

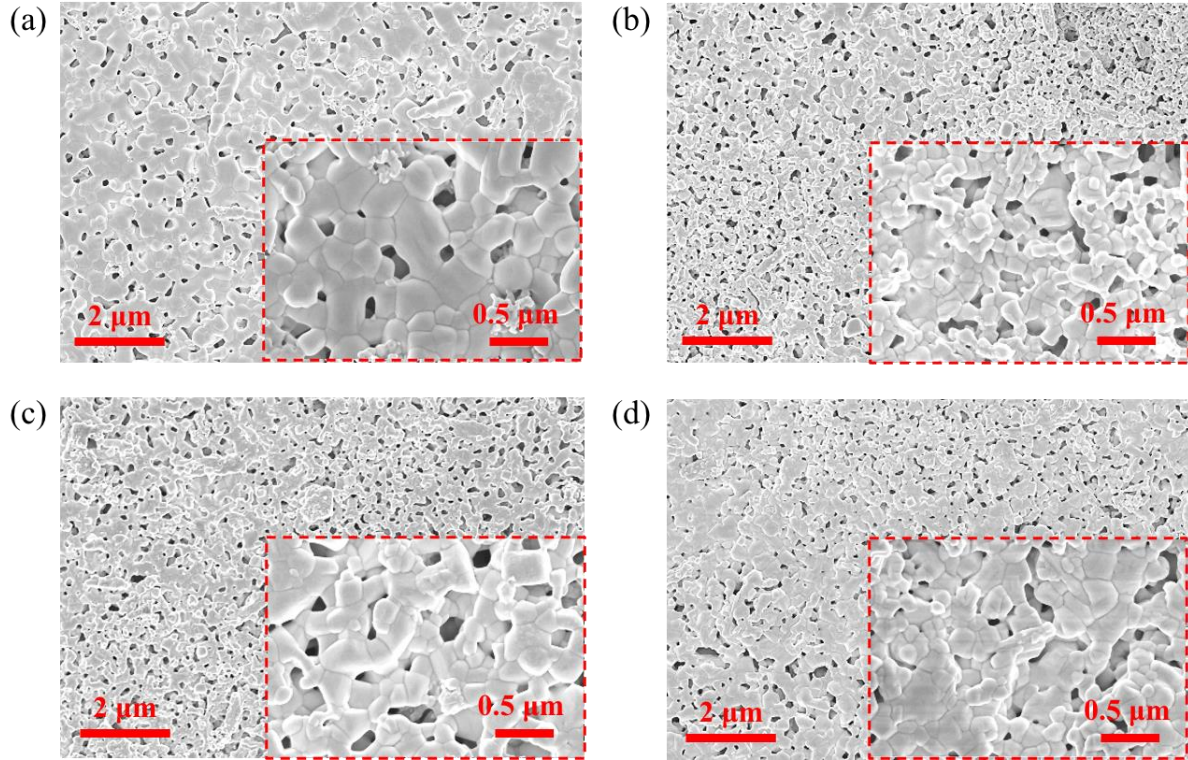


**Figure 6.3** SEM images of the  $\text{CsPbBr}_3$  QD films on Ag/AAO substrates with different pore sizes. (a) Bare AAO, Ag/AAO with pore sizes of (b) 120, (c) 170 and (d) 220 nm. Insets are the corresponding SEM images of the localised morphologies.

The crystal structure was subsequently examined by XRD, as shown in Figure 6.4. The position of characteristic peaks remained the same for all samples, and there were no additional peaks observed. This confirms that the geometry of the AAO does not impact on the phase purity, consistent with morphological measurements.

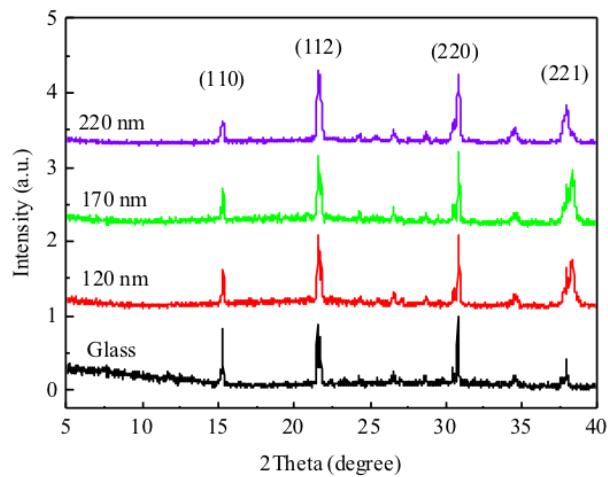


**Figure 6.4** XRD measurements of CsPbBr<sub>3</sub> QD samples on glass and Ag/AAO plasmonic nanostructures with different pore sizes.

Accordingly, QD photodetectors based on Ag/AAO matrices were fabricated to further investigate the induced impact by varying the pore sizes. A schematic illustration of the fabrication process is shown in Figure 6.5, including AAO fabrication, NP assembly, active layer coating and electrode deposition. The detailed methodology of the metallic decorated AAO structure was described in Chapter 3.

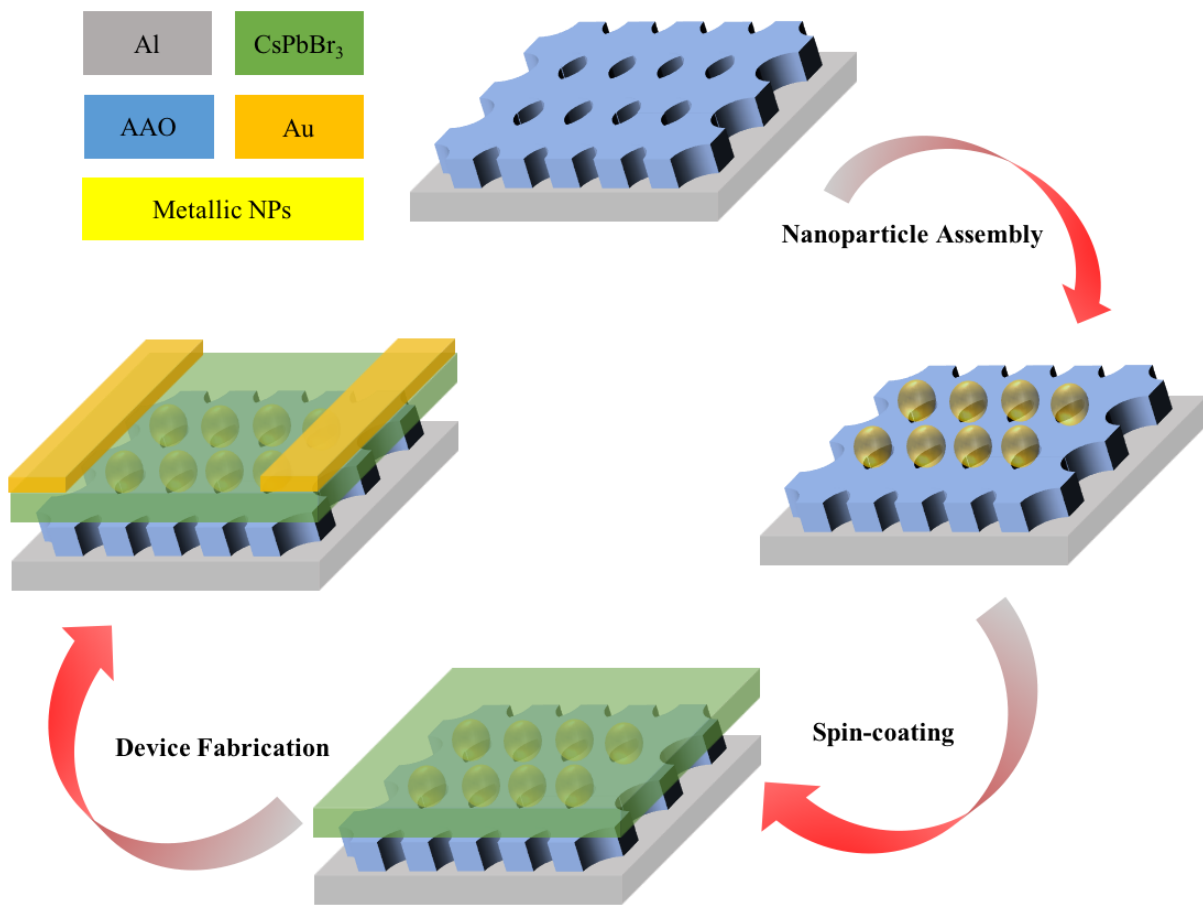


**Figure 6.5** Schematic fabrication of the perovskite AAO structure-based photodetectors. Reproduced from ref. [19] with permission from John Wiley and Sons, copyright 2020.

Photoresponsive features of the QD-based Ag/AAO photodetectors with pore sizes of 120 nm, 170 nm and 220 nm were examined, as shown in Figure 6.6. A photodetector fabricated on bare glass was employed as a control device. The dark current demonstrated a slight increase but remained <4 nA when enlarging the pore size from 120 nm to 220 nm, as

displayed in Figure 6.6a. This can be attributed to the higher conductivity of Ag NPs.<sup>[20]</sup> In terms of the photocurrent, it was significantly amplified when introducing the Ag/AAO matrix. As shown in Figure 6.6b, the current increased from ~10 nA to ~200 nA at 1 V bias voltage under 490 nm laser illumination, owing to the effective light utilisation induced by the spatial coupling. Moreover, when increasing the pore size from 120 nm to 220 nm, the light current reached 278 nA, which was over 20-fold higher than that of the control device. It is worth noting that the improvement in current became less significant from 170 nm to 220 nm, implying the limit of pore size.

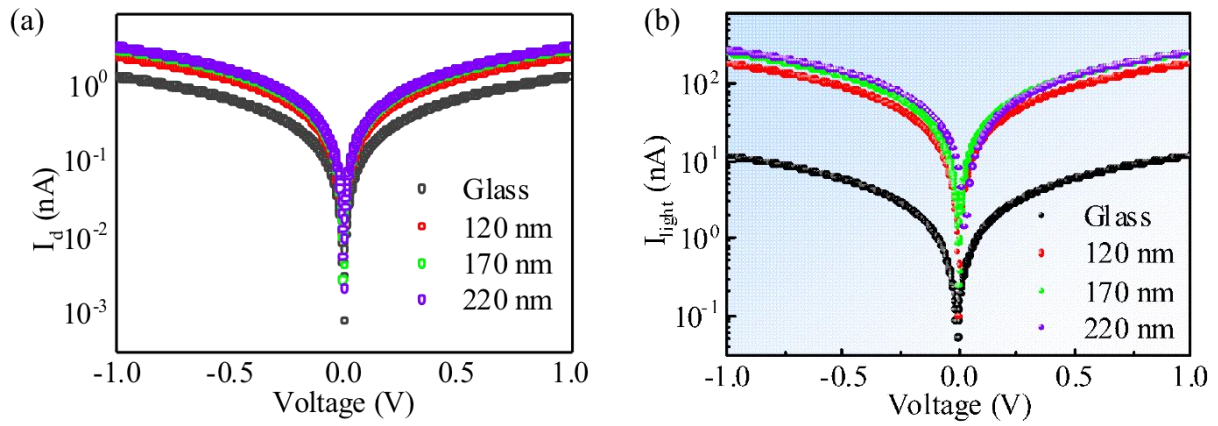


**Figure 6.6** *I*-*V* curves of as-fabricated devices (a) in dark and (b) under 490 nm light illumination.

The responsivity (*R*), as one of the critical parameters in photodetectors, was measured at 1 V bias with excitation of a 490 nm laser with power intensity of 13.4 mW cm<sup>-2</sup>. Notably, the active area of each photodetector was 0.8 mm<sup>2</sup>. As shown in Figure 6.7, the trend of pore size-dependent responsivity can be divided into two phases (Phase I and Phase II). In Phase I, the value of *R* dramatically increased from 0.1 mA W<sup>-1</sup> on glass substrate to ~2.5 mA W<sup>-1</sup> on Ag/AAO matrix with a pore size of 170 nm. This 25-fold enhancement confirms the benefits of applying Ag/AAO plasmonic nanostructures. However, *R* slowly reached 2.6 mA W<sup>-1</sup> when increasing the pore size to 220 nm, suggesting a limit of detection ability.

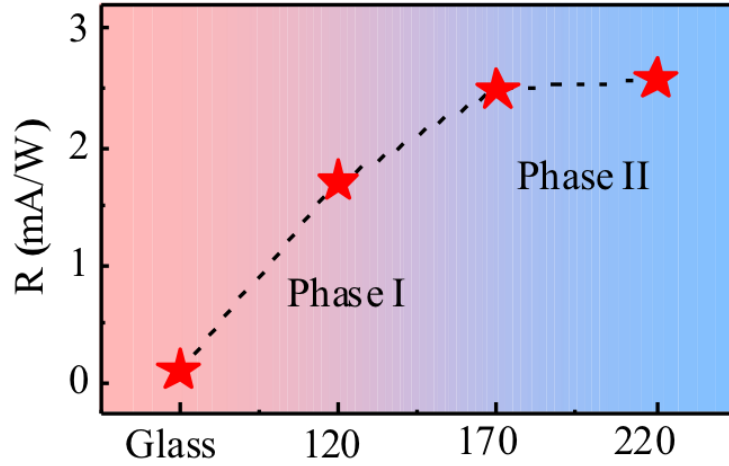


**Figure 6.7** Responsivities of the photodetectors fabricated with difference pore sizes.

The introduction of plasmonic coupling was explained by simulating the cross-sectional EM field distribution of devices using finite-difference time-domain (FDTD, Lumerical) software. As shown in Figure 6.8, with the enlargement of the pore size, an intensified EM field formed around the surface and hence enhanced the light utilisation. This improved EM field may originate from the increase in reflected light confined by Ag NPs, which is strongly supported by the improved photoresponse.

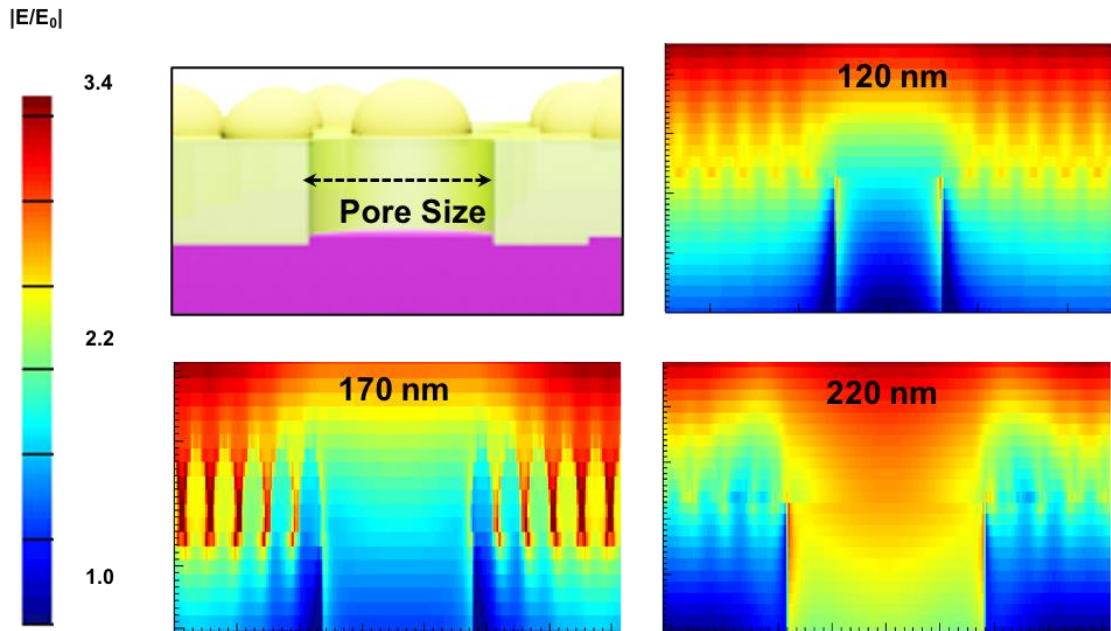


**Figure 6.8** The EM field distribution of the Ag/AAO plasmonic structures as a function of pore sizes. Reproduced from ref. [19] with permission from John Wiley and Sons, copyright 2020.

To gain more insight into the effect of pore size, the transient photoresponse of devices as a function of light intensity was measured. The 490 nm laser was employed as the light source with the light intensity varying from 2.9 mW cm<sup>-2</sup> to 12.1 mW cm<sup>-2</sup>. As shown in Figure 6.9, the devices fabricated on Ag/AAO plasmonic structures exhibited a sensitive and reproducible photoresponse, while those on bare glass demonstrated no obvious response. With the increment of light intensity, the currents were all improved due to the increased population of excited photocarriers. Specifically, the QD device with a pore size of 220 nm exhibited a dominant light current (278 nA) at the intensity of 12.1 mW cm<sup>-2</sup>.

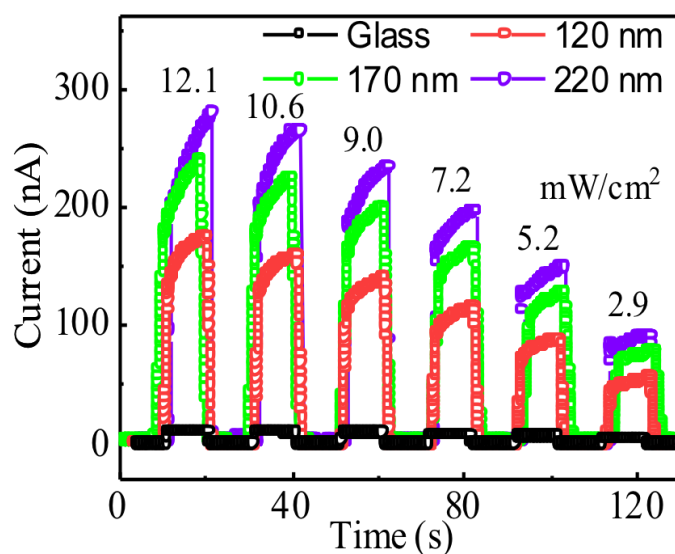


**Figure 6.9** Power-dependent transient photoresponse of CsPbBr<sub>3</sub> QD photodetectors as a function of pore sizes.

The corresponding photocurrent fitting is shown in Figure 6.10a. Each power exponent was over 0.5, indicating a relatively high quality of CsPbBr<sub>3</sub> QD thin films with fewer defects, and an efficient carrier generation and recombination process.<sup>[21]</sup> It is worth noting that the power exponent increased with the expansion of pore size, suggesting more efficient electron-hole pair generation and recombination enabled by spatial plasmonic coupling.<sup>[22]</sup> Accordingly, the highest current was delivered in photodetectors with 220 nm pore size, as validated by the

$I$ - $V$  and  $I$ - $t$  curves. The improvement in  $R$  is also observed in Figure 6.10b, which increased by over 30-fold compared to the photodetector on glass substrate, further confirming the advantages of the AAO plasmonic nanostructure with improved light-matter interaction.<sup>[23]</sup>

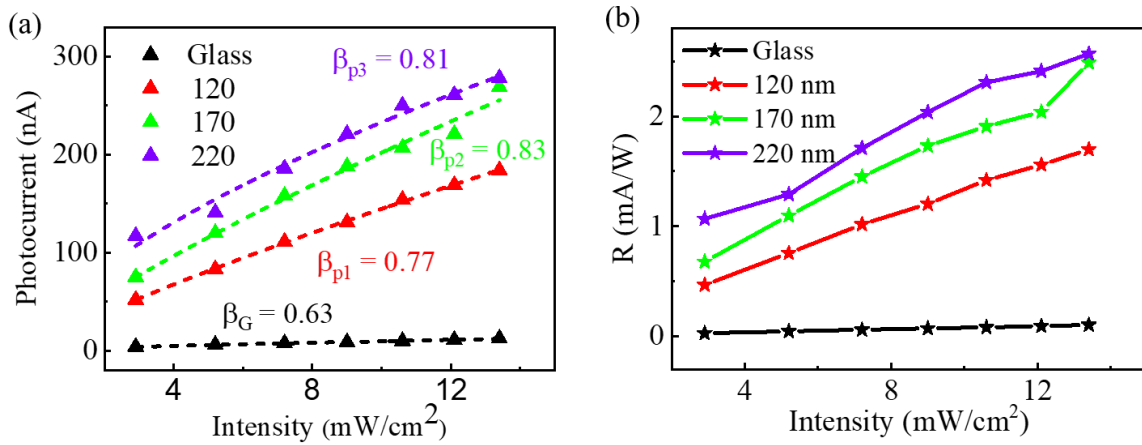


**Figure 6.10** Power-dependent (a) current and (b)  $R$  of the perovskite photodetectors under 490 nm light illumination.

The response speed is measured in a single on-off cycle, as shown in Figure 6.11. The response time of each device was similar, with a value of  $\sim 1$  s.

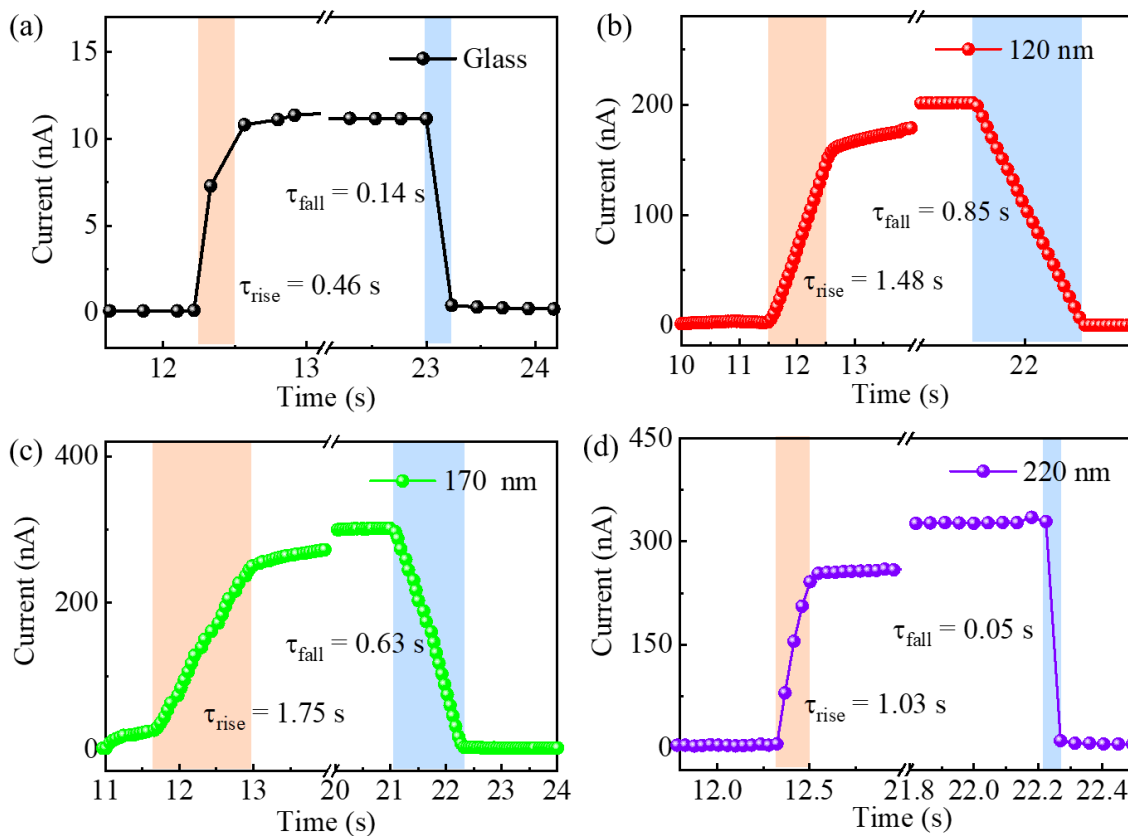


**Figure 6.11** Response speed on different substrates under 365 nm light illumination at 1 V bias.

(a) Bare glass. Ag/AAO with a pore size of (b) 120 nm, (c) 170 nm and (d) 220 nm.

### 6.3 Metallic NP-Decorated AAO Matrix

Although an improved photoresponse was realised in the Ag/AAO nanostructure (220 nm) by optimising the pore size, the response speed was much longer than others. Therefore, another two metallic NPs were employed in the AAO system, i.e. aluminium (Al) and copper (Cu) NPs. As shown in Figure 6.12, the average diameters of each NP formed on AAO could be determined as ~23.3 nm (Ag), ~11.5 nm (Al) and ~21.4 nm (Cu), respectively. The smaller size of the Al NPs can be attributed to their suppressed agglomeration enabled by the limited surface diffusion, as explained by Equation 6.1.<sup>[24]</sup>

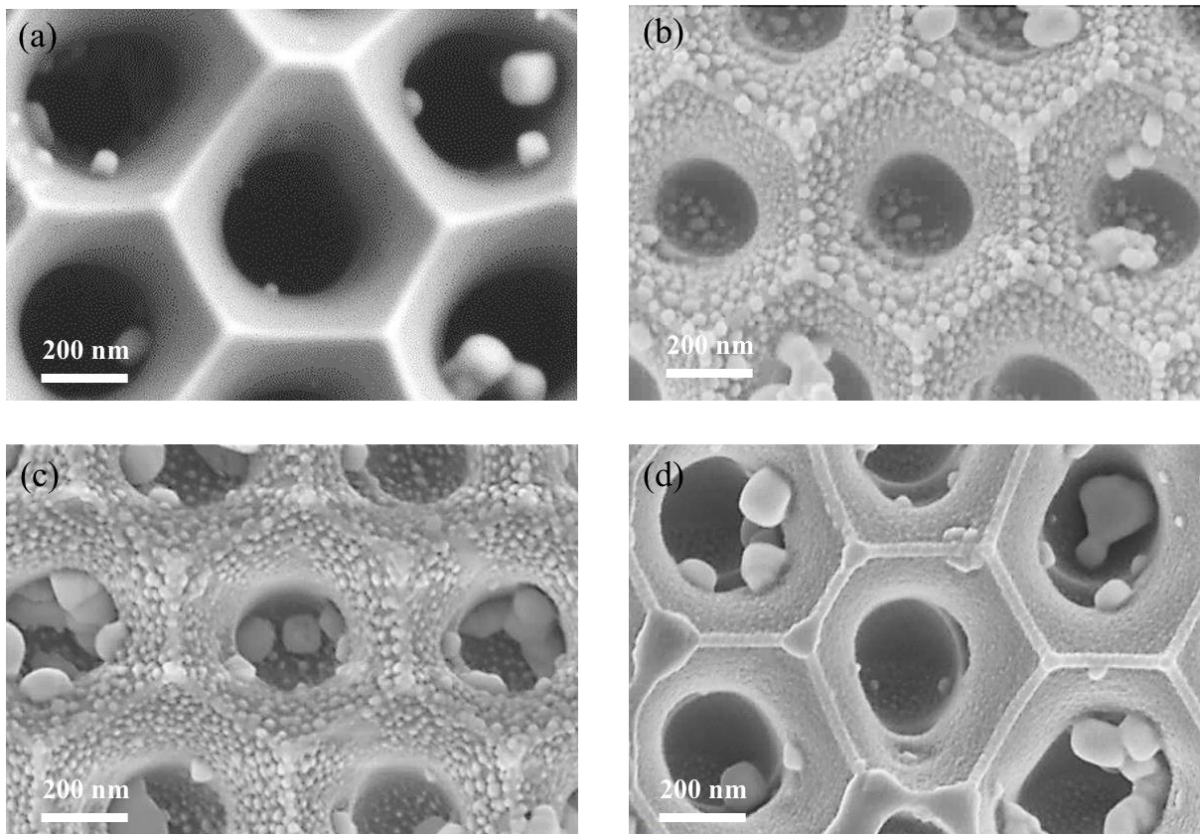


**Figure 6.12** SEM images of (a) bare AAO matrices, (b) Ag/AAO, (c) Al/AAO and (d) Cu/AAO plasmonic nanostructures.

Meanwhile, an attenuation of reflectance was observed, as shown in Figure 6.13. It is worth noting that the Cu NP-decorated AAO matrix exhibited the lowest reflection, which can be attributed to the strong extinction around the characteristic peak of Cu ( $\sim 520$  nm).<sup>[25]</sup>

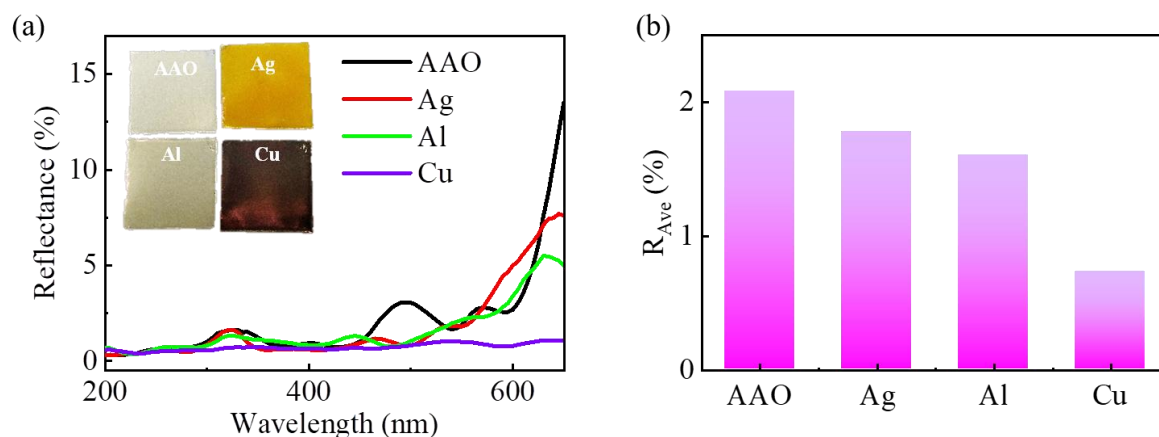


**Figure 6.13** (a) Reflection and (b) average reflectance of the AAO nanostructures decorated with metallic NPs.

The morphological features of CsPbBr<sub>3</sub> QD films on metallic NP-assisted AAO matrices were investigated by conducting SEM. As shown in Figure 6.14, relatively larger pinholes were observed in the Al/AAO plasmonic structure, which can probably be attributed to the introduction of in-plane strain by Al NPs.

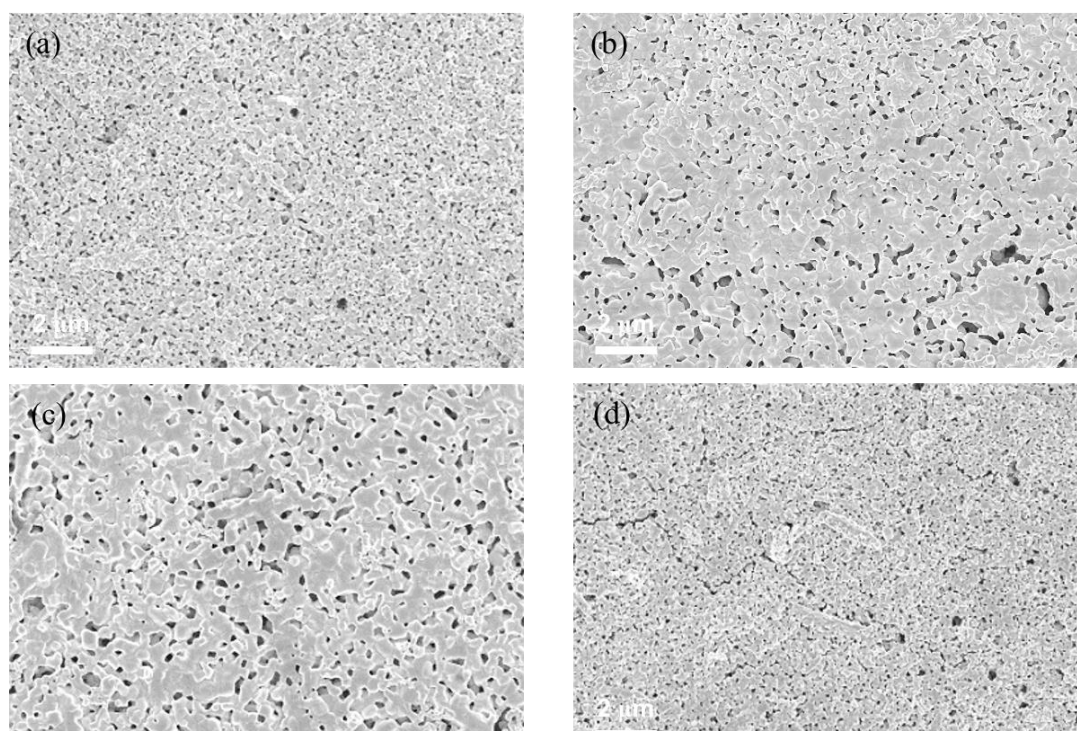


**Figure 6.14** SEM images of CsPbBr<sub>3</sub> QD films on (a) bare AAO matrices, (b) Ag, (c) Al and (d) Cu NP-decorated AAO matrices.

As shown in Figure 6.15a, all samples exhibited the same characteristic peaks, revealing high-quality QD films. Similar reflectance of each film is also observed in Figure 6.15b. In addition, the emission characteristics of films were measured, as shown in Figure 6.15c. It is clear that the film deposited on the Ag/AAO plasmonic nanostructure exhibited the highest PL peak among all samples.

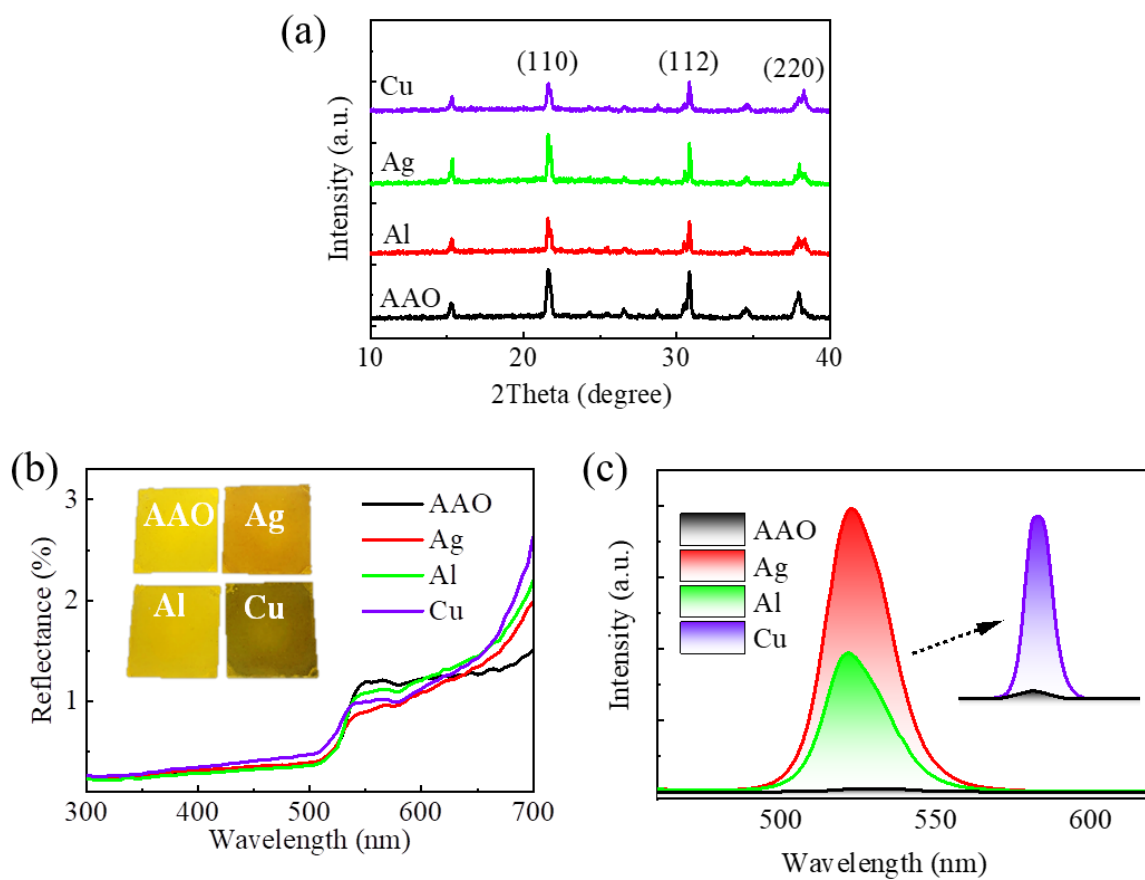


**Figure 6.15** (a) XRD and (b) reflection measurements of the CsPbBr<sub>3</sub> QD film AAO structures with different metallic NPs. Insets are optical images of the samples. (c) Room-temperature PL spectra.

In order to verify the impacts of introducing various metallic NPs, the *I*–*V* characteristics of each device were measured in the dark and under light illumination (490 nm

laser with a power intensity of  $13.4 \text{ mW cm}^{-2}$ ). As shown in Figure 6.16a, the photodetectors with Al and Cu NP decoration exhibited a low level of dark current comparable to that of the device fabricated on bare AAO. In addition, the dark current of the Al and Cu NP-decorated device was also two-fold lower than that of the Ag NP-based device. It is worth noting that the Al NP-assisted photodetector exhibited the highest light current under excitation with the 490 nm laser diode, which reached up to  $\sim 500 \text{ nA}$  (Figure 6.16b).

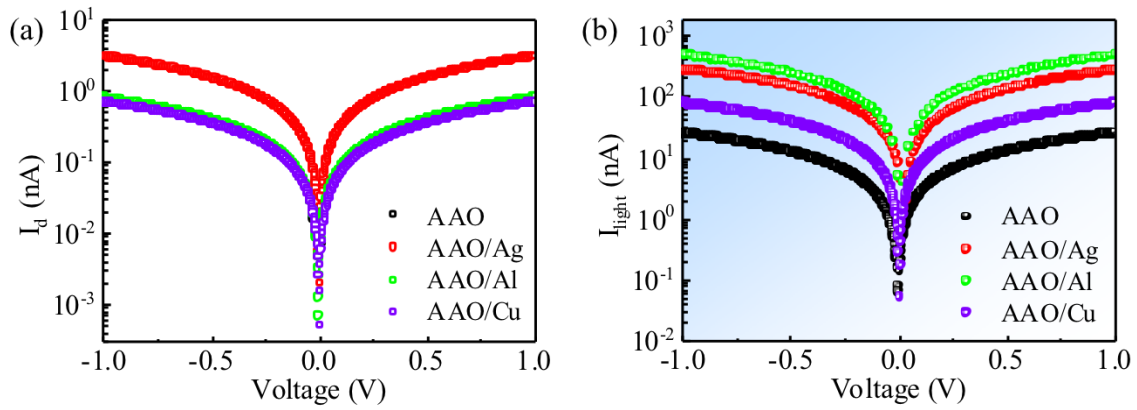


**Figure 6.16** (a) Dark current and (b) light current of the photodetectors under 490 nm light illumination ( $13.4 \text{ mW cm}^{-2}$ ).

Benefiting from the device configuration and optoelectrical properties, a sensitive and reproducible photoresponse was achieved in all devices, as well as excellent on/off switching features, as presented in Figure 6.17a. Except for the Ag NP-treated photodetector, the photocurrent of other devices reached the steady state immediately, implying a fast response speed. As with the results obtained in Figure 6.16a, the steady-state light current produced in the Al/AAO plasmonic structure-based photodetector was improved to as much as  $\sim 510 \text{ nA}$ , much higher than other devices. Moreover, the same device exhibited a  $\sim 50$ -fold improvement in  $R$  ( $4.8 \text{ mA/W}$ ) on applying  $1 \text{ V}$  bias voltage, as well as a boosted EQE from  $0.03\%$  to  $1.21\%$ , as displayed in Figure 6.17b.

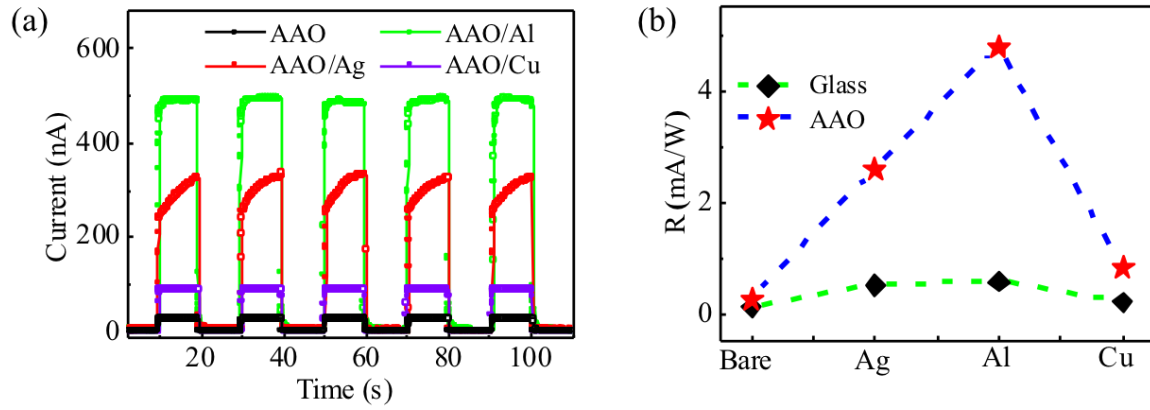


**Figure 6.17** (a) Transient photoresponse of each device at 1 V bias under illumination (490 nm,  $13.4 \text{ mW cm}^{-2}$ ). (b) Responsivity.

Meanwhile, the response time of each of the photodetectors was measured. As shown in Figure 6.18, a slight variation of  $\tau_{\text{rise}}$  and  $\tau_{\text{fall}}$  was observed. Compared to the device on bare AAO, the response time of Al and Cu NP-treated photodetectors was slightly shorter, confirming the benefits of introducing metallic NPs in AAO structures.

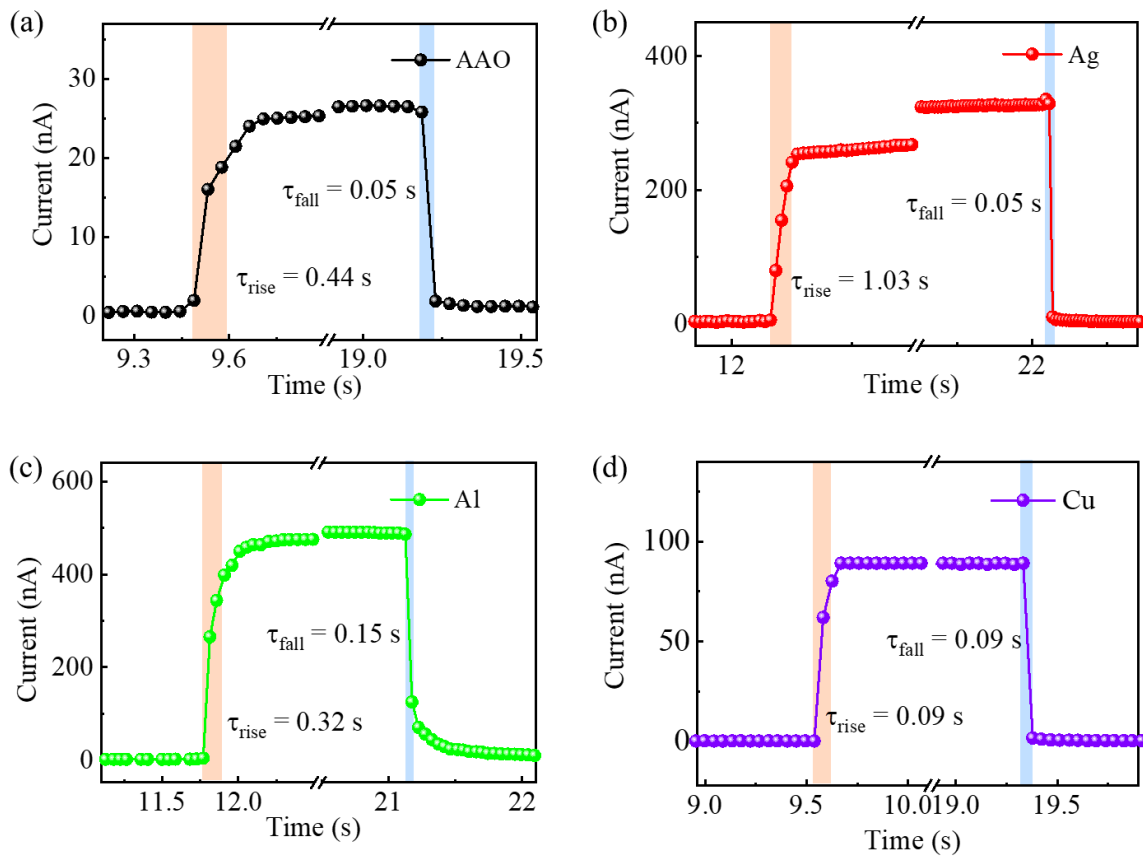


**Figure 6.18** Response time of photodetectors with different structures within a single on-off period under 490 nm light illumination. (a) Bare AAO matrices, (b) Ag/AAO, (c) Al/AAO and (d) Cu/AAO plasmonic nanostructure.

The power dependence feature was investigated by measuring the photoresponse with varied light intensities from  $2.9 \text{ mW cm}^{-2}$  to  $13.4 \text{ mW cm}^{-2}$ , as shown in Figure 6.19a. The power exponent was determined by fitting the data with the power law. They were all higher than 0.59, suggesting an efficient carrier generation, transport and recombination process. As the power intensity increased, all devices exhibited an increased photoresponsivity. In particular, as shown in Figure 6.19b, the Al/AAO plasmonic structured-based photodetector exhibited a dominant responsivity, achieving  $\sim 6 \text{ mA W}^{-1}$  at an intensity of  $13.4 \text{ mW cm}^{-2}$ , which was an improvement of over one order of magnitude. This enhancement can be attributed to the multiple interferences, and further verifies the benefits of Al NP decoration.

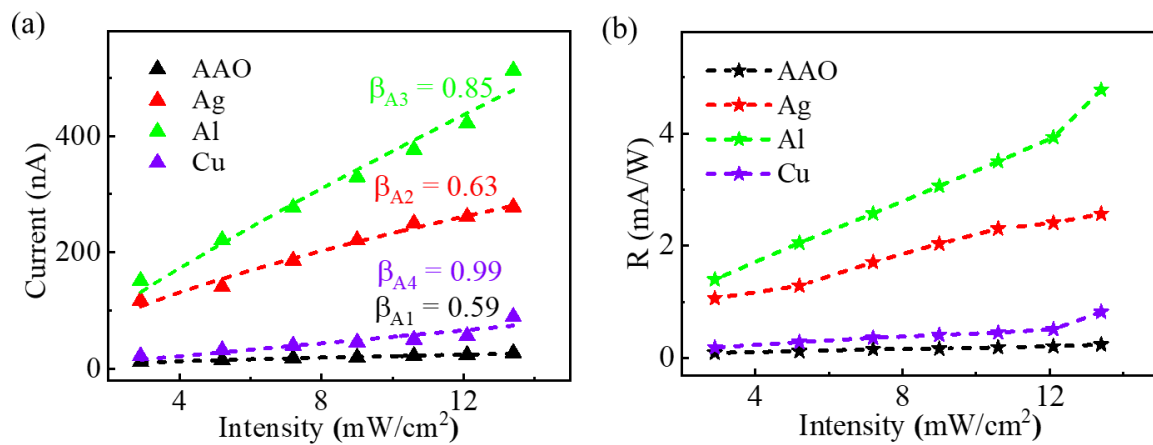


**Figure 6.19** The power-dependent (a) light current and (b) responsivity of photodetectors under 490 nm laser illumination at 1 V bias voltage.

The wavelength-dependent photoresponse and responsivity were subsequently recorded, as shown in Figure 6.20a and 6.20b, respectively. In Figure 6.20a, a distinct wavelength selectivity is demonstrated, as well as reproducible on/off cycles. Moreover, Al/AAO photodetectors exhibited the most sensitive detection for the 490 nm light source, with

a high  $R$  of  $5.9 \text{ mA W}^{-1}$ . Owing to the limitation of the optical bandgap of  $\text{CsPbBr}_3$  QD thin films ( $\sim 2.38 \text{ eV}$ ), it has a limited detection range.

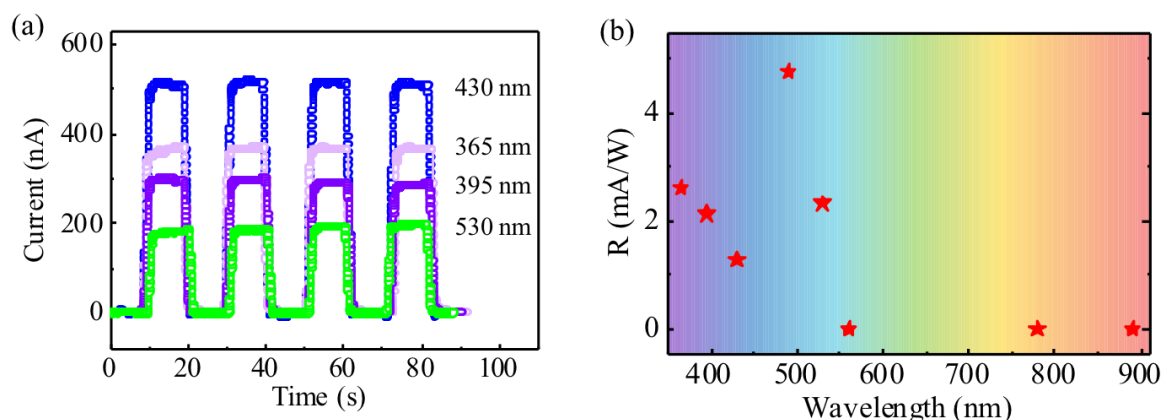


**Figure 6.20** (a) Transient photoresponse and (b)  $R$  of the Al/AAO plasmonic nanostructure photodetectors as a function of incident light wavelength.

## 6.4 Summary

To summarise, metallic NP-decorated AAO nanostructures were employed in perovskite QD photodetectors, with a fine control over the geometry and metallic NPs. Benefiting from the spatial light confinement introduced by optimising the pore size from 120 nm to 220 nm, the light loss was effectively suppressed. Extensive interference was generated as a function of pore size, enabling efficient collection of the transmitted photons and resulting in an improved device performance. Moreover, the photoresponse was further enhanced by introducing Al NPs, promoting the concentration of the incident and reflected light beams. The resulting optimal photodetector showed a 43-fold enhancement in the light current, as well as a short response time ( $\tau_{\text{rise}}$  of 320 ms and  $\tau_{\text{fall}}$  of 150 ms).

## 6.5 References

- [1] E. Yoo, S. V. N. Pammi, K. Y. Kim, T.-V. Dang, J.-H. Eom, Y. J. Choi, S.-G. Yoon, *J. Alloys Compd.* **2019**, *811*, 151999.
- [2] J. Song, J. Li, L. Xu, J. Li, F. Zhang, B. Han, Q. Shan, H. Zeng, *Adv. Mater.* **2018**, *30*, 1800764.
- [3] Q. A. Akkerman, M. Gandini, F. Di Stasio, P. Rastogi, F. Palazon, G. Bertoni, J. M. Ball, M. Prato, A. Petrozza, L. Manna, *Nat. Energy* **2017**, *2*, 16194.
- [4] T. Chiba, Y. Hayashi, H. Ebe, K. Hoshi, J. Sato, S. Sato, Y.-J. Pu, S. Ohisa, J. Kido, *Nat. Photonics* **2018**, *12*, 681.
- [5] J.-N. Yang, Y. Song, J.-S. Yao, K.-H. Wang, J.-J. Wang, B.-S. Zhu, M.-M. Yao, S. U. Rahman, Y.-F. Lan, F.-J. Fan, H.-B. Yao, *J. Am. Chem. Soc.* **2020**, *142*, 2956.
- [6] V.-D. Tran, S. V. N. Pammi, B.-J. Park, Y. Han, C. Jeon, S.-G. Yoon, *Nano Energy* **2019**, *65*, 104018.
- [7] H.-D. Kim, S. V. N. Pammi, H.-W. Lee, S. W. Lee, S.-G. Yoon, J. Park, Y. J. Kim, H.-S. Kim, *J. Alloys Compd.* **2020**, *815*, 152404.
- [8] J. H. Eom, H. J. Choi, S. V. N. Pammi, V. D. Tran, Y. J. Kim, H. J. Kim, S. G. Yoon, *J. Mater. Chem. C* **2018**, *6*, 2786.
- [9] Y. Fu, H. Zhu, C. C. Stoumpos, Q. Ding, J. Wang, M. G. Kanatzidis, X. Zhu, S. Jin, *ACS Nano* **2016**, *10*, 7963.
- [10] Y. Dong, Y. Gu, Y. Zou, J. Song, L. Xu, J. Li, J. Xue, X. Li, H. Zeng, *Small* **2016**, *12*, 5622.
- [11] Z. Sun, L. Aigouy, Z. Chen, *Nanoscale* **2016**, *8*, 7377.
- [12] S. Kim, J. M. Kim, J. E. Park, J. M. Nam, *Adv. Mater.* **2018**, *30*, 1.
- [13] R. D. Rodriguez, E. Sheremet, M. Nesterov, S. Moras, M. Rahaman, T. Weiss, M. Hietschold, D. R. T. Zahn, *Sensors Actuators, B Chem.* **2018**, *262*, 922.

- [14] M.-Y. Li, Q. Zhang, P. Pandey, M. Sui, E.-S. Kim, J. Lee, *Sci. Rep.* **2015**, 5, 13954.
- [15] S. Kunwar, M. Sui, Q. Zhang, P. Pandey, M.-Y. Li, J. Lee, *Nano-Micro Lett.* **2017**, 9, 17.
- [16] C. C. Zheng, S. J. Xu, F. Zhang, J. Q. Ning, D. G. Zhao, H. Yang, C. M. Che, *Appl. Phys. Lett.* **2012**, 101, 2010.
- [17] M. Li, M. Yu, S. Jiang, S. Liu, H. Liu, H. Xu, D. Su, G. Zhang, Y. Chen, J. Wu, *Mater. Horizons* **2020**, 6, 130.
- [18] Y. Tian, H. Wang, W. Xu, Y. Liu, S. Xu, *Sensors Actuators, B Chem.* **2019**, 280, 144.
- [19] M. Li, K. Shen, H. Xu, A. Ren, J. Lee, S. Kunwar, S. Liu, J. Wu, *Small* **2020**, 16, 2004234.
- [20] Q. Li, H. Wang, J. Ma, X. Yang, R. Yuan, Y. Chai, *J. Alloys Compd.* **2018**, 735, 840.
- [21] R. R. Prabhakar, N. Mathews, K. B. Jinesh, K. R. G. Karthik, S. S. Pramana, B. Varghese, C. H. Sow, S. Mhaisalkar, *J. Mater. Chem.* **2012**, 22, 9678.
- [22] Y. Li, Z. F. Shi, S. Li, L. Z. Lei, H. F. Ji, D. Wu, T. T. Xu, Y. T. Tian, X. J. Li, *J. Mater. Chem. C* **2017**, 5, 8355.
- [23] H. Zhang, X. Su, H. Wu, C. Liu, *J. Alloys Compd.* **2019**, 772, 460.
- [24] W. Wang, M. Wang, E. Ambrosi, A. Bricalli, M. Laudato, Z. Sun, X. Chen, D. Ielmini, *Nat. Commun.* **2019**, 10, 81.
- [25] F. Parveen, B. Sannakki, M. V. Mandke, H. M. Pathan, *Sol. Energy Mater. Sol. Cells* **2016**, 144, 371.

## CHAPTER 7. CONCLUSION AND FUTURE PLANS

### 7.1 Overall Discussion and Conclusion

Perovskite, an emerging novel optoelectronic semiconductor, has recently received extensive attention and has been widely studied in academia. As one of the fundamental components, perovskite photodetectors have been considered to have the most potential owing to their low cost, facile fabrication and high performance. Accordingly, the objectives of this PhD programme consisted of the synthesis of a high-quality perovskite material and the construction of high-performance perovskite photodetectors with a suitable bandgap for visible light detection.

The main challenge in constructing high-performance photodetectors lies in the material quality, device architecture and stability. The quality of perovskites is associated with the synthesis procedure; good synthesis can lead to high-quality materials. In addition, the material quality of low-dimension perovskites is related to their defect densities. As many ligands are involved in the synthesis, some of the long-chain ligands can be considered as an unwanted insulation barrier that hinders the carrier transport, resulting in a poor photoresponse. The device architecture also plays an important role in fabricating high-performance photodetectors. Various structures can be considered, including a lateral structure (photoconductor, phototransistor) and a vertical structure (photodiode). Moreover, additional structures can be designed to enhance the light confinement and achieve a good performance. Stability is the main challenge for perovskite-based optoelectronics, and there is an urgent requirement to optimise and solve this issue, paving the way to commercialisation.

Prior to the start of the present PhD project, the team of Professor Jiang Wu and Professor Kwang-Leong Choy achieved early successes with conventional and novel nanomaterials in various fields. Initial investigations consequently focussed on facile and cost-

effective novel low-dimension semiconductors, such as the aforementioned perovskite pathway.

In this thesis, all-inorganic perovskites ( $\text{CsPbBr}_3$  QDs) are employed as the active layer for absorbing and converting light into electricity. Compared to its organic counterparts,  $\text{CsPbBr}_3$  exhibits better thermal stability, while maintaining its excellent optical and electrical properties. Meanwhile, the characteristics of QDs enable them to be applied in LEDs, broadening their applications. Accordingly,  $\text{CsPbBr}_3$  QD-based photodetectors were fabricated and further investigated regarding their optoelectrical characteristics and the relationship between the fabrication process and device structure. The main work and conclusions in this PhD thesis are listed as follows:

- (1) According to the needs of scientific research, a spectral response test system was designed and built, and photocurrent measurements and responsivity and detectivity calculations were realised.
- (2) In order to learn more about the synthesised materials, various equipment was systematically trained, studied and used, including UV-Vis, PL, TRPL, XRD, XPS, UPS, AFM, SEM, TEM and EDX.
- (3) A simple and facile synthesis procedure of  $\text{CsPbBr}_3$  QDs under ambient conditions was investigated. Short-chain ligands and environmentally friendly solvents were utilised to prepare  $\text{CsPbBr}_3$  QDs. Moreover, by adjusting the quantity of each chemical, relatively high-quality  $\text{CsPbBr}_3$  QDs were grown. In addition, the annealing temperature and time of  $\text{CsPbBr}_3$  QD films were further optimised, and the optimal parameters were found to be 100 °C for 5 min, confirmed by various characterisation methods, such as PL, UV-Vis and AFM.
- (4) The  $\text{CsPbBr}_3$  QDs were further optimised with ZnO NPs, and a planar heterojunction photodetector was fabricated. The ZnO NP-assisted QD film not only exhibited a better

surface morphology with fewer pinholes and lower surface roughness, it also contained fewer trap states, thereby enabling more efficient carrier transport. The optimised QD photodetectors possessed a higher photocurrent and a lower dark current than the pristine device. Moreover, a self-powered characteristic was observed, realising the purpose of energy saving. The response speed was also enhanced from ~180 ms to ~70 ms, which is comparable to other system detectors. Most importantly, the device was able to operate for at least 7 months with negligible degradation.

- (5) As an alternative to ZnO NPs, a CsBr/KBr additive strategy was developed for improving CsPbBr<sub>3</sub> QDs in all aspects. By comprehensively characterising and analysing the obtained results, the optimal fraction of CsBr/KBr additive was confirmed (0.025). It is found that this ratio of blending enables a more compact and smoother surface, which is favourable for high-performance devices. Meanwhile, after optimal treatment of CsBr/KBr, the carrier lifetime was prolonged from 4.95 ns to 7.53 ns, and higher PL efficiency was observed, revealing the reduction of non-radiative recombination path and defect densities. The photodetectors were subsequently fabricated on flexible substrate to meet the increasing demand for wearable electronics. In order to achieve an impressive photoresponse, a sandwich structure was adopted in the photodetectors. Owing to the effective additive strategy and structural design, the optimal photodetectors exhibited an open-circuit voltage of 1.3 V, and realised the operation without an external power source. Under self-powered mode, the device exhibited a high responsivity of 10.1 A W<sup>-1</sup>, a large detectivity of 9.35 x 10<sup>13</sup> Jones, and an on/off ratio of up to ~10<sup>4</sup>. Moreover, excellent flexibility and electrical stability were achieved after 1600 bending cycles. This performance is a result of the enhanced material quality and strictly controlled fabrication. Considering practical imaging applications, photodetector arrays were further constructed.

(6) Instead of optimising perovskite itself, we applied an AAO matrix to enhance the spatial light confinement. The geometric control of pore size in AAO nanostructures was firstly investigated. It was confirmed with various characterisations that the device performance was significantly improved when the pore size was 220 nm, due to the effective collection of the reflected photons. Moreover, the incident and reflected light were further concentrated into QD films after decorating AAO matrices with metallic NPs. The best performance was achieved in Al NP-treated AAO nanostructure (pore size of 220 nm)-based perovskite photodetectors, with a 43-fold enhanced photocurrent.

Although three different methods were demonstrated in this thesis, they shared the same aim of enhancing the device performance and ultimately realising efficient and sensitive detection.

## 7.2 Future Plans and Outlook

On the basis of the work in this article, I believe that further research work can be carried out as follows:

### (1) Developing a lead-free perovskite system

The perovskite materials used in this thesis are CsPbBr<sub>3</sub> QDs, which contain the toxic lead element. The leakage of lead would cause environmental pollution, which is harmful for human beings and lifecycles, and does not obey the laws and regulations in some countries. This issue significantly limits the practical applications of such devices. Therefore, it is of great significance to develop lead-free perovskite systems for practical applications.

In order to compensate the toxicity issue, Sn<sup>2+</sup>, Mn<sup>2+</sup> or Ge<sup>2+</sup> will be considered to fully or partially replace Pb<sup>2+</sup>.<sup>[1-3]</sup> In particular, Sn<sup>2+</sup> substitution has great potential. However, Sn<sup>2+</sup> is sensitive to moisture and oxygen, and is easily oxidised to Sn<sup>4+</sup> when

exposed in air, resulting in a poor photoresponse. Moreover, Sn-based solar cells show a lower PCE than Pb-based solar cells, suggesting that the substitution of  $\text{Sn}^{2+}$  would sacrifice the device performance.<sup>[1]</sup> Therefore, it is a great challenge to develop stable lead-free perovskite photodetectors while maintaining the performance.

## (2) Broadening the spectral response

The as-synthesised  $\text{CsPbBr}_3$  QDs have a limited spectral response and are not able to detect NIR light. Therefore, broadening the spectral response of photodetectors is another work intended for the future. As mentioned previously, although the bandgap can be adjusted to the NIR range by replacing  $\text{Br}^-$  with  $\text{I}^-$  and alloying the material with  $\text{Sn}^{2+}$ , the resulting perovskite is unstable in air, which causes it to become metallic. In addition, the synthesis of such perovskite needs to be carried out in a glove box under  $\text{N}_2$  atmosphere, which is relatively inconvenient. Therefore, it would be better to find other narrow-bandgap semiconductors to enhance the absorption in the NIR region, e.g. PbS QDs, which could be a candidate for combining with perovskites.<sup>[4–6]</sup> As shown in Figure 7.1, the active layers are comprised of perovskite and PbS QDs, which is expected to enhance the photosensitivity in the NIR region, offering the benefit of broadening the spectral response.

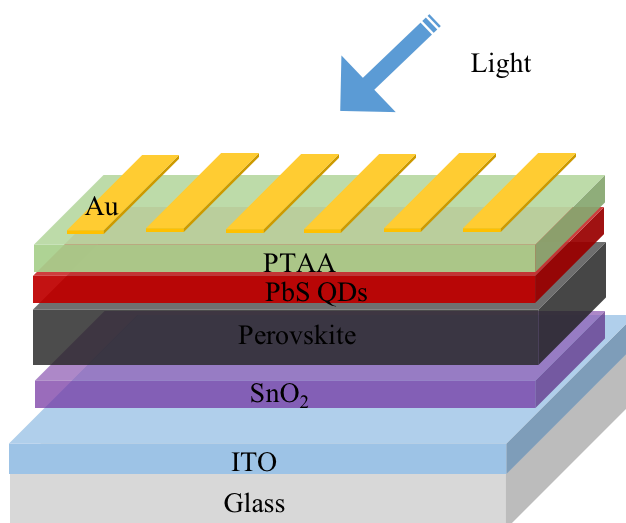


**Figure 7.1** The proposed device architecture for extending the spectral response.

### (3) Developing perovskite-based nanosystem

With the rapid development of the Internet of Things (IoT) and 5G, the demand for smart electronics is ever-increasing. Although many achievements have been made in conventional semiconductors, they are relatively complex and expensive. Therefore, it is highly desired to develop multifunctional nanosystems with perovskite materials. For example, visible light communication can be achieved by coupling commercial photodetectors with LEDs equipped with perovskite colour converters.<sup>[7–9]</sup>

However, the reports of nanosystems based on perovskite devices are very limited. Therefore, a simple flexible perovskite solar charger is proposed to meet the requirements of wearable devices, as shown in Figure 7.2. Perovskite solar cells and supercapacitors will be integrated onto the flexible substrate, realising the function of solar charging.

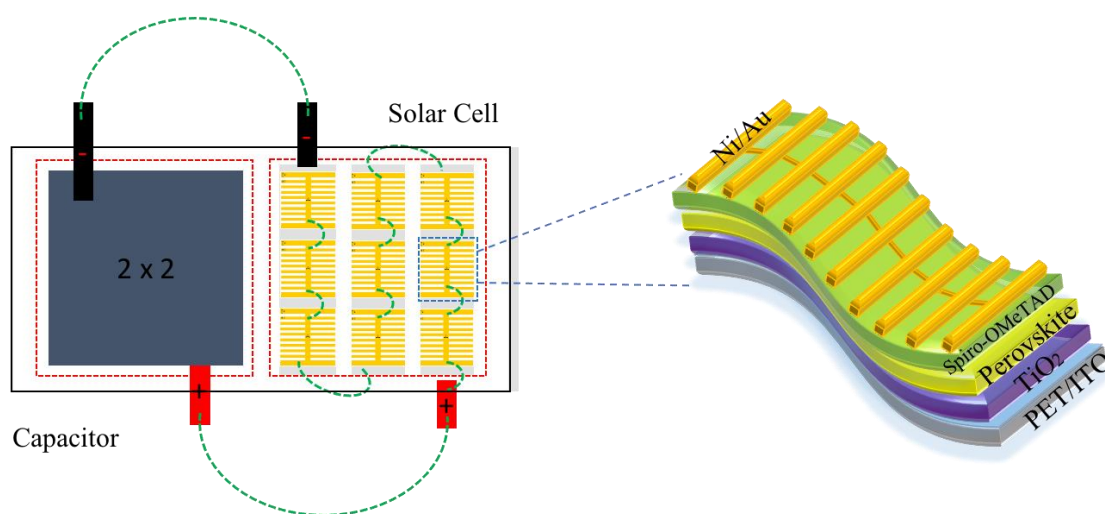


**Figure 7.2** Schematic illustration of flexible perovskite solar capacitor nanosystem.

### (4) Perovskite-based focal plane arrays

Integrated circuits based on complementary metal-oxide-semiconductors (CMOS) have been at the heart of the technological revolution of the past 40 years, enabling low-cost imaging systems. However, the difficulty of integrating non-silicon electro-optical materials with silicon-integrated circuits has been a serious impediment to unlocking

their vast potential for imaging beyond the visible range in on-chip low-power optical data communication and sensing systems. In 2017, a graphene-CMOS integrated imaging sensor was already developed, showing great potential in integrated photonics and array sensors.<sup>[10]</sup> Therefore, perovskite focal plane arrays are planned to be fabricated on readout circuits, achieving real-time and high-resolution imaging. The device structure is shown in Figure 7.3.

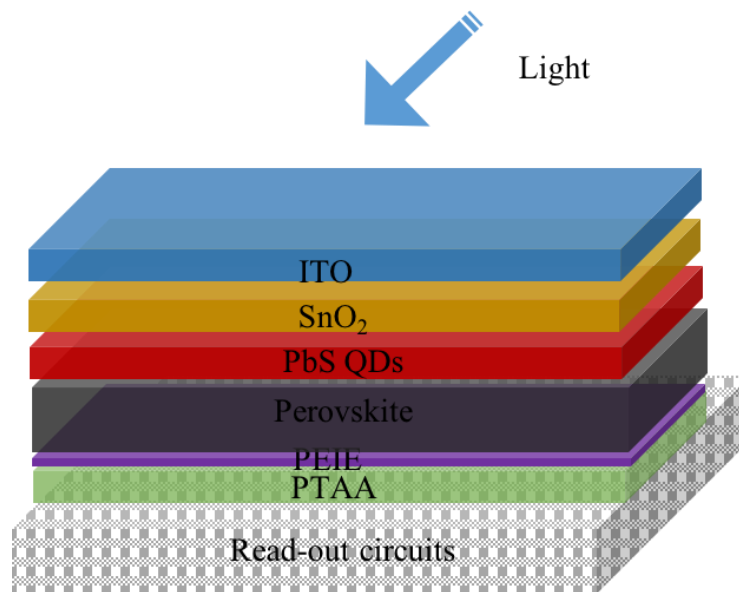


**Figure 7.3** The illustration of photodetector arrays for real-time imaging.

At present, research into perovskite materials and perovskite devices is rapidly growing. A lot of high-quality literature is being reported, and numerous novel structures and optimisations are being demonstrated. In addition, the industrialisation of perovskite-based optoelectronics is steadily developing. For example, mass-produced large-scale perovskite solar cells and QD-based displays have already appeared at some technology exhibitions.

It is reasonable to believe that perovskite material systems, as one of the most promising optoelectronic materials, will be widely used in all aspects of humans' daily lives. Perovskite photodetectors will also benefit our way of life via fast visible light communication, visible light imaging and other practical applications.

### 7.3 References

- [1] X.-L. Li, L. Gao, Q. Chu, Y. Li, B. Ding, G. Yang, *ACS Appl. Mater. Interfaces* **2019**, *11*, 3053.
- [2] M. Chen, M. G. Ju, H. F. Garces, A. D. Carl, L. K. Ono, Z. Hawash, Y. Zhang, T. Shen, Y. Qi, R. L. Grimm, D. Pacifici, X. C. Zeng, Y. Zhou, N. P. Padture, *Nat. Commun.* **2019**, *10*, 1.
- [3] H. C. Wang, Z. Bao, H. Y. Tsai, A. C. Tang, R. S. Liu, *Small* **2018**, *14*, 1.
- [4] C. Liu, K. Wang, P. Du, E. Wang, X. Gong, A. J. Heeger, *Nanoscale* **2015**, *7*, 16460.
- [5] C. Liu, H. Peng, K. Wang, C. Wei, Z. Wang, X. Gong, *Nano Energy* **2016**, *30*, 27.
- [6] J. Tang, K. W. Kemp, S. Hoogland, K. S. Jeong, H. Liu, L. Levina, M. Furukawa, X. Wang, R. Debnath, D. Cha, K. W. Chou, A. Fischer, A. Amassian, J. B. Asbury, E. H. Sargent, *Nat. Mater.* **2011**, *10*, 765.
- [7] S. Mei, X. Liu, W. Zhang, R. Liu, L. Zheng, R. Guo, P. Tian, *ACS Appl. Mater. Interfaces* **2018**, *10*, 5641.
- [8] I. Dursun, C. Shen, M. R. Parida, J. Pan, S. P. Sarmah, D. Priante, N. Alyami, J. Liu, M. I. Saidaminov, M. S. Alias, A. L. Abdelhady, T. K. Ng, O. F. Mohammed, B. S. Ooi, O. M. Bakr, *ACS Photonics* **2016**, *3*, 1150.
- [9] M. F. Leitao, M. S. Islim, L. Yin, S. Viola, S. Watson, A. Kelly, X. Li, D. Yu, H. Zeng, S. Videv, H. Haas, E. Gu, N. Laurand, M. D. Dawson, in *2017 IEEE Photonics Conf.*, IEEE, **2017**, pp. 69–70.
- [10] S. Goossens, G. Navickaite, C. Monasterio, S. Gupta, J. J. Piqueras, R. Pérez, G. Burwell, I. Nikitskiy, T. Lasanta, T. Galán, E. Puma, A. Centeno, A. Pesquera, A. Zurutuza, G. Konstantatos, F. Koppens, *Nat. Photonics* **2017**, *11*, 366.